



LUND UNIVERSITY

Search for beyond Standard Model physics with same-sign dileptons

Hawkins, Anthony; ATLAS Collaboration

2014

[Link to publication](#)

Citation for published version (APA):

Hawkins, A., & ATLAS Collaboration (2014). *Search for beyond Standard Model physics with same-sign dileptons*. [Doctoral Thesis (monograph), Particle and nuclear physics]. Department of Physics, Lund University.

Total number of authors:

2

General rights

Unless other specific re-use rights are stated the following general rights apply:

Copyright and moral rights for the publications made accessible in the public portal are retained by the authors and/or other copyright owners and it is a condition of accessing publications that users recognise and abide by the legal requirements associated with these rights.

- Users may download and print one copy of any publication from the public portal for the purpose of private study or research.
- You may not further distribute the material or use it for any profit-making activity or commercial gain
- You may freely distribute the URL identifying the publication in the public portal

Read more about Creative commons licenses: <https://creativecommons.org/licenses/>

Take down policy

If you believe that this document breaches copyright please contact us providing details, and we will remove access to the work immediately and investigate your claim.

LUND UNIVERSITY

PO Box 117
221 00 Lund
+46 46-222 00 00

978-91-7623-089-3

978-91-7623-090-9

Search for beyond Standard Model physics with same-sign dileptons

Thesis submitted for the degree of
Doctor of Philosophy
by

Anthony Hawkins



LUNDS
UNIVERSITET

DEPARTMENT OF PHYSICS
LUND, 2014

To be presented, with the permission of the Faculty of Science of Lund University, for public criticism in Rydbergs Lecture Hall in the Department of Physics on Friday, the 28th of November 2014, at 10.00.^I

^IThe front cover of this thesis is a modification of a figure first used in CERN courier magazine [1]

Organization LUND UNIVERSITY Department of Physics Lund University Box 118 SE-221 00 Lund SWEDEN		Document name DOCTORAL DISSERTATION
		Date of issue October, 2014
		CODEN LUNFD6/(NFFL-7235)2014
Author(s) Anthony Hawkins		Sponsoring organisation
Title and subtitle Searches for beyond Standard Model physics with same-sign dileptons		
Abstract An introduction into the theory and experimental background of particle physics and the ATLAS detector is given. The transition radiation tracker (TRT) which is vital to the particle tracking and identification is then described giving particular credence to the calibration. The automation of this calibration is explained. The second half of this thesis and the central part dwells on the analyses searching for beyond Standard model physics at the ATLAS detector using same-sign dilepton pairs ($e^{\pm}e^{\pm}, e^{\pm}\mu^{\pm}, \mu^{\pm}\mu^{\pm}$) during both the 7 TeV and 8 TeV data taking periods at the Large Hadron Collider (LHC). In both searches no significant excess from the standard model (SM) was seen. Limits were set on the fiducial cross-section for new physics as a function of invariant mass. Exclusion limits are also derived for a specific model of doubly charged higgs boson production and are seen to improve from the 7 TeV analysis to the 8 TeV analysis.		
Key words: LHC, ATLAS, Beyond Standard Model, Doubly Charged Higgs, TRT, Same-sign leptons		
Classification system and/or index terms (if any)		
Supplementary bibliographical information:		Language English
ISBN (PDF) 978-91-7623-090-9		ISBN (Print) 978-91-7623-089-3
Recipient's notes	Number of pages 206	Price
	Security classification	

Distribution by (name and address)

Anthony Hawkins
 Department of Physics
 Div. Particle Physics
 Box 118, SE-221 00 Lund, SWEDEN

I, the undersigned, being the copyright owner of the above-mentioned dissertation, hereby grant to all reference sources permission to publish and disseminate the abstract of the above-mentioned dissertation.

Signature 

Date 20/10/2014

To my Family

Contents

Contents	7
Preface	i
1 Introduction	1
1.1 Atoms, Electrons, Quarks and all that jazz	1
1.2 Enter Standard Model	3
1.3 Standard Model Lagrangian	5
1.3.1 The Higgs Mechanism and Higgs Boson	13
1.3.2 Spontaneous Symmetry breaking and the Higgs Mechanism	14
1.3.3 Beyond the Standard Model	17
2 Machines and Dectectors	19
2.1 The Large Hadron Collider	19
2.1.1 Why a Proton Synchrotron Collider?	20
2.1.2 The Proton Adventure	21
2.1.3 The Big Four	22
2.1.4 Luminosity	23
2.2 ATLAS Detector	25
2.2.1 Overview	27
2.2.2 Magnet System	28
2.2.3 Inner Detector Tracker	28
2.2.4 Calorimeters	30
2.2.5 Muon Spectrometer	32
2.2.6 Beam Monitoring and Luminosity	33
2.2.7 Triggers and Data Acquisition	34
2.2.8 Event Reconstruction and Data Quality	34
3 TRT	37
3.1 Tracking with the TRT	38
3.2 Making a hit in the TRT	40
3.3 Calibration	42
3.3.1 T_0 Calibration	43
3.3.2 $r - t$ relation Calibration	43
3.3.3 Validity of Calibration	45

3.4	Automating the Calibration	46
3.4.1	Structural Overview	46
3.4.2	Calibration Steps	47
3.4.3	Monitoring	49
3.4.4	Configuration	49
3.4.5	Outlook	50
4	Same Sign Dilepton Analysis Motivation	51
4.1	Six impossible things to believe before breakfast	53
4.1.1	Supersymmetry	53
4.1.2	Heavy Majorana Neutrinos	53
4.1.3	Doubly Charged Scalars	55
4.1.4	Zee-Babu	56
4.1.5	Microscopic Black Holes and Extra Dimensions	56
4.1.6	Same-sign Top Quarks	57
4.2	Layout of analysis sections	58
5	Same Sign: Event Selection	59
5.1	Electron Selection	59
5.2	Muon Selection	61
5.3	Jet Selection	62
5.4	Event Selection	63
6	Same Sign: Data and Backgrounds	65
6.1	Prompt SM Backgrounds	65
6.2	γ Conversions	67
6.3	Data taken	68
6.4	Charge Misidentification	69
6.4.1	Electron Charge Misidentification	69
6.4.2	Muon Charge Misidentification	78
6.5	Non-Prompt (Fake) Leptons	80
6.5.1	Fake Factor Method Summary	80
6.5.2	Electron Fake Factors	82
6.5.3	Muon Fake Rates	88
7	Same Sign: Validation Regions	93
7.1	Opposite-sign Validation Region	93
7.2	Prompt Validation region	95
7.3	Fake Validation Regions	97
7.3.1	Charge Flip Validation Region	98
8	Same Sign: Uncertainties	105

9	Same Sign: Results of the Inclusive Search	109
9.1	Limit Setting	110
9.1.1	Limit Plots	120
9.1.2	Comparison to 7 TeV results	124
10	Same Sign: Doubly Charged Higgs Interpretation	127
10.0.3	Mass binning	128
10.0.4	Total Efficiency	129
10.0.5	Signal Systematics	131
10.0.6	Setting the Limits on the Doubly Charged Higgs Boson Production Cross-section	132
10.0.7	Comparison to 7 TeV results	137
11	Summary and Conclusions	139
11.0.8	Conclusions	139
11.0.9	Outlook	139
	Appendices	143
A		145
A.1	Standard Model Reference Table	145
A.2	7 TeV Results Appendix	146
A.3	Electron Charge Flip Systematics for 8TeV analysis	151
A.4	Electron Fake Factor systematics	151
A.4.1	Away side jet kinematics and prompt subtraction	151
A.4.2	Systematic Uncertainty Associated with the light/heavy Flavour Com- ponents	151
A.5	Electron Intermediate Isolation Fakes	154
A.5.1	Intermediate isolation Numerator and Denominator	154
A.5.2	Medium++ Numerator and Denominator	155
A.6	Muon Fake Systematics	155
A.6.1	Systematic uncertainty associated with the light-flavor component	155
A.7	Muon Intermediately Isolated Fakes	158
A.8	Additional Validation Region Plots	160
A.8.1	Prompt Validation Region	160
A.8.2	Fake Validation Region	162
A.9	Fake Rate Dependence on Pile-Up	166
A.10	Additional plots for 8 TeV signal Regions	166
A.11	Jet Multiplicity Distributions	169
A.12	Number of Same Sign pairs per Event	171
A.13	Fiducial Efficiencies	171
	Glossary	179

Preface

This thesis represents the last four years of my life as a PhD student and researcher here in Lund. Having everything one has done in a big tidy book is a very satisfying and complete thing to do. During my time as a student I have learnt an incredible amount from programming to physics to working in large collaborations to writing articles to dealing with stress to applying for conferences to a new language as well as everything in between. It has been a long road to arrive here.

The thesis will begin with a basic introduction to the field of particle physics in Chapter 1. I first started my experience with my technical task which was to help with the Transition Radiation Tracker (TRT) Calibration (a sub-detector of the ATLAS detector... all will be explained later). Chapters 2 and 3 go into detail about the ATLAS detector and the latter specifically the TRT and its calibration. I was thrown into the software side of things where I needed to develop a way of automating the calibration of the TRT. I really had to get to grips with the detector, the calibration methods, python scripting and software and computing structures at ATLAS, which is tough but useful. I did not need to re-do or improve on any of the calibration algorithms but to implement them in one neat automated package.

After completing my technical work for ATLAS with the TRT it was time to get stuck in with the analysis side of things. Having Else as my supervisor it was natural that I would be interested in exotics searches with leptons. I was immediately drawn to the general inclusive searches. I didn't have any great feeling for which one of the countless Beyond Standard Model theories was more likely or interesting. Rather, I liked the idea of doing a general search for new physics, holding up my hands and saying I am not looking for anything specific but I know there is more out there for the universe to reveal.

Chapters 4 to 11 document my work with the same sign dilepton Analysis for both the 7 TeV and 8 TeV searches. So over the past couple years of my PhD I have been involved in the same-sign dilepton analysis, firstly analysing the 7 TeV collisions recorded by the ATLAS detector in 2011 and most recently analysing the 8 TeV collisions recorded in 2012 by ATLAS. For the first analysis my involvement was mostly in the electron charge misidentification prediction however I also was strongly involved in providing cross-checks for the $\mu\mu$, $e\mu$ and ee channels and developing the validation regions for the $e\mu$ channel. In the 8 TeV analysis I played a much larger role. As the senior PhD student in the analysis my role was to work on the fake/non-prompt electron and muon predictions, make the

event and lepton selections, study the MC inputs, provide cross-checks to all channels, advise on charge misidentification methods for both electrons and muons, design validation regions and various other odds and ends. In essence I played a more active role in the recent analysis which is why for these chapters I will describe the 8 TeV analysis (except for the charge misidentification) but will point out the crucial differences between the two analyses along the way. At the end of the results chapters I will present the 7 TeV results and briefly compare the two. Here the different chapters are split according to the different sections of the analysis. The chapters pertaining to these analyses are based on the papers and conference notes below as well as their corresponding internal notes and hence contain tables, figures, equations and phrases taken directly or modified from these sources. At the end of the thesis I have included a glossary section which very briefly reminds readers of some of the more jargon-like terms and abbreviations used reccurringly in this thesis and at ATLAS. The caveat is of course that these definitions are helpful prompts and are thus are not necessarily complete in and of themselves. Furthermore, some of the definitions are specific to this thesis and may be used alternatively elsewhere in literature.

List of Publications

- I *Search for anomalous production of prompt like-sign lepton pairs with the ATLAS detector*, ATLAS Collaboration, ATLAS-CONF-2012-069, these preliminary results were superseded by following papers.
- II *Search for anomalous production of prompt like-sign lepton pairs with the ATLAS detector*, ATLAS Collaboration, Published in JHEP12 (2012) 2244.
- III *Search for doubly-charged Higgs bosons in like-sign dilepton final states at $\sqrt{s} = 7$ TeV with the ATLAS detector*, ATLAS Collaboration, Published in EPJC 72 (2012) 007.

Pending Publication

- I *Search for anomalous production of prompt like-sign lepton pairs and doubly charged Higgs bosons with $\sqrt{s} = 8$ TeV pp collisions using the ATLAS detector*, ATLAS Collaboration, to be published in JHEP - pending approval (2014)

Populärvetenskaplig Sammanfattning (Popularised Summary in Swedish)

Frågorna som partikelfysiker ställer är samma frågor som folk har ställt under hela mänsklighetens tid på jorden, nämligen: Var kommer vi från? Vad är det som bygger upp det universum som vi ser? Hur håller allting ihop? Fysiker, historiens stora tänkare och hobbyfilosofen i pubben har alla funderat över de här frågorna (vissa mer än andra). Partikelfysiker försöker hitta svaret från perspektivet av universums minsta beståndsdelar, partiklar. Under de senaste hundra åren ha vi förstått mer och mer av de små partiklarna

som bygger upp allt vi ser från igelkottar till planeter, hur de interagerar med varandra och vilka krafter som håller universum samman. Denna skattkista av kunskap, experiment och teori heter Standardmodellen.

Standardmodellen (SM) har varit grymt bra på att förutsäga och förklara i princip allting som vi ser från experiment. Upptäckten av Higgsbosonen var den sista delen av pusslet. SM är inte det sista kapitlet i vår historia. Det vet vi fysiker väl, oavsett hur vacker och kraftfull den är, så vet vi att den inte är komplett. Det finns vissa frågor som skrika efter att bli besvarade:

- Hur ska vi förena gravitationskraften med de andra krafterna i Standardmodellen? (Gravitationskraftens styrka är enormt mycket mindre än de andra tre krafterna: Den svaga, starka och elektromagnetiska. Därför är den försummad i SM.)
- Varför har Higgsbosonen den massa som den har ? (Hierarkiproblemet)
- Varför har vi bara tre generationer av partiklar? Varför har partiklarna den massa och de kopplingskonstanter som vi observerar?
- Varför finns det mer materia än antimateria i universum?
- Hur passar mörk materia in i SM?
- Finns det någon energiskala där alla krafter förenas?

Det finns oändligt många olika teorier som försöker svara på de här frågorna. Alla de teorier som försöker utöka och bygga på SM kallas för Beyond Standard Model (BSM) fysik. Vissa modeller löser mer än en av frågorna men nästan alla leder till flera nya partiklar eller krafter som borde kunna observeras direkt eller indirekt i experiment. Ett experiment som försöker besvara vilka BSM-modeller som är rätt (kanske ingen) är ATLAS-detektorn vid Large Hadron Collider (LHC). I princip är experimentet väldigt enkelt. Kollidera två protoner vid otroligt hög energi (så att de färdas nära ljusets hastighet) i mitten av ATLAS-detektorn. Einstein visade under tidigt 1900-tal hur energi och materia är releterade, så tanken med högenergikollisioner är att ju högre energi desto mer massiva partiklar kan skapas. Förhoppningsvis kan vi observera en ny partikel eller kraft som en eller flera av BSM-modellerna förutsäger.

LHC är begränsad av sin maxenergi (14 TeV) vilket betyder att den bara är känslig för de BSM-modeller som förutsäger partiklar eller krafter lägre än denna energi. Det finns många sätt att observera dessa hypotetiska partiklar i vår ATLAS-detektor. De absolut flesta sönderfaller till lättare partiklar som existerar i SM, till exempel elektroner och myoner. Man kan konstruera en specifik analys för att leta efter en bestämd modell eller designera en analys som letar efter en stor mängd av olika modeller. I den här avhandlingen har den senare metoden använts. Många BSM-modeller förutspår partiklar som sönderfaller till par av leptoner med samma laddning (e^+e^+ , $e^+\mu^+$, $\mu^+\mu^+$). Dock finns det inte så många processer i SM som leder till sådana par. Följaktligen finns det en bra chans att observera ny fysik om den existerar. Så min forskningsuppgift var att leta igenom miljarder av kollisioner för att hitta de kollisioner där par av leptoner med samma laddning

observerades i detektorn. Därefter kan man uppskatta hur många sådana kollisioner man förväntar sig från processer i SM och jämföra det med hur många kollisioner man faktiskt observerar. För varje leptonpar kan man rekonstruera massan av moderpartikeln. Nu kan man undersöka i olika massregimer om man har observerat en statistiskt signifikant skillnad mellan Standardmodellens förutsägelse och datan från ATLAS.

Som jag kommer att visa i det här avhandlingen, ingen statistiskt signifikant skillnad observerats mellan Standardmodellens förutsägelse och experimentell data. Det betyder att man, med en viss sannolikhet, kan säga att ingen ny fysik som leder till par av leptoner med samma laddning existerar under en viss energi. Så även om ingen ny fysik upptäcktes tack vara min forskningsuppgift så har vi lyckats begränsa eller utsluta vissa teorier och däremed tagit ett litet steg närmare upptäckten av ny fysik.

Acknowledgements

This thesis would not exist without the love, support, laughter, distraction, guidance, wisdom and help of a great deal of people, too many to be named here. First of all I would like to thank my supervisor Else Lytken whom gave me the chance to pursue a PhD in particle physics and whom guided me along my winding path to this thesis and through the exotic world of BSM physics. Torsten Åkesson my co-supervisor whom has always been gracious in taking the time to discuss my work, thesis and career and help create a great atmosphere here at the division. Thanks also to Anders Oskarsson and Anders Floderus for extensive proof-reading of this thesis. I would like to thank all the other staff at the department whom I have shared many the exciting lunch time and corridor conversation discussing everything from grand unified theories of physics to Englands recent football form to which Skåneleden trail to pursue. I would like to thank Bozena too, whom orchestrated life here at the department and helped settle me in at the division from day one until now (as well as discussing how to make jams and pick cantarelle mushrooms). Over the years all the PhD and masters students both in the ALICE and ATLAS offices have made life at the department just that little more fun and provided a great deal of discussion of all kinds of stuff: physics, grammar, code bugs, gender equality, meaning of life, beer brewing you name it. The list is long but you know who you are, so thanks. I would like to especially thank Alejandro Alonso whom took me under his wing the first couple of years as a PhD student and put up with all my stupid questions about the TRT and ATLAS and helped me get to grips with everything and stay on track.

There are scores of people whom I have had the pleasure to work with and learnt so much from my years working on the same-sign analyses at ATLAS: Beate Heinemann, Dominick Olivito, Francesco Nuti, Kenji Hamano, Louise Skinnari, Martina Hurwitz, Monika Wielers, Nick Rodd and Oleksandr Viazlo. Thanks to these peoples patience, expertise and willingness to help and work together I have learnt so much.

Of course one cannot live on physics alone! So I am very grateful for the many friends I have both here in Sweden and across the seas whom I have had such a great time with living and enjoying life outside of the physics bubble, you all know who you are! I am so

thankful to my family whom encouraged me to move from merry old England to the frozen viking Sweden to pursue my PhD and take the next step in my journey, they have been a constant source of encouragement and support. Lastly I would like to thank my girlfriend Ylva without whom I am certain I would not have the strength to finish this thesis whilst still holding a smile. Thank you so much for you unwavering love, support, enthusiasm and for putting up with all the high and lows of my PhD experience.

There is a theory which states that if ever anyone discovers exactly what the Universe is for and why it is here, it will instantly disappear and be replaced by something even more bizarre and inexplicable. There is another theory which states that this has already happened.

Douglas Adams, *The Restaurant at the End of the Universe*

1

Introduction

Particle physics from the outside can seem to be some hideously abstract, complex, inhuman and far-removed entity. But in fact, the underlying questions of particle physicists are the very same as humans have been posing to themselves, one way or another, from the dawn of time. In essence How did everything we see, touch, feel, experience come about and stay together? What makes up this fantastic universe we see? What laws govern the natural world we live in?

After this sufficiently pretentious start, I would like to take it down a notch and say from the very beginning that, like all interesting research areas, there is an incredible amount science has learnt in pursuing the answers to these questions. However there is a seemingly infinite amount more we don't or can't know and is waiting to be discovered! Firstly, thank you for reading thus far in my thesis. The idea of this chapter is to introduce particle physics in a broad sense and some of the topics I have looked at in my thesis. In this introduction I imagine the readers stem from people who have been studying this field for 40 years to those who haven't done any physics since school. With that in mind I will start gently and slowly build the complexity so hopefully all readers can enjoy some part of this introduction. The proceeding chapters will follow a similar model whereby the first paragraph or two will be a layman's explanation of the chapter so that everyone can follow and thereafter shall we delve into the juicy details.

1.1 Atoms, Electrons, Quarks and all that jazz

The idea that life, the universe and everything we see, from a cup of tea to a killer whale to a distant galaxy are all made from the same building blocks is a remarkable notion. It was

the ancient Greeks in the 6th century who first penned the idea of the "Atmos" which was an un-splittable, indivisible object from which the splendours of the universe were built on. Indeed, the entire narrative of particle physics is led by the exploration of matter at a smaller and smaller level and detail to try and arrive at what these fundamental building blocks, the cosmic Lego, are and which rules they follow in order to lead us to the behaviour we see in the natural world.

It was not until 1805 when the scientific world began to embrace the atom not only as a beautiful concept but as a means to explain scientific experiments. It was John Dalton who first used the "law of multiple proportions" to explain why elements react in ratios of whole numbers due to their constituent make-up of atoms [2]. Then later on in the century people began to question whether the atom really was the most fundamental of all building blocks after all. It wasn't until 1896 when using cathode rays (an evacuated glass tube with a high voltage across it) J.J.Thomson could prove the existence of what we now know as the electron [3], a tiny negatively charged particle that was neither wave nor atom. Having made this discovery, it was clear to Thomson that since atoms were supposedly neutral, and these electrons which made up in some part the atom were negative, that there must be some positively charge component to the atom in order to balance.

This led to the rather quaintly named "Plum Pudding" model, with the idea that the atom was like a positively charged pudding with small raisins (electrons) baked in. This was consequently examined by Rutherford in 1911 [4], who managed to show that this model was in fact incorrect and rather surprisingly that the atom must consist of a highly dense, concentrated, positive core which we call the nucleus. In fact the vast majority of the atom was empty, nothingness; so bizarre that if you took out all the empty space out of the atoms that make up all the humans on the planet we could fit into an apple! Over the next 20 years many scientists postulated as to what this core could be. Then came the concept of the proton, similar to the electron yet much heavier and positively charged. Then perhaps even more surprisingly, it was shown that the nucleus also contained another neutral, uncharged particle as heavy as the proton, the neutron. So here we have arrived at the basic model of the atom, the most fundamental of life's building blocks (see Fig. 1.1), or so was thought at the time... In fact there were many more particles to be discovered, in 1932 the incredulous idea of anti-particles were proposed [5] and then later on in 1964 the concept of quarks (constituents of protons/neutrons...) arrived on our doorstep [6] [7]. The story of particle physics is being written even now...

The reason why I am racing through this history lesson of particles is manifold. It is partially to show just how many great minds have grappled with these questions over such a long span of time, and how much great work has been done just to get to the point we are at today. But it is also to show the rapidity that this field has developed in the past 100 years and continues to develop. Moreover, it shows the scientific method in its glory, great minds coming together to create models to help understand the universe, then ten, twenty, fifty years later realising they were wrong or that their models were incomplete and plunging into the abyss of the unknown time and again to find more answers. Such is

the nature of research.

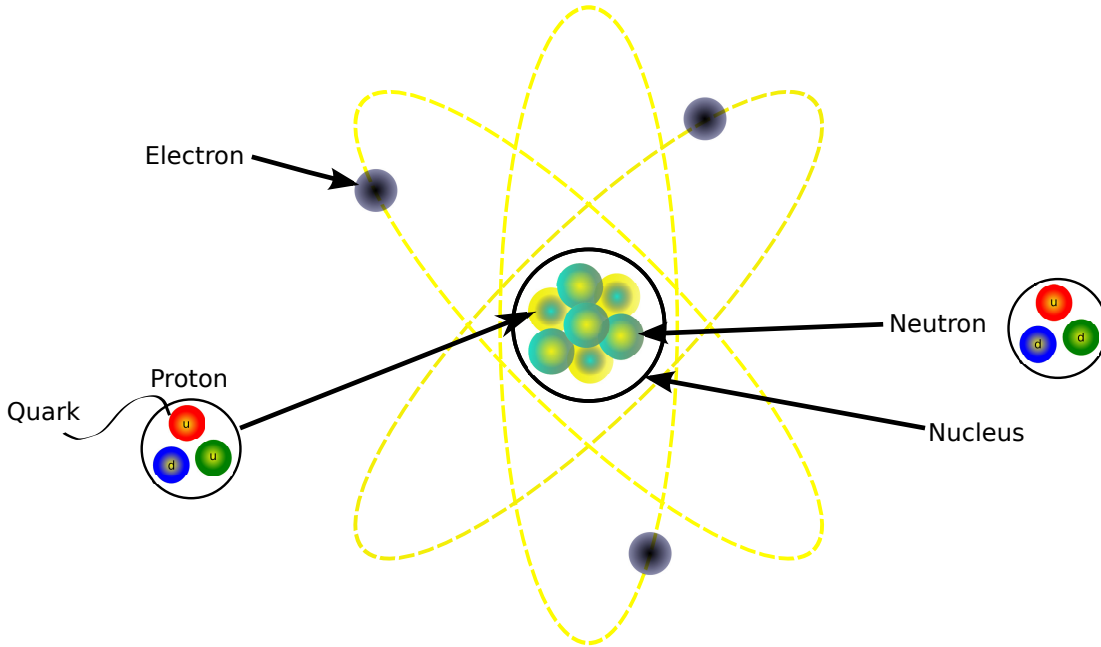


Figure 1.1: A simple illustration of an atom. The nucleus is built of protons and neutrons and orbited like planets round a star by electrons. The neutrons and protons are then built from quarks of various colour and charge.

1.2 Enter Standard Model

The Standard Model (SM) is the name for the theory which incorporates, more or less, everything we know about particle physics up until now [8]. In layman terms, it is a theory for how all the known particles interact with each other at the most basic level. It is a set of laws, rules and equations by which we can predict and describe all that we currently observe at the particle level. Even though it is one of the most beautiful theories in modern physics, we know that it is not the whole story. It is incomplete in part and has shortcomings, but these we shall get to later. For now let me introduce the particle zoo. This is the collection of all known fundamental particles (i.e. they are un-splittable, as far as we know) which make up all the known universe.

As seen from figure 1.2, a representation of the particle zoo, there are in fact only seventeen known fundamental particles which are responsible for all matter that we know and almost all the forces we know¹. It is also at this point that I should mention one of the caveats of the Standard Model, namely that it does not describe how gravity works at the small scale in which we consider these tiny particles interacting. However, for all intents

¹For more comprehensive information on charge, mass, name etc. of particles please refer to Appendix A.1

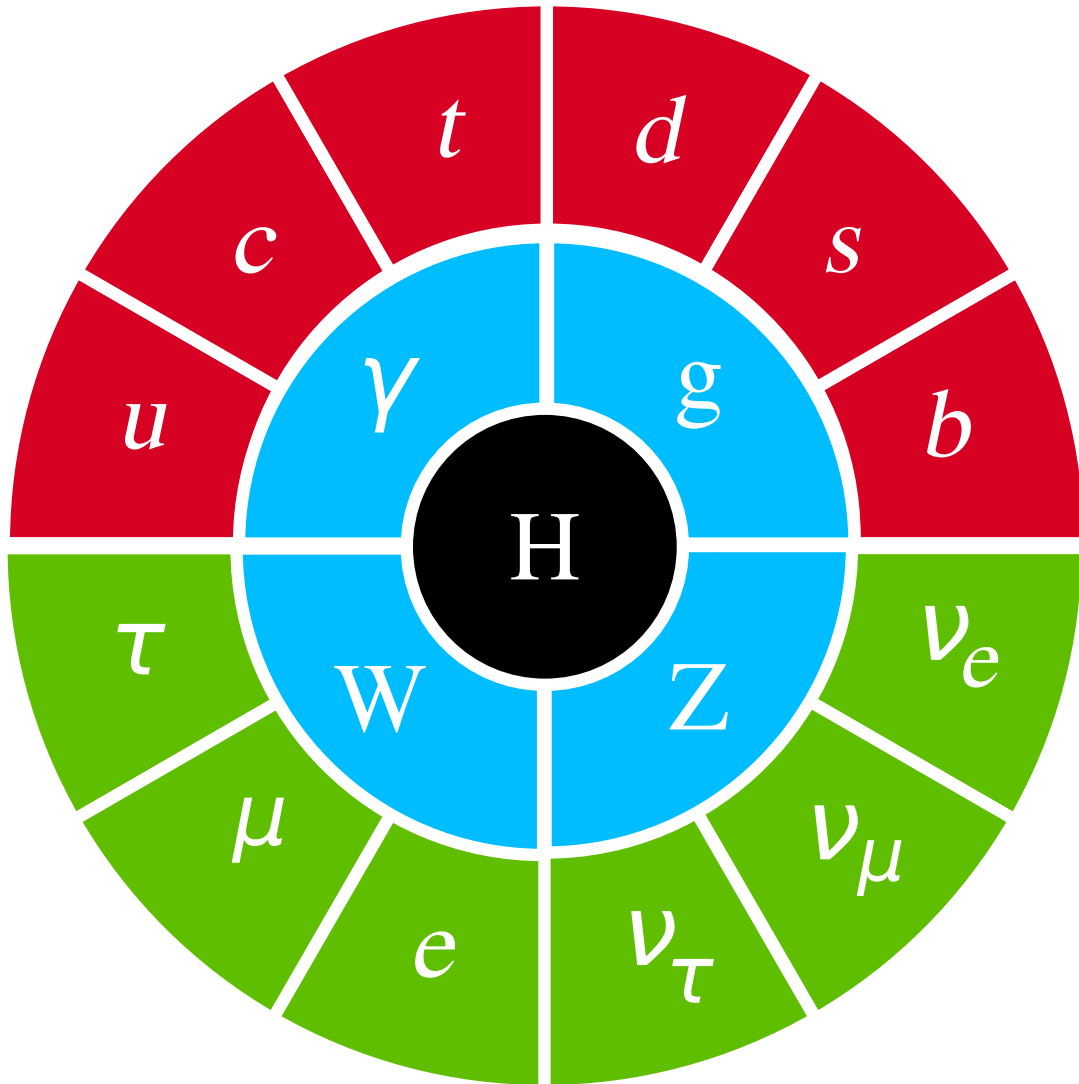


Figure 1.2: The Particle Zoo

and purposes gravity has an almost negligible effect on the particles at this subatomic scale, and hence its exclusion from the SM is not a problem.

So typically we can divide these particles into two main categories, fermions (outer circle) and bosons (inner circles), the former having half-integer ($\frac{1}{2}, \frac{3}{2}, \frac{5}{2}, \dots$) spin and the latter integer spin ($0, 1, 2, 3, \dots$). Here one can think of *spin* as the intrinsic angular momentum of a particle, an inherent property of the particle, like its mass. From these we make a further classification. We separate out the fermions into quarks (top outer red arc) and leptons (bottom outer green arc). Quarks are the particles which build to give protons and neutrons whereas leptons include electrons which we learnt were orbiting around the nucleus to build up the atom. In fact most of the visible matter in the universe is made from just three particles: the up and down quark and the electron. That is incredible to

think about! Now being physicist we like to group things, the set of quark pair (up and down) and electron/neutrino pair is called the first generation, since they are the lightest set of fundamental fermions. Remarkably (and puzzling to physicists) nature has two more generations which are exact copies of the first generation in every possible way except that they are successively heavier. Indeed the difference between the lightest quark in the first generation (up quark) and heaviest quark in the third generation (top quark) is the same as the difference between a kitten and a blue whale.

The bosons (the inner blue ring) in the SM are often called "force carriers". Just as computers need to send bits of data between each other to transfer information or cause a robot to move, so too do particles need something which communicates information and *cause* change; these carriers are our bosons. The photon is the force carrier for the electromagnetic force, which is responsible for most of modern technology. The W and Z bosons are responsible for carrying the weak force. Despite its name it is incredibly important. Without it we would not exist. By it, the sun's radioactive decays occur which initiates solar fusion leading to our sunlight and warmth and life on earth. Finally, we have the gluon which mediates the strong force responsible for binding up all the protons and neutrons into the core of an atom. Lastly, but not by any means least and the latest addition to the family, the Higgs boson (in black). Unlike the other bosons it is not responsible for mediating a force, but it is the means by which all the particles in the universe experience "mass". But this little fellow will have a whole subsection dedicated to herself.

So there you have a very simple introduction to the family of Standard Model particles. However to truly appreciate how these particles interact one needs to delve a little deeper into the mathematics. In order to fully understand nature at a fundamental level one needs to know: the intrinsic building block particles, which forces they experience and how to calculate mathematically the behaviour of the particles under those forces.

1.3 Standard Model Lagrangian

Here we will jump in the deep end so to speak and go straight to the lagrangian which describes all the known fermions and their interactions according the SM in one neat equation. I will then dissect the equation to give a brief overview of the different components of the lagrangian and go on to explain other parts of the SM theory such as how particles get mass. To express something in terms of lagrangians is nothing specific to particle physics. Indeed we can express classical mechanics and electrodynamics in terms of lagrangians which naturally lead to the Newton laws and the Maxwell equations respectively. In essence a lagrangian, \mathcal{L} , is given by $T - V$, the kinetic energy minus the potential energy. We wish to express the SM by a lagrangian for two reasons; firstly it contains all the dynamics, laws and forces in one equation, and secondly a lagrangian is by definition conserved between different frames of reference. In other words it does not matter if we are doing particles physics on the earth, the moon or 50 years ago or on a spacecraft travelling

near the speed of light, the physics is the same. If that were not so, it would make doing science near impossible. There are many different ways to derive or arrive at this equation, for one example you may read [9], which also explains the notations and representations I am using. So without further ado:

$$\mathcal{L}_{ferm} = \sum_f \bar{f} i \gamma^\mu D_\mu f \quad (1.1)$$

where the sum over f is the sum over all the fermions, γ incorporates all the information about the spin of the particles and D is the covariant derivative which contains all of the information about the interactions.

$$D_\mu = \partial_\mu - ig_1 \frac{Y}{2} B_\mu - ig_2 \frac{\tau^i}{2} W_\mu^i - ig_3 \frac{\lambda^a}{2} G_\mu^a \quad (1.2)$$

I do not wish to encumber the reader with too much notation declaration, but rather hope to elucidate the meaning of this equation in a more qualitative sense. So before adding even more terms and complexity, let's break down what we are really saying here. I will describe what all the terms in this equation mean in due course. In physics, the concept of symmetries is very important and underpins much of the Standard Model. A symmetry in nature is some physical or mathematical feature (either observed or intrinsic) which is preserved under some change. Take a sphere for instance, if we rotate it in any direction and then stop it will appear exactly the same as it did before. That is well and good, but how can physical laws of nature be *symmetrical*? Well, in essence the question is what can we change to a physical situation or phenomenon such that the results of an experiment are still the same. Symmetries are so beautiful due to the fact that from symmetries we obtain conservation laws, which give us information about the physical phenomena we are studying. This was first shown by the remarkable Noether's theorem [10].

In nature we have seen that there are three fundamental internal symmetries which lead to all our forces and their fundamental force carriers. One can think of these symmetries as rotations in particular spaces. Just as one rotates a sphere in regular 3-D space leaving the sphere looking the same. So too do these fundamental rotations leave the particle dynamics the same after their transformations. Why nature exhibits these three symmetries is unknown, and is one of the great questions of particle physics. Whether there are more than these three symmetries is yet another.

So in nature, we see all of the particle dynamics as the combination of three rotations (symmetries).

$$U(1) \times SU(2) \times SU(3) \quad (1.3)$$

Here one can think of $U(1)$, $SU(2)$, $SU(3)$ as a representation of those rotations in some special phase-space, some set of matrices which have all possible transformations in this phase-space encoded.

The SM is fundamentally a quantum theory, whereby we express all the forces and particles in terms of fields, and the observables depend on $|\psi|^2$ (ψ being the field). Gauge

symmetries are fundamental to particle physics, there are two types of gauge symmetries. Global symmetries are those where one changes the phase of the field by a constant for all time and space, $\psi \rightarrow \psi' = e^{-i\alpha}\psi$. Imagine simply looking at a sphere from one angle and then rotating the sphere some phase angle α and looking again. Then there are local gauge symmetries, where one can change the phase depending on the position (space) and time, $\psi(\vec{x}, t) \rightarrow \psi'(\vec{x}, t) = e^{-i\chi(\vec{x}, t)}\psi(\vec{x}, t)$. This is a little more complicated to imagine pictorially. Think now of many small spheres sitting on a desk. Now we connect them all up with rubber bands or springs. Now we can rotate all the individual spheres as much as we like whenever we like and then we wish for the overall symmetry to be preserved. What happens here is that when we rotate one sphere it rotates the neighbouring spheres in the opposite way due to the springs, hence compensating the original rotation so that the net effect on the system of spheres on the table is zero. Essentially there is a *force* connecting the spheres (the rubber bands/springs). In a very analogous way this is what happens mathematically too and is why local gauge symmetry is so beautiful. The invariance of local gauge symmetries is important to us as physicists because it says that the laws of physics should be the same on Jupiter as on Earth, in the past or in the present. Without this holding one could never do a repeat experiment and indeed the entire scientific method would fall apart. The brilliance of these symmetries is that one can start from a free field, unbound to a source, and then add the requirement that there is a specific symmetry, say $U(1)$. Then one asks oneself: if I would expressly require this symmetry to be invariant under any transformation how would I need to modify my basic lagrangian in order to incorporate this. Mathematically, one is simply including some extra terms which cancel under this transformation leaving the equations invariant. Physically what one is doing is introducing another field(s) (a gauge field) with an associated particle. In other words one is introducing a new force, how it behaves and new associated particle(s) which mediate this force.

Quantum Electrodynamics

The second and third terms of (1.2) come from the introduction of the $U(1)$ and $SU(2)$ gauge symmetries. Their generators (the combination of basis matrices which lead to the representation of the symmetries), Y and τ^i , reveal the associated vector boson fields which underpin the electromagnetic and weak forces. Indeed, the photon, W and Z bosons which we observe in nature are all combinations of the fields introduced by these two symmetries. The $U(1)$ symmetry can be expressed by a 1x1 matrix, i.e. a number, with one associated field B_μ where the conserved quantum number of the symmetry is hypercharge Y . The $SU(2)$ gauge symmetry can be expressed by three 2x2 matrices and three associated fields W_i^μ , where $i = 1, 2, 3$. Sometimes the gauge group is written as $SU(2)_L$ to denote that the weak interaction is seen to distinguish left- and right-handed chirality states of fermions. Indeed, only left-handed fermions (and right-handed anti-fermions) interact with $SU(2)_L$ gauge fields. This constraint comes directly from experimental observations. Therefore left-handed states are written as doublets, while right-handed states are singlets (hence cannot interact with the 2-D $SU(2)_L$). According to the above model, the vector bosons

introduced by these symmetries should have a zero mass (indeed the photon does) but experimentally it is clear that the W and Z bosons have a mass. This is solved with the Higgs mechanism which I shall explain later.

Screening

Here we can observe an interesting phenomenon which manifests itself in quantum electrodynamics (QED), namely that of *screening*. Consider an electron as observed by a positron. As the electron is travelling there is a non-negligible probability for it to emit a virtual photon which may produce a pair of charged fermions that later annihilate back into a photon and are reabsorbed by the electron. In effect we have virtual pairs of electrons and positrons popping in and out of existence around the electron, producing a kind of fuzzy screen, as depicted in Fig. 1.3. What this means is that a positron observed an effective charge which is slightly reduced from its nominal value due to this screening of virtual electrons and positrons. So in this sense thinking of electrons as point like balls is not helpful. Perhaps more helpful a picture is a fuzzy electron cloud with charge concentrated at the centre and reducing the further out one goes.

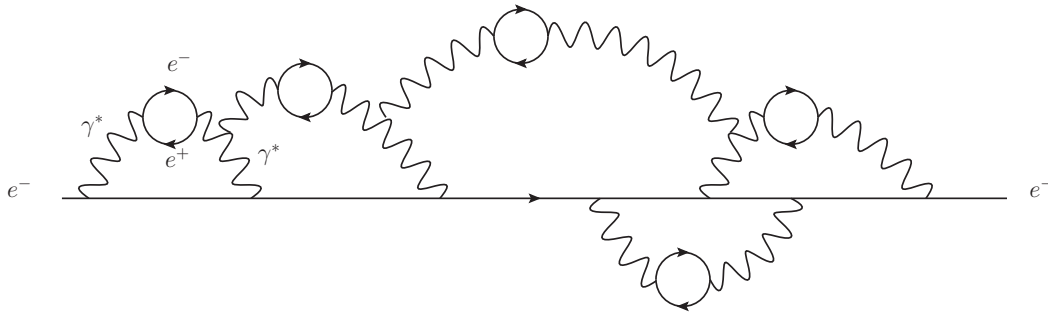


Figure 1.3: An illustration of how a bare electron looks like from the perspective of a positron.

Quantum Chromodynamics

The final term in Eq. (1.2) has the generator, λ^a , for $SU(3)$ space, since it is a 3×3 space it has eight associated fields introduced, G_μ^a , called gluons. These are responsible for the behaviour of all *coloured* particles. One can imagine *colour* as analogous to electric charge. In fact it has nothing to do with the colour we see.

The reason we call the conserved quantity of Quantum Chromodynamics (QCD) colour is two-fold: Firstly, just as there are three primary colours of light there are three distinct colour states in QCD. Secondly, when one mixes all the three primary colours together one obtains white; in the same way when one composite particle contains all three colour states it is *colourless* to QCD interactions.

Another important distinction between QCD and QED is that the gluons (unlike the photons) carry the conserved quantum number, colour. Hence gluons can interact both

with quarks and with other gluons. This leads to interesting properties of the strong interaction and its coupling strength, α_s . The strong coupling strength α_s depends on the energy scale of the interaction, or more precisely the momentum transfer Q involved in the interaction:

$$\alpha_s(Q^2) \approx \frac{1}{\ln(Q^2/\Lambda)} \quad (1.4)$$

where Λ is the non-perturbative scale of QCD. The dependence on the energy scale and the cut off Λ leads to two important features: *confinement* and *asymptotic freedom*. Asymptotic freedom is the behaviour seen as the energy scale increases ($Q \rightarrow \infty$). The coupling strength decreases, effectively meaning that at sufficiently high energies quarks and gluons can be treated as free particles. Conversely, confinement is the concept that with increased particle separation there is an increased coupling strength. This leads to the fact that quarks and gluons cannot exist as free particles, but are confined within colourless states of hadrons consisting of two or more quarks. Practically, for the LHC this means that due to the high energies, quarks and gluons are treated as free particles in interactions involving large momentum transfer. However due to confinement the particles will not appear free in the detector. They in fact will *hadronize*, appear as a collection of stable hadrons, in a hadronic spray. These hadronic showers typically form a conical shower in the direction of the original quarks and gluons which hadronize. Sophisticated detector algorithms try and reconstruct these hadronic showers in objects known as *jets*.

Screening and anti-screening Another way of thinking about these two special phenomena of confinement and asymptotic freedom is *screening* and *anti-screening*. Analogously to QED we have screening effects from virtual quark anti-quark loops. However, since gluons carry colour charge we also uniquely get virtual gluon loops, which have the opposite effect, in other words they add to the colour charge of the bare quark and make it appear stronger at greater distances from the source. The screening and anti-screening loops are illustrated in Fig. 1.4. So these two competing effects manifest themselves in Eq. (1.4) giving the two limiting phenomena we have talked about.

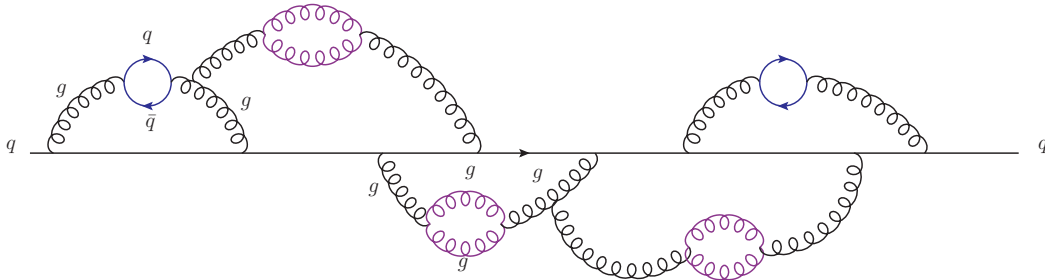


Figure 1.4: An illustration of what a quark looks like from the perspective of an anti-quark. The virtual quark loops are shown in blue and screen the bare colour charge whilst the virtual gluon loops are shown in purple and anti-screen the bare colour charge.

So now we have a great description of how all the particles interact under the different

forces and how the bosons mediate the forces. However, there is one rather gaping hole in our theory: what describes how the fundamental particles have any mass?

There are no mass terms in the lagrangians presented so far, which means even though we experimentally observe that particles in nature have a mass, our mathematical model does not account for it! If one naively were to just add a mass term onto the lagrangian ($m\bar{\psi}\psi$) one could easily show that this would break the local gauge symmetries of $SU(2)$, i.e. particle physics would no longer be invariant for all space and time. So we need some mechanism which gives the fundamental fermions and bosons mass whilst still retaining the invariance of the symmetries.

Feynman Diagrams and probabilities

Anyone who has done some level of particle physics has come across Feynman Diagrams. To the uninformed they probably just look like a picture of dashed and squiggly lines showing what comes in and and what comes out of particle interactions, but they are so much more. They are beautiful illustrations of some of the deeper mathematics we have considered in this section, indeed they can help us calculate the probability for a particular process or interaction happening. Let's deconstruct a simple Feynman diagram and calculate the probability for this process occurring.

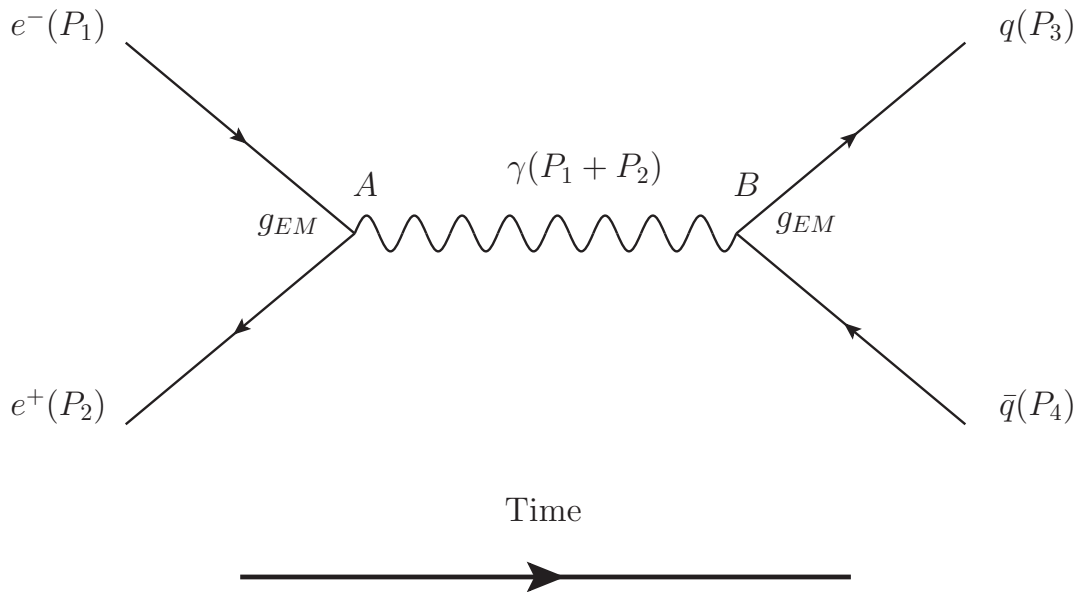


Figure 1.5: Electron Positron annihilation

Let us consider Fig. 1.5 this is an illustration of an electron and a positron annihilating into a photon which then produces a quark anti-quark pair. The way one interprets these diagrams is to imagine time moving from left to right. So on the left one has incoming particles and on the right outgoing. Each line drawn (squiggly, straight, loopy or dashed^{II})

^{II}I started just serendipitously writing the first line innocently and thought I would continue into a

represents a particle. The straight lines represent fermions (electron, positron, quark) and the squiggly line represents a boson (in this case a photon which is the force carrier of the electromagnetic force). Now each vertex on the diagram represents an interaction between the particles. Vertex A is the interaction of the electron and positron annihilating to give the photon whilst Vertex B depicts the interaction of the photon producing a pair of quark, anti-quark. On top of this we have the little added subtleties of the arrows on the particle lines. By convention we draw arrows pointing from left to right for particles (electrons and quarks) but right to left for anti-particles (positrons and anti-quarks), this convention is just to highlight that there is a difference between particle and anti-particle, especially when one considers the mathematics. Now that we have depicted the interaction in its fullness we wish to calculate the probability for this particular process occurring. We can use a simple set of rules (Feynman Rules) to calculate the quantum amplitude of this particular process, then as for any quantum process we take the square of the amplitude as the probability.

To get a good estimate for the likelihood of this process occurring is relatively simple:

1. Each interaction vertex has an associated **vertex factor** which essentially includes the strength, coupling or probability between the incoming and outgoing particles. In our case this is the coupling constant which represents the strength of interaction between the particle (electron/anti-electron) and force carrier (photon) which is simply defined as the electromagnetic coupling constant, g_{EM} .
2. Then each force carrier, also called a propagator, has an associated **propagator factor**. These propagators are **virtual particles** because they do not satisfy the usual relativistic energy-momentum constraint $P \cdot P = m^2$, which says that a particles four-vector squared is equal to its invariant mass and comes about due to momenta and energy conservation. This seems strange, and is why they are called virtual particles (sometimes they are said to be off their mass shell, **off-shell**) in that we can never measure their momenta and energy but only see the effects they have on the other objects they interact with. They simply transfer energy, momenta and other quantum numbers. For a particle with no spin the relevant propagator factor is $\frac{1}{P \cdot P - m^2}$. Propagators inside a Feynman diagram can also be called **internal lines** since the lines are connected at both ends to vertices. They never leave or enter and

Dr.Seuss like poem:

Squiggly, straight, loopy or dashed.

All baked together, lines that are mashed

"A quark, on a fork, that's the cork" cried the hawk.

"But what about spin, momenta or torque?"

Photons, protons bamboozling-otons

Gluinos and winos, atomic casinos

Weighted and freighted and sent off for tea

We've measured this puzzle, just look up and see.

are not part of the observed final or initial states, hence never measured and thus virtual.

3. The particles coming in and out of the Feynman diagram (only connected to a vertex on one end) are called **external lines**. These particles are never virtual since they are always observed. These particles have a given **wavefunction** which incorporates the particles spin, momentum, energy etc. But for our simple derivation we shall ignore these as well as the charge of particles and spin matrices and so forth.

Now we know that at each vertex energy and momentum must be conserved, therefore $P_1 + P_2 = P_\gamma = P_3 + P_4$. If we say that now $P_1 = (E, \mathbf{p})$, $P_2 = (E, -\mathbf{p})$ by choosing the centre-of-momentum frame.^{III} Then $P_\gamma = (2E, 0)$ So now adding everything together, two interaction vertex factors (green) and the propagator factor (red), and remembering from quantum mechanics that a probability is a quantum amplitude squared:

$$Prob \propto |g_{EM}^2 \cdot \frac{1}{P_\gamma^2 - m_\gamma^2}|^2 \quad (1.5)$$

Now, inserting the momenta and remembering the photon is massless:

$$Prob \propto |\frac{g_{EM}^2}{4E}|^2 \quad (1.6)$$

Hence we have an estimate for the probability for this process to occur which is visually depicted in the Feynman diagram.

In the wondrous world of quantum mechanics, if we measure two particles at a given time and then again some time later, the particles can literally do anything and everything before the second measurement. This includes turning into new particles, merging, radiating particles and so on. In quantum mechanics these infinitely many histories or possibilities are referred to as paths, such that each path represents one possible history the particles took between measurements. As we have shown above using Feynman rules (which stem from our SM lagrangian) one can calculate the amplitude of a given path. However, to calculate the probability (or cross-section, σ) for $AB \rightarrow XY$ one needs to sum up the amplitudes, A , for all possible histories and then square them:

$$\sigma(AB \rightarrow XY) \propto |\sum A_{\text{path}}|^2 \quad (1.7)$$

But since there are infinite paths^{IV} this sum is incalculable! So one has to make simplifications and approximations. The standard approximation for QED is called the Born Approximation. Here one only calculates a few paths which dominate the sum and then

^{III}In other words what we say is that we can always find a frame such that the electron and positron are back to back and collide with equal and opposite momenta. This is in fact called the centre-of-momentum frame. Here is a great illustration of the beauty of invariance, in that because the physics is invariant we are free to consider any frame of reference and thus here just the centre-of-momentum frame to make our lives easier

^{IV}Here the sum is over all paths from AB to XY.

neglects the other infinite paths with increasingly diminishing amplitudes. In the case for $\sigma(e^+e^- \rightarrow q\bar{q})$ there is only one path (the one calculated above) which dominates the sum. This most basic path with only two vertices is called a Leading Order(LO) processes since it dominates. If one considers a more complicated path with an extra interaction vertex this is called "next to leading order" (NLO) and another term is "next to next to leading order" (NNLO) and so on. The reason this approximation works for QED is that each additional vertex introduces a new vertex factor g_{EM} which is very small and hence the amplitudes decrease accordingly. Hence the leading order term is a good approximation. However, if one considers QCD the vertex factors are no longer small and hence the NLO and NNLO terms can still be very important.

1.3.1 The Higgs Mechanism and Higgs Boson

Before going into the nitty gritty of the mechanism, I'd like to try and explain the mechanism in more laymans terms, the kind of explanation you might give to someone in the pub ^V. In order to do so I will try to appeal to two different analogies. Imagine a big cocktail party in a large room, at this party everyone is equally spaced and talking with the people in their vicinity. Now in comes a very important person, say Obama. Of course all the people around Obama are attracted to him and want to talk to him, thus as Obama moves around the room he attracts the people nearby to join the cluster around him, whilst some who have spoken to him enough leave back to their original conversations, equally spaced. But since Obama has a constant cluster of people around him he has a greater *mass* than normal. In other words, he has more momentum for the same speed of movement. Once moving he is harder to stop, and once stopped it is harder to get moving again. Translating this into three dimensions and including all the relativity and quantum theory gives you a description of the Higgs mechanism. We imagine the universe filled with the Higgs field (like the cocktail party filled with people) such that when a particle (a VIP) moves through the field a distortion of the field is created, the distortion, a clustering of the field around the particle, generates the particles mass. The more important the VIP (particle) the larger the clustering (mass) it has. Similarly, in the physics of solids, when an electron is modelled moving through a lattice, one imagines a field spread throughout all space with positively charged crystal atoms. As the electron moves through the lattice it attracts the positive atoms to itself and thereby gains an effective mass which can be 40 times as large as the free electron mass!

If we go back once again to our cocktail party scenario, imagine that someone comes in with some pressing news, those near the door hear the rumour first and cluster together to get the details, they in turn turn around to tell those they were originally talking to about the news. The rumour then spreads like a wave of clustering across the room. The rumour may spread out to all corners of the room or form a compact bunch which carries the news along a line of people until it finds its way to some other VIP (particle) across the room. The information has been carried by a cluster of people. Just as the cluster

^VIn fact I have given this explanation in the pub a couple of times. People seem more susceptible to particle physics after a couple of beers.

of people around Obama gave him a mass, so too is this cluster of information travelling something massive, the Higgs boson. It essentially is the information carrier from the Higgs field which conveys the universe to the particles. Again in the physics of solids we have a very analogous concept, a crystal lattice can carry waves of clustering without needing an electron to move and attract the atoms. These waves behave as particles and are known as phonons^{VI}. This explanation is an adaption of that proposed by Mr. Waldegrave, UK science Minister in 1993.

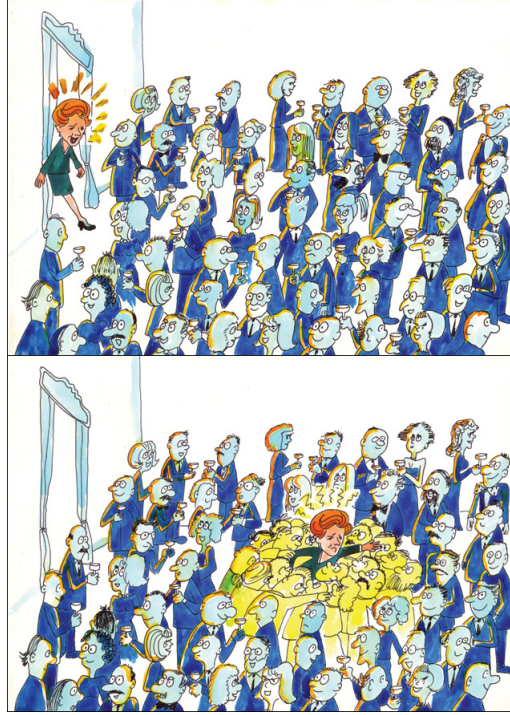


Figure 1.6: Cartoon which accompanied Waldegrave's explanation of the Higgs mechanism. [11]

1.3.2 Spontaneous Symmetry breaking and the Higgs Mechanism

In terms of the mathematics of the Higgs, one of the most important concepts is that of spontaneous symmetry breaking [12]. This in essence is a system where the underlying laws are invariant under a transformation, however the system as a whole changes under this transformation. For instance the fundamental equations of motion from a lagrangian describing the physical system may obey certain symmetries, but after transforming to the lowest energy state of the system the lagrangian does not display these features.

^{VI}They are pseudo-particles

The most classical picture of this is to think of the bottom of a wine bottle or a Mexican hat, which has a mound in the middle and a ditch in a circle around the mound. Then imagine placing a ball at the top of this mound. Clearly, the ball itself has rotational symmetry as does the Mexican hat. However, now the ball may spontaneously roll down the mound and find a place at the bottom of the Mexican hat. Now the ball and the Mexican hat still individually retain their rotational symmetries however the system as a whole no longer has the symmetry it once had due to this spontaneous symmetry breaking (the ball rolling down). For a depiction see Fig. 1.7

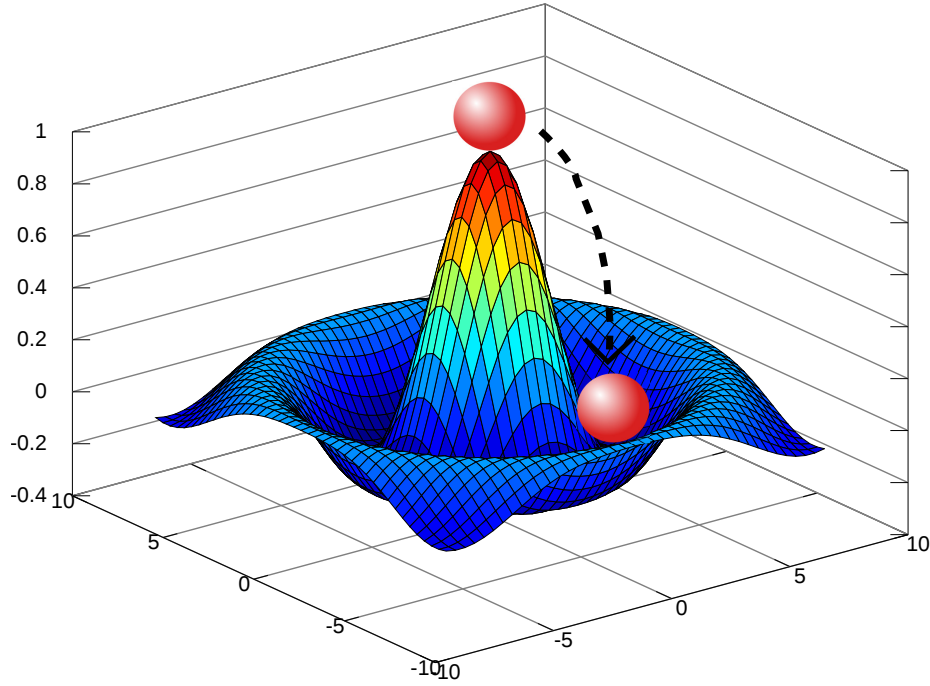


Figure 1.7: A depiction of a Mexican hat potential with a ball spontaneously breaking the rotational symmetry when choosing a specific vacuum potential, thereby breaking the symmetry of the system.

Let's consider this simple example lagrangian^{VII},

$$\mathcal{L} = T - V = \frac{1}{2}\partial_\mu\phi\partial^\mu\phi - \left(\frac{1}{2}\mu^2\phi^2 + \frac{1}{4}\lambda\phi^4\right) \quad (1.8)$$

Here we have a simple scalar field, ϕ , and two parameters of the potential λ, μ . If we require λ to be positive, this allows the lagrangian to be bounded below as $\phi \rightarrow \infty$. Here we note that the lagrangian is symmetric under the transformation $\phi \rightarrow -\phi$. Now we have our lagrangian and we wish to find the minimum potential which is classically considered the systems ground state. Then classically one might perturb the system from its ground states to try and understand its excitations. Minimising the potential (the second term

^{VII}The following formulation is taken from [9]

in the lagrangian) we have two scenarios. The first is where $\mu^2 > 0$ then the minimum is clearly given by $\phi = 0$. The second is where $\mu^2 < 0$, which is the more interesting case. One can easily calculate the minimum by derivation, giving the ground state (vacuum expectation value) as

$$\phi = \pm \sqrt{\frac{-\mu^2}{\lambda}} \equiv v \quad (1.9)$$

Then as per usual one expands around the ground state to understand the system dynamics, so looking at the region around the minimum $\phi = v + \eta(x)$, where we are expanding around $\eta = 0$. We could just as well have chosen to expand as $\phi = -v + \eta(x)$. However the physics is the same at the end of the day due to the original symmetry of the lagrangian, $\phi \rightarrow -\phi$. Setting this perturbation back into the lagrangian eventually leads us to:

$$\mathcal{L} = \frac{1}{2} \partial_\eta \phi \partial^\eta \phi - (\lambda v^2 \eta^2 + \lambda v \eta^3 + \frac{1}{4} \lambda \eta^4) \quad (1.10)$$

The term with η^2 can be interpreted as a mass term, hence this lagrangian describes a particle of mass $m_\eta^2 = 2\lambda v^2 = -2\mu^2$, it also has two interaction terms which describe how the particle interacts with itself and other particles with some unknown strength proportional to λ . Notice however that this perturbation no longer contains any of the original reflection symmetry $\phi \rightarrow -\phi$! The symmetry was in effect broken when we chose a specific vacuum ($\phi = +v$ not $\phi = -v$). In other words, the ball rolled to a specific point at the bottom of the potential well, and hence the system can no longer retain the original symmetry of the lagrangian. Et viola, spontaneous symmetry breaking.

Now instead of using the case of the simple scalar field, we can take a field which is an $SU(2)$ doublet of complex fields, and then go through the above procedure. When one does this one ascertains the masses of the vector bosons, W and Z much in the same way as we arrived at the mass of the η particle. Now that we have successfully created a theory with an $SU(2)$ complex Higgs field, we can add some interaction terms of this field with the known fermions. The remarkable thing is the strength with which the particles interact with the Higgs field is directly coupled to their masses!

So rounding up all the parts of the SM lagrangian so far we have seen that there are three internal symmetries intrinsic in nature: $U(1) \times SU(2)$ which describe the electroweak and QED theories, $SU(3)$ which describes quantum chromodynamics (QCD) and finally the last piece of the puzzle the Higgs mechanisms which spontaneously breaks the electroweak symmetry allowing the SM particles a non-zero mass. So as a qualitative representation of the SM, we can write:

$$\mathcal{L} = \mathcal{L}_{QCD} + \mathcal{L}_{EW} + \mathcal{L}_{Higgs} + \mathcal{L}_{kinematics} \quad (1.11)$$

where the first two terms are simply the interaction terms for the three fundamental forces, the third term is for the Higgs mechanism allowing the fundamental fermions and bosons to take on mass and the last term incorporates all the kinematical terms of the particles. With this we can describe almost all known fundamental interactions and experimental

observations. However, as I hinted at earlier there are few gaps and imperfections in the theory...

1.3.3 Beyond the Standard Model

The first thing to say is that up until now, there is no experimental result which is in direct contradiction to the SM.^{VIII} With that being said, there are a number of known open problems which remain unaddressed by the Standard Model, here are the largest:

- The first is there are eighteen free parameters in the SM which we can only be determined experimentally: for instance masses, strengths of forces and mixing angles. There are no *reasons* as to why these parameters have the values they have. Is there some background physics which explains these values? Are they just random? Could multiple universes explain this?
- In the universe today, we clearly have more matter than antimatter (otherwise they would collide and annihilate each other, or else separate out into different pockets of the universe). The question is how did we arrive at this point? Was there some physics process which biased the creation of matter over anti-matter in the beginning of the universe? Did the antimatter simply decay away?
- From cosmology and astrophysics we can see that the Standard Model explains only 4% of all energy/matter that we see in the universe! Of the rest, 27% is dark matter (DM) which is similar to normal matter but interacts very, very loosely with the Standard Model fields, thus it is non-luminous. We now there is dark matter by measuring the rotation curves of galaxies and gravitational lensing. The SM has no good fundamental particles which could be candidates for dark matter. The rest of the universe is made of the magnanimously named *Dark Energy* which is something not at all well understood. The postulate from cosmological arguments is that there is a constant energy density for the vacuum which drives the expansion of our universe. In other words, there is a vast majority of the universe which we haven't even begun to understand!
- Gravity. The SM does not even begin or attempt to explain how gravity fits in to our quantum field theories of the SM, nor does it explain why the force of gravity is so stupendously weaker than all other SM fields. The SM is (in most peoples opinion) incompatible with general relativity (the best theory of gravity which is widely accepted). Was there some point in time when all the forces where unified, and there is only one grand unified theory (GUT)?
- The Neutrino mystery. According to the classical SM, neutrinos should have no mass. However, through neutrino oscillation experiments we know that neutrinos have a non-zero mass [13]. One can simply append the SM lagrangian with terms for the neutrino mass, but this comes with added problems, and it is not entirely certain that neutrinos gain mass in the same way as the other SM fermions and bosons.

^{VIII}At least to a 5σ level or greater, if one considers massive neutrinos a simple addition to the SM.

- The Hierarchy Problem. We know that there should be new physics at much higher energies than the Higgs boson. Theoretically these new physics models will introduce heavier particles which must couple to the Higgs field in order to obtain mass. Henceforth, these particles will contribute to the mass of the Higgs through loops. Thus the Higgs mass should be on the same scale as these new particles. But we observe the Higgs mass to be relatively light compared with the expected new physics.

With the Standard Model (with the exception of the Higgs which has been newly discovered) being more or less complete for 30+ years, theorists have had plenty of time to construct all kinds of weird and wonderful models which either extend or re-write the SM in order to address some or all of the above questions. In general these models and theories are known as Beyond Standard Model (BSM) models. Some are perhaps more popular than others due to their simplicity, ability to answer more questions or ease to test experimentally. Indeed much of the analytic power of physicists in the past 30+ year has been to investigate these models to find out whether they are correct or to rule them out where/if possible. A good chunk of this thesis is dedicated to just this. Later I will describe a handful of these BSM models, and their merits and phenomenology.

So at the end of this introduction chapter I would love the reader to be left with the impression that a tremendous work by many great physicists has been done over many years to arrive at the point that we are today, with a truly fantastic theory (SM) which explains how all known fundamental particles and forces interact and behave and that moreover it explains almost all experimental results. However, there is an even more staggering amount of work to be done and things to be discovered, theories to be built and others to be knocked down. It was with this bated breath, enthusiasm and expectation that the LHC began and particle physicists thrust themselves into the future!

There is nothing like looking, if you want to find something. You certainly usually find something, if you look, but it is not always quite the something you were after.

J.R.R.Tolkien, *The Hobbit*

2

Machines and Dectectors

2.1 The Large Hadron Collider

So now comes the question of how, as experimental physicists, we can probe the Standard Model. How can we test the plethora of theories out there? Indeed when I started my PhD the Higgs had not even been discovered and the mechanism by which particles gained mass was by no means certain. How can we address all the known short-comings of the SM? How do we measure our current model more accurately?

Well, there are many kinds of experiments big and small, cheap and expensive which all aim to answer these questions. One of the most common methods used as a probe for particle physics are accelerators. In essence, one takes some tiny particles (electrons, protons, lead atoms...) and accelerates them to near the speed of light and then crashes them together inside some kind of viewing device (a detector) and stands back and tries to figure out what happened. The concept is simple. At the beginning of the birth of our universe, the universe was small, highly dense and full of energy, and very, very hot. Then gradually, it spread out, cooled down and settled down. As physicists we think that if we could somehow create conditions similar to those at the beginning of time, we could learn something more about the fundamental nature and forces of the universe. Add in turn Einsteins idea that energy and matter are interconnected deeply, in other words when we collide these particles together at super high speeds when they collide the pure energy available can be *used* to create all kinds of particles and forces which are much too energetic to occur in our normal regular day to day lives.

Enter the Large Hadron Collider (LHC), currently the worlds largest and most powerful particle accelerator, tens of years in its making and design. It truly is an impressive piece of

engineering and science. The main ring is 27 km in circumference, spanning two countries. It's superconducting magnets are cooled down lower than outermost space. It's magnets used to bend the paths of the particle beams are 1 million times stronger than the earths magnetic field. The precision used in guiding the particles near the speed of light into a collision is like firing two peas from across the solar system and getting them to collide in the middle. Without going into all the incredible details and work that has gone into literally every fibre of the machine, it is sufficient to say that just to build this machine is an astounding feat. For those who like numbers Table 2.1 highlights some of the most important quantities of the LHC.

Table 2.1: Some important quantities pertaining the LHC, taken from [14]

Quantity	number
Circumference	26 659m
Dipole operating temperature	1.9 K (-271.3°C)
Number of magnets	9593
Number of main dipoles	1232
Number of main quadrupoles	392
Number of RF cavities	8 per beam
Nominal energy, protons	7 TeV
Nominal energy, ions	2.76 TeV/u(*)
Peak magnetic dipole field	8.33 T
Min. distance between bunches	$\approx 7\text{m}$
Design Luminosity	$10^{34} \text{cm}^{-2} \text{s}^{-1}$
No. of bunches per proton beam	2808
No. of protons per bunch (at start)	$1.1 \cdot 10^{11}$
Number of turns per second	11245
Number of collisions per second	600 million

(*) Energy per nucleon

2.1.1 Why a Proton Synchrotron Collider?

So why do we collide protons? The LHC from the get-go was a "Discovery Machine", in other words its specific goal (rather than precision measurements) was to try and push into the unknown. To try and discover new physics, whose model parameters were not yet known and whose proposed particles masses were not known. It was clear that we needed a machine which could probe as large a range of energies as possible, to as large an energy

as possible and could scan this energy space. Now from particle physics it is easy to show that energy available for particle creation is much higher in two beam collisions than using a stationary target. The protons main advantage over its classical competitor the electron is that, due to the proton being much heavier it does not lose as much energy through synchrotron radiation as it is bent around in the ring. (Hence one can accelerate protons to higher energies).¹

But why do we choose to use a ring as opposed to a linear collider? Indeed there are many pro's and con's to both. This has both to do with the amount of space one has to use and the growing accelerator expertise. However, when considering protons a circular ring is clearly advantageous. In order for the particles to get the same energy as the LHC one would need a hugely long linear accelerator, whereas in a circular accelerator one can keep the particles in a closed loop and accelerate them every revolution until they reach the desired energy. Furthermore, one can keep colliding the same bunches in a ring over and over again. But more than that there are many practical and engineering reasons to do with the using the old CERN infrastructure.

2.1.2 The Proton Adventure

Accelerating the protons to near the speed of light is no easy feat, and the journey of the proton is a long and treacherous one. Here I will describe briefly its pilgrimage. The proton starts in very humble beginnings, as part of a hydrogen atom stored in a compressed bottle on the side of a wall underground in Switzerland. The hydrogen gas is then fed into the machine where a large electric field slowly strips off the electrons from it, leaving the bare hydrogen nucleus, a proton. The proton will then undergo a chain of increasingly larger and higher energy accelerators:

Linac 2 [50 MeV] \rightarrow Proton Synchrotron Booster (PSB) [1.4 GeV] \rightarrow Proton Synchrotron (PS) [25 GeV] \rightarrow Super Proton Synchrotron (SPS) [450 GeV]

Then finally the protons are split into two separate beam pipes and fed into the LHC rings as two counter-rotating streams. They are filled in less than 5 minutes, then accelerated up to the final 4 TeV energy over the following 20 minutes. Then over the next few hours, ranging from a couple to 24, these beams are focused ever so precisely so that collisions take place smack in the middle of the four different detectors: ATLAS, CMS, LHCb and ALICE. Fig 2.1, displays the schematic layout of the booster rings and the positions of the detectors in the LHC ring, it also shows some of CERN's other accelerators and other experiments. The proton does not make this journey alone, as we mentioned it is ridiculously difficult to focus beams of this energy such that they collide precisely in

¹Since it contains a sea of quarks whose individual momenta are not known, when two protons collide the two quarks in the hard interaction can access an entire range of energies. Hence in a proton-proton collision one is scanning a huge range of energy phase space simultaneously in one collision. Whereas when one collides two electrons, the momenta of the two is very well known and hence the energy phase space one covers in a collision is very small, hence one would need to shift the energies of these electron beams and take very many collisions in order to scan the same energy phase space

the middle of the detector, furthermore how do we know that if one proton collides with another one that something exciting will happen? The answer is we don't. So in order to maximise exciting events and the probability of collision we accelerate a whole bunch of protons together, in fact 100 billion of them per bunch and many bunches per beam, which results in about 600 million collisions per second!

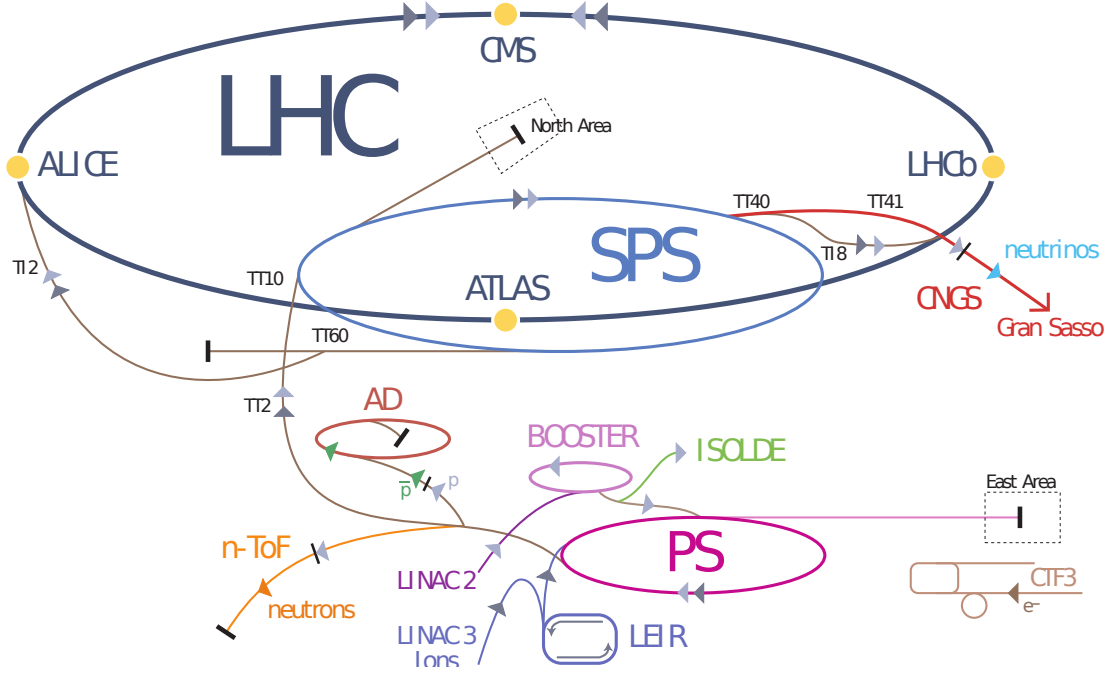


Figure 2.1: LHC booster system schematic [14]

2.1.3 The Big Four

As mentioned, there are four larger detectors on 4 of the points along the LHC ring where maximal collision efficiency can be achieved. Here is a brief description of the detectors seen here in Fig. 2.2:

- **CMS** (Compact Muon Solenoid) is one of the two specialised multi-purpose detectors designed to investigate a wide range of physics from the Higgs to Supersymmetry to Extra-Dimensions and quantum gravity. In order to search for so many different types of physics means that that the detector should not be overly specialised and be able to measure the largest range of particle type and energies. [16]
- **ATLAS** (A Toroidal LHC Apparatus) The other multi-purpose detector and the biggest of the four. This will be covered in great detail in the next section. [17]
- **ALICE** (A Large Ion Collider Experiment) A much more specialised detector which aims (predominantly) at exploring the so called Quark Gluon Plasma (QGP) a proposed state of matter which existed very early on in the universe as a hot, dense

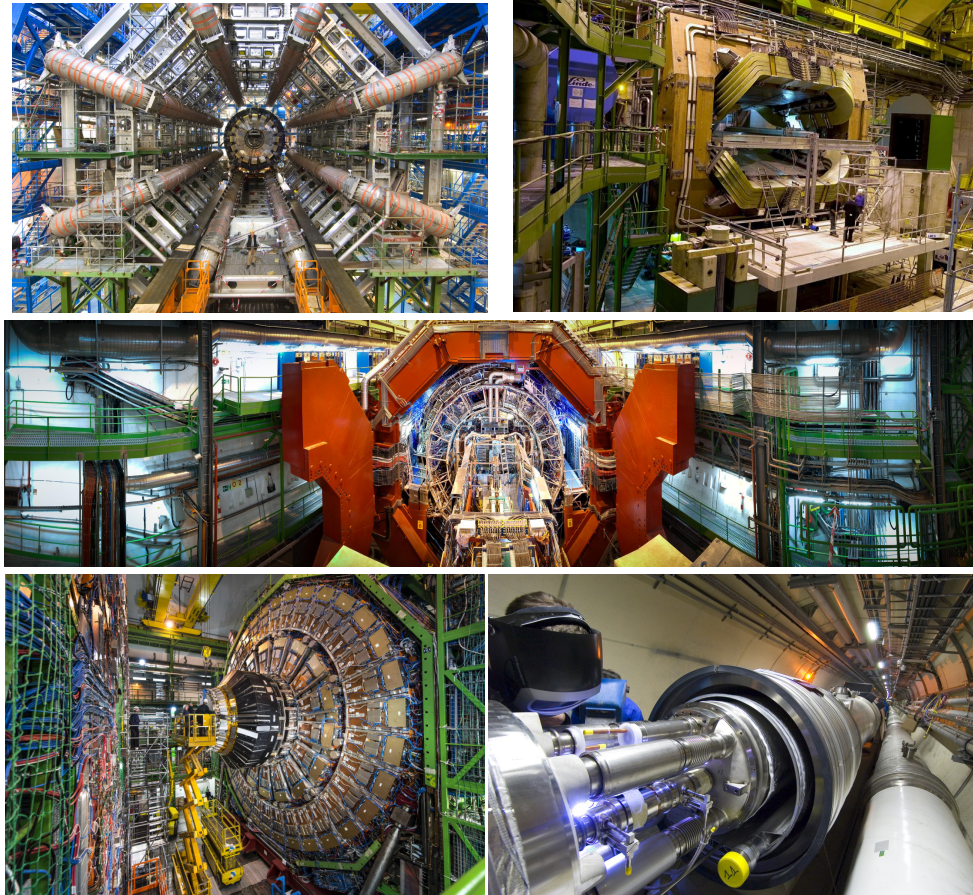


Figure 2.2: Top Left: ATLAS system toroidal magnets. Top Right: LHCb magnet system, Middle: ALICE panorama, Bottom Left: CMS calorimeter, Bottom Right: Welding on the LHC. All images from [15]

plasma. A primordial soup of quarks and gluons, life's aperitif in the dinner of the universe. [18]

- **LHCb** (No flashy, silly acronym here) Another specialised experiment which aims to understand the curious world of the b-quark, the second heaviest (but more stable) sister in the SM family. In particular it hopes to understand more about the matter to anti-matter asymmetry observed in our universe. [19]

2.1.4 Luminosity

The concept of luminosity, \mathcal{L} , is vital to both the design of the LHC and to the discovery of new physics and in turn my analysis. Luminosity is in essence a measure of how many particles are colliding per unit area per unit time. In other words the rate of particle collisions. It is defined by the accelerators (LHC) design parameters [20]:

$$\mathcal{L} = F \frac{N_1 N_2 n_b f_r \gamma}{\beta \epsilon} \quad (2.1)$$

Where N_1, N_2 are the number of particles in beams 1 and 2. n_b is the total number of bunches stored in the ring, f_r is the revolution frequency, γ is the relativistic factor, β is the beta function (defined by the accelerator and magnet geometry), ϵ is the normalised transverse beam emittance (a handle on how the bunches spread out in the beam) and F is a geometric luminosity reduction factor which comes from the fact that there is a crossing angle in which the beams collide (i.e it is not head on).

This is important since it is the luminosity of the machine which limits how many events from a specific process will be produced.

$$n = \sigma \int_0^\tau \mathcal{L} dt \quad (2.2)$$

Here σ is the cross-section for a specific process, n is the number of events which would be produced by the machine if it ran for a time τ . So clearly if you are trying to study a model whose cross-section for a particular particle is small then one wants to have as large a luminosity as possible so one can have the most amount of events possible in order to *see* the events and say something statistically meaningful.

However, whilst one can design an accelerator for a given luminosity it is much harder to measure its operating luminosity, especially one which can be changing from beam to beam and run to run. But measuring the luminosity correctly is vital, for without knowing the luminosity one cannot predict how many events we *should* have observed, as depicted by Eq. (2.2)

So the desire is to measure the luminosity on a run by run basis. The luminosity team uses a Van Der Meer scan method [21] (a few times a year), as an absolute calibration. In essence the scan works by moving one of the beams so that the two beams begin by not colliding at all and move them so they are colliding maximally and then so they are not colliding at all again. Whilst the scan is being made, the particle flux in detectors such as LUCID which are 17m away from the collision point is measured. In this way the luminosity team can develop a relationship between the particle flux in LUCID and the absolute luminosity. Thus during every run the particle flux can be measured at LUCID and the luminosity derived.

The final important concept often used is that of Integrated Luminosity. Very simply it is the integral of the instantaneous luminosities over time, thus it has units of cm^{-2} . This is often what is quoted (see Fig. 2.3) when referring to how much data one has collected over the course of a year. Due to the increase in luminosity between 2010-2012 one can clearly see the fantastic gain in data that was achieved. However, apart from the obvious engineering and accelerator constraints on increasing the luminosity more and more there are in fact physics reasons why this may also be non-optimal, namely that with a higher luminosity comes a large number of interactions per collision, Fig. 2.4. This can be problematic if one is studying a rare process due to the many other interactions which are happening simultaneously it becomes harder and harder to pick out the event of interest under the messy background of the other interactions.

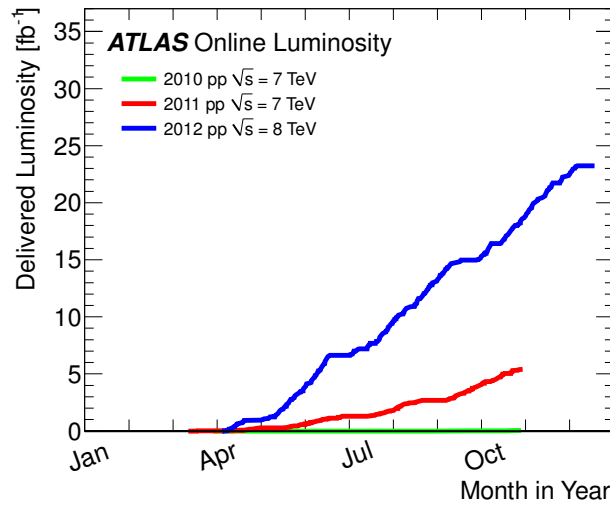


Figure 2.3: The amount of data delivered to ATLAS from 2010-2012 [22]

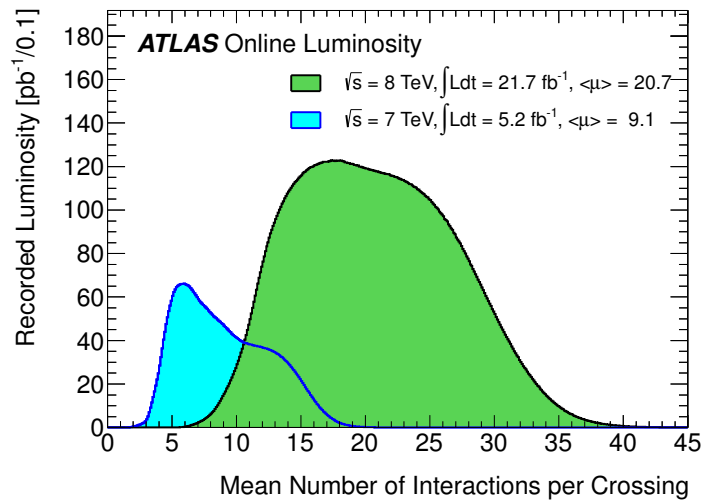


Figure 2.4: The mean number of interactions per bunch crossing for the different luminosities used in 2011 and 2012 [22]

2.2 ATLAS Detector

ATLAS is the largest detector at CERN and like CMS is a multi-purpose detector. The detector's job is manifold, it should detect (directly or indirectly) all nature of particles both known (photons, electrons, quarks, gluons....) and unknown (Higgs, super-particles, majorana neutrinos...) and then measure all kinds of kinematics (their energies, momenta,

angles...). In essence a detector tries to reconstruct as much information as possible from this super high energy collision, and in some way filter through to find the *interesting* events. The detector as such is built from many different subdetectors each specialised for tracking, identifying and measuring a range of particles. The detector in all its glory can be seen in the schematic of Fig. 2.5

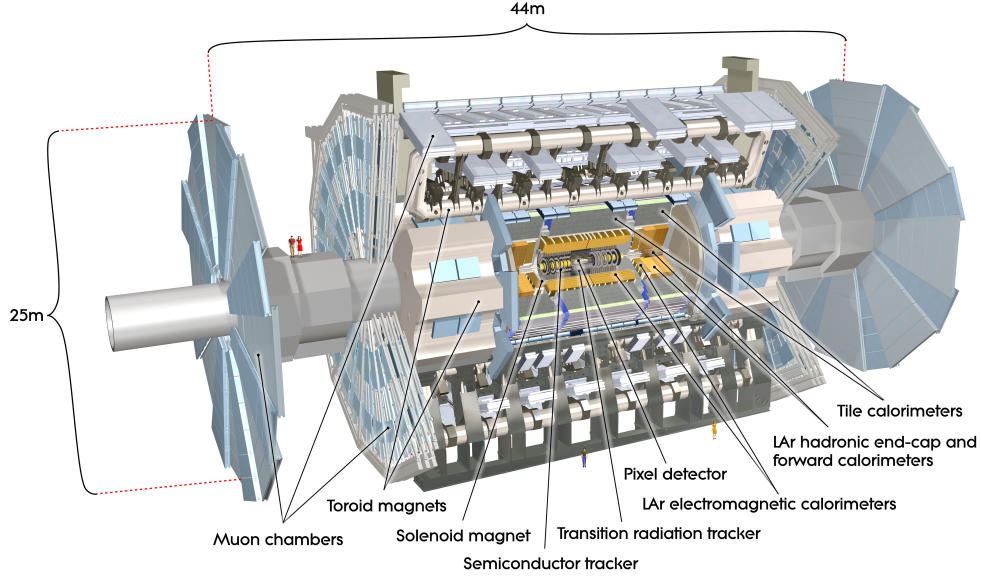


Figure 2.5: A schematic of the entire ATLAS detector, note the persons on the wheel for scale reference [22]

The ATLAS detector demands were set to a large extent by what would be necessary to detect the Higgs. The SM Higgs should decay to a whole gamut of final states and have a fairly narrow mass resonance. Henceforth, if the detector was designed to cope with detecting and resolving the Higgs (since it manifests itself in multiple final ways) then it should be sufficient to detect a multitude of different potential theoretical models. The ATLAS design strategy can be condensed to these goals [17]:

- Very good electromagnetic calorimetry for electron and photon identification and measurements, complemented by full-coverage hadronic calorimetry for accurate jet and missing transverse energy (E_t^{miss}) measurements
- High-precision muon momentum measurements, with the capability to guarantee accurate measurements at the highest luminosity using external muon spectrometer alone
- Efficient tracking at high luminosity for high- p_T^{II} lepton-momentum measurements, electron and photon identification, τ -lepton and heavy flavour identification, and full

^{II} p_T is the momentum component of a particle in the direction transverse to the beam

event reconstruction capability at lower luminosity

- Large acceptance in pseudorapidity (η)^{III} with almost full azimuthal angle (ϕ) coverage everywhere. The azimuthal angle is measured around the beam axis, whereas pseudo-rapidity relates to the polar angle (θ) where θ is the angle from the z-direction^{IV}
- Triggering and measurements of particles at low- p_T thresholds, providing high efficiencies for most physics processes of interest at the LHC.

2.2.1 Overview

I find it quite useful to have a schematic picture of the different parts of the detector like onion as in fig 2.6. The figure also conveniently depicts which particles leave deposits and are detected by the different parts of the detector. These individual parts I shall explain in the proceeding sections.

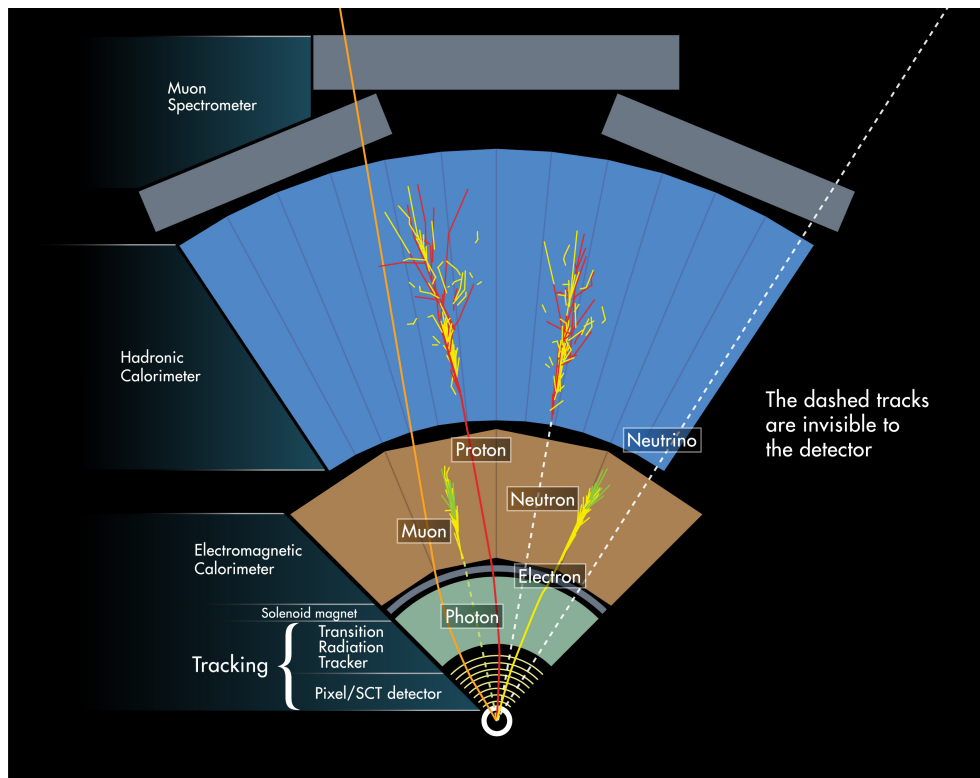


Figure 2.6: A schematic view of the different detector parts in ATLAS. Note that the parts of the detector where energy is deposited are shown as colourful showers. The dashed line illustrates that that part of the detector cannot detect that particular particle. [22]

^{III}defined as $\eta = -\ln(\tan(\theta/2))$

^{IV}Which is the direction of the beam

2.2.2 Magnet System

Before discussing the various tracking and calorimetry parts of the detector it is important to address the magnet system which encases and entwines the entire detector suite. Very strong magnetic fields are crucial for high-energy physics detector as they are used to bend the trajectories of charged particles, containing them in our detector and allowing us to measure their momenta by measuring the bending curvature under the magnetic field.

The ATLAS detector has two main systems of super-conducting magnets [23]:

- **Central Solenoid:** This is situated around the inner detector but inside the calorimeter systems. It is designed to have a magnet field of 2T in the inner tracker. The strength was chosen such that the inner tracker has good resolution for low momenta particles (a too large field strength would result in the particle paths curling-up in the field before even reaching the other parts of the detector). At the same time as one wants a strong field one desires that the magnets are not too thick otherwise it may stop particles and reduce their energy before they can be measured in the calorimeters. Hence the solenoid is a single-layer coil with a total thickness only 0.66 radiation lengths^V. However ideally, if it was feasible to have a 4T magnetic field of the same thickness and single-layered that would be ideal, however this a large feat of engineering.
- **Toroid Magnet System** This system is split into three parts with a barrel part installed outside the hadronic tile calorimeter and two end-caps outside the liquid argon calorimeter. These operate independently providing fields of 0.5 T and 1T for the muon detectors and end-cap regions respectively.

2.2.3 Inner Detector Tracker

The inner detector of ATLAS is the heart of the tracking system [24]. It can be thought of as three separate parts as depicted in Fig. 2.9. Its role is the tracking and momenta measurements of charged particles as well as particle identification. The tracking occurs for tracks above a 500 MeV/c threshold for a range of $|\eta| < 2.5$ and identification $|\eta| < 2.0$.

The pixel detector

As the innermost detector the pixel detector [25] is located very close to the interaction point. The first of the two silicon semi-conductor detectors, it provides a very high granularity measurement of the tracks as close to the Interaction Point (IP) as possible. It is designed specifically with the idea that it should be able to study the decays of heavy quarks, which have a decay length of roughly 100-400 μm , thus the detector is required to have a better spatial resolution than this. The pixel detector is made from three concentric barrels and a couple of end-caps. Where each barrel is made from 1456 modules each with

^VA radiation length is the thickness of a material for which an electron has a probability $P = 1 - 1/e$ of radiating a proton

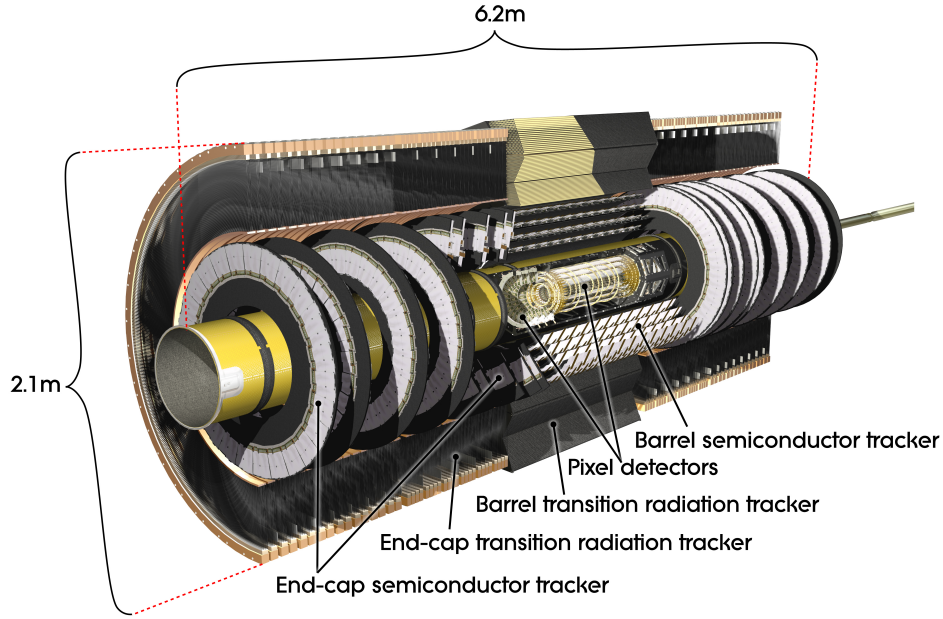


Figure 2.7: The ATLAS inner detector schematic, depicting the various parts. [22]

46080 tiny pixel elements. These so called pixels are rectangular sensors made from highly negative (n+) and positive (p+) doped silicon on a wafer. Having such a configuration allows the creation of a depletion region which occupies the entire bulk of the wafer, in this way maximising the active area. As a charged particle traverses one such wafer it creates electron-hole pairs in the active volume which are then read off to tell us information on position. Using highly granular pixels allows for very precise momenta measurements, furthermore pixels minimise the leakage current and the detector is better protected against radiation damage. In order to maximise the detector coverage the different modules are tilted by 1 degree to ensure some overlap between the modules so nothing is lost. ^{VI}.

The Semi-Conductor Tracker (SCT)

Moving further out in the ATLAS onion of detectors comes SCT [26], the second silicon based detector. Many of the same concepts utilised for the pixel detector are used here. The main difference being that instead of using pixels to ensure granularity, SCT uses micro-strip sensors. Here the active area of the strips is a p+ diode strip implanted onto an n-type silicon base. The resolution of the strips is clearly best when particles traverse the strips perpendicularly. This is however alleviated by requiring that there are two layers of strips which are at a small angle to each other. This allows position to be measured in 3 co-ordinates, r , ϕ and z .

^{VI}The resolution of the pixel detector is better than the resolution of one pixel due to the fact that tracking calculates the centroid from a cluster of pixel hits whose error is less than one pixel width

Transition Radiation Tracker

This detector is very different compared to the previous two, being a gas detector. This detector is based on 2mm polyanamide straw tubes filled with a gas mixture (70% Xe, 27% CO_2 and 3% O_2) at slightly over-pressure. Between the straws a radiator is placed which passing electrons emit x-ray photons when travelling through as transition radiation. The X-ray photons are then absorbed by the Xenon in the straws producing large electrical signals in the gold-plated tungsten anode wires which are suspended in the straws. The TRT is not only used for tracking but also for particle identification, in that it can distinguish particles by the degree of transition radiation they emit. The straws are bundled into a cylindrical barrel with 50,000 straws divided into two electrically independent sections. The endcaps then has 320,000 radial straws. Since I worked directly with the calibration of this detector I will discuss the detector in much greater detail later in Section. 3.

2.2.4 Calorimeters

The Calorimeters in the ATLAS detector are designed to measure the energies of both charged and neutral particles over the range $0 < |\eta| < 4.5$ for a large range of energies and particle types. In general, the calorimeters consist of metal plates (absorbers) and sensing elements. The metal plates enhance the probability for hadronic showering and electromagnetic Bremstrahlung, thus slowing down the particles, causing the particles to begin to *shower* other particles which are detected in the various sensing elements.

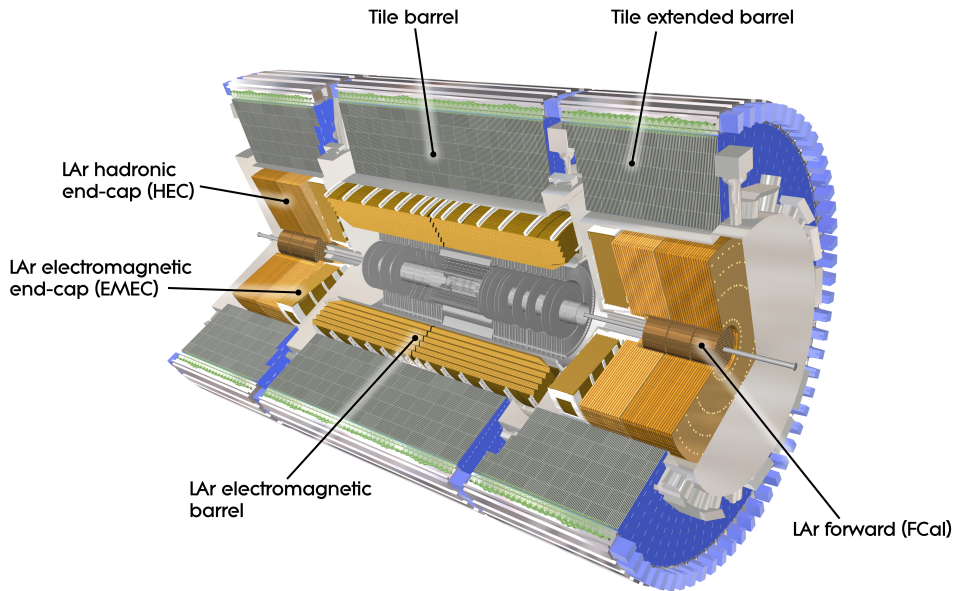


Figure 2.8: Schematic of the ATLAS calorimeters [22]

Electromagnetic Calorimeters

Just outside the solenoid magnet which wraps up the inner detectors lies the Electromagnetic (EM) calorimeter. The EM calorimeter uses lead absorbers and liquid argon active modules [27]. It is a sampling calorimeter with an accordion geometry, covering the entire ϕ space, with a barrel part which covers $|\eta| < 1.475$ and an end-cap section which covers $1.375 < |\eta| < 3.2$. Both the barrel and end-caps are split into three parts, the three *samplings*. The part of the calorimeter closest to the inner detector has highest granularity and precision allowing the detector to differentiate partially overlapping showers. The second sampling is the thickest and is the section where electrons and photons deposit most of their energy. The third is like a safety-net catching the energy deposits of the most highly energetic particles. Hadrons leave some energy deposit in the EM calorimeter but continue to travel through to the Hadronic Calorimeter, the EM calorimeter is designed predominantly to measure electrons and photons. As the showers pass through the Liquid Argon tanks they ionise the Argon, liberating electrons which are collected and recorded.

Hadronic Calorimeters

The Final Frontier for most particles, the elephant graveyard of hadrons. Most particles created in the proton-proton collisions are expected to have deposited the bulk (if not all) of their energy between the interaction point and the outermost layer of the hadronic calorimeters ^{VII}. The hadronic calorimeters consist of three parts: The Tile Calorimeter [29] (Tile-Cal), the liquid argon Hadronic End-cap Calorimeter (HEC) and the liquid-argon Forward Calorimeter (FCal) [27].

The tile calorimeter is placed directly outside the EM calorimeter, here the expected radiation level is low. The tile-cal differs from the EM cal in that it uses steel as the passive absorber and tiles of scintillating plastic as the sensor elements. The tile-cal is fairly standard fare for particle detectors apart from the orientation of the tiles. They are placed radially outwards from the Interaction Point (IP) which means that the particles traverse the tiles longitudinally which means better precision on shower shapes for particles with high p_T and allowing a better handle on missing energy in the detector.

HEC is similar to the EM cal except that it uses Copper as its absorbing material. It is placed further out than the tile-cal where the radiation is greater, since Liquid argon is seen to be more radiation resistant. Likewise the FCal which is also a liquid Argon calorimeter has a simple behaviour except that being so forward it must receive an even greater particle flux, as such it has very thick tungsten and copper absorbers

^{VII}For jets, 40% of the total energy is carried by charged pions and 25% is carried by photons (mainly coming from π^0 decays) which means the bulk of the reconstructed energy is actually deposited in the EM calorimeter [28]

Calorimeter Overview		
EM Calorimeter	Barrel	End-Cap
Coverage	$ \eta < 1.475$	$1.375 < \eta < 3.2$
Channels	102400	62208
Samplings	3	3
Aprox. Thickness	> 24 Radiation Lengths	
Composition	Liquid Argon elements and lead absorbers	
Tile-Cal	Barrel	Extended Barrel
Coverage	$ \eta < 1.0$	$0.8 < \eta < 1.7$
Channels	5760	1792
Samplings	3	3
Approx. Thickness	7-8 pion decay lengths	
Composition	Scintillating Tiles and steel absorbers	
Hadronic End-Cap		
Coverage	$1.5 < \eta < 3.2$	
Channels	3072	
Samplings	4	
Composition	Liquid Argon and copper absorbers	
Forward Calorimeters		
Coverage	$3.1 < \eta < 4.9$	
Channels	1792	
Samplings	2	
Composition	Liquid Argon and copper/tungsten absorbers	

Table 2.2: An overview of the ATLAS calorimeters

2.2.5 Muon Spectrometer

Muons are the only detectable particles which can penetrate through the inner detectors and calorimeters. Outside of the calorimeters lies the muon spectrometers which define the size of the ATLAS detector. Entangled in gargantuan superconducting toroidal coils sits the muon spectrometer. It is designed to measure the exiting muons momenta in a range of $|\eta| < 2.7$. The magnetic fields are necessary for bending the muons trajectories and thus enabling their momenta to be measured. There are two types of muon trackers [30]:

- The Monitored Drift Tube (MDT) chambers, whom are similar to the straw tubes of the TRT only much larger cover the low $|\eta|$ region.
- The Cathode-Strip detectors are multi-wire proportional counters whose wires are oriented in the radial direction and cover the high $|\eta|$ region.

Furthermore, the muon spectrometer has a fast trigger system: the Resistive Plate chambers (RPCs) in the barrels and the Thin Gap Chambers (TGCs) in the end-caps. The muon triggers are defined to provide bunch crossing identification as well as p_T threshold cuts.

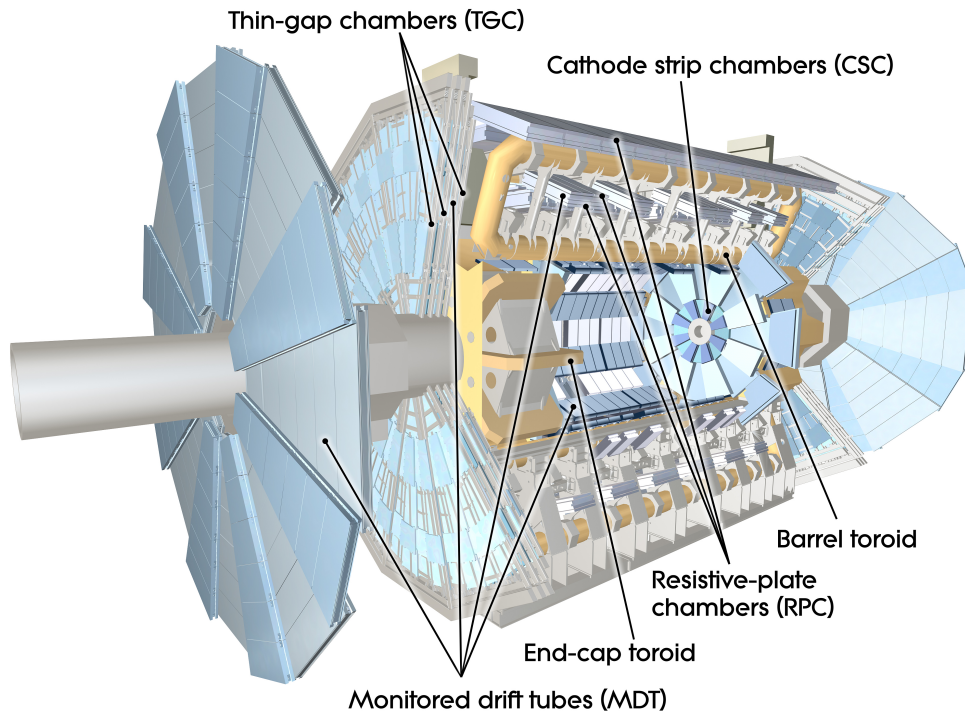


Figure 2.9: Schematic of the muon detector system [22]

2.2.6 Beam Monitoring and Luminosity

During the run time it is of great imperative to measure the instantaneous luminosity and to ensure that the quality of the colliding beams are satisfactory. In order to do so a set of detectors were developed [17]:

- **LUCID** (Luminosity measurement using Cerenkov Integrating Detector) As mentioned LUCID determines the luminosity by measuring the particle flux it receives when charged particles create Cerenkov radiation which are then read by photomultipliers. It is situated 17m from the IP, very close to the beam pipe ($|\eta| \approx 5.8$).
- **ALFA** (The Absolute Luminosity For ATLAS) Another detector designed to determine luminosity. ALFA consists of roman pots [31] and aims to measure the absolute luminosity by measuring the elastic scattering of p-p collisions at small angles. Its calibration is obtained during special runs with dedicated conditions. As the detector consists of roman pots, one can move the detectors very close to the beam and being situated 240m from the IP either side the detector is capable of measuring minute angles of $\approx 0.3\mu rad$.
- **ZDC** (Zero Degree Calorimeter) The primary purpose is to detect forward neutrons and photons with $|\eta| > 8.3$ in both p-p and heavy ion collisions. It is particular useful for heavy-ion collisions where the centrality of such collisions is determined by the number of very forward neutrons. On top of this it is a useful tool for studying

diffractive processes and is used as additional minimum-bias trigger. It is situated 140m on either side of the IP.

- **MBTS** (Minimum Bias Trigger Scintillators) These were designed to trigger on events where the beam conditions were sub-optimal, the inner detector had errors and for low luminosity beam settings. MBTS consists of 32 scintillator tiles in 2 disks 3.64m on either side of the IP. MBTS was thought damaged due to radiation due to high luminosity runs in 2011 and 2012, but it is still deemed useful as a trigger for the first proton-proton runs at newer energies and low luminosity, van Der Meer scans and Heavy ion collisions.
- **BCM** (Beam Condition Monitor) Its purpose is two-fold, firstly to check whether the beams are colliding with the collimators designed to protect the detector parts (and if so halt the beam) and secondly to measure the bunch by bunch luminosity by counting in-time and out-of-time collisions. It is situated only 1.84m on either side of the IP and only 5.5 *cm* from the beam. It needs to be so close in order to have a very speedy time response on the nanosecond timescale. It consists of two diamond sensors, which are readout in parallel, which can measure the time-of-flight and pulse height to distinguish events resulting from beam loss and regular collisions.

2.2.7 Triggers and Data Acquisition

At the LHC design luminosity, with 25ns bunch spacing and an average of 25 proton-proton interactions per bunch crossing, there are 1 billion collisions per second. Each of these events produces 1.3 Mbytes of information which requires a few seconds to process and store. Couple that with the fact that, due to limited resources and technology, data acquisition is limited to about 200 events per second. This means a required reduction factor of 5×10^6 . The challenge is to reduce the amount of data stored whilst maximising the efficiency for detecting events with *interesting* physics. Thus a trigger system is crucial to the success of the ATLAS detector.

The ATLAS detector has three levels of trigger, each with progressively more stringent cuts and utilise more information from more parts of the detector. The first set of triggers the Level One (L1) triggers are hardware triggers, they use only a limited amount of the detector information to make a trigger decision in less than $2.5\mu\text{s}$, reducing the rate to about 75kHz. Then there are level two (L2) triggers and event filter (EF) triggers, both of which are software based triggers and refine the cuts made at L1 and apply additional more stringent cuts. The combination of L2 and EF triggers is referred to as the high-level trigger, they reduce the rate to 200 Hz (the maximum frequency for recording events). The trigger chain and timings can be seen in Fig. 2.10.

2.2.8 Event Reconstruction and Data Quality

Once the various events have been selected by the trigger system the next unenviable task is data processing, event reconstruction and checks on the data quality. When running,

Event rate and decision stages

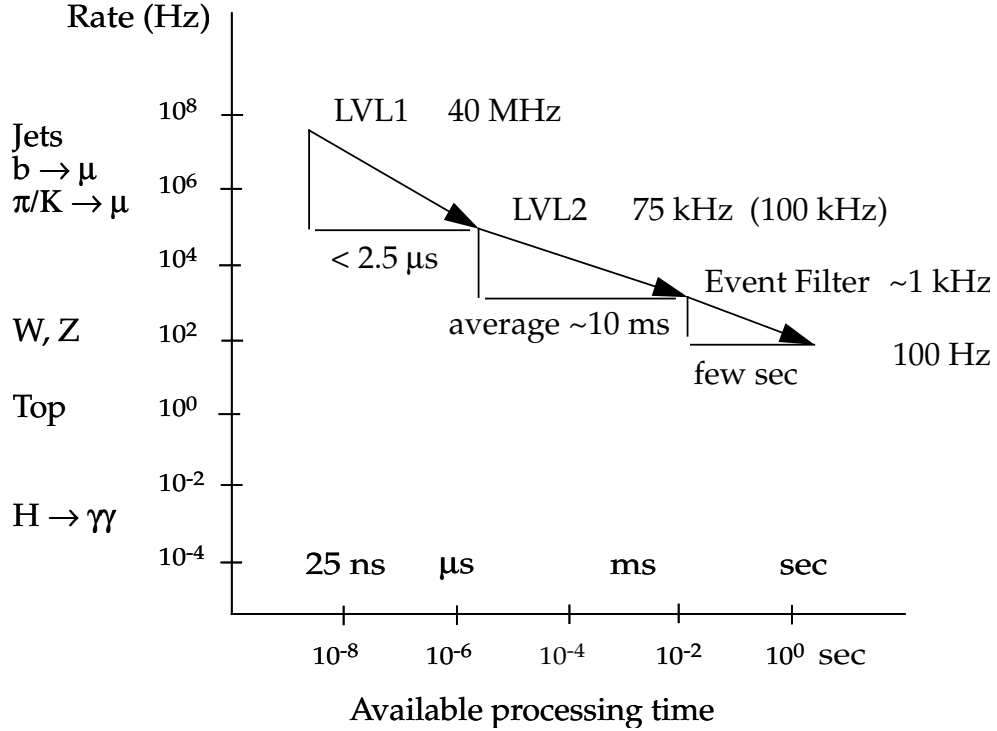


Figure 2.10: Event and Trigger Rates and Response Times [17]

the ATLAS experiment produces copious amounts of raw data which needs to undergo processing. One wishes to recognise and diagnose any potential problems with the data as soon as possible, hence a set of tools for data monitoring to check the integrity and quality of the data were designed, the Data Quality Monitoring Framework (DQMF) [32]. DQMF is a combination of offline (after processing) and online (before/during data taking).

The EF separates the data into several physics streams, triggered on different objects (Electromagnetic, Muon, Jets...) and one *Express Stream*. They are then sent to CERN Tier-0 centre (computing clusters, servers and storage) where they are stored on tape. The express stream is important for the Data Quality Checks, it contains roughly 10% of the data, most of which being high- p_T events with triggered leptons and jets. In other words it contains a good fraction of the interesting physics events to give a good picture as to the quality of the dataset. The express stream is processed in (quasi-real time) such that various detector parts (such as the TRT) can calibrate the detector in real time. The express stream means that any potential problems with calibration or software can be fixed and the data can be reprocessed correctly. A "sign-off" for the express stream is needed (whereby the data quality of the express stream is verified along with the calibration of the various detector parts) before the processing of the rest of the data from the physics triggers, known as the Bulk, can be processed.

Once green-lighted the bulk is processed, creating Event Summary Data (ESD) from the raw data , which then is turned into Analysis Object Data (AOD) and finally Derived Physics Data (DPD) which contain all the reprocessed information about the event necessary for Physics Analyses. These three separate types of datasets contain progressively less information about the events and become more optimised with reconstruction and the necessary variables for physics analyses. For instance ESD's contain much more tracking and trigger information then the majority of analyses require. The AODs and DPDs are spread over computing facilities around the world on a grid. These Centres are called Tier-1 centres.

So there you have it, a whistle stop tour of the ATLAS detector. Hopefully by now you the reader should have a reasonable idea about the make-up of the detector, what the jobs of the various constituents are, which particles can be detected and how the detector parts loosely work. All these parts of the detector I have utilised in my analysis in one way or another.

*An expert is a person who has
made all the mistakes that
can be made in a very narrow
field*

Niels Bohr

3

TRT

The Transition Radiation Tracker (TRT) is the part of the ATLAS detector with which I am best acquainted. I spent the first year of my PhD getting to grips with the TRT, its framework, its methods of calibration and its monitoring tools. It was my task to transform the calibration procedure into an automated system where the human monitor would need to do as little as possible. In this chapter I will give an overview of how the calibration for the TRT is done and how I automated this procedure. The TRT's main role is to measure the trajectories of charged particle and to help with particle identification.

The TRT is a so called straw detector. It consists of roughly three hundred thousand straws with a diameter of 4 mm. Each straw is a small cylindrical proportional chamber, with an anode wire in the centre at a potential of ≈ 1.5 keV, and the straw wall acting as a cathode. Charged particles passing through the straw ionise the gas in the straw (The gas is comprised of 70% Xe, 27% CO_2 and 3% O_2). The ionisation cluster is amplified when drifting in the electric field. The amplification factor is about $2.5 \cdot 10^4$, and the maximum drift time is 45 ns. The intrinsic resolution, obtained by measuring the drift-time of the ionisation cluster, is about 130 micrometres.

The space between the straws is filled with material, in order that relativistic particles travelling through the material produce transition radiation. This is radiation created at the boundary between two materials leading to photon emissions. Transition radiation consists of photons, which are strongly forward peaked (angle is relative to $1/\gamma$, where $\gamma = E/m$)

The Xenon in the straw gas absorbs the photons and a signal is produced which has a higher amplitude than the normal signal originating from particles passing by. Electrons produce transition radiation when their momentum is above 1 GeV, while pions radiate

only when their momentum is close to 100 GeV - thus, the TRT is able to distinguish an electron from a pion, Fig.3.1. We can distinguish the two particles using a measurement of time over thresholds which will be explained further down.

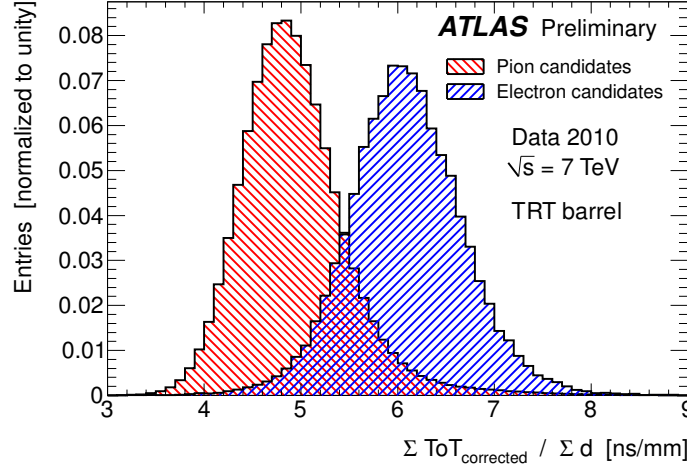


Figure 3.1: The separation in time over threshold t_{ToT} for pions and electrons in the TRT [33]

3.1 Tracking with the TRT

The coordinate system and tracking for the inner detector is well documented and has improved over the years and continues to improve as new methods develop and better understanding of our detector is garnered [34] [35]. The ATLAS coordinate system used for tracking and particle identification is illustrated by Fig. 3.2, this parametrisation is useful both for this chapter but also for the proceeding ones. A charged particle track is parametrised by the parameters $(z_0, d_0, \theta, \phi, q/p)$ at the reference point known as the *perigee*. This is the point along the particles track closest to the z axis. There are two impact parameters d_0, z_0 which describe how close this point is to the interaction point (or origin). Z_0 being the longitudinal distance of the perigee to the origin and d_0 being the transverse impact distance in the x-y plane to the beam axis. The polar angle, θ and ϕ are the two angles previously described and q/p is the ratio of particle charge to momentum ¹.

The inner detector has two main strategies for assigning *clusters* to tracks: [36]

- **Inside-to-outside:** Here as the name suggests the tracks start from seeds in the innermost layer of the pixel detector and candidate tracks are propagated outwards, in the SCT and then the TRT.

¹When the magnetic field is off the final parameter is 0 since the track is not bent and hence it's momentum cannot be measured

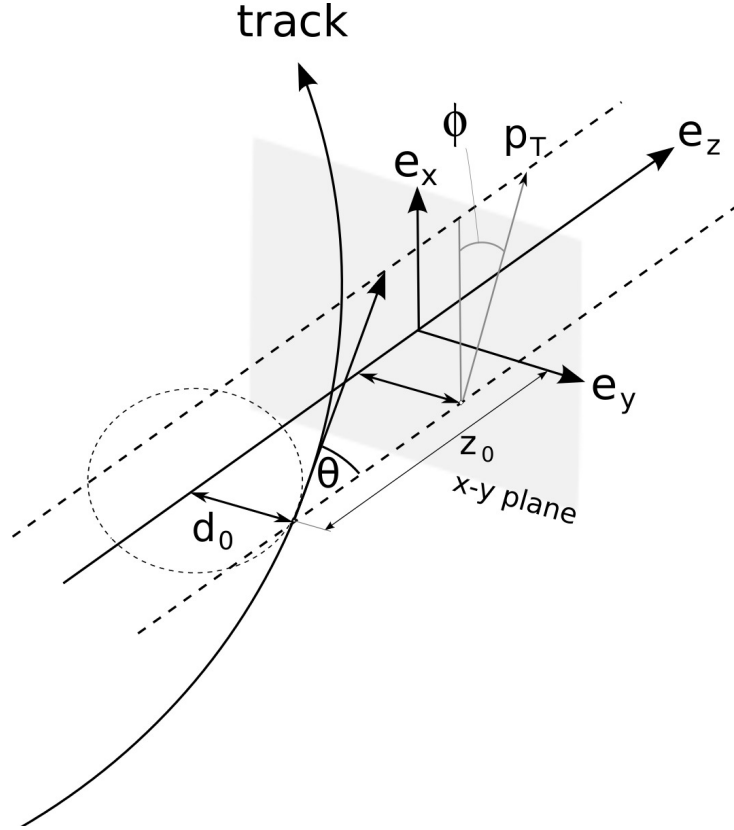


Figure 3.2: Track parametrisation in the ATLAS coordinate system [34]

- **Backtracking:** Very similar except here one starts with the TRT track segments and propagates those backwards to the SCT and Pixel detectors.

In order to create the *clusters* necessary for tracking the detectors have to translate raw electronic readouts to spatial information. For the Pixel and SCT detectors this is straightforward, nearby hits in the silicon are grouped into clusters. Whereas for the TRT one converts the measured drift time in the straws to a drift radius with an appropriate error. As we shall see later, the size of the errors on the cluster positions are crucial to the tracking, this in turn implies that the calibration of the detector is vital to good clustering and hence tracking and consequently momentum resolution.

The two main methods for track fitting in ATLAS are [34]:

- **Kalman Filter:** A now standard tool in the particle physicist arsenal [37], it combines forward filtering, backward smoothing and outlier rejection. In essence it subdivides the detector into various detector *planes*. One begins from a seed at a certain plane and propagates that measurement to the next detector plane, hits which are found near to predicted path in the next plane are added to the prediction and are used in the propagation to the next plane. This is completed until all track candidates cross all detector planes. The main concept of the Kalman Filter Technique is

that one can use a gain matrix to drive the prediction of the track through the sub planes based on actual measurements.^{II}

- **Global χ^2 :** Another age-old method is the χ^2 check. The track fit is done by minimising:

$$\chi^2 = \sum_i \left(\frac{x_i - e_i}{\sigma_i} \right)^2 \quad (3.1)$$

Here x_i is the measured position of a cluster, e_i is the predicted value from the fitted track and σ_i is the error on the measurement. The minimisation is achieved by solving a set of linear equations through matrix inversion.

Using a combination of the track building and track fitting methods, it is possible to build tracks from the primary vertex through the entire Inner Detector. As seen by Eq. (3.1) the errors on the cluster positions σ_i plays a large part in the overall track resolution and thereby momentum resolution. The curvature of a track, ρ , in a homogeneous magnetic field, B , is directly proportional to that particle's transverse momentum, p_T :

$$\rho = \frac{p_T}{0.3B} \quad (3.2)$$

The momentum resolution with respect to the detector can be shown to be [38]:

$$\frac{\delta p}{p^2} = \frac{\sigma}{0.3BL^2} \sqrt{4C_N} \quad (3.3)$$

Where σ is the spatial resolution, L the length of the track trajectory and C_N is a weighting based on the number of hits in the track. In other words whilst the detector design and collision kinematics define L and C_N , the spatial resolution, σ , is directly correlated to the quality of calibration and alignment.

3.2 Making a hit in the TRT

When a charged particle produces transition radiation, this leads to ionisation in the gas in the straw tubes. The ionisation in turn produces a current in the anode wire of the straws which are then read off by the electronic readouts of the TRT. The electronic readout produces a 24 bit pattern readout which covers a time scale of three bunch crossings (75 ns) each bin is therefore 3.125 ns in time.^{III}. This 24 bit value is then used to ascertain the drift time and drift radius thereby producing a cluster position used for tracking.

^{II}Generically a Kalman filter is an algorithm which uses a sequence of measurements with associated errors, taken over a certain time interval, and produces a statistically optimal estimate of an unknown quantity which is better than that which would be obtained from a single measurement.

^{III}The following explanation in this chapter is using the default p-p collision settings for the 7 TeV 2011 run as this was the period in which I was working on the TRT and the period in which the public plots and information adhere to [39]

The time difference between the two edges ($t_{ToT}=t_{TE}-t_{LE}$) is defined as the Time over Threshold, which is directly related to the ionisation power of the charged particles in the gas. As such it is one of the tools successfully used to distinguish electrons from heavier particles. TRT hits where the first bin is 1 are rejected since they can include hits produced from a previous bunch crossing.

$$t = t_{LE} - (t_{collision} + t_{ToF} + t_{SP}) \quad (3.4)$$

Here $t_{collision}$ is the time difference between the actual collision taking place and the LHC clock which the electronics operate on. In other words an offset to account for time synchronisations. t_{ToF} is simply the time it takes for a particle to travel from the interaction point to the straw it ionises. Finally t_{SP} is the time that the current induced in the wire takes to travel to the front-end electronics. For the TRT detector as a whole during a run these timing correction do not vary much, hence they are often considered as just one value ($T_0 = t_{collision} + t_{ToF} + t_{SP}$) per straw

Once one has the drift time one can calculate the distance from the wire to the track (called the drift radius)(r) as long as one knows the relationship between the two, often called the $r - t$ relation ($r(t)$). This relation is determined from data and fitted by a third degree polynomial (further explained in section 3.3.2) of the form [39]:

$$f(t) = a_0 + a_1t + a_2t^2 + a_3t^3 \quad (3.5)$$

When the drift radius has been calculated the only other necessary quantity is the uncertainty (δr_{hit}), which is necessary for the χ^2 track fit. The uncertainty is related to the number of clusters created by a charged particle and by the properties of the ionised electrons in the drift gas. However, the distance from the clusters to the wire plays a large role because if the clusters are created far from the wire, due to the large drift time the smaller effects of the electron-gas properties and discrete cluster number are minimised whereas if the cluster is created near the wire these effects have a much greater importance.

In the TRT we utilise two types of *hits*:

- **Precision Hits:** These are the types described above, whose positions are ascertained from the cluster information and by interpreting the electronic readout.
- **Tube Hits:** These are a much coarser type of hit aimed at just giving a rough estimate for the track position used as a basis for the track fitting. Here the drift radius is automatically assigned zero and the drift error $\delta r_{hit} = d/\sqrt{12}$, where d is the tube diameter. Once the pattern recognition has found the hits associated with the track, these hits are converted to precision hits, by using the tube hits one does not degrade the fit due to *bad hits* from other bunches.

3.3 Calibration

The aim of the TRT calibration is to have the best estimate for the so called *track-to-wire* distance based on measuring the leading edge time. The Calibration is done using an iterative approach, whereby the tracks are reconstructed based upon some starting values of T_0 and the $r - t$ relation. The new reconstructed tracks are then used to derive some new T_0 value and $r - t$ relation which can be used as inputs to the next iteration until one is satisfied with the results. Often only one iteration is required since the calibration values do not change much between runs, hence the initial values can be validated very quickly.

The value for T_0 as well as the $r - t$ relation are calculated at different detector levels (or granularity) ranging from the individual straw level, to a chip to one layer of the wheel to the Whole TRT. This is of interest to see the variation across different detector levels to get a better idea of the entire detector response.

3.3.1 T_0 Calibration

In order to determine the T_0 calibration constants one can study the variation of time residuals Δt .

$$\Delta t = t - t_{track} \quad (3.6)$$

Here t_{track} is the most probable value for the drift time which is calculated by taking the inverse of the $r-t$ relation thereby translating a given track-to-wire distance to a time, t as previously described in Eq. (3.4). This distribution fits a Gaussian which is properly fitted and its mean value extracted and used to correct the old T_0 to correct for the new value. An example of a measured time residual is shown in Fig. 3.4.

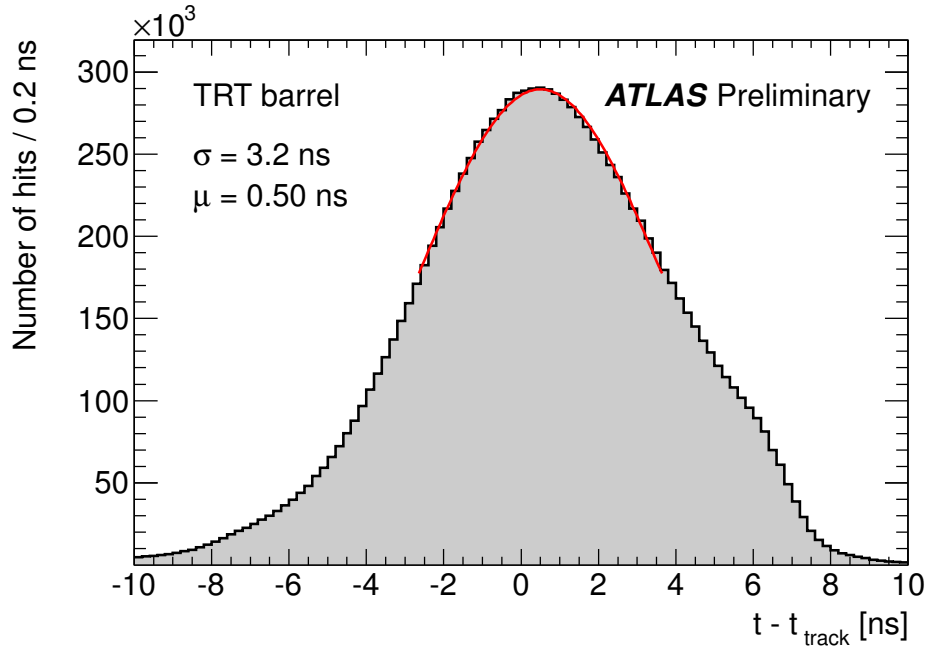


Figure 3.4: Time residual distribution for barrel, side A. The quoted parameters σ and μ are obtained from a Gaussian fit to the $\pm 1\sigma$ range of each distribution (red line)

3.3.2 $r - t$ relation Calibration

As mentioned the drift radius r is converted from the drift time by a third order polynomial, Eq. (3.5). It is necessary to define boundary conditions for the function to fit with the physical reality, such that if the $r - t$ relation predicts a distance larger than the straw radius one assumes $r(t) = 2 \text{ mm}$ the straw size. Likewise if the function predicts a radius

less than 0 mm one assumes 0 mm. Here we assume that the drift radius is always positive. We choose a third degree polynomial purely as a simple arbitrary function, it is possible that better forms describing the relation exist. The predicted best estimate of r differs from the true distance travelled by the electron due to the presence of the magnetic field bending the primary electrons path and due to the finite number of primary ionisations. Since the path is bent, the true distance travelled by the electron is always slightly longer than the distance of closest approach between the track and anode wire, Fig. 3.5

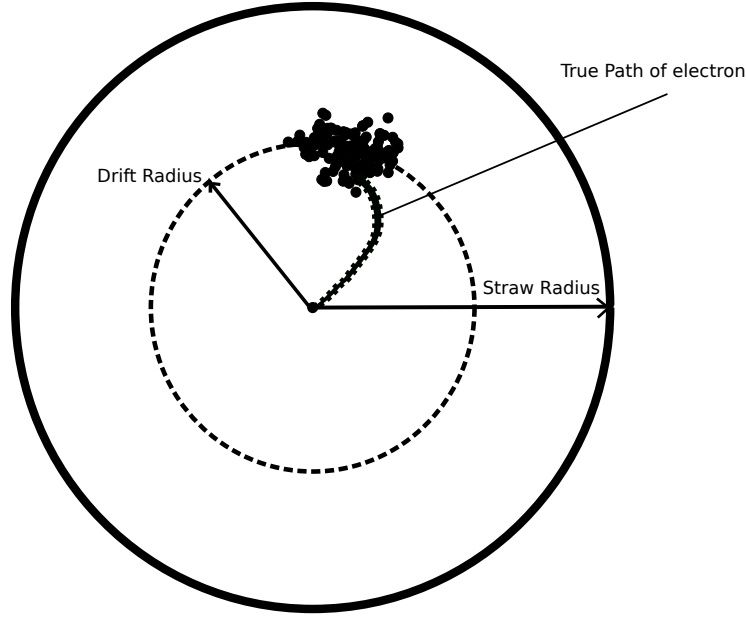


Figure 3.5: A picture illustrating the difference in path length between the drift radius (closest approach of track to wire) compared to the true electron drift path in the magnetic field

To ascertain the constants in Eq. (3.5) one constructs several histograms of the reconstructed track-to-wire distances for a specific electron drift time interval of 1 ns (in other words the reconstructed distances measured for electrons with drift time between 5-6 ns, 7-8 ns e.t.c). Each of these time slices creates a Gaussian distribution which is consequently fitted and then the mean values are extracted and plotted as a function of drift time as illustrated by Fig. 3.6.

One known problem with this $r - t$ relation is that any shift along the time axis is indistinguishable from a shift in the T_0 constants. In order to avoid this ambiguity one can either fit to a fourth parameter, an offset, or artificially introduce an offset to the T_0 . The latter is chosen by fixing one point of the $r - t$ relation at the point $f(t = 18ns) = 1mm$, which is in the middle of the straw and means that $f(t = 0) \approx 0$.

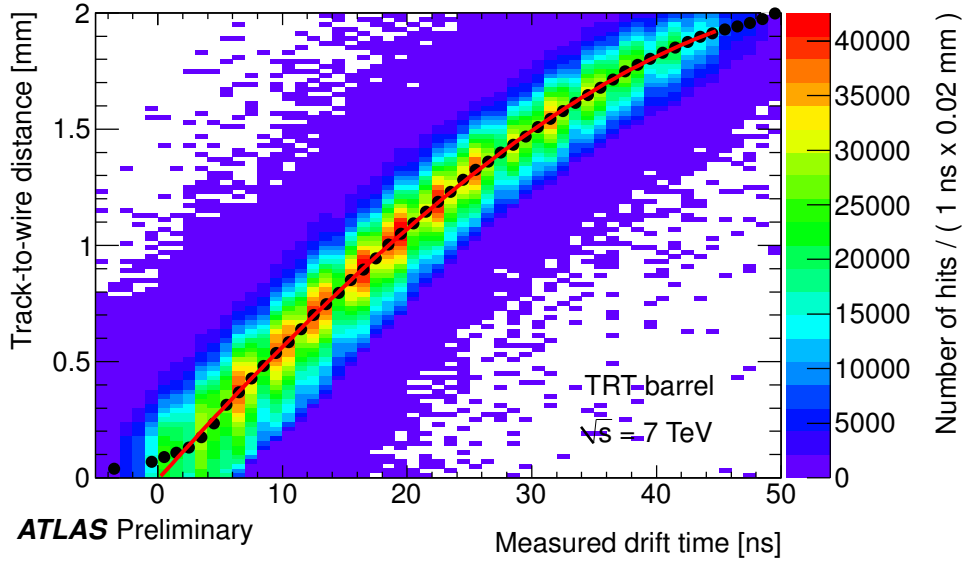


Figure 3.6: A plot of the $r - t$ relation, where each point comes from the mean of the fitted Gaussian per time slice which leads to a three degree polynomial fit, as measured in the TRT barrel [39]

3.3.3 Validity of Calibration

So now we have managed to reconstruct the tracks based on our starting calibration constants and have calculated new calibration values based on the reconstructed tracks. The task now is to validate whether the initial constants have done a good job, whether further iterations to improve the tracks should be done or whether the TRT has some problem. In order to validate the calibration various so called *figures of merit* need to be assigned:

- The width of the **position residual**, $\Delta r = r(t) - r_{track}$, distribution is used as a figure of merit, after several calibrations the idea is to minimise the width. Due to the fact that the distribution is not entirely Gaussian one only fits in the range $\pm\sigma_r$. Due to symmetry the distribution is centred on 0mm, because of this symmetry the position residual mean is not sensitive to miscalibrations but only missalignments. However the width is sensitive to both.
- The **time residual**, $\Delta t = t - t_{track} = t_{LE} - t_0 - t_{track}$, distribution is one of the best figures of merit. Again the distribution is roughly Gaussian fitted in the range $\pm\sigma_t$, the mean value is directly related to detector timing and as such one desires the mean, μ_t , to be as close to zero as possible. The width of the Gaussian is linked to the $r - t$ relation and hence the final resolution and therefore also should be minimised.
- The final merit is the **Absolute position residual**, $\Delta|r| = |r_{track}| - |r|$. Using the absolute position removes the symmetry and makes the distribution sensitive to miscalibration. Hence if the mean, $\mu_{|r|}$ differs from 0 mm it shows that there is a

systematic offset between the drift radius and track-to-wire distance which is the result of a poor T_0 or $r - t$ relation.

Using these three distributions one can check the quality of the calibration and decide whether the initial calibration constants were good enough or whether further iterations are required. The calibration constants are updated when the expected improvement in the width of the Δr distribution is about 1%, i.e of the order of $1\mu\text{m}$

3.4 Automating the Calibration

The TRT calibration is complex and of great importance for particle identification and tracking not only in the TRT but as part of the whole inner detector. The motivation for automating the previously described calibration is simple, the TRT team has a responsibility to calibrate each stable beam run within 36 hours from a completed run. This run must be flagged as "Good" or not based on whether the TRT has managed to reconstruct the tracks effectively. Previously, this required a weekly offline shifter to search the Atlas Run Query for newly completed Stable beam runs; Then to manually configure the calibration procedure, check that it was running, verify that the outputs were acceptable and report back. This clearly is a time consuming process and means that the calibration is done in a time frame constrained by the shifter and their available time. Thus, the idea of the automated system ensures that a lot of time for the shifter is saved. Furthermore, it means that the calibration procedure can be started as soon as a run is completed (or before, once a sufficient number of events have been processed) thereby allowing more time to run the calibration over a greater number of events or to pursue multiple iterations before the 36 hour calibration loop finishes. This results in a more streamlined procedure and better quality calibration constants.

As mentioned previously when there is a stable run, an express stream is produced in quasi-realtime, it is this stream of data which is used for the calibration of the TRT. There is already a computing system and mainframe in place to produce the stream, the Tier0 computing infrastructure. It was decided that for the automated calibration one should use this infrastructure already in place. So the question was how to implement the calibration using this framework and how one could monitor the calibration.

3.4.1 Structural Overview

In order to automate the procedure we utilised the pre-existing Tier0 Management System (**TMS**). The basic concept behind TMS is that a user creates a configuration file which they submit to the Tier 0 mainframe (a computer cluster called EOWYN) which creates a Tier0 Manager (**TOM**) instance based on the configuration. EOWYN then accumulates all the datasets from the *caf^w*^{IV} database, for those datasets which match the criteria pre-defined in the TOM configuration file, these datasets are then sent to the TOM instance.

^{IV} the database name where the datasets are stored on Tier0

Then in accordance with the configuration file, the TOM instance sets up the initial task and proceeds with a *Transform* (in our case a set of python scripts created which run the calibration in various steps which I will soon explain). These tasks can then be monitored online.

Firstly a quick note on some of the nomenclature and terminology:

- An **instance** is what a user creates once they connect to the TMS computer base named *EOWYN*. Each *instance* can hold several different **Tasks** with different datasets as inputs and can apply different *transformations*.
- A **transformation** is simply the code/program which is applied to the input dataset. For example all the parts of the calibration chain are configured in one *instance* by the user “txtrtcalib”, each part is a *task*, such as “trtaccum” which is the accumulation part of the chain (Described in the following section).
- When the TMS finds a suitable dataset(s), it calls the appropriate *task* and creates a **process** to run this task. So, there can be multiple *processes* created from the same task, if multiple input datasets are provided.
- Each *task* splits the files in a given dataset into bunches of a pre-defined size. Each bunch is then processed as an individual **job** within that *task*.

So now hopefully it is somewhat clear to you the way a user interacts with the Tier-0 mainframe, it will become clearer with a specific example. As in illustration please see Fig. 3.7.

3.4.2 Calibration Steps

The calibration of the TRT is broken down into 4 different *tasks* in order to be processed by the Tier0 most effectively:

- **Accumulation** - The files from the input RAW dataset (express stream) are sorted into bunches by the TMS, then the transform reconstructs and collects hits for each bunch of files in parallel. An email is sent out once a run has started to be processed in order to notify the calibration team that a stable beam run has been initiated. This can be initiated as the run is still ongoing as long as there is a minimum of 10,000 events (the minimum for a good TRT calibration). This ensures that the data is being analysed from the moment they are ready, hence vastly improving the efficiency and time response of the calibration.
- **NTUP Merge** - This transform simply merges all the NTUPLE’s with the hit information created in the Accumulator stage into a single file of binary histograms (used to save space and improve efficiency). The beauty of this stage is that the merging can be done as the first task (accumulator) is still processing jobs, thus

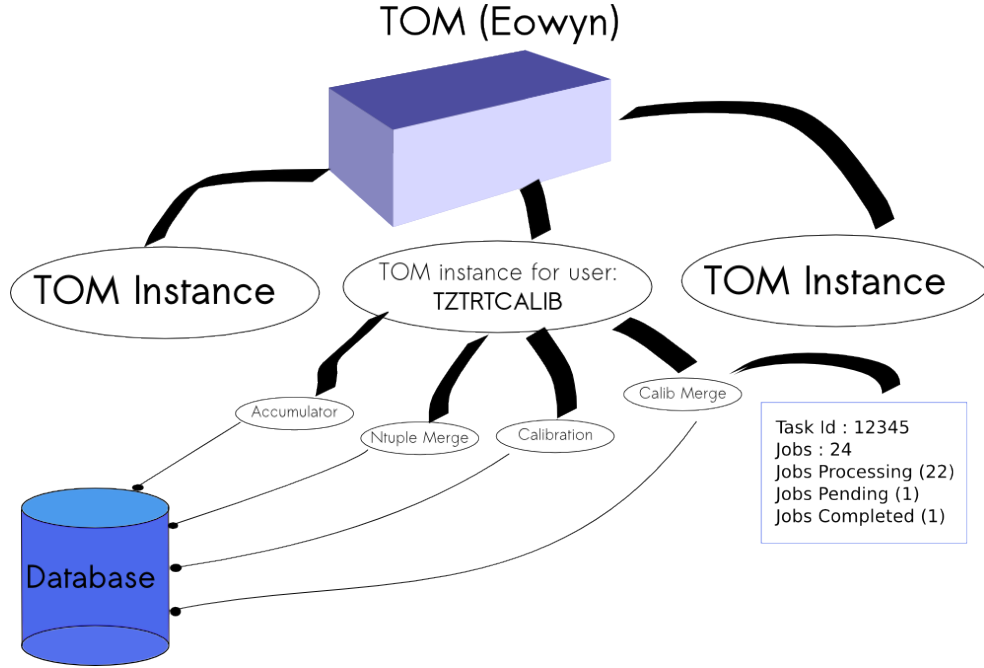


Figure 3.7: A schematic of how the Tier 0 mainframe interacts with its users, jobs and databases.

continuously merging. In order to do so we had to develop a special merging and functionality with the Tier0 team. As a job is completed in the first task it is merged to the previous merged files. This again improves the speed and efficiency allowing the accumulation and merging to be done in quasi-real time.

- **Calibration** -Once the hit information files have been finally merged the calibration transform then analyses the hit information and computes new calibration constants for each detector layer in parallel. The calibration method are those described in the previous sections. Here the calibration is split into different detector level granularities and are all analysed simultaneously.
- **Calibration Merge and Plot** - Finally we merge all the calibration outputs created for each part of the detector back into a single ROOT file and a textfile. The task then proceeds to e-mail the expert calibration shifter group notifying that the job has finished and what the output calibration residuals are.

So clearly the human involvement is minimal, the expert calibration shifter receives an email at the beginning and the end of each run and calibration, they can then look at the residual values (figures of merit) in the email sent and check the actual output plots for each run. As long as they are of sufficient quality they can then green light the run and calibration or if insufficient repeat the calibration chain with a new iteration by using the new calibration constants. A run can take anywhere from a few hours to a full day.

3.4.3 Monitoring

It was important for us to have some way of monitoring each step of the calibration chain. Fortunately the Tier0 already had an inbuilt task monitoring system which I configured for the TRT Calibration. Each step in the calibration chain run as individual processes by the Tier0 Manager.

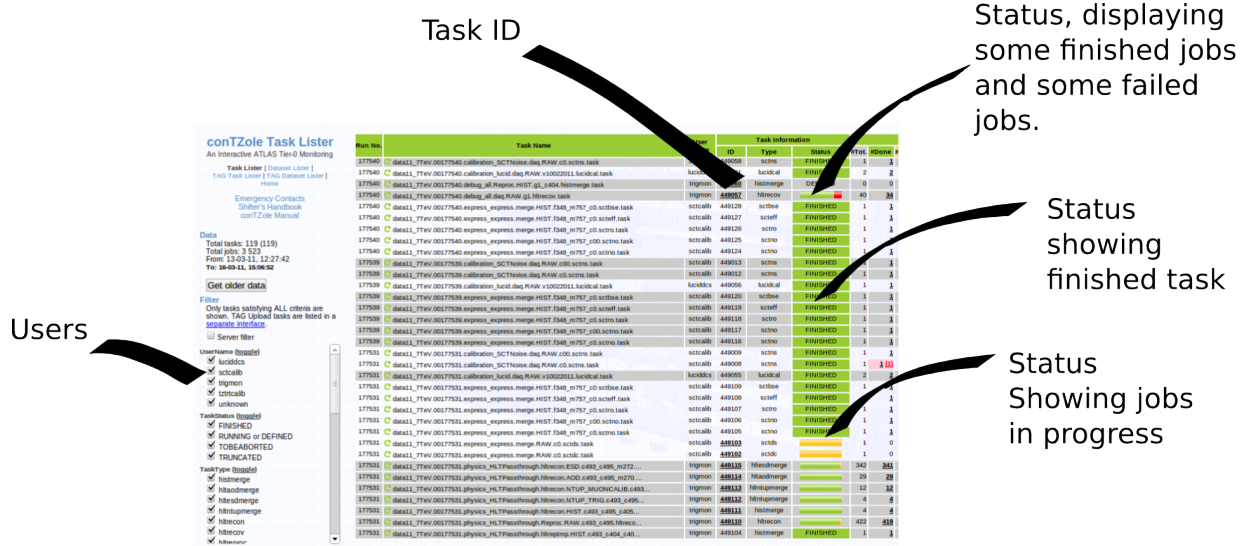


Figure 3.8: Tier 0 Monitoring

One can select only tasks submitted by use **tzttrtcalib** (our username), by ticking the relevant check box on the left side panel. A list of current and finished tasks is provided, the *Status* column indicates the progress of each task. Blue means the job is pending in the queue, Yellow means the job is running, Green shows which jobs have been successfully completed, Red indicates the jobs which have failed. When all jobs in the task are completed successfully the status will go green and read "Finished". From this monitoring page, one can truncate tasks which are running or re-activate jobs which have failed should one need to.

3.4.4 Configuration

The technical details for how one configures the Tier-0 interface with the the TRT calibration and looks for datasets is described in an internal note for ATLAS. The configuration scripts in essence create the instances for each part of the TRT calibration chain, specify which datasets to use from an oracle database search and then specify where to find the python script which I have made which run the calibration code and call all of the various tracking algorithms.

The other part of the configuration is for the actual calibration and tracking algorithms. For each calibration of a run a configuration file is needed which contains the starting calibration constant values, the geometry for the detector, its material description a list of

known problematic straws/detector parts, a material description, whether the run is heavy ion or proton-proton e.t.c From run to run this does not change much so the expert shifter monitoring the calibration should normally not have to change anything, however when there is a change in beam conditions, for example, the expert shifter simply needs to modify one configuration file with the relevant details and then the scripts I have made for the calibration can update automatically.

3.4.5 Outlook

In general the automatisisation of the calibration was a great success, and was utilised for the entire 2012 data taking period as well as a large fraction of the 2011 data taking period for both p-p and heavy ion collisions. Thus freeing up the calibration shifters and improving on the efficiency and efficacy of the calibration. However there are still ways in which one can improve the automation even more. At the moment the procedure to run further iterations is cumbersome and requires quite a lot of intervention from the shifter. It is possible to improve this and make this more automatic by automatically checking the figures of merits in a python script and suggesting whether further iterations are required or not. As the TRT calibration develops further figures of merit will be invented and newer improved calibration and tracking procedures invoked, this means that the automation of such procedures are always in flux.

*Why sometimes I've believed
as many as six impossible
things before breakfast*

Lewis Carroll, *Alice in
Wonderland*

4

Same Sign Dilepton Analysis Motivation

As stated in the introduction it is well known that the Standard Model is incomplete and there is more to the story than we have heard so far. There are many ways to look for physics beyond the Standard Model. Within the ATLAS collaboration there are a whole host of analyses looking for all kinds of exotic and BSM models from Supersymmetry to Extra Dimensions to Hidden Sector models to Miniature rotating black holes and other Sci Fi sounding models. The vast majority of these analyses are specific, fine tuned searches looking for a particular model, often even for a specific decay from that model. For our analysis we decided to take a slightly different approach, a broader fish-eyed lens approach and say that whilst we know there is definitely new physics out there, we do not necessarily know which, if any, of these specific models postulated are correct or even most likely. Furthermore, there is a good chance that none of these models are correct and nature is more strange and wonderful than we could ever imagine. So now we wish to design an analysis which is more general and sensitive to as many different models as possible (even those not dreamt of), such that we can catch any new physics we may have missed from the specific searches. Thus we are not limiting or biasing our searches using the ATLAS detector.

In order to do such an analysis we wish to look at event types which have clean signatures and little expected background from the Standard Model. One such event type are those with same-sign (SS) dileptons. That is events where the final state contains one or more pairs of leptons and where both leptons in the pair have the same charge ($e^\pm e^\pm, \mu^\pm \mu^\pm, e^\pm \mu^\pm$)¹. As we shall discuss in section. 6 there are few processes in the SM which give this final state but many BSM models do, henceforth the sensitivity to new physics with this final state signature is high. Furthermore, using high momentum leptons

¹In our analysis we do not consider hadronically decaying taus.

as the signature particles means the final state is clean, typically well isolated and easy to trigger on. Same-sign dileptons are hence a great probe for BSM physics. In the following subsections I shall describe just some of the models our analysis is sensitive to.

Motivation Summary

- SM is an incomplete theory
- There are plenty of BSM models with same-sign dilepton final states
- Same-sign dileptons provide a very clean signal
- Very few SM processes lead to same-sign dileptons
- High signal/background ratio is expected
- Inclusivity means that we probe a huge range of models

Strategy

1. Make model-independent cuts to select prompt lepton pairs:
 - Minimal kinematic cuts on leptons
 - No cuts on missing energy in events
 - Minimal cuts on jets in events
2. Blind analysis ^{II}
3. Investigate the invariant mass distribution of same-sign dilepton pairs
4. If no new physics observed, then one can set limits on fiducial cross-section (explained later) for new physics.
5. Set limits on the production cross-section and mass for left-handed and right-handed doubly charged Higgs bosons.

^{II}Do not look at the data in the signal region until the methods to predict the expected backgrounds are finalised and validated.

4.1 Six impossible things to believe before breakfast

4.1.1 Supersymmetry

Supersymmetry (SUSY) is probably the most *popular* model leading to same-sign dilepton pairs in terms of papers published and workforce. Supersymmetry is a spacetime symmetry that assumes for every Standard Model particle there is a superpartner that is entirely the same, with respect to all quantum numbers, except that its spin differs by one-half unit [40–42]. The introduction of such particles provides a potential solution to the hierarchy problem. If one also conserves R-parity^{III} [43] then SUSY particles must always be produced in pairs and the lightest supersymmetric particle (LSP) is a great candidate for dark matter. These are the two strongest motivations for SUSY. Furthermore, SUSY can be used to explain why protons don't decay and help to unify the three fundamental SM forces at very high energy scales.

Of course, if supersymmetry were an exact unbroken symmetry we should have already seen these superpartners, so where are they? Thus it is asserted that SUSY must be a broken symmetry whereby the superpartners are in fact much heavier than the regular particles. There are many different mechanisms for breaking SUSY (gauge mediated, gravity mediated or otherwise), however most breaking mechanisms lead to the introduction of a large number of parameters: masses, mixing angles and CP violating phases. This variety of phase space leads to a gamut of potential experimental signatures. The different incarnations of SUSY also have very different properties in terms of how they solve or don't solve the hierarchy problem and which particle is the LSP. (Here is a very simplistic overview of SUSY and its motivations).

Same-sign leptons can be produced in a multitude of decays, depending on the models allowed decays [44]. A prime example is neutralino pair production. The neutralinos can then further decay to lighter gauginos such as (the lightest supersymmetric particle (LSP), a dark matter candidate) and a vector boson. The vector bosons can then decay to leptons as seen in Fig. 4.1. There are many more mechanisms for such decays, but the majority result in large missing energy and jets, which is why many of these decay modes have specific analyses that have additional jet and missing energy requirements to improve sensitivity for the specific SUSY signal.

4.1.2 Heavy Majorana Neutrinos

The discovery of neutrino oscillations made it indisputable that neutrinos had mass, albeit tiny. The mechanism for generating neutrino masses is currently unknown in the SM. The simplest extension is adding a heavy chirally right-handed Majorana neutrino (m_R) and assume that the chirally left-handed neutrino is a Dirac particle (M_D), the same as all the other SM fermions. In such a model way one can show that the mass eigenstates is

^{III}SM particles are defined as having an R-Parity of 1 and supersymmetric particles -1, where R-Parity is defined as: $p_R = (-1)^{2(B-L)+2s}$. Here B is the baryon number, L lepton number and s spin.

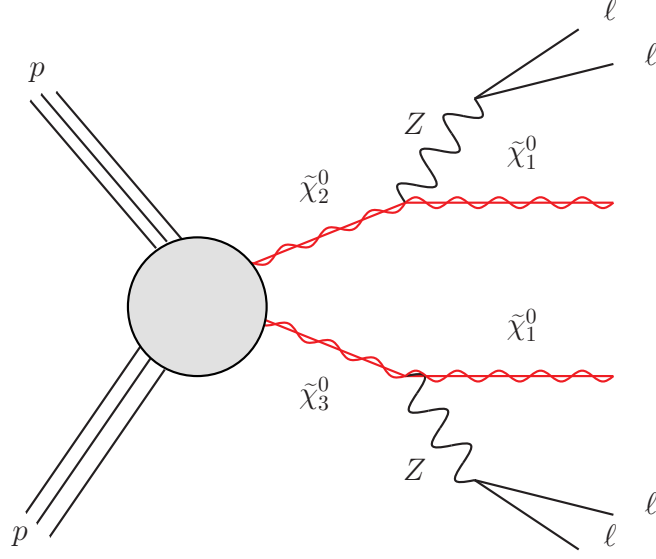


Figure 4.1: Example of a SUSY decay leading to a same-sign dilepton pair.

given by $m_1 \approx m_D^2/M_R$ and $m_2 = M_R$ (with $m_R \gg m_D$). This mechanism explains why physical neutrino masses are so small, because the right-handed Majorana mass m_R is so large we can construct a mass for a light neutrino m_1 which is on the scale that we observe the neutrino mass. This mechanism is generally known as the see-saw mechanism [45] [46] [47]. In the SM's simplest extension one adds at least two right-handed heavy neutrinos N . Being right-handed, chargeless, and colourless they do not add any additional interactions to the SM. However, being of Majorana nature they allow for processes which violate lepton flavour conservation. Traditionally see-saw mechanisms imply that the heavy Majorana neutrino mass needs to be several orders of magnitude heavier than the light SM neutrino. However more complex see-saw mechanisms which allow for intergenerational mixing allow the heavy neutrino mass to be on the electroweak scale and hence accessible at the LHC [48] [49]. An example of an interaction with a heavy Majorana neutrino leading to a same-sign dilepton pair is depicted in Fig. 4.2

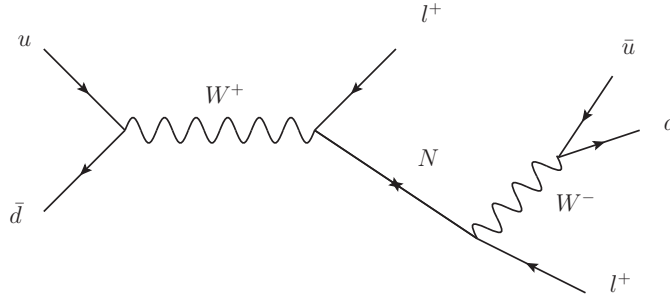


Figure 4.2: Example of a process with a heavy Majorana neutrino leading to a pair of same-sign leptons

4.1.3 Doubly Charged Scalars

There are many extensions to the Standard Model which generate a doubly-charged scalar particle [50–52]. Often it is some exotic Higgs boson but not exclusively (such as in the Zee-Babu model described below). In most of these models the production and decay mechanisms are essentially the same. The dominant production mode for SS final states is pair production with a Z/γ^* mediating, as depicted in Fig. 4.3. These doubly-charged scalars can then decay into a pair of same-sign charged leptons. The two leptons can in general be any flavour, and the branching-ratio depends on the specific model. Depending on the mass of the scalar another common decay is to pairs of same-sign W bosons or even another singly charged Higgs boson, but those scenarios are not included in the analysis.

The branching ratio for the decay of such doubly charged scalar to a pair of leptons depends on the mass of the scalar, $\Phi^{\pm\pm}$, the coupling parameter h_{ll} and whether the lepton pair have the same flavour ($k == 2$) or different flavour ($k == 1$):

$$\Gamma(\Phi^{\pm\pm} \rightarrow l^{\pm}l^{\pm}) = k \frac{h_{ll}^2}{16\pi} m(\Phi^{\pm\pm}) \quad (4.1)$$

These decays are considered prompt if the decay length is less than 10 microns^{IV}. This corresponds to having a coupling strength $h_{ll} > 10^{-6}$ for $m(\Phi^{\pm\pm}) = 300$ GeV.

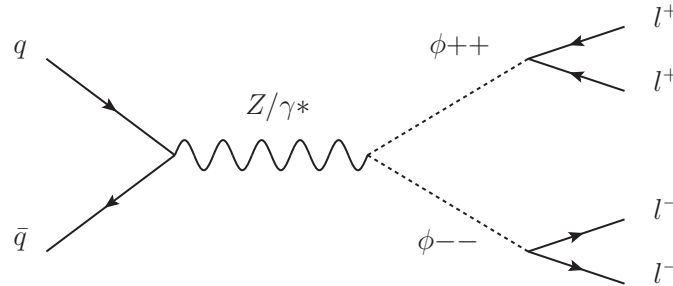


Figure 4.3: Example of a process with a doubly charge scalar leading to pairs of same-sign leptons

Left-right Symmetric Models

Another class of mechanism which generates a neutrino mass term, the Left-Right symmetric models (LRSM) contain the gauge group $SU(2)_L \times SU(2)_R \times U(1)_{B-L}$ [53] [54]. Clearly from experimental constraints the $SU(2)_R$ symmetry must be broken in nature, and much like the Higgs mechanism breaks electroweak symmetry, this is done spontaneously. The breaking of the gauge group must be done by the $SU(2)_R$ triplets. This type of symmetry can also be found in supersymmetry, but with the additional requirement that

^{IV}Implicitly we require that the doubly charged scalars are not long lived so that they decay before coming to our detectors.

R-parity must be violated in order to give a massive Higgs particle. If one considers the SUSY variety of the Left-Right symmetric model, eight neutral scalars, six pseudoscalars, six singly charged scalars and two doubly charged scalars come as a result. The doubly charged scalars, which are of mass ≈ 200 GeV, which would decay into a same-sign pair.

Little Higgs

A rather quaintly named model, the Little Higgs model aims to solve the hierarchy problem without using strong dynamics or SUSY [55] [56]. In this model the Higgs boson arises as a pseudo-Nambu-Goldstone boson whose mass is protected from divergencies by approximate global symmetries. It assumes that the current SM is just an approximate effective theory and that there is a cut-off for the SM as we know it. Crucially the model produces new states at around the TeV scale in order to cut off the most important divergencies and keep the Higgs mass stable, which means that this model can be probed at the LHC. These models also create a more complicated Higgs sector including a Higgs triplet with a doubly charged Higgs having a mass on the EW scale and decaying into two leptons.

4.1.4 Zee-Babu

This is yet another model which aims to be a minimal extension to the SM. It provides neutrino masses consistent with experimental constraints [57] [58]. The most common and economical way to account for neutrino masses is to invoke a right handed neutrino in a kind of see-saw mechanism. This has the drawback that these new right-handed particles are often very heavy and they must by necessity couple to the Higgs, thus inflating its mass. Hence we would still need another theory such as SUSY in order to stabilise the Higgs mass. Alternate ideas try to use existing SUSY fields to produce the neutrino mass and fix the hierarchy problem with SUSY simultaneously. This model, however, endeavours to account for the neutrino mass using radiative corrections. In this model the neutrino mass is a Dirac mass which is generated at the 2-loop level. The extension adds two complex singlet scalar fields, one singly-charged and one doubly-charged. This lead to neutrino masses proportional to the Yukawa couplings of the new scalars and inversely proportional to their masses squared, hence restricting the available parameter space. This allows for a realistic neutrino mass, a stable Higgs mass and the potential for these new scalars to be observed at the TeV scale, whereby one of the scalars can decay to a same-sign lepton pair in the same way as depicted in Fig. 4.3.

4.1.5 Microscopic Black Holes and Extra Dimensions

A perhaps even more exotic model to fix the hierarchy problem is that of Extra Dimensions. In some models of Extra Dimensions the gravitational field also propagates into the other dimensions and hence is seen as significantly weaker in our localised 4D world compared to the other Standard Model fields which are confined into their 4D cage [59]. The fundamental Planck scale, m_D , might be pushed to the EW scale in such a superdimensional world. If that is the case then TeV scale microscopic black holes could exist and be produced at

the LHC [60]. They can be produced when the distance between the colliding protons is of the same order of magnitude as an event horizon on a multi-dimensional black hole which is of the same mass as the proton-proton system. These black holes will then evaporate by emitting Hawking radiation [61] resulting in all sorts of high-momentum particles. Same-sign pairs can come directly from the black hole or from SM particles produced by the black hole which decay [62]. A microscopic black hole (μBH) is depicted decaying in Fig. 4.4.

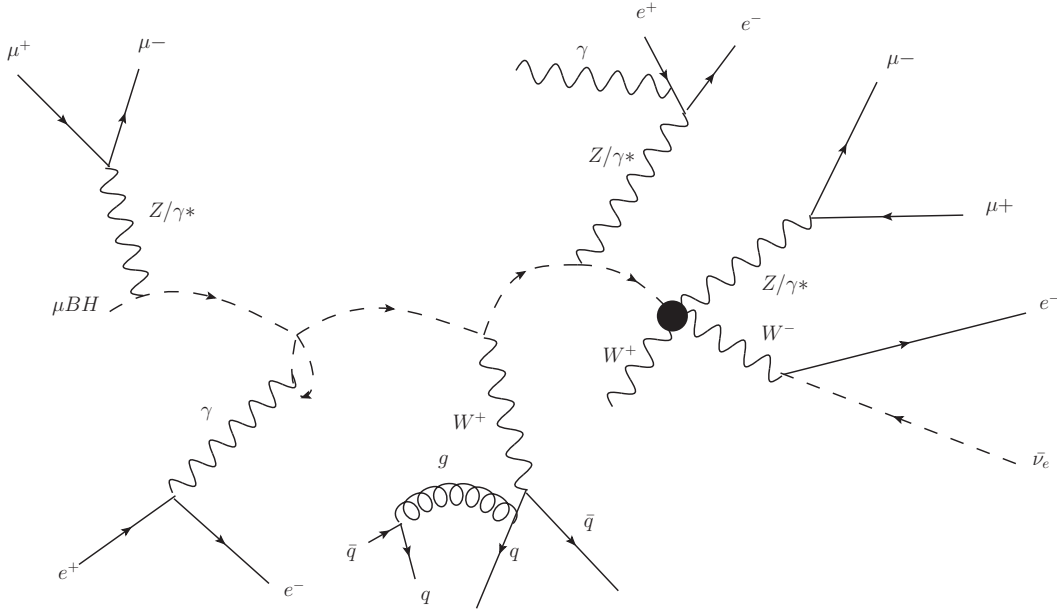


Figure 4.4: An example of a microscopic black hole (μBH) travelling and decaying via hawking radiation until finally *exploding* in a firework of particles. Such a decay leads to many particles and tracks in the final state, including for the possibility of a same-sign muon pair. The dashed line depicts the path of the microscopic black hole.

4.1.6 Same-sign Top Quarks

Same-sign top quarks can be produced in a number of different ways [63], as shown in Fig. 4.5. Either same-sign tops can be produced by some s-channel production mediated by a colour-triplet or colour-sextet with a $4/3$ charge or by a t-channel exchange of a neutral colour-singlet Z' or colour-octet g' . Either way, if the resonant masses are much larger than the electroweak symmetry breaking scale they can both be considered as some four-fermion interaction leading to same-sign tops. The same-sign tops can then of course go on to decay into a cascade of jets, missing energy and leptons, including a same-sign lepton pair. Since the top quark is the heaviest of all quarks it is potentially very sensitive to new physics. After the discovery of the Higgs particle the existence of a fourth-generation is more or less put to rest, but there are yet a number of exciting models producing same-sign tops

which our analysis would be sensitive to.

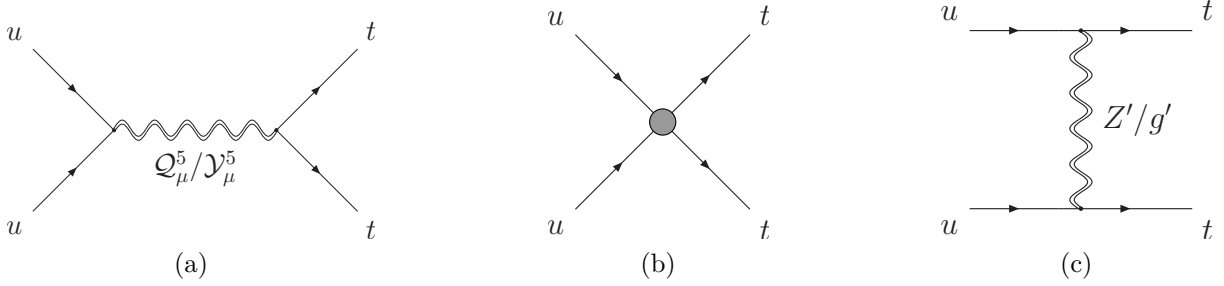


Figure 4.5: Production of same-sign top quark pairs via the production of a heavy vector boson (such as a colour-triplet or colour-sextet [64]) in the s-channel (a) or exchange of a heavy vector boson (such as Z' or g') in the t-channel (c). for large resonance masses, both cases can be described by a four-fermion interaction (b). [63]

4.2 Layout of analysis sections

For the first analysis (7 TeV) my involvement was primarily in the electron charge misidentification prediction as well as providing cross-checks for the $\mu\mu$, $e\mu$ and ee channels and developing the various cuts and control regions. In the latest analysis (8 TeV) I played a much bigger role. Being the most senior PhD student with experience my task was arguably the most technically complex: to work on the fake/non-prompt electron and muon predictions as well as make the event and lepton selections, study the MC inputs, provide cross-checks to all channels, advise on charge misidentification methods for both electrons and muons and various other odds and ends. In essence I played a most active role in the recent analysis which is why for the rest of my thesis I will describe the 8 TeV analysis (except for the charge misidentification, where I will explain the 7 TeV methodology which I did and that the 8 TeV builds from) but will point out the crucial differences between the two analyses along the way. I aim to split the analysis into various subsections (similar to what was done for our paper) and to delve into their details. The results for the 7 TeV analysis are given at the end of the results sections for comparison, additional tables and kinematic distributions are given in the Appendix A.2. As mentioned in the preface: The chapters pertaining to these analyses are based on the papers and conference notes given in the preface as well as their corresponding internal notes and hence contain tables, figures, equations and phrases taken directly or modified from these sources.

*I am enough of an artist to
draw freely upon my imagination.
Imagination is more important
than knowledge. Knowledge is
limited. Imagination encircles
the world*

Albert Einstein

5

Same Sign: Event Selection

First things first, of all the the hundreds of millions of events recorded by the ATLAS detector over the course of a year how does one select those of interest? One could say it is like trying to find a needle in a haystack but that is an understatement. It is more akin to trying to find one particular grain of sand in all the beaches on Earth. Fortunately, we know the final state of our signature events and their characteristics:

- Select high momentum leptons ($p_T > 20$ GeV)
- Select prompt leptons (here defined that they originate from/or very close to the primary interaction and hence a primary decay)
- Select isolated leptons (as they are prompt and high momentum their tracks should have little showering and associated jets around a small cone surrounding the path)
- Select events with same-sign pairs (as mentioned this cuts heaps and heaps of background)

So the job of an ATLAS analysis is to consider these final state characteristics and translate them into quantities that the detector can measure within the constraints of the detector capacity. I will state the cuts used for our analysis and then aim to explain and motivate their choices. The cuts highlighted in **green** are additional or modified cuts from the 7 TeV analysis.

5.1 Electron Selection

Table. 5.1 summarises the cuts applied to electrons in the signal region. The motivations for these cut criteria are explained in the following discussion.

Selection	Electron requirement
Lepton p_T	$p_T > 20 \text{ GeV}$
Lepton η	$ \eta < 1.37 \text{ or } 1.52 < \eta < 2.47$
Impact Parameters	$ d_0 /\sigma(d_0) < 3$
Identification Criteria	<i>Tight</i>
Track Isolation	$\text{ptcone30}/p_T < 0.1$
Calorimeter Isolation	$\text{Etcone20} < 3 \text{ GeV} + (E_T - 20) \cdot 0.037$
Jet Overlap	$\Delta R(e, \text{jet}) > 0.40$

Table 5.1: Summary of requirements on electrons in the signal region.

Breaking the cuts in Table. 5.1 down. The η cut is simply so that the electron is in the η range where the electromagnetic calorimeter can effectively measure the electron energy depositions (the crack is the gap between the barrel and endcap parts of the calorimeter). The p_T cut is to ensure that we have high momenta electrons but also to remove some ugly background electrons, thus improving our sensitivity to new physics. In ATLAS three reference sets of selection criteria for electrons are defined with increasing background rejection while accepting a moderate loss in efficiency: loose, medium and tight [65]. These selections apply cuts on the transverse shower shapes in the first and second layer of the electromagnetic calorimeter, leakage into the hadronic calorimeter, ID track quality, cluster-track matching and vetoing of conversions. The selection is done by applying cuts on each of these criteria and are optimised as a function of η and p_T . With increasing tightness of the selection more criteria are used and more stringent requirements are applied. At trigger level the selections used are typically slightly looser. The most stringent (tight) criteria are required for electrons in our signal region. The impact parameters, d_0 and z_0 are the variables discussed in the previous section and these ensure that the electrons are prompt and originate from close to the primary vertex rather than from some other particle which decays in flight further in the detector to an electron. The final two cuts are simply to ensure the electron is well isolated, that is it is not surrounded by jets or has some unusual showering making it appear to be a higher energy electron when it is not.¹ The calorimeter isolation (Etcone) used here is a cell-based isolation. It is depicted in Fig. 5.1. Simply put, a cone of specific size ΔR is constructed in the η - ϕ phase space centred on the calorimeter cell that the electron track passes. Then the energy deposited in the adjacent cells within the cone are summed (ignoring the 5x7 cells in the centre cone). Hence in this case Etcone20 refers to a cone of size, $\Delta R = \Delta\sqrt{(\Delta\eta)^2 + (\Delta\phi)^2} = 0.2$. The exact isolation cuts (for both electrons and muons) were optimised for the analysis in order

¹The sum of the energies in the (electromagnetic and hadronic) calorimeter cells around the electron direction in a cone of radius $\Delta R = \Delta\sqrt{(\Delta\eta)^2 + (\Delta\phi)^2} = 0.2$ must be less than $3 \text{ GeV} + (E_T - 20 \text{ GeV}) \cdot 0.037$. The core of the electron energy deposition is excluded and the sum is corrected for transverse shower leakage and pile-up from additional pp collisions to make the effect of the isolation cut essentially independent of p_T . Furthermore isolation is also applied using the inner detector track information. The sum of the p_T of all the tracks excluding the electron one in a cone of size $\Delta R = 0.3$ divided by the electron p_T must be less than 0.1

to have the best background rejection whilst still achieving a good signal efficiency over a range of lepton p_T [66]. The $ptcone$ variable is similar in concept to the $Etcone$. It is the sum of the transverse momenta of all charged particles in a cone of size ΔR excepting that of the lepton itself. Hence, again it allows us some discriminating power between isolated and non-isolated leptons (in other words signal and background).

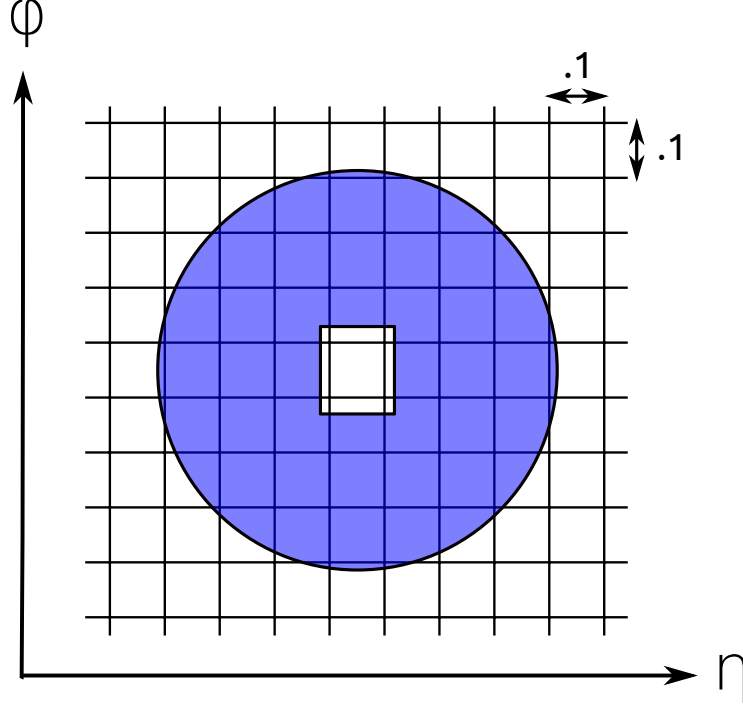


Figure 5.1: The $Etcone$ variables are calculated using the calorimeter cells in a cone around the object axis, ignoring a central core of 5×7 cells in (η, ϕ) in the centre of the cone. a cone size of $\Delta R = 0.40$ is depicted here. Inspired by an internal note [67]

5.2 Muon Selection

The **Staco** muon identification algorithm is used to identify muons [68]. The **Staco** algorithm basically reconstructs the muon independently in the Inner Detector and Muon Spectrometer, then it combines the tracks based on a statistical combination of the two independent measurements using the parameters of the reconstructed tracks and their covariance matrices. Additional cuts imposed on these muons are summarised in Table. 5.2.

The motivations for these cuts are mostly the same as for electrons. The cuts that differ in reasoning are those requiring inner detector cuts (these are analogous to some of *tight* electron identification criteria). Furthermore the η cut rather than to cover the EM calorimeter range covers the effective range of the muon spectrometers and inner detectors. The requirement that $Q_{ID} == Q_{MX}$ is simply to suppress muons whose charge

Selection	Muon requirement
Lepton p_T	$p_T > 20 \text{ GeV}$
Lepton η	$ \eta < 2.5$
Impact Parameters	$ d_0 /\sigma(d_0) < 3, d_0 < 0.2 \text{ mm}$
Identification Criteria	ID hit requirements, $Q_{ID} == Q_{MX}$
Track Isolation	$\text{ptcone30}/p_T < 0.07$
Calorimeter Isolation	$\text{Etcone30} < 3.5 - (p_T - 20) \cdot 0.06$
Jet Overlap	$\Delta R(\mu, \text{jet}) > 0.40$

Table 5.2: Summary of requirements on muons in the signal region. Cuts highlighted in green are those which are additional to those used for 7 TeV analysis.

are misidentified. Here Q_{ID} is the muon charge as measured in the inner detector and Q_{MX} is the charge as measured in the muon spectrometer. There are some muon specific requirements on the number of hits on different sub-systems of the inner detector. These help in muon identification and background rejection. The final cut checking the size of muon and jet overlap is simply to ensure that the muons are well isolated from jets. The jet overlap cut was seen to be particularly important for the muons. The additional non-constant cut value on the jet p_T is placed to maintain a high efficiency for very high- p_T muons. The exact isolation cuts were again optimised to have the best signal to background ratio.

5.3 Jet Selection

There is some minimal selection on jets. These jets are used both when checking for overlap with leptons (as indicated above) but also when selecting the number of associated jets with each same-sign dilepton pair. Jet are reconstructed from topological clusters formed from the energy deposits in the hadronic calorimeter using the anti-kt algorithm [69] with a radius of 0.4. The energies of measured jets need to be corrected for known detector inhomogeneities as well as the non-compensating response of the calorimeter using factors derived from test beam, cosmic ray and pp collision data. Furthermore, there is some impact from pile-up^{II} which is corrected on an event-by-event and jet-by-jet basis. On top of these corrections the following are applied:

- Jet passes *looser* ID requirement
- Jet $|\eta| < 2.8$
- Jet $p_T > 25 + 0.05 \times p_T(\ell)$
- $|\text{JVF}|^{\text{III}} > 0.5$ if $p_T < 50 \text{ GeV}$

^{II}Pile-up is the impact of multiple overlapping pp interactions in same bunch crossing

^{III}Here JVF stands for the jet vertex fraction, so this cut means that the sum of the transverse momenta

5.4 Event Selection

So now that we know how to select the leptons in our events the question remains as to how we select the SS dilepton pairs in the events.

- Select events where there are at least two leptons passing the above lepton cut criteria.
- In order to be as inclusive as possible all combinations of pairs from leptons in an event are recorded as a separate pair.
- In each dilepton pair, the higher momentum (leading) lepton must have $p_T > 25$ GeV whilst the lower momentum (sub-leading) lepton only need pass the 20 GeV threshold.
- Select events where the dilepton invariant mass $m_{ll} > 15$ GeV (avoid low mass resonances, e.g. J/ψ)
- Pairs are split into same-sign (SS) and opposite-sign (OS) regions^{IV}.
- A Z-veto is applied which removes OS lepton pairs whose mass is within 10 GeV of the Z resonance ($|m_{ll} - m_Z| < 10$ GeV). This removes a lot of the background events coming from prompt diboson processes.
- The three channels require a trigger to be fired and all leptons to be matched to the trigger: ^V
 - $\mu\mu$: EF_mu18_tight_mu8_EFFS - A dilepton trigger where the leading muon must have $p_T > 18$ and the subleading $p_T > 8$ GeV.
 - $e\mu$: EF_e12vh_medium_mu8 - A dilepton trigger where the electron must have $p_T > 12$ and subleading $p_T > 8$ GeV.
 - ee : EF_2e12Tvh_loose1 - A dilepton trigger where both electrons must have $p_T > 12$ GeV

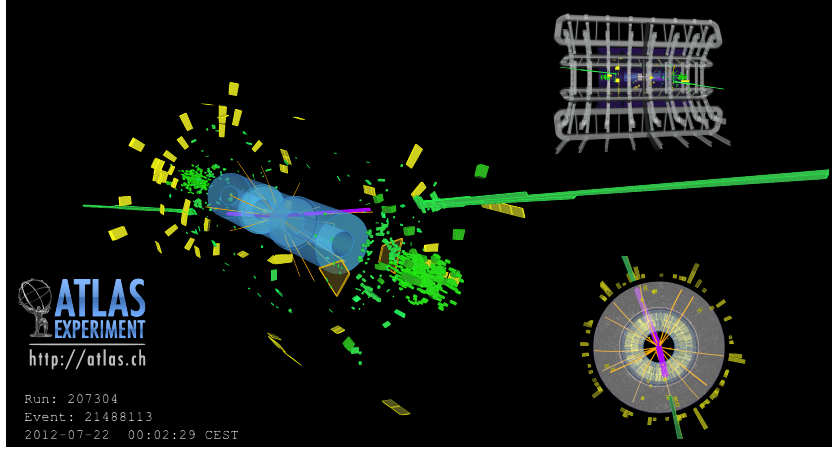
For our analysis we count the number of same-sign pairs in all the events rather than the number of events themselves. This means that there is a small chance to have one event with multiple same-sign pairs in the different channels and even within the same channel. This is seen to be negligible, on the order of 0.1% in each channel and is discussed in Appendix A.12.

As an example of high mass same-sign dilepton events please refer to Fig. 5.2.

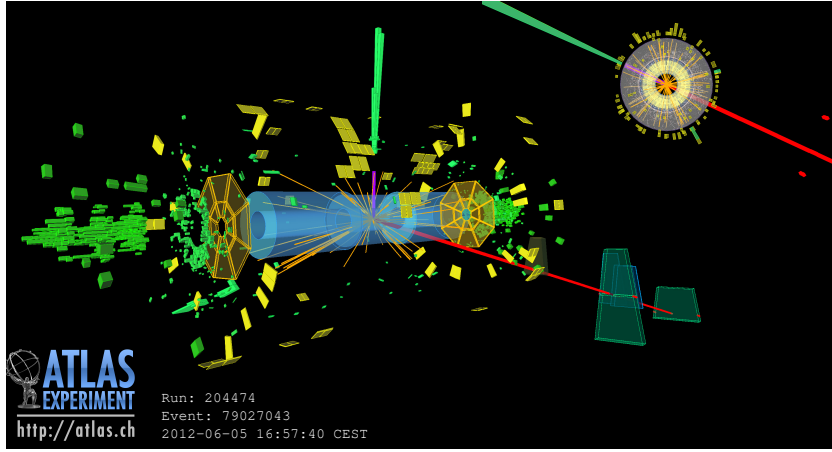
of tracks associated to the jet and originating from the primary vertex is required to be at least 50% of the sum of all tracks inside associated to the jet. The primary vertex here is defined as the vertex which has the highest squared p_T sum of associated tracks (with $p_T > 0.4$ GeV) found in the event.

^{IV}The latter only used for validation purposes.

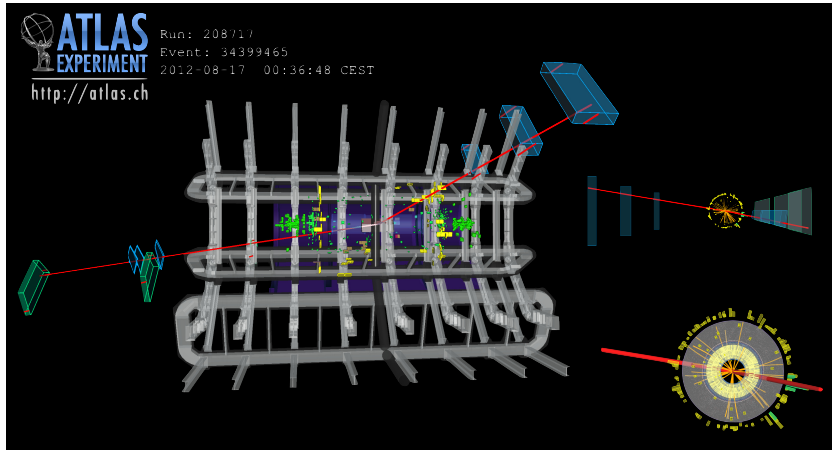
^VIn the trigger, whilst the cut-offs are fixed for a given p_T the efficiency for the trigger at that threshold is usually poor so in order to get a reliable and flat efficiency often one should use only leptons triggered at least 1 GeV above the threshold, fortunately in our analysis our cuts are much higher than the trigger thresholds. In the 7TeV analysis only the recommended single lepton triggers were used.



(a)



(b)



(c)

Figure 5.2: Event displays for some of the same-sign dilepton pairs with the highest invariant mass in the 2012 data. Here the magenta cones represent electrons which pass the signal selection criteria; the red tracks depict muons which pass the signal selection criteria; the blue boxes depict hits in the muon spectrometers; the green and yellow boxes display projections of the electromagnetic calorimeter energy depositions and the orange tracks are charged particles in the inner detector (shown as a transparent blue cylinder). The event shown in (a) contains an e^+e^+ pair with a mass of 964 GeV. The leading (subleading) electron has $p_T = 145$ (131) GeV, $\eta = -1.7$ (2.2) and $\phi = 1.9$ (-1.3). The event in (b) contains an $e^-\mu^-$ pair with a mass of 736 GeV. The electron (muon) has $p_T = 204$ (282) GeV, $\eta = 0.0$ (-2.0) and $\phi = 2.7$ (-0.4). The event in (c) contains a $\mu^-\mu^-$ pair with a mass of 628 GeV. The leading (subleading) muon has $p_T = 154$ (133) GeV, $\eta = -0.8$ (2.0) and $\phi = 3.0$ (-0.2).

A scientist in his laboratory is not a mere technician: he is also a child confronting natural phenomena that impress him as though they were fairy tales.

Marie Curie

6

Same Sign: Data and Backgrounds

In this section I will discuss the various different background processes which make up the same-sign dilepton landscape. The contributions which lead to same-sign leptons can be broken down so:

- Prompt SM processes (WZ, ZZ, Double-Parton Interactions, $t\bar{t}W$, $t\bar{t}Z$, SS WW)
- Charge flip ^I($t\bar{t}$, Drell-Yan, WWjj)
- Non-Prompt/Fake (these I will explain in the proceeding section)
- Conversions ($W\gamma$ events where the photon converts to a pair of leptons)

The exact ratio of these backgrounds depends on which channel (ee , $e\mu$ and $\mu\mu$) one considers. I will now discuss the different components in the same-sign landscape and how we predicted these backgrounds.

6.1 Prompt SM Backgrounds

There are very few processes leading to same-sign dileptons. In our analysis the bulk of these processes come from diboson production, that is when a W and Z boson or two Z bosons are produced and decay leptonically ($WZ \rightarrow ll\nu$, $ZZ \rightarrow ll ll$). WZ decays are the most dominant of all the prompt processes. An example is shown in Fig. 6.1. Sherpa-1.4.1 [70] was used to model these processes. However, there are some other processes with much smaller cross-sections such as $t\bar{t} + V$ (V is a vector boson: W,Z) where the $t\bar{t}$ decays semi-leptonically to produce an opposite sign pair and the vector boson further decays leptonically to produce leptons resulting in a final state with a same-sign pair.

^IEvents which produce prompt opposite-sign lepton pairs where one of the lepton charges is misidentified

These processes as well as $W^\pm W^\pm + 2 \text{ jets}$ are simulated using MADGRAPH-5.1.4.8 [71]. When it comes to fragmentation and hadronisation Pythia-8.165 [72] is used for $t\bar{t}V$ and Pythia-6.426 [73] for $W^\pm W^\pm$. Examples of these processes with smaller cross-sections are given in Figures 6.2 to 6.4. For processes with a Z boson in the final state the contribution from $\gamma^* \rightarrow l^+ l^-$ from internal or external bremsstrahlung of final state quarks or leptons is included for $m(l^+ l^-) > 0.1 \text{ GeV}$. Even less likely are the double-parton interactions which produce dibosons. They are simulated using Pythia-8.165. All these processes are predicted by Monte Carlo (MC) simulated data. The generator, PDF set and order of cross-section used for normalisation are shown for all MC samples in Fig. 6.1.

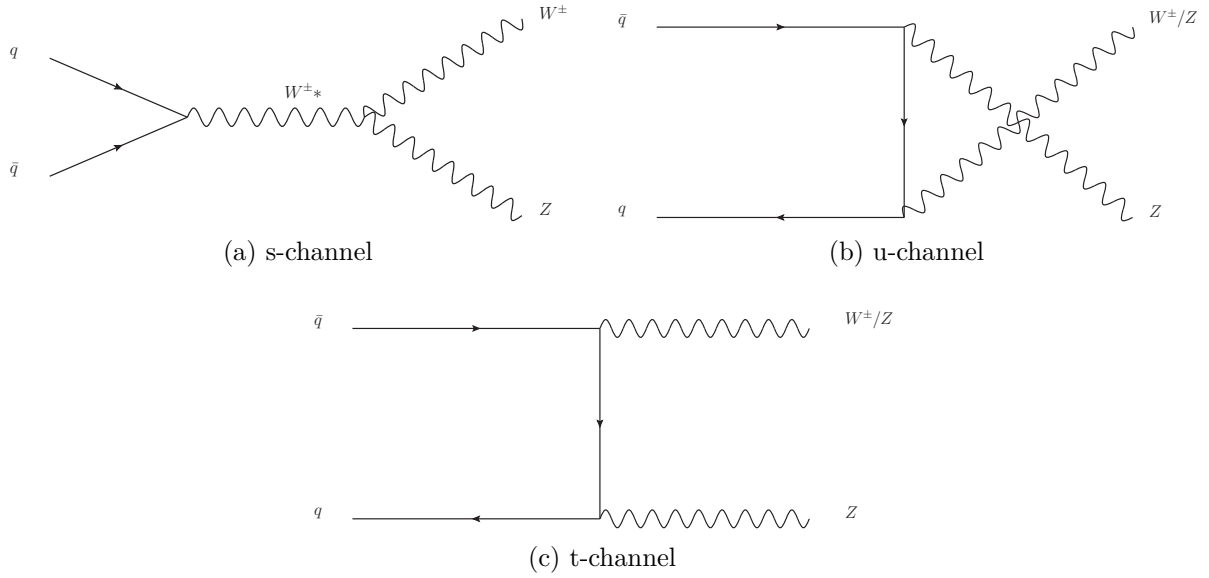


Figure 6.1: Possible production channels for dibosons leading to same-sign dileptons.

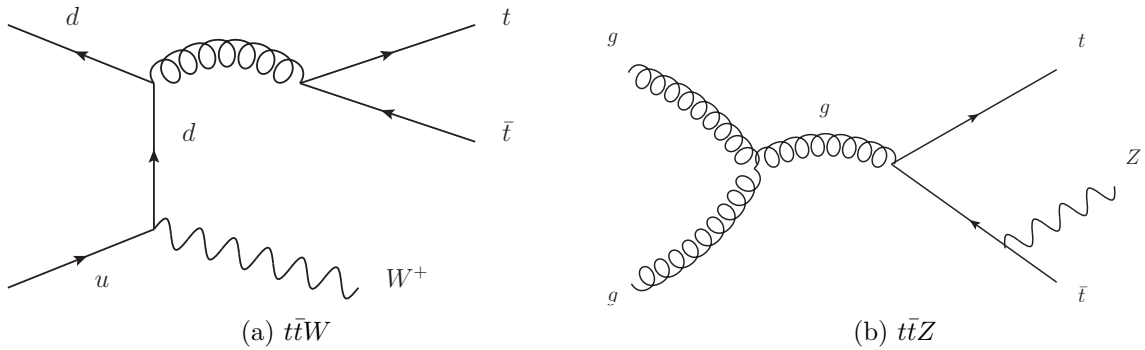


Figure 6.2: Feynman diagrams depicting the production mechanisms for prompt leptons through low cross-section processes

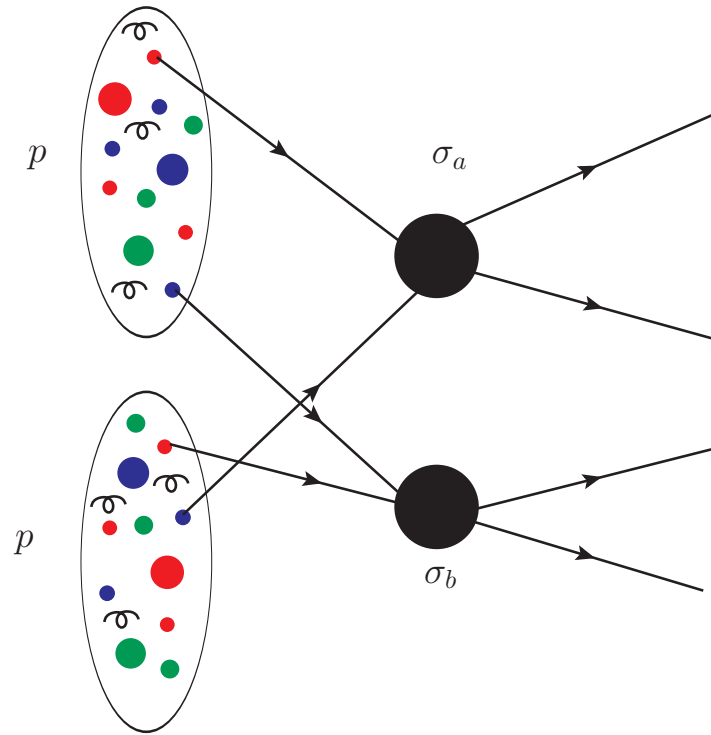


Figure 6.3: Simplistic Feynman diagram depicting a double parton interaction

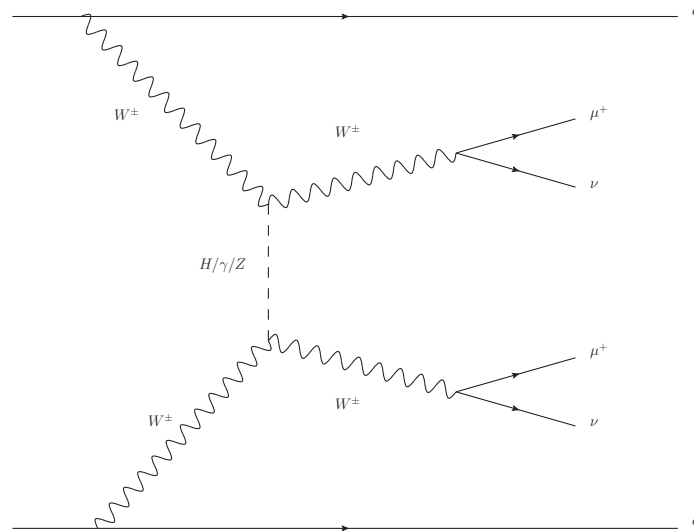


Figure 6.4: Feynman diagram for the production of same-sign WW

6.2 γ Conversions

Conversions of γ to an electron positron pair only contribute significantly in the ee and $e\mu$ signal regions, and essentially arise from $W\gamma$ events where one electron comes from a W and the other same-sign lepton comes from a photon which has converted into a lepton

Process	Generator + fragmentation/ hadronisation	PDF set	Normalisation based on
WZ	SHERPA-1.4.1 [70]	CT10 [74]	NLO QCD with MCFM-6.2 [75]
ZZ	SHERPA-1.4.1	CT10	NLO QCD with MCFM-6.2
$W^\pm W^\pm$	MADGRAPH-5.1.4.8 [71] PYTHIA-8.165 [72]	CTEQ6L1 [76]	LO QCD
$t\bar{t}V$, $V = W, Z$	MADGRAPH-5.1.4.8 + PYTHIA-6.426	CTEQ6L1	NLO QCD [77, 78]
MPI VV $V = W, Z$	PYTHIA-8.165 [72]	CTEQ6L1	LO QCD
$Z/\gamma^* + \text{jets}$	ALPGEN-2.14 [79] + HERWIG-6.520 [81]	CTEQ6L1	DYNNLO-1.1 [80] with MSTW2008 NNLO [82]
$t\bar{t}$	MC@NLO-4.06 [83, 84] + HERWIG-6.520	CT10	NNLO+NNLL QCD [85–90]
Wt	MC@NLO-4.06 + HERWIG-6.520	CT10	NNLO+NNLL QCD [91, 92]
$W^\pm W^\mp$	SHERPA-1.4.1	CT10	NLO QCD with MCFM-6.2
$W\gamma$	SHERPA-1.4.1	CT10	NLO QCD with MCFM-6.3

Table 6.1: MC samples used for background estimates. The generator, PDF set and order of cross-section calculations used for the normalisation are shown for each sample. The upper part of the table shows the MC samples used for the SM background coming from leptons with the same charge. The lower part gives the background sources arising in the $e^\pm e^\pm$ or $e^\pm \mu^\pm$ channel due to electron charge misidentification. MPI stands for multiple parton interactions.

pair. This type of event is very similar to charge-flip events and hence the same scale factors are applied on these events. The MC used to predict this background is also from Sherpa-1.4.1.

6.3 Data taken

For the 8 TeV analysis the full 2012 dataset is used from period A-L. This amounts to 20.3 fb^{-1} of usable data for runs considered *Good*^{II}. For the 7 TeV analysis the full 2011

^{II}Which essentially means all parts of the detector and triggers were fully operational and calibrated correctly

dataset was used which amounted to 4.7 fb^{-1} of usable data.

6.4 Charge Misidentification

There are a number of processes which produce opposite-sign (OS) dilepton pairs with a sizeable cross-section. There is also a non-negligible fraction of these events where one (or both) of the leptons in the final state have their charge misidentified. It is precisely these kinds of events that can show up in our signal region. The estimation (and cause) of such events for muons and electrons is slightly different so I will divide these up here. The Monte Carlo generators used to simulate the different backgrounds sensitive to charge-misidentification and significant in the signal regions are:

- Drell-Yan ($Z/\gamma^* \rightarrow l^+l^-$) - ALPGEN-2.14 [79] interfaced with HERWIG-6.520 [81] for fragmentation and hadronisation, and JIMMY-4.31 [93] for the underlying event.
- Top production ($t\bar{t}$ and tW) - MC@NLO-4.06 [83, 84].
- W^+W^- - Sherpa-1.4.1.

6.4.1 Electron Charge Misidentification

There are two ways in which an electrons charge can be misidentified. The first (and by far the most common method) is a process where we obtain so called *trident* electrons. Simply put, a prompt electron has the possibility of emitting a photon due to bremsstrahlung radiation as it travels through the detector and is slowed down. The photon may then create an electron-positron pair. Often the electron momentum is very high hence the emitted photon (and the consequent electron-positron pair) is co-linear to the original electron (that is, they travel almost parallel to the original electron). Now, if the granularity in the inner detector is not good enough the track reconstruction may follow the track created by the positron instead of the original electron track and hence misconstruct the charge. A Feynman diagram depicting the type of process (a trident event) leading to a misconstructed electron is shown in Fig. 6.6.

The other method of charge misidentification is much less common, but with very high momentum electrons the tracks may be only bent a little in the B-field and the radius of curvature may be so small that the detector precision cannot sufficiently differentiate a positively charged particle from a negatively charged particle. Indeed, this is a small to negligible effect for electrons with p_T less than 1TeV which the bulk of electrons in our analysis are. This charge misidentification was anticipated already in the Technical Design Report where it was predicted that 1 TeV electrons would produce at least one secondary with $p_T > 10 \text{ GeV}$ (100 GeV) 19% (8%) of the cases [94]. The anticipated fraction of misidentified electrons at high p_T is shown in Fig. 6.5.

To understand the modelling of charge misidentification, three separate methods were used to determine the charge misidentification rates (that is, the probability for an electron

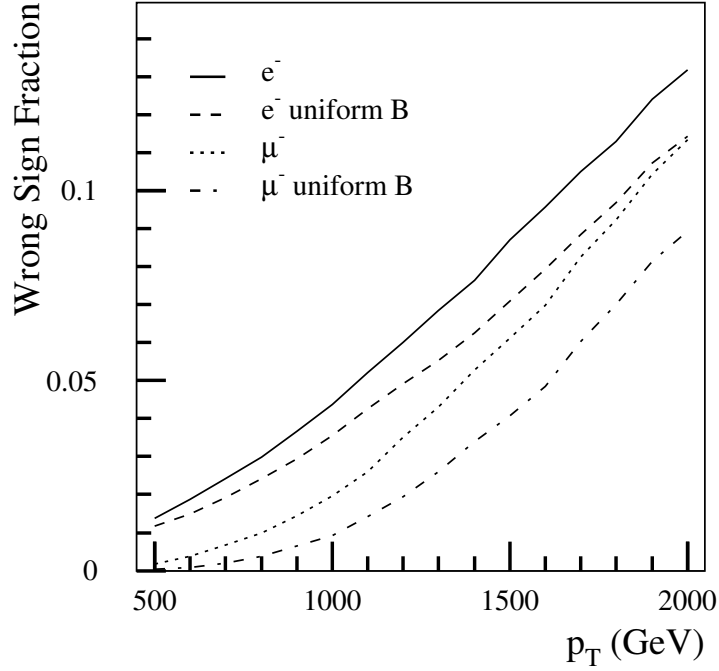


Figure 6.5: Expected wrong sign fraction as a function of p_T for muons and electrons as predicted for the ATLAS inner detector. [94]

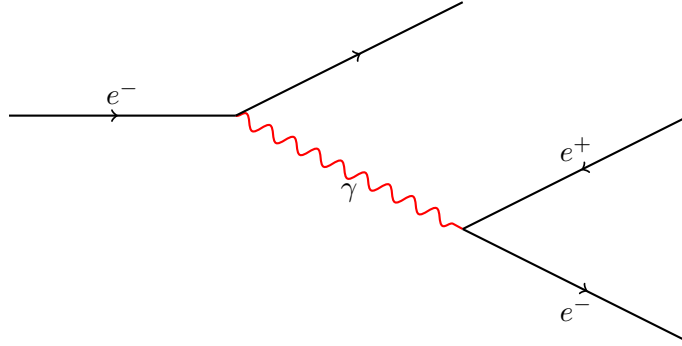


Figure 6.6: A Feynman diagram for the process producing a *trident* electron, possibly leading to charge misidentification

to have its charge misidentified). In order to evaluate these values, dielectron events from within the Z peak ($80 < m_{\ell\ell} < 100$ GeV) were utilised. Drell-Yan processes are by far the dominant background in the Z peak mass distribution. Any other background process is found to be negligible in this region. The three different methods for obtaining the charge flip probability were first advocated by the same-sign top-quark analysis [38].

- Tag-and-probe
- Direct extraction

- Likelihood

Tag-and-probe method

This is a tried and true method for many types of analyses in ATLAS and prior experiments. Here one chooses a region (the Z peak) rich in a process that we wish to observe. Then one makes a *Tag* whereby one assumes one can be confident of the particle type/characteristic and use a probe another lepton in the event, (related to the tag) to probe the properties. The tag is chosen to be a reconstructed electron passing all signal selection cuts. It must also have $|\eta| < 0.8$ and be in the Z peak. The criterion is imposed since central electrons have the lowest charge flip probability (this is because the central part of the Inner Detector has the best resolution and granularity as well as the calorimeters). Electrons in this region are therefore assumed to be (for the most part) correctly measured. Events are then chosen which have two electrons in the Z peak mass range (80-100 GeV) where one (or both) pass the tag condition. The number of like-sign events and opposite-sign events are then evaluated for each η bin depending on the probe electron. Charge misidentification rates are obtained by (per $|\eta|$ bin i):

$$\delta_e^i = \frac{N_{SS}^i}{N_{OS}^i + N_{SS}^i} \quad (6.1)$$

In other words, the fraction of events which are same-sign compared to the total number of Z peak events (both SS and OS) per η bin tells you the probability for an electron of a given η having its charge misidentified. But there is one correction necessary:

$$\epsilon_{chg}^i = \delta_e^i - \epsilon_{chg}^0 \quad (6.2)$$

where $\epsilon_{chg}^0 = \frac{\delta_e^0}{2}$ is a correction for the tag electron charge flip probability, in other words the probability for a tag electron to be mismeasured. The charge flip probability, ϵ_{chg}^i , is the probability for an electron from η bin i (one needs to divide by two to avoid the double-counting from measuring the tag rate twice from having two tag electrons in the pair).

Direct extraction method

The direct extraction method is very similar to the tag and probe method, however rather than choosing a tag electron, one requires that both electrons from the Z peak mass range are from the same η bin. Thus the charge flip probability (per η bin i) is given by:

$$\epsilon_i = \frac{N_{SS}^{ii}}{2N^{ii}} \quad (6.3)$$

where $N^{ii} = N_{OS}^{ii} + N_{SS}^{ii}$

Statistical Likelihood Method

This method has been seen to be the best for calculating charge flip probability because it utilises the most statistics available and does not kinematically bias the result by choice of η bin like the previous two methods.

- Start by assuming that the charge flip probability for different η regions are independent. Thus the probability to observe N_{SS}^{ij} events in η regions i and j as a function of the total number of events (opposite- and same-sign) N^{ij} is:

$$N_{\text{SS}}^{ij} = N^{ij}(\epsilon_i + \epsilon_j) \quad (6.4)$$

- In principle the number of same-sign events for a given η bin can be expressed as a poissonian:

$$f(k|\lambda) = \frac{\lambda^k e^{-\lambda}}{k!} \quad (6.5)$$

Where $\lambda = (\epsilon_i + \epsilon_j)N^{ij}$.

- Taking the negative log likelihood^{III} ($-\ln(L)$) for the probability of two electrons to charge flip and simplifying, one can obtain:

$$-\ln L(\epsilon|N_{\text{SS}}, N) \approx \sum_{i,j} \ln(N^{ij}(\epsilon_i + \epsilon_j))N_{\text{SS}}^{ij} - N^{ij}(\epsilon_i + \epsilon_j) \quad (6.6)$$

- This function can then be minimised to find the charge flip probability and errors.

Method comparison

The three methods have their pros and cons but the likelihood method is objectively better. The reasons for this are two-fold:

- Both the direct method and tag-and-probe one are selecting kinematically biased events by selecting events from electrons with a specific η . With tag-and-probe one always requires that at least one electron is central ($|\eta| < 0.8$) and in direct one only uses events where both electrons from the Z are from the same η region, thus leading to potentially biased charge flip probability.
- Because the tag and probe and direct methods use only the events from specific eta bins to evaluate the charge-flip probability in those η bins, those methods make use of limited statistics compared to the likelihood method which uses all events in all η bins in order to minimise the log likelihood and improve the charge flip probability in all bins.

For these reasons, for both the 7 TeV and 8 TeV analyses, we use the likelihoods methods charge flip probability as nominal. In the 7 TeV analysis we used the difference in rates between the three methods as a systematic as I shall explain.

^{III}In statistics, a likelihood function is a function of the *parameters* of a statistical model. Thus the likelihood function provides the likelihood for a set of parameters θ given a particular outcome x . This likelihood is equivalent to the probability for a observing outcome, x , given a set of parameters, θ . Although often used synonymously, *probability* and *likelihood* are distinguished on the roles of the outcomes and parameters of a model, $L(\theta|x) = P(x|\theta)$.

Application of charge flip probability

Once one has ascertained the charge flip probabilities, the common way to apply them is to simply select events which produce opposite-sign dilepton pairs, such as Drell-Yan. Then apply the charge flip rates are applied as a weighting (depending on the eta of the two electrons) to predict the probability for that dilepton pair to have one electron which is charge flipped. In this way one can build up a prediction for the number of charge flipped events we expect given the number of OS MC events. The majority of ATLAS analyses used this method at the time.

However, for our analysis (both 7 TeV and 8 TeV) we chose to adopt a slightly different approach which was novel from the other 7 TeV analyses. Rather than using the charge flip probability measured to scale the opposite-sign MC to get a prediction for the same-sign contribution we chose to calculate the charge flip probability in both data (the full available dataset for 7 TeV and 8 TeV respectively) and MC (the Drell-Yan MC). Then for each eta-bin one can use the ratio of data to MC as a scale factor. In effect then one can use the prediction directly from MC for SS events but correct for the data-MC discrepancy by using this scale factor. This is advantageous because it reduces the error on the charge flip probability (as using a ratio of data-MC any common errors are minimised). We also saw that the kinematics in MC for SS in both η and p_T were better modelled in SS MC than in OS MC (or data) which one then weighted with the basic charge flip probability.

So for our analyses one simply took the SS MC prediction from the various processes which could contribute in our signal region and then for each pair one could look into the truth to see which of the two SS leptons had flipped charge, then measure its η and weigh that event with the appropriate scale factor.

Validation checks and systematic error

In order to validate the charge flip probability obtained for both data and MC, a sanity check was constructed. Simply put, one can display the number of SS events in the Z^0 mass peak for data and MC and compare that to the number of OS events which are then weighted with the charge flip probability to see how the two compare. The integral of the two peaks should be the same within errors. However as one can clearly see from Fig. 6.7 the SS peak is shifted downwards compared to the OS peaks scaled by the three different charge flip probabilities. This is due to the very nature of charge flip being that one electron converts to a photon and then a pair, hence the mismeasured electron is by definition less energetic and hence the corresponding dielectron mass is lower than it *should* be had it not flipped charge. This is again a good reason for using scale factors instead of raw rates.

So once validated, the scale factors and their associated errors can be calculated. Using the three methods described above one can derive charge flip probabilities in both data and MC and then obtain the scale-factors as shown in Fig. 6.8.

The raw charge misidentification rates for data and MC and their corresponding scale factors are summarised in Table 6.2 and displayed in Fig. 6.9 for the Likelihood method.

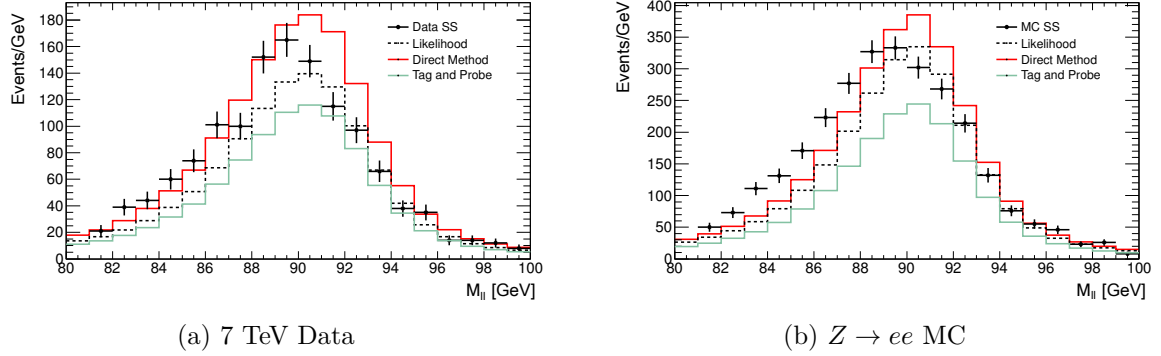


Figure 6.7: The closure test for the charge flip probabilities derived from the (a) data taken at $\sqrt{s} = 7$ TeV and (b) Alpgen MC $Z \rightarrow ee$ samples. The distribution shows the dilepton invariant mass within the Z peak. The black points are the observed number of SS pairs with the statistical error on the error bars. The three other histograms are the expected number of events as predicted by weighting the OS Z peak with the three different methods for extracting the charge-flip probabilities.

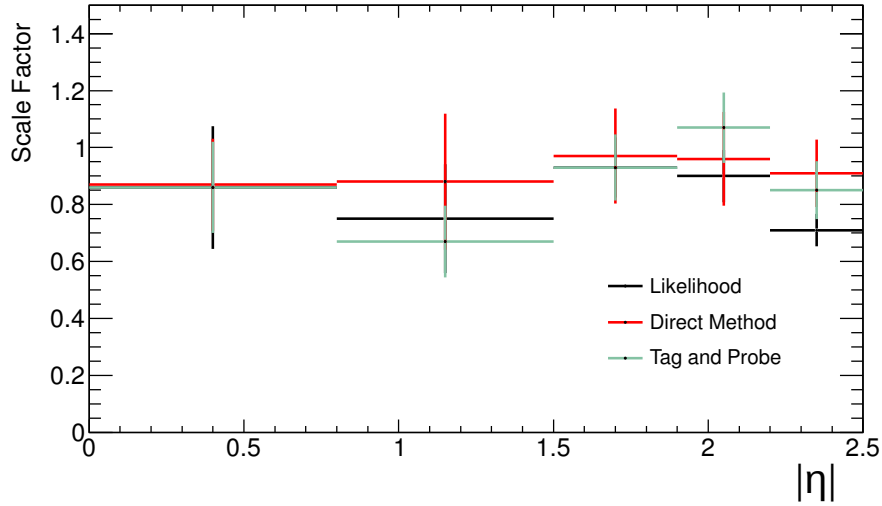


Figure 6.8: The charge flip scale factors as a function of $|\eta|$ derived from the full 4.7 fb^{-1} of data taken at $\sqrt{s} = 7$ TeV with respect to Alpgen MC $Z \rightarrow ee$ samples. The three datasets are the scale factors derived from the three different methods for extracting the charge-flip probabilities. The error bars display the statistical uncertainty associated with each method.

As mentioned, initially the plan was to use the differences between the three methods as a measure of the systematic error, or at the very least cross-check that the likelihood values made some sense. In the end for the 7 TeV analysis, the statistical errors were so large, that we simply used these as our errors on the likelihood scale factors since the errors from the three methods were much smaller and as mentioned we knew the other

Table 6.2: Electron charge-misidentification probabilities as a function of $|\eta|$ for data (full dataset, 4.7 fb^{-1}) and MC, together with the resulting scale factors.

Method	$ \eta < 0.8$	$0.8 < \eta < 1.5$	$1.5 < \eta < 1.9$	$1.9 < \eta < 2.2$	$2.2 < \eta < 2.5$
T& P (Data)	0.00013 ± 0.00002	0.00020 ± 0.00003	0.00122 ± 0.00012	0.00251 ± 0.00023	0.00435 ± 0.00035
T& P (MC)	0.00014 ± 0.00002	0.00029 ± 0.00003	0.00131 ± 0.00010	0.00234 ± 0.00017	0.00513 ± 0.00043
Direct (Data)	0.00013 ± 0.00002	0.00019 ± 0.00003	0.00201 ± 0.00028	0.00296 ± 0.00041	0.00912 ± 0.00087
Direct (MC)	0.00013 ± 0.00002	0.00022 ± 0.00003	0.00208 ± 0.00021	0.00309 ± 0.00031	0.01001 ± 0.00074
Likelihood (Data)	0.00012 ± 0.00002	0.00021 ± 0.00004	0.00162 ± 0.00015	0.00270 ± 0.00022	0.00576 ± 0.00039
Likelihood (MC)	0.00013 ± 0.00002	0.00027 ± 0.00003	0.00174 ± 0.00011	0.00300 ± 0.00018	0.00808 ± 0.00035
Direct SF	0.87	0.88	0.97	0.96	0.91
Likelihood SF	0.86	0.75	0.94	0.90	0.71
Tag and Probe SF	0.87	0.67	0.93	1.07	0.85

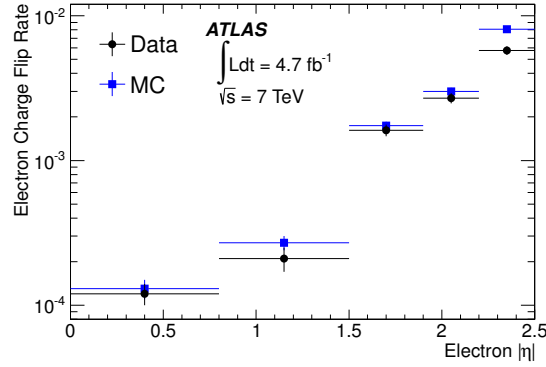


Figure 6.9: Electron charge flip probability versus $|\eta|$ for data (circle markers) and MC (square markers), measured using the Likelihood method. The errors shown are statistical only.

two methods were kinematically biased. However for the 8 TeV data because we had much better statistics we were able to evaluate the systematics in a better way. This is discussed further in Appendix A.3.

Control Region

In order to derive the scale factors we needed to use same-sign data events which would have been in our signal region in the Z mass peak. Hence as mentioned for the analysis we removed this region from our signal region. But this region also provides a validation region to test our scale factors. In figures 6.11 and 6.10 you see the data and MC agreement for the Z peak region which is dominated by charge-flip events (predominantly Drell-Yan). The agreement is good which gives us confidence that the charge-flip scale factors are doing their job.

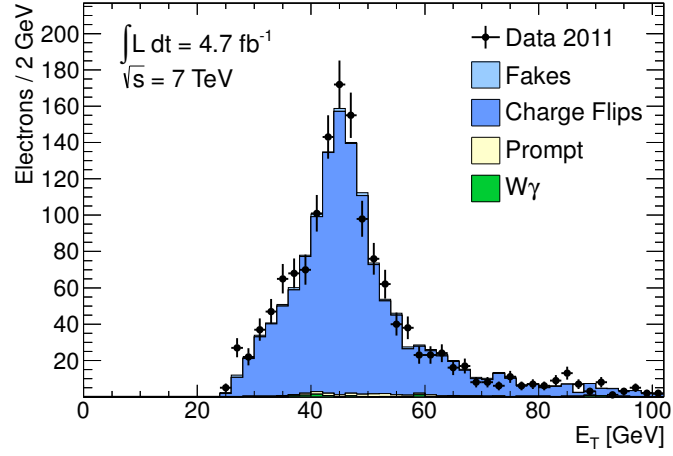
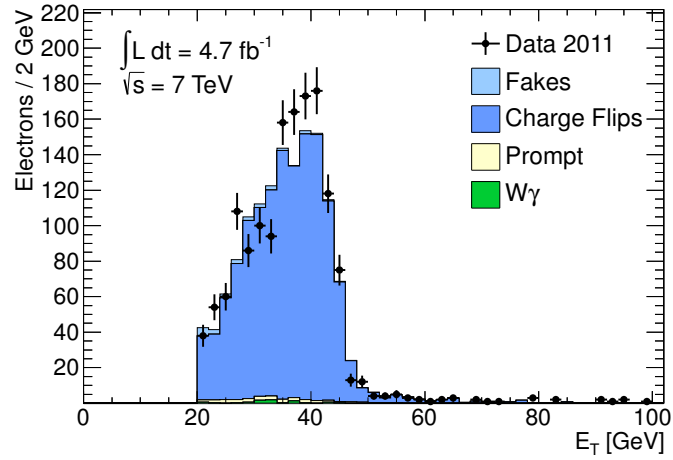
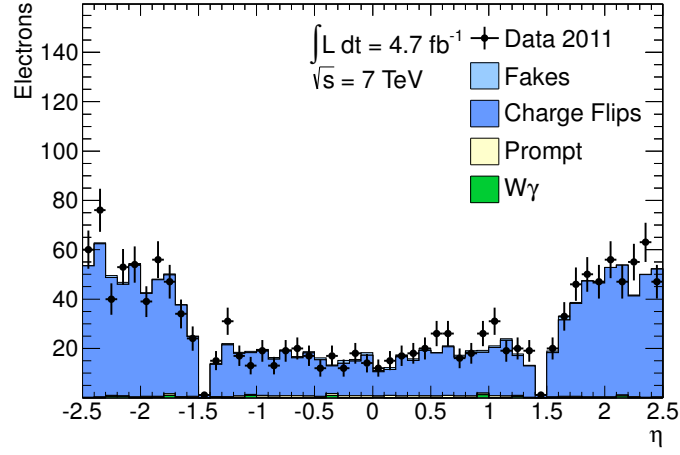
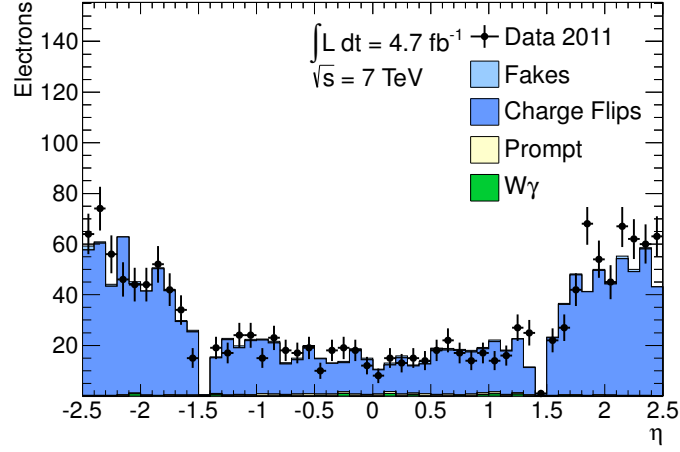
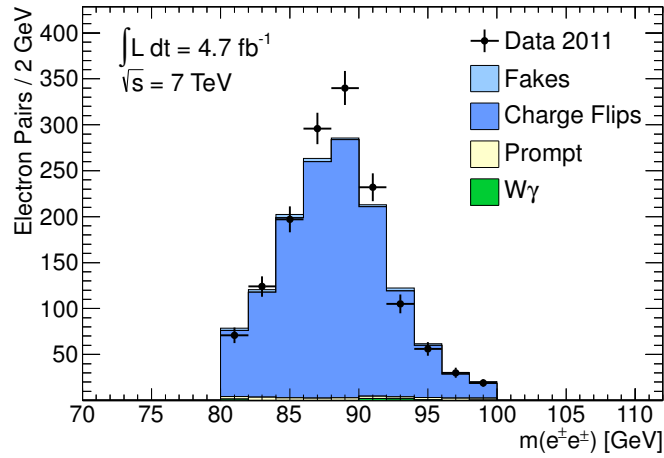
(a) Leading electron E_T (b) Subleading electron E_T

Figure 6.10: Leading (a) and subleading (b) electron E_T distributions in the same-sign Z peak validation region with two isolated electrons.

(a) Leading electron η (b) Subleading electron η 

(c) Invariant mass

Figure 6.11: Leading (a) and subleading (b) electron η , and invariant mass (c) in the same-sign Z peak validation region with two isolated electrons.

p_T dependence and extensions

For both the 7 TeV and 8 TeV analyses the p_T dependence of the scale factors was analysed and shown to be flat in the region considered within the statistical uncertainty. This, however, highlights one of the limitations of the used method to evaluate charge flips, namely that we only use events from within the Z peak. The problem here is that the p_T range available to study is limited in statistics above about 80 GeV because we are only using the tails of the Z peak distribution, hence we cannot say so much about very high momentum electrons (> 100 GeV). However, there is no physics reason as to why the probability to bremstrahlung should increase with momentum so we have to assume that the behaviour at high momentum is the same as that derived in our region.

Here is another advantage of using a scale factor as opposed to the raw charge flip probability. It was shown that whilst the charge flip probability varies quite a lot as a function of p_T , the scale factor (that is the data to MC correction scale factor) remains fairly constant as a function of p_T (at least from the p_T range accessible by the Z peak). Hence it was decided to have no p_T dependence on our charge flip scale factors for the 7 TeV analysis. For the 8 TeV analysis a similar study was done, reaching the same conclusion but this time with greater statistics available. In the 8 TeV analysis we used MC to get some handle on high p_T electrons. Events at high p_T have very stiff tracks which means that it can be hard for the detector to resolve the tracks as to which way they are bending, and hence the charge is misidentified. In order to estimate this effect we compared our standard scale factors to those where the events were simulated in a detector of distorted geometry (i.e the detector was misaligned and material distribution was incorrectly modelled). In doing so we saw that the difference was up to 20%, hence we used this as an upper limit on the high electron p_T scale factor.

Clearly, in the future better methods for calculating the scale factors at higher p_T should be investigated. An additional method which I developed was to potentially use $t\bar{t}$ events rather than Z peak events. The advantage here is that one would have access to much higher p_T electrons. The disadvantage is that there are fewer $t\bar{t}$ events than Z peak events, hence the statistical error will be larger. Another disadvantage is that it is harder (and less efficient) to select $t\bar{t}$ events. In our analysis we could clearly not use this method regardless because $t\bar{t}$ events appear in our signal region as charge-flip over the entire range. But perhaps this method can be developed next year with more statistics and for an analysis with a different signal region.

6.4.2 Muon Charge Misidentification

For both the 7 TeV and 8 TeV analyses it was seen that the charge misidentification for muons was negligible.^{IV} In order to demonstrate this a validation region was needed. Since we expected (as in 7 TeV) that the charge flip for muons was negligible we wanted to avoid using the Z peak since that meant removing it from the signal region and reducing our signal region unnecessarily. We knew that charge flip was already minimised due to the cut requiring that the charge measured in the inner detector should be the same as that

^{IV}Note that now I will proceed by describing the 8 TeV analysis as I contributed most here

measured in the muon spectrometer. Furthermore using a *staco_combined* muon means that the muon track is well reconstructed and has hits in 3 or more stations. For the muon charge flip measurements the Z peak was utilised but it was required for at least one of the muons have $10 < p_T < 20$ and hence remain orthogonal to our signal region. Of course, by selecting pairs with this transverse momentum constraint biases the kinematics a little but it does not change the validity of the results.

To check we can firstly study the number of pairs from the Z peak in both data and MC and check that they agree, Fig. 6.12. Then one can look at the mass distribution of opposite sign dimuon pairs compared to SS dimuon pairs in data. There it is clear that there is an obvious Z peak in the OS distribution but in the SS peak there are orders of magnitudes fewer events and an absence of any peak around the Z mass, indicating that the charge flip is negligible, displayed in Fig. 6.12. Furthermore one can explicitly check in the truth information how many SS to OS pairs are reconstructed. This was done for both Drell-Yan and $t\bar{t}$ events where no SS events were observed.

Again in MC, because of the lack of statistics at high momentum in the Z peak, we studied the effect of charge-flip at high momentum by selecting MC events where the mass of the dilepton pairs were greater than 100 GeV. We then looked at the truth information to see the ratio of muons which flip charged using the truth information as a function of p_T . Once more even up to 500 GeV the effect was seen as negligible.

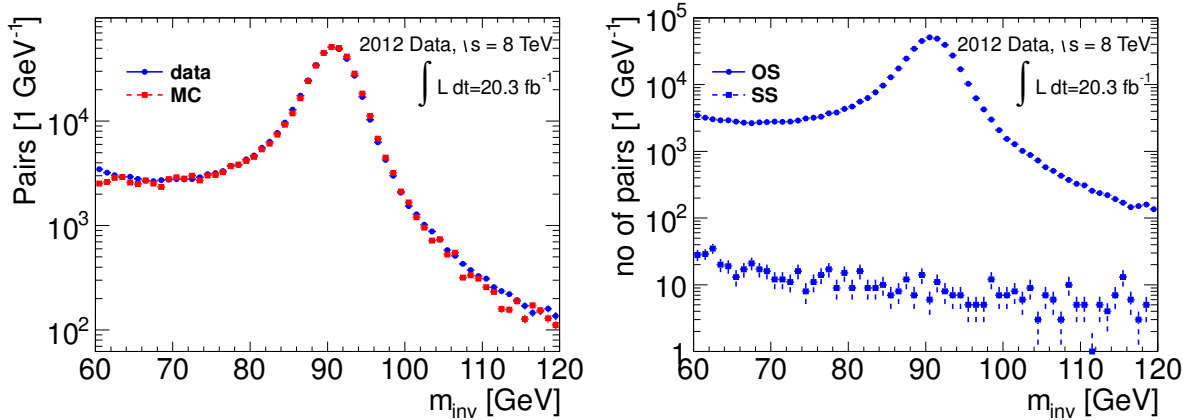


Figure 6.12: Invariant mass distribution of dimuon events around the Z peak. The left hand plot shows the invariant mass distribution of muon pairs for both data and Monte-Carlo. Note that the MC distribution is scaled to the data statistics. The right hand plot shows the opposite-sign (OS) and same-sign (SS) distributions as obtained from data. [95]

6.5 Non-Prompt (Fake) Leptons

A large background in all channels in our signal region consists of events with at least one *fake* lepton. By fake leptons what we shall mean from now on are either:

- A jet, hadron or photon which is reconstructed as an electron or muon (in that sense a *true* fake)
- Another particle from the primary interaction, say a *b*-jet, that decays in-flight to give an electron or muon; in this sense the lepton is *real* but non-prompt.

Both these scenarios we consider *Fake* and we use the terminology thusly.

These fakes originate from a plethora of sources; For electrons the main sources are low momentum jets that are misidentified as electrons or semi-leptonic decays of heavy-flavour quarks (*b*, *c*). For muons, fakes arise predominantly from semi-leptonic decays from heavy flavour jets. A tiny contribution from pions and kaons which decay in flight. There is also a small contribution where misidentified muons, originating from hadronic showers in the calorimeter who reach the Muon Spectrometer, are incorrectly matched to a reconstructed Inner Detector Track.

The dominant processes leading to these fakes are events producing $W + \text{jets}$ and QCD multijet events. A smaller contribution comes from $Z + \text{jets}$ and $t\bar{t}$ events. To assess this background a data-driven method, known as the fake factor method, is employed. This method is used in several ATLAS analyses, particularly diboson measurements and searches and is complementary to another common method, the matrix method [96].

6.5.1 Fake Factor Method Summary

The fake factor method is designed to predict the contribution from fake events in a specific region (most importantly the signal region) by utilising data from a mutually exclusive fake-dominated region and deriving the probability for a lepton of a given p_T , η , d_0 (or whichever parameter) to be a fake yet still pass our selection and appear as a lepton in our signal region. The general derivation and application of the fake factor method is expounded below:

Derivation

- Define a region in data which is as similar to the signal region as possible yet independent, high in statistics, and enriched in fakes.
- Define numerator (N) and denominator (D) objects.^V

The numerator selection is identical to the analysis selection described in Section 5,

^VSometimes called *tight* and *loose*

while the denominator selection reverses one or more lepton identification cut to select a fake lepton enhanced sample. These definitions are mutually exclusive by construction.^{VI}

- Measure the number of numerator and denominator objects in one-dimensional p_T and η binning.
- Subtract the residual contribution of prompt leptons using MC.
- Apply corrections/scalings if necessary (for example trigger prescale^{VII}).
- Calculate the ratio called the “fake factor,” defined as:

$$f \equiv \frac{n_N}{n_D} \quad (6.7)$$

where n_N is the number of numerator objects and n_D is the number of denominator objects. In essence the probability for a denominator object to appear as a signal lepton for a given p_T or η .

Thus the real difficulty comes in defining the region in which to derive the fake factors and to decide on the criteria for the denominator leptons which are rich in fakes and not prompt leptons. Furthermore, as we shall see evaluating the systematics is non-trivial.

Application

To obtain the fake background prediction for the dilepton channels, all possible dilepton combinations of numerator and denominator objects are selected: N+N (both leptons pass numerator selection), N+D (lead lepton passes numerator, subleading passes denominator), D+N (lead numerator, sub-lead denominator), and D+D (both pass denominator selection). N+N represents the signal region and does not enter into the prediction. There are three types of fake pairs:

- Type A: only the leading lepton is fake
- Type B: only the subleading lepton is fake
- Type C: both leading and subleading leptons are fake

Fakes evaluated from (D+N) include Type A and C, and fakes from (N+D) include Type B and C. Thus, if we simply added them together, Type C would be double counted. The

^{VI}For the 8 TeV analysis a conscious choice was made to keep the electron and muon fake factor methods as similar as possible, in this particular case that meant defining a denominator based on isolation inversion

^{VII}Some triggers have a purposefully lessened rate than the rate at which data is recorded nominally. This is generally because the prescaled triggers have much looser thresholds and hence would fire on an impossible larger fraction of collisions, most being uninteresting, hence one needs to correct for the difference in rates by weighting according to the prescale.

regions with denominator objects are scaled by the fake factor and combined according to the following equation to give the fake background prediction:

$$n_{fakes} = \sum_{i \in (N+D)} f_2(p_{Ti}, \eta_i) + \sum_{i \in (D+N)} f_1(p_{Ti}, \eta_i) - \sum_{i \in (D+D)} f_1(p_{T1i}, \eta_{1i}) f_2(p_{T2i}, \eta_{2i}) \quad (6.8)$$

where for example $\sum_{i \in (N+D)}$ is the sum over lepton pairs where the leading lepton passes numerator selection and the sub-leading denominator selection, and $f_1(p_{Ti}, \eta_i)$ [$f_2(p_{Ti}, \eta_i)$] is the fake factor for the leading [subleading] lepton in the i -th pair (the fake candidate) with transverse momentum and pseudo-rapidity, (p_{Ti}, η_i) . The last term is necessary to avoid double counting of the fake background from (Denominator, Denominator) pairs. Prompt and charge flip contamination in both the numerator and denominator objects are subtracted using MC. As electrons and muons have different handles available to discriminate fakes from prompt leptons, the denominator definitions differ as well as the regions used to derive the fake factors. The specifics for each channel are described in more detail below. Also described below are the systematic uncertainties associated with the fake factors for each lepton flavour. An assumption of the fake factor method is that the region used to derive the fake factors is similar in kinematics and composition to the region where the fake factors will be applied. Binning in p_T and η accounts for the lepton kinematics, but other differences can remain, especially in composition. The systematic uncertainties for both electrons and muons attempt to quantify the effects of these differences.

The fake predictions are tested in data in fake-dominated validation regions as described in the following chapter.

6.5.2 Electron Fake Factors

Fake-enriched Region

As described previously, one must first choose a region rich in electron fakes and mutually exclusive to the signal region. In order to do so, I tried to build a dijet validation region where there was one near-side *electron* candidate (probably a jet), an away side^{VIII} jet and exactly one reconstructed electron in the event (hence making the region orthogonal). The main sources of prompt electrons which contaminate the region come from W and Z production, namely W+jets, Z+jets plus a few $t\bar{t}$ events. These events are largely removed by making the following requirements:

- Reject events with two reconstructed electrons with invariant mass between 80 and 100 GeV (Removing Z+jets)
- Reject events with two or more loose electrons (Removing Drell-Yan/ $t\bar{t}$ events and making the region orthogonal to signal region)

^{VIII}An away-side jet is a jet which is separated from the reconstructed electron by $\Delta\phi > 2.4$.

- Reject events where the electron candidate has transverse mass $m_T > 40 \text{ GeV}^{\text{IX}}$ (Removing W +jets)
- Require an away-side jet to the electron candidate with $p_T > 30 \text{ GeV}$.^X

The majority of the electrons in the events after the above selection are non-prompt electrons/jets. Other than the p_T threshold, the jet selection is the same as used in the $\Delta R(e, \text{jet})$ cut, namely passing looser selection with $|\eta| < 2.8$ and $|\text{JVF}| > 0.5$.

By these requirements, we have one non-prompt electron/jet and one away-side jet in a event; we call it a *dijet* sample.

Electron Numerator and Denominator Definitions

Electron fakes come primarily from jets and hadrons which decay in flight or jets which are reconstructed as electrons. Therefore, a good handle on these fakes is the isolation of reconstructed electron tracks and energy depositions. I utilised this in the denominator selection in order to enhance the fakes.^{XI}

The numerator objects follow the same selection as signal region electrons summarised in Table. 5.1. However the denominator objects differ in two ways. Firstly, they are only required to pass the *medium*^{XII} identification criteria (rather than the tight for signal electron). But the major difference is that denominator electrons are required to fail either the calorimeter or track isolation criteria on signal.^{XIII} By reversing one or more of the isolation cuts one captures both the light and heavy flavour fakes together, which is advantageous compared to previous years analysis as one does not rely on reversing $\sigma(d_0)$ to capture heavy fakes and hence share the same phase space as the charge-flipped electrons. Furthermore there is more symmetry in the electron and muon fake denominator definitions. However, clearly the disadvantage is that one has a lessened feel of how the different components of the fakes affect the signal region separately. This is addressed in the systematics. Various other exotic groups also advocate a similar definition using isolation. Moreover the electron ID cuts on denominator are slightly looser with respect to previous years.

Prompt and charge flip contamination subtraction

Any remaining prompt and charge flip electron contamination can be estimated from MC simulations such as ZZ , WZ , Drell-Yan, $t\bar{t}$, etc. The number of numerator and denominator objects are counted using those MC simulations and are subtracted from data events.

^{IX} $m_T = \sqrt{2E_T^e E_T^{\text{miss}}(1 - \cos(\phi))}$, where ϕ is the angle between the transverse momentum of the electron and E_T^{miss} .

^X This was a change from the 7TeV analysis, which required only awayside jets of 20 GeV, the reason for this difference will be explained later.

^{XI} The boldened cuts are the cuts which differ between the numerator and denominator objects

^{XII} Typically, shower shape variables of the second calorimeter layer and hadronic leakage variables are used in the loose selection. First calorimeter layer cuts, track quality requirements and track-cluster matching are added at the level of the medium selection. The tight selection adds E/p, b-layer hit requirements and the particle identification potential of the TRT.

^{XIII} **Fail standard isolation:** $\text{Etcone20} > 3 \text{ GeV} + (E_T - 20 \text{ GeV}) \times 0.037$ OR $\text{ptcone30}/E_T > 0.1$.

A systematic uncertainty is assessed for this subtraction as described later.

Awayside jet p_T threshold

In the dijet fake region we require the existence of an away-side jet from the electron we are probing for our fake rates. An illustration of such an event is given by Fig. 6.13. For a jet faking an electron, apart from the energy/momentum taken away by the electron itself or by neutrinos, the rest of the jet energy should be deposited within the isolation cone of the electron. Hence there is a direct correlation with the p_T of the *underlying jet* (the jet which fakes the electron) and the fake lepton $p_T + E_T^{cone20}$. Since we use a dijet fake region, the two jets are found back-to-back in the azimuthal plane. Thus one can assume that the two jets are balanced and have the same transverse momentum. This assumption is used to calibrate the jet energies from a measurement using dijet events. Therefore by measuring the away-side jet p_T we are effectively measuring the underlying jet p_T and can thus probe the relation between underlying jet p_T and fake lepton $p_T + E_T^{cone20}$ shown in Fig. 6.14. The fit on the figure is purely empirical and is very nearly straight in the middle, but curves more at the extremes. It serves to illustrate the relationship between the average awayside jet p_T and the electron candidate reconstructed. Based on the mapping in this figure we can say that on average a 20 GeV electron comes from a slightly greater than 30 GeV jet. Consequently we require that the tag jet p_T threshold is 30 GeV for the electron fake factor measurement in order to avoid bias from low E_T jets.

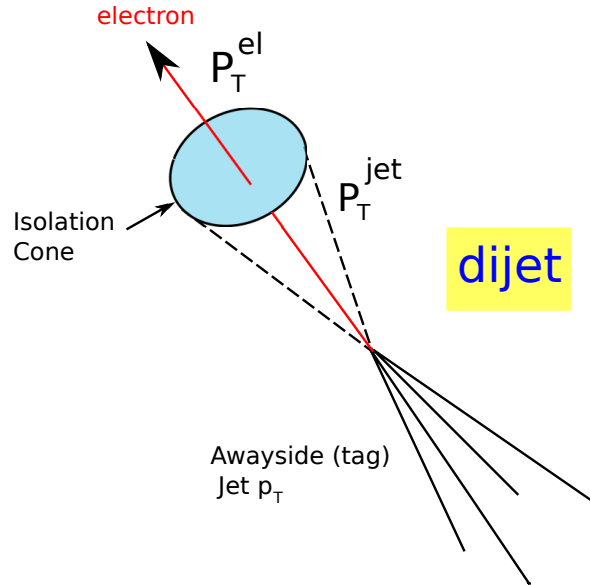


Figure 6.13: An illustration of a dijet event where a fake electron with a given p_T is produced from an underlying jet of a different p_T

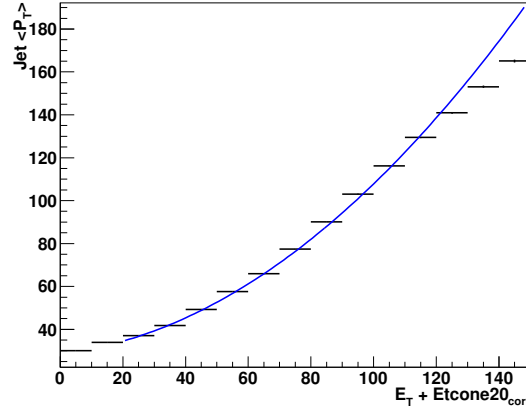


Figure 6.14: Average away-side jet p_T versus denominator electron $E_T + E_T^{cone20}$. The blue curve is an empirical fit to the data.

Trigger consideration

Numerator and denominator objects are selected by requiring a specific trigger given in Table 6.3. The numerator and denominator samples are by definition mutually exclusive, hence they can fire different triggers. The advantage is that one can probe much lower momenta and EM ID if one uses the supporting prescaled trigger (as long as the relative prescale is taken into account). Typically one uses a primary trigger for the numerator objects but a series of the supporting triggers for the electron which cover different p_T ranges. Table 6.3 describes the trigger strategy used for each p_T range. In order to correct for the prescales, a simple formula is utilised:

$$f \equiv \frac{n_N}{(\text{effective prescale}) \cdot n_D} \quad (6.9)$$

where the relative effective prescale between the two triggers is used.

Trigger Bias Ideally one tries to choose triggers such that they do not bias the final fake factors. One hopes that if the trigger thresholds and cuts are lower/the same than both the numerator and denominator requirements that should not influence the fake factors. Furthermore, one has the added complication that the triggers used in the derivation of the fake factors may be (and were) different from those used in selecting events in the signal region. Again as long as all thresholds and cuts on the triggers are lower/the same as the ones used when deriving the fake factors, theoretically no bias should be observed. However since trigger and cut efficiencies and scale factors are not perfectly uniform and efficient this is not the case, as was observed by a number of analyses. In our analysis the triggers used in the $e\mu$ channel and ee channel were both different from each other and from the the ones used to measure the fake factors below.

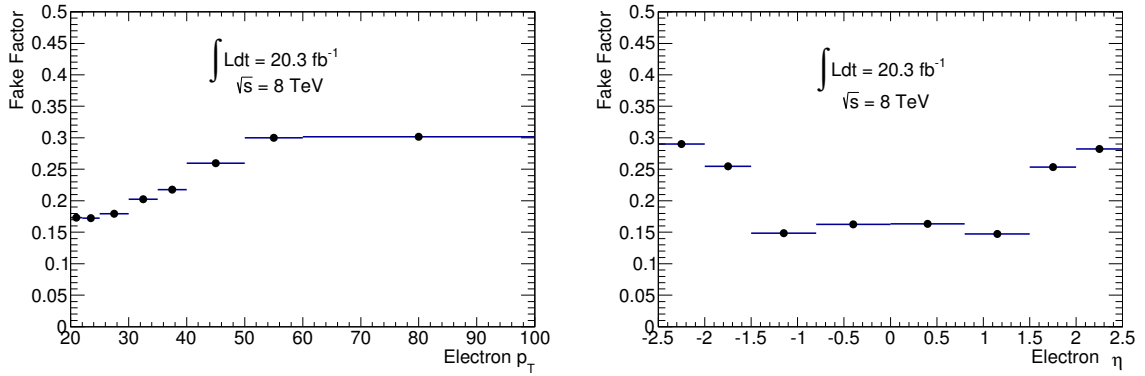
Table 6.3: Triggers used to collect numerator and denominator single electron samples for fake factor calculations. These triggers require an electron candidate with the specified E_T threshold and electron ID requirements. The effective prescale for each trigger, calculated for the full 2012 dataset, is also given.

E_T range [GeV]	Trigger	Prescale
$20 < E_T < 25$	EF_e15vh_medium1	975.97
$25 < E_T < 60$	EF_e24vh_medium1	7.397
$60 < E_T < 300$	EF_e60_medium1	1.0

Electron fake factor and its dependence on p_T and η

The central values for the electron fake factors binned versus p_T and η are shown in Fig. 6.15. The fake factors are relatively flat to slightly increasing for $p_T > 25$ GeV, and increase at high p_T . Note that the fake factors are just ratios of numerator and denominator objects and not necessarily proportional to *true* fake rates.

A series of single electron triggers (see Table. 6.3) cover the entire p_T region down to 20 GeV. To cover the full phase space, the EF_15_medium1 trigger is used for lower p_T .



(a) Electron fake factor versus p_T (Full range)

(b) Electron fake factor versus η

Figure 6.15: Electron fake factor versus p_T and η , the error bars shown are purely the statistical errors on the fake factors

Systematic uncertainty on the electron fake factors

The following sources of systematic uncertainty from the fake factor derivation are considered:

- the statistical uncertainty on the derived fake factors. The statistical uncertainty is shown in Fig. 6.15. It ranges from 0.3% to 2.6%.
- variation on the prompt MC subtraction of 10%. This number is somewhat arbitrary but is chosen to cover luminosity ($\sim 3\%$) and cross section ($\sim 7\%$) uncertainties. The variation is shown in Fig. A.3.
- variation of the away side jet p_T requirement up to > 50 GeV. This probes the dependence of the fake factors on the kinematics of the jets faking electrons. As dijet events tend to be balanced in p_T , this acts as a proxy for the near side jet p_T . This variation is shown in Fig. A.4.
- light/heavy flavor composition: To assess the impact of the light flavor (LF) versus heavy flavor (HF) composition of the fake background sample for electrons, an alternative method was developed with separate fake factors for LF and HF. Difference from the nominal prediction is taken as a systematic uncertainty. The HF/LF separation method relies on an assumption of b -tagging efficiency from MC for candidates after the numerator selections. This efficiency is varied and the largest differences seen between the varied HF/LF separation method and the nominal method are taken as a systematic uncertainty. Full details are in Appendix A.4.2.
- The dependence of the fake rates on the number of primary vertices (pile-up) was studied. No dependence was observed (see Appendix A.9).

Resulting total systematic uncertainty

The total systematic uncertainty bands for the fake factors are shown in Fig. 6.16 and a breakdown for each p_T bin is given in Table 6.4. For candidates with $p_T > 100$ GeV, we have very poor statistics to calculate their fake factor; thus the fake factor from the highest bin is used with an uncertainty of 100%.

Table 6.4: The central values for the electron fake factors for each p_T bin. The percentage uncertainty due to each systematic is given as well as the total systematic error.

p_T Bin [GeV]	Central Value	Total Error	Stat Error	Prompt MC sub	Away Jet Var	LF/HF
(20,22)	0.173	29.5%	2.6%	0.4%	28.9%	5.0%
(22,25)	0.172	38.3%	2.6%	0.6%	37.8%	5.0%
(25,30)	0.179	38.1%	0.3%	1.1%	37.7%	5.0%
(30,35)	0.203	38.8%	0.4%	1.9%	38.5%	5.0%
(35,40)	0.218	36.3%	0.6%	3.0%	35.8%	5.0%
(40,50)	0.260	28.5%	0.7%	4.7%	27.7%	5.0%
(50,60)	0.300	20.8%	1.4%	6.8%	18.9%	5.0%
(60,100)	0.301	12.9%	1.4%	9.1%	7.5%	5.0%

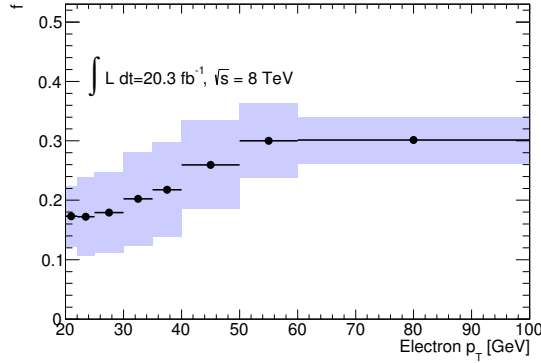


Figure 6.16: The fake factors central values as function of electron p_T as evaluated for the full $\sqrt{s} = 8 \text{ TeV}$ dataset. The error bars display the statistical error on the data, whilst the blue boxes show the combined total systematic uncertainty.

6.5.3 Muon Fake Rates

Fake enriched region

The muon fake factor is determined from data using control samples enhanced in non-prompt muons. The region is as close as possible to the signal region yet exclusive and rich in fakes. As mentioned the scenarios for producing muon fakes are very different from the case of the electrons hence we do not use a similar dijet region to evaluate the fake factors. Since the majority of muon fakes are in fact non-prompt muons from secondary decays we choose to use a fake region with dimuons. In contrast to the electron fake factor case, we can select dimuon events using the same `EF_mu18_tight_mu8_EFFS` trigger as we used for signal selection. Furthermore, due to an increase in statistics (compared to the 7 TeV analysis) same-sign dimuon pairs were utilised which is advantageous both because it uses muons which are closer to the signal region and because the prompt subtraction becomes almost negligible. For the signal region both muons must have $p_T > 20 \text{ GeV}$. By utilising a dimuon trigger with a low Pt threshold (`EF_mu18_tight_mu8_EFFS`) one can trigger both denominator and numerator objects to sufficiently low pt without any additional isolation cuts. The fake enriched region is defined by selecting same-sign dimuon events but in order to be different from the signal region and to enhance in fake candidates fake muons are selected by reversing and loosening the impact parameter cuts. Namely,

- $|d_0| < 10 \text{ mm}$
- $|d_0|/\sigma(d_0) > 3$

Since the fakes come almost entirely from secondary non-prompt muons using the $\sigma(d_0)$ cuts is the most sensible choice to define the fake enriched region. Denominator and numerator objects are selected out of the selected muons. Just as in the signal region we require that the mass of any same-sign pair pass $m(\mu^\pm\mu^\pm) > 15 \text{ GeV}$ to avoid low mass resonances.

Nominal Denominator and Numerator

Fake muons arise primarily from b -jets, pions and kaons which decay in flight. This background is estimated directly from data using the fake factor method described in Section 6.5.

Numerator muons have identical selection criteria as signal muons summarised in Table. 5.2 except for the requirements on $|d_0|$ and $|d_0|/\sigma(d_0)$. The denominator muons pass the same cuts as the numerators except that they are required to fail either the track isolation or the calorimeter isolation criteria imposed on signal muons. Explicitly, $\text{ptcone30}/p_T > 0.07$ OR $\text{Etcone30} > 3.5 + (p_T - 20) \times 0.06$. However, they are required to pass a very loose isolation of $\text{ptcone40}/p_T < 1.0$. The isolation is a good probe for distinguishing fake candidates from true prompt muons.

Prompt contamination subtraction

Any remaining prompt muon contamination can be estimated from W +jets, Z +jets and $t\bar{t}$ MC simulations. Since we select same-sign pairs, the prompt muon contamination is negligible. Therefore, no systematic error is assigned.

Correcting for isolation dependence on the impact parameter significance

Using MC simulated events, we can observe a dependence of the estimated fake factor on the impact parameter significance cut. The fake factor is determined from data using muons with $|d_0|/\sigma(d_0) > 3$ and $|d_0| < 10$ mm, while muons in the signal region are required to have $|d_0|/\sigma(d_0) < 3$ and $|d_0| < 0.2$ mm. We correct for the difference in fake factor between muons with high and low impact parameter significance by deriving a scale factor from $b\bar{b}/c\bar{c}$ MC (contributions from other sources such as $t\bar{t}$ and W +jets are negligible). As no significant p_T dependence is observed, the scale factor is derived using muons with $p_T > 20$ GeV in dimuon events with $m(\mu\mu) > 15$ GeV. The MC fake factors integrated over this p_T range and corresponding scale factors are shown in Table 6.5 for signal region isolation and intermediate isolation. Figure. 6.17 shows the fake factors and the scale factors as a function of muon p_T .

Table 6.5: Fake factors derived from MC for muons with low and high impact parameter significance. The factors are shown separately for signal isolation and intermediate isolation. The rightmost column shows the resulting scale factor.

	$ d_0 /\sigma(d_0) > 3, d_0 < 10$ mm	$ d_0 /\sigma(d_0) < 3, d_0 < 0.2$ mm	scale factor
Signal isolation	0.146 ± 0.05	0.191 ± 0.005	1.30 ± 0.05
Intermediate isolation	0.53 ± 0.03	0.53 ± 0.04	1.0 ± 0.08

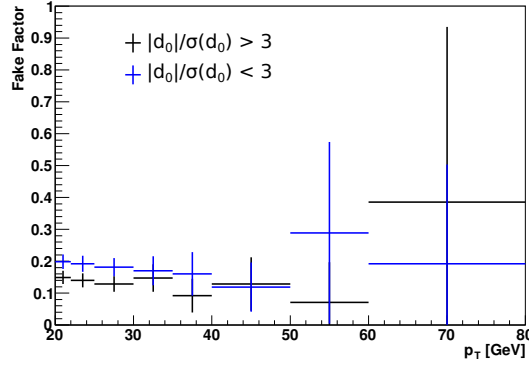


Figure 6.17: The fake factors as a function of muon p_T as derived in $b\bar{b}$ MC dataset for different cuts on impact parameter, $|d_0|/\sigma(d_0)$.

Muon fake factor and its dependence on p_T and η

The fake factors as a function of muon p_T and η before applying the correction factor from high to low impact parameter significance are shown in Fig. 6.18.

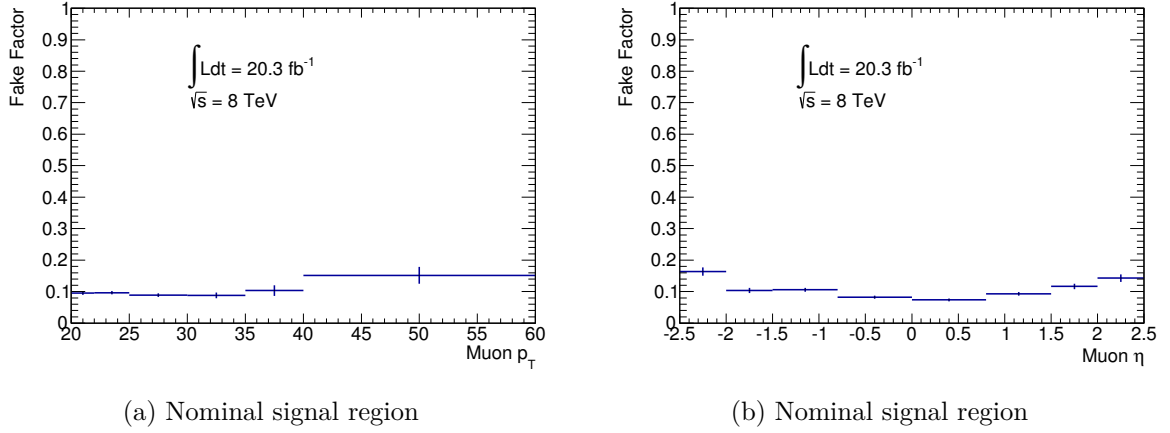


Figure 6.18: Fake factor as function of muon p_T and η before applying correction factor for high vs low impact parameter significance. Data points are purely statistical errors.

Systematic uncertainty on the muon fake factor

Several effects are taken into account when determining the systematic uncertainty on the muon fake factor:

- Statistical uncertainty on the data (from limited statistics of denominator objects particularly at high muon p_T). This is given directly from data and ranges between 5.1 – 16.6%.

- The uncertainty associated with the scale factor from low to high impact parameter significance. In calculation of the scale factor, we require two or more muons in a event. If we require exactly 2 muons, the scale factor becomes 1.14 ± 0.12 . We take the difference between these scale factors as a systematic uncertainty, which results in 16%.
- The uncertainty associated with fake muons from heavy-flavor vs light-flavor. In our method we do not distinguish the fake rates for fake muons from light and heavy flavour fakes. In reality there can be some difference in the rates. The derived fake rates are in effect an average of both light and heavy components evaluated based on the composition of the two in our derivation region. The derivation region does not need be the same composition as in our signal region. The systematic obtained taking into account this is described in detail in the appendix, and results in a small systematic uncertainty of $\pm 0.6\%$ on the fake factor.
- The dependence of the fake rates on the number of primary vertices (pile-up) was studied, no dependence was seen. (see Appendix A.9)

Resulting total systematic uncertainty

Table 6.6 shows the systematic uncertainty in bins of muon p_T for the different sources together with the central value and the total error. For muon $p_T > 60$ GeV, the statistics are very limited and the fake factor from the highest bin is used with a $\pm 100\%$ systematic uncertainty.

Table 6.6: The central values for the muon fake factors for each p_T bin. The percentage uncertainty due to each systematic is given as well as the total systematic error.

p_T Bin [GeV]	Central Value	Total Error	Stat Error	Prompt MC sub	LF/HF	$d_0/\sigma(d_0)$
(20,22)	0.125	16.8%	5.1%	0.0%	0.6%	16.0%
(22,25)	0.126	16.9%	5.3%	0.1%	0.6%	16.0%
(25,30)	0.113	17.3%	6.4%	0.1%	0.6%	16.0%
(30,35)	0.109	19.1%	10.4%	0.2%	0.6%	16.0%
(35,40)	0.131	22.7%	16.0%	0.3%	0.6%	16.0%
(40,60)	0.201	23.1%	16.6%	0.5%	0.6%	16.0%
(> 60)	0.201	100%	-%	-%	-%	-%

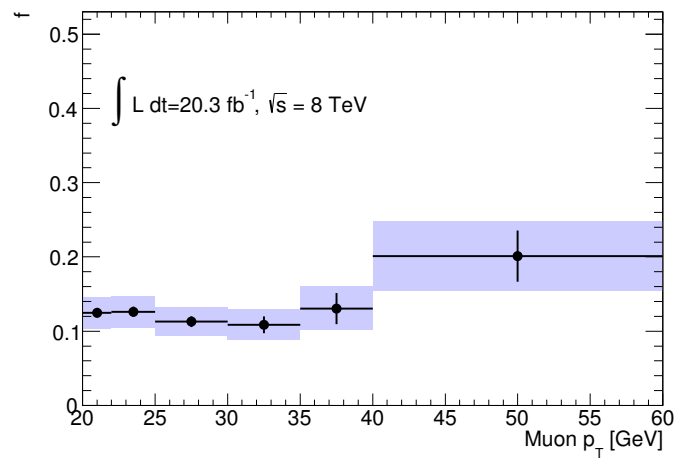


Figure 6.19: Fake factor central values as a function of muon p_T as evaluated for the full $\sqrt{s} = 8 \text{ TeV}$ dataset. The error bars display the statistical error on the data, whilst the blue boxes show the combined total systematic uncertainty.

It would be possible to describe everything scientifically, but it would make no sense; it would be without meaning, as if you described a Beethoven symphony as a variation of wave pressure

Albert Einstein

7

Same Sign: Validation Regions

In the previous section we have seen how for our analysis we wish to predict the various SM backgrounds which should be present in our signal region. The question now we wish to address is whether these background predictions are really doing a good job and whether we can validate them. In order to validate the different background components various validation regions are designed to test the components. Typically they are chosen such that the validation region is rich in the component of the background we wish to validate, for instance the fakes. There are a whole host of validation regions used for each and every channel, and not all of the plots have been made public. A summary table (Table. 7.1) describes the names of the different validation regions and what the primary backgrounds they are validating are.

7.1 Opposite-sign Validation Region

For both the electrons and muons various scaling and smearing tools and corrections are needed to be applied to the MC to correct for the fact that there are known data-MC differences in for instance the width of the Z peak due to mismodelling, detector response e.t.c Moreover, the different lepton triggers used in this analysis have different efficiencies for firing as a function of lepton p_T . Another scale factor is used to correct for the different efficiencies seen in data and MC. Lastly, there are corrections necessary for the isolation to account for the fact that the calorimeters are not 100% efficient and energy is lost in the calorimeter material. However the most important isolation correction is due to the fact that there is different amounts of *pile-up* in MC and data. Pile-up is the concept that with the high luminosity runs at the LHC there will be multiple collisions per bunch crossing, meaning multiple primary vertices per event. All these collisions contribute to

Validation method	Primary background or validation criterion
Weak isolation VR's	Electron and muon non-prompt background
Fail- d_0 VR's	Electron and muon non-prompt background
Medium VR	Electron and muon non-prompt background
Low muon p_T VR	Muon non-prompt background
Opposite-sign VR	Normalisation, efficiencies, lepton p_T scale and resolution.
Prompt VR	Prompt MC background predictions
Same-sign dielectron Z peak closure test	Charge misidentification correction applied to opposite-sign MC background samples

Table 7.1: A summary of the validation methods used and an explanation of the type of background the methods are testing or which data-driven estimates they validate. These tests are carried out using validation regions (VR) or closure tests and are discussed in detail in the text.

the event, but most of the collisions are contain no new physics and are simple underlying events. However, the particles created in these other *boring* collisions still register in the calorimeters and contribute to the energy depositions measured. There is, as one would assume, a correlation between the number of primary vertices and energy deposited in the calorimeters, thus any discrepancies between data and MC need to be corrected for. I shall not go into detail on all of these corrections here, but will mention them a little further in the systematics section 8. With all these corrections to MC we wish to design a validation region which validates these corrections as well as tests some of the MC samples and their normalisation to data ¹.

A very simple validation region was chosen which uses the exact same selection criteria for signal region leptons except that we require OS dilepton pairs. Here we expect the agreement between data and MC to be very good, which it is. For the ee and $\mu\mu$ channels over the full mass range, and for the $e\mu$ channel at low mass, this validation region is dominated by Drell-Yan. At high mass in the $e\mu$ channel, $t\bar{t}$ is the largest contribution. The total event yields for this validation region are given in Table 7.2. For all the plots and numbers, PYTHIA Drell-Yan samples are used. The observed number of events in data is higher than the MC prediction by 3%, 2%, and 5% in the ee , $\mu\mu$, and $e\mu$ channels respectively. The errors in the table are only statistical and smaller than these differences, but the cross section error of the Z/γ^* process is larger than the differences in ee and $e\mu$ channels.

¹Often the MC data sets contain many more events than one should see for the corresponding data, based on their production cross-sections. Hence we need to re-weight the MC to normalise the MC such that the amount of MC corresponds to the amount of data taken. This is done by this formula: $w = \frac{L_{data} \cdot \sigma_{MC}}{N}$ where w is the re-weighting, L_{data} is the integrated luminosity for the data period we consider (in our case 20.3 fb^{-1}), σ_{MC} is the production cross-section for the MC process considered and N is the number of events produced for the MC dataset. Filtering efficiency for final states is also included where necessary

Table 7.2: Observed and expected number of lepton pairs for the validation region with opposite-sign, isolated leptons.

Process	Number of lepton pairs
$\mu^+\mu^-$	
Z/γ^*	8081500 ± 6700
Non-prompt	30100 ± 7500
$t\bar{t}$	13125 ± 58
Dibosons	19194 ± 39
Total predictions	8140000 ± 10000
Observation in data	8317039

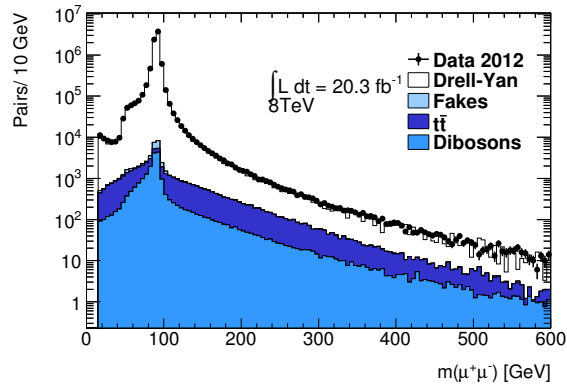


Figure 7.1: Invariant mass distributions for $\mu\mu$ in the opposite-sign validation region with two isolated leptons. The error bars show the statistical error on the data.

From fig. 7.1 it is clear that the agreement is adequate in both normalisation and shape.

7.2 Prompt Validation region

The previous validation region, as well as validating the normalisation, scaling, smearing, corrections, predominantly tested the Drell-Yan (and to a lesser extent) $t\bar{t}$ MC. In order to validate the Prompt (mostly diboson) MC a separate validation region was constructed. This validation region was particularly important for the $\mu\mu$ channel which is dominated by prompt MC in the signal region. As discussed, for the 8 TeV analysis we vetoed events with OS dilepton pairs of the same flavour in order to reduce the prompt background coming

from WZ and ZZ processes. However, by selecting events with such a Z candidate we got a bonus validation region in which to validate the prompt MC background prediction.

The agreement between data and MC was good and within errors as one can see from fig. 7.2 and table. 7.3. In the appendix A.8.1 one can see the other kinematics distributions.

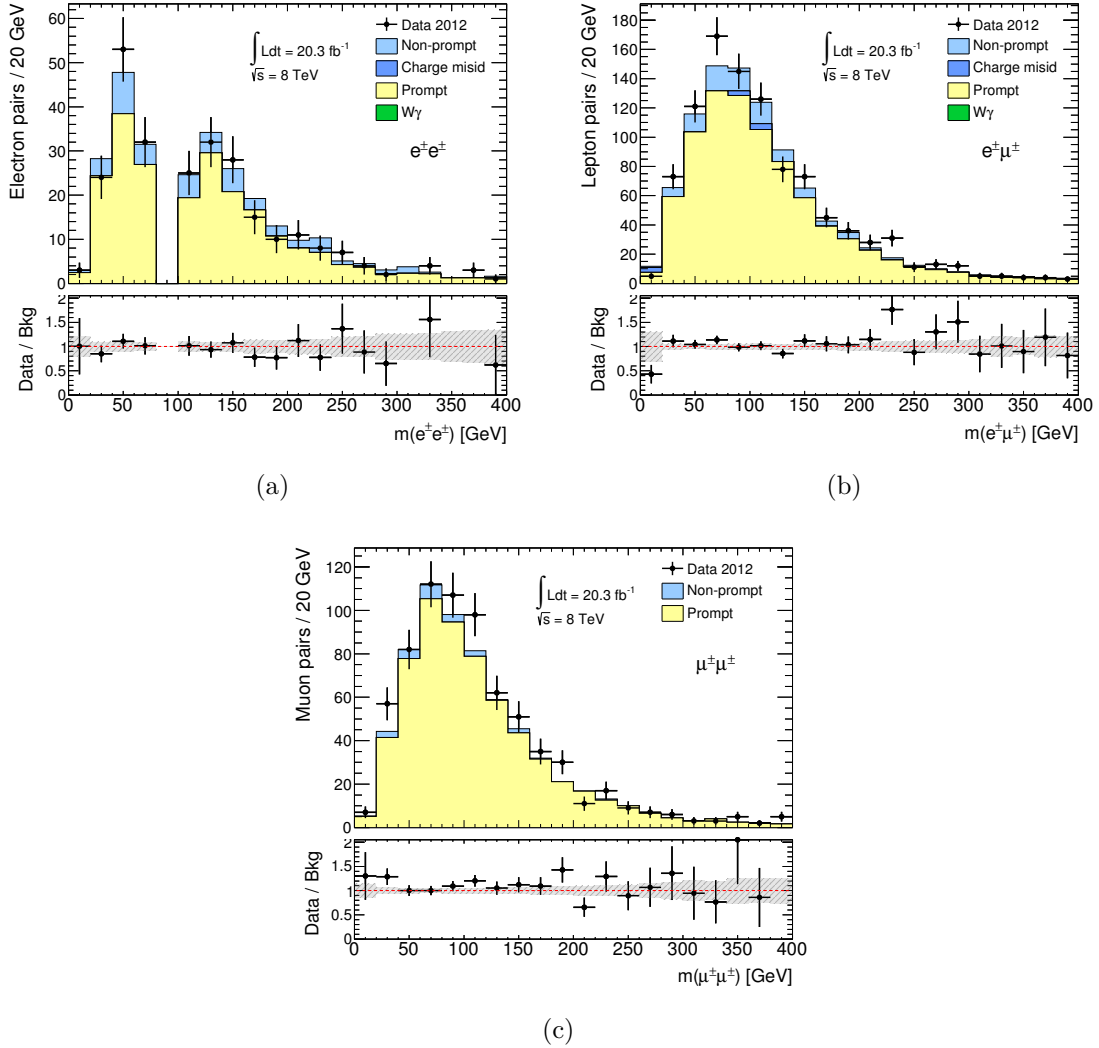


Figure 7.2: Invariant mass distributions of isolated SS (a) ee , (b) $e\mu$, and (c) $\mu\mu$ pairs in the prompt background validation region. This region is mainly composed of WZ and ZZ events and contains events with at least a same-flavour opposite-sign pair with invariant mass ($m_{\ell\ell}$) $|m_{\ell\ell} - m_Z| < 10$ GeV. The contributions from the various physics processes are shown. The lower plot shows the ratio of pairs found in data compared to the SM predictions. In the ee channel prompt processes constitute a minor contribution. The prompt SM processes contribute dominantly to the same-sign pair backgrounds in the $\mu\mu$ channel and have magnitude comparable to the non-prompt background in the $e\mu$ channel.

Table 7.3: Ratio between observed and expected same-sign pairs in the WZ and ZZ validation region for ee , $\mu\mu$ and $e\mu$ channels. The uncertainties account for both statistical and systematic errors.

ee	$\mu\mu$	$e\mu$
0.90 ± 0.09	1.12 ± 0.09	1.01 ± 0.07

7.3 Fake Validation Regions

Finally we needed to construct regions in which to validate the fake background and fake factor methods. Due to the nature of the fakes being different for electrons and muons we defined slightly different fake regions to test the two different fake rates (electrons, muons). I will list the various validation regions for each channel and briefly explain them either in this section or the appendix.

ee Validation Regions

- Both Electrons Weakly Isolation (Weak Isolation requirements, exact definition in app. A.5.1)
- Leading Electron Fully Isolated, Subleading Electron Weakly Isolated.
- Leading Electron Weakly Isolated, Subleading Electron Fully isolated.
- Both Electrons pass EM Medium++ (fail EM tight++, definition in app. A.5.1)

$\mu\mu$ Validation Regions

- Both Muons Weakly Isolated (Weak Isolation, app. A.7)
- Leading Muon Fully isolated, Subleading Muon Weakly Isolated.
- Leading Muon Weakly Isolated, Subleading Muon Weakly Isolated.
- Both muons fail $\sigma(d_0)$ cuts.

$e\mu$ Validation Regions

- Electron Weakly Isolated, Muon Fully Isolated
- Electron Fully Isolated, Muon Weakly Isolated.
- Electron Fully Isolated, Muon Fails $\sigma(d_0)$ cut.
- Electron pass EM medium++, Muon Fully Isolated.

Table 7.4 shows the expected and observed numbers of muon pairs for the fake-enhanced validation regions. The uncertainties quoted include statistical and systematic uncertainties. For the uncertainty on the fake predictions, this includes the uncertainty associated with limited statistics where the fakes are estimated together with the resulting fractional systematic uncertainty on the fake factor as propagated through for the signal region. Fig. 7.3 shows the invariant mass distributions for the four validation regions. The agreement between observation and prediction is generally good and within one sigma of error. Additional plots of fake-enhanced validation regions can be found in Appendix A.8.2.

Similarly for completeness sake the fake validation regions for the ee and $e\mu$ channels are also shown in figures 7.4 and 7.5 respectively. Accompanying them are the tables 7.5 and 7.6 which give the overall level of agreement between data and MC.

Table 7.4: Expected and observed numbers of muon pairs for the different like-sign $\mu\mu$ fake validation regions. The uncertainties on the predictions include the statistical and systematic uncertainties. For the fake predictions, the systematic uncertainty derived for the signal region is assumed ($\pm 15\%$).

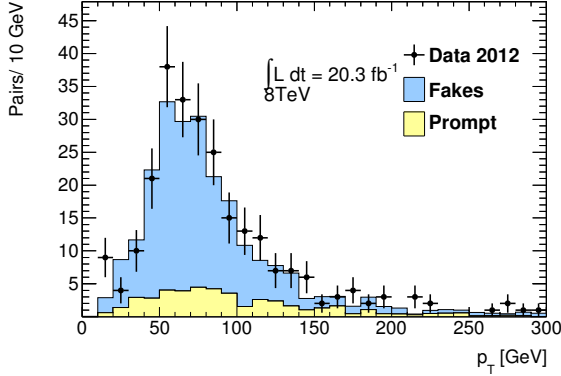
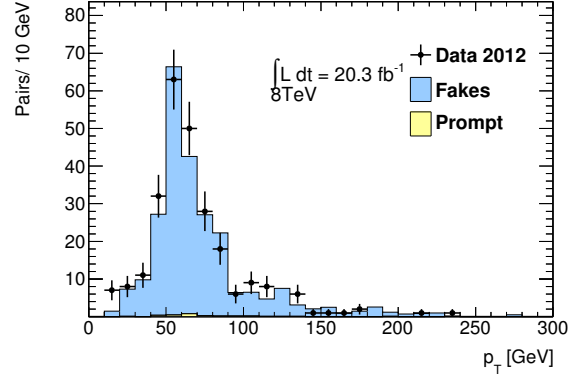
Region	Total Pred	Data	Agreement(σ)
Fail d_0 VR	250 ± 31	255	-0.15
Weak iso on both leptons VR	270 ± 40	283	-0.2
Weak Iso on leading lepton VR	199 ± 25	199	+0.01
Weak Iso on sublead. lepton VR	700 ± 90	652	-0.01

Table 7.5: Expected and observed numbers of electron pairs for the different like-sign ee fake validation regions. The uncertainties on the predictions include the statistical and systematic uncertainties (fake factor and charge flip uncertainties have been included; other systematic uncertainties are negligible in these regions).

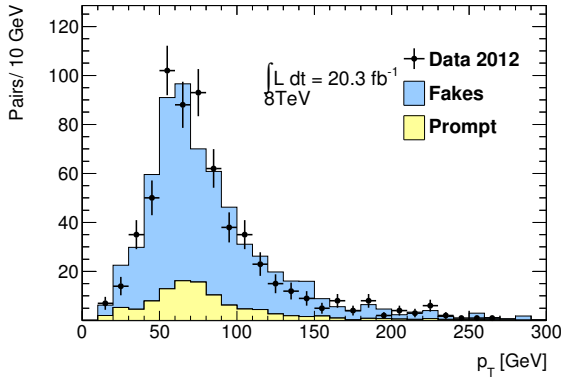
Region	Total Pred	Data	Agreement(σ)
Medium VR	195.18 ± 32.2	217	-0.62
Weak Iso on both leptons VR	283.47 ± 134.02	285	-0.01
Weak Iso on sublead. lepton VR	622.42 ± 121.72	574	0.39
Weak Iso on leading lepton VR	189.33 ± 59.19	224	-0.57

7.3.1 Charge Flip Validation Region

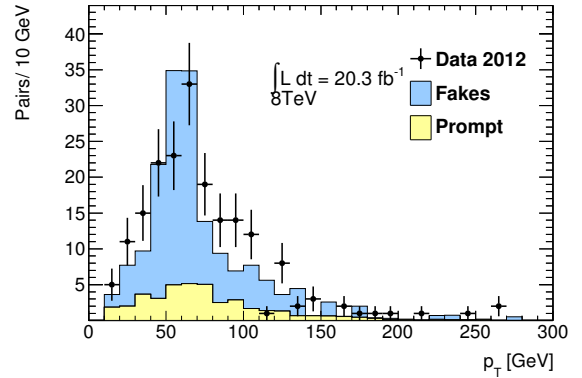
Similarly as for the 7 TeV analysis discussed in Section. 6.4.1, we created a validation region for the charge misidentification scale factors derived. The region is the SS Z peak region where the MC is weighted by the scale factors derived as a function of electron η . The agreement is $< 1\sigma$ and is more or less a sanity check to see the scale factors work, since this is the same region as we derived the fake factors in, however this is a mass distribution

(a) Same-sign $|d_0|/\sigma(d_0) > 3$ for ≥ 1 muon

(b) Same-sign intermediate isolation



(c) Same-sign muon pairs with leading muon isolated and subleading muon intermediately isolated

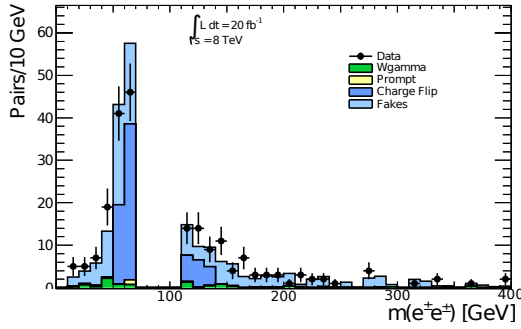


(d) Same-sign muon pairs with leading muon intermediately isolated and subleading muon isolated

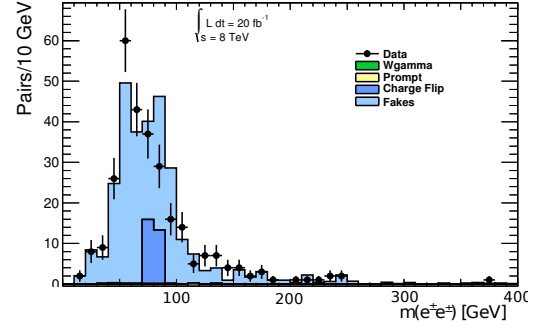
Figure 7.3: Invariant mass distributions for different $\mu^\pm\mu^\pm$ validation regions enhanced in fake background. The error bars show the statistical error on the data.

Table 7.6: Expected and observed numbers of electron-muon pairs for the different like-sign $e\mu$ fake validation regions. The uncertainties on the predictions include the statistical and systematic uncertainties (fake factor uncertainties and Charge flips uncertainties have been included: Monte Carlo uncertainties are negligible in these regions). For the fake predictions, a systematic uncertainty derived for the signal region is assumed.

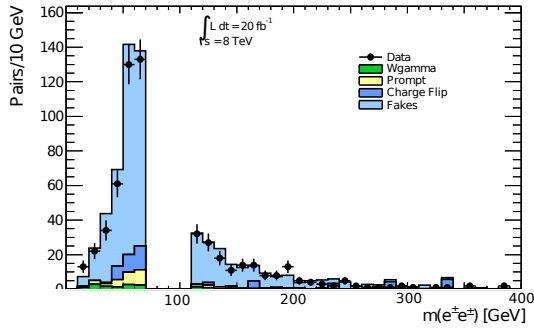
Region	Total Pred	Data	Agreement(σ)
Fail D0 μ	249 ± 19	216	1.7
Weak Iso μ	790 ± 130	800	-0.07
Weak Iso e	750 ± 150	965	-1.4
Low μ p_T	211 ± 12	201	0.8



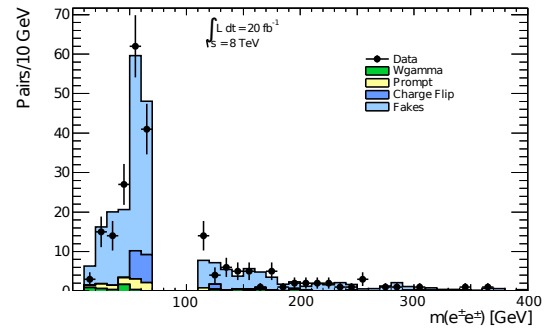
(a) Same-sign Medium++



(b) Same-sign electron pairs with both electrons weakly isolated



(c) Same-sign electron pairs with leading isolated and subleading weakly isolated



(d) Same-sign electron pairs with leading weakly isolated and subleading isolated

Figure 7.4: Invariant mass distributions for different e^+e^- validation regions enhanced in fake background. The error bars show the statistical error on the data.

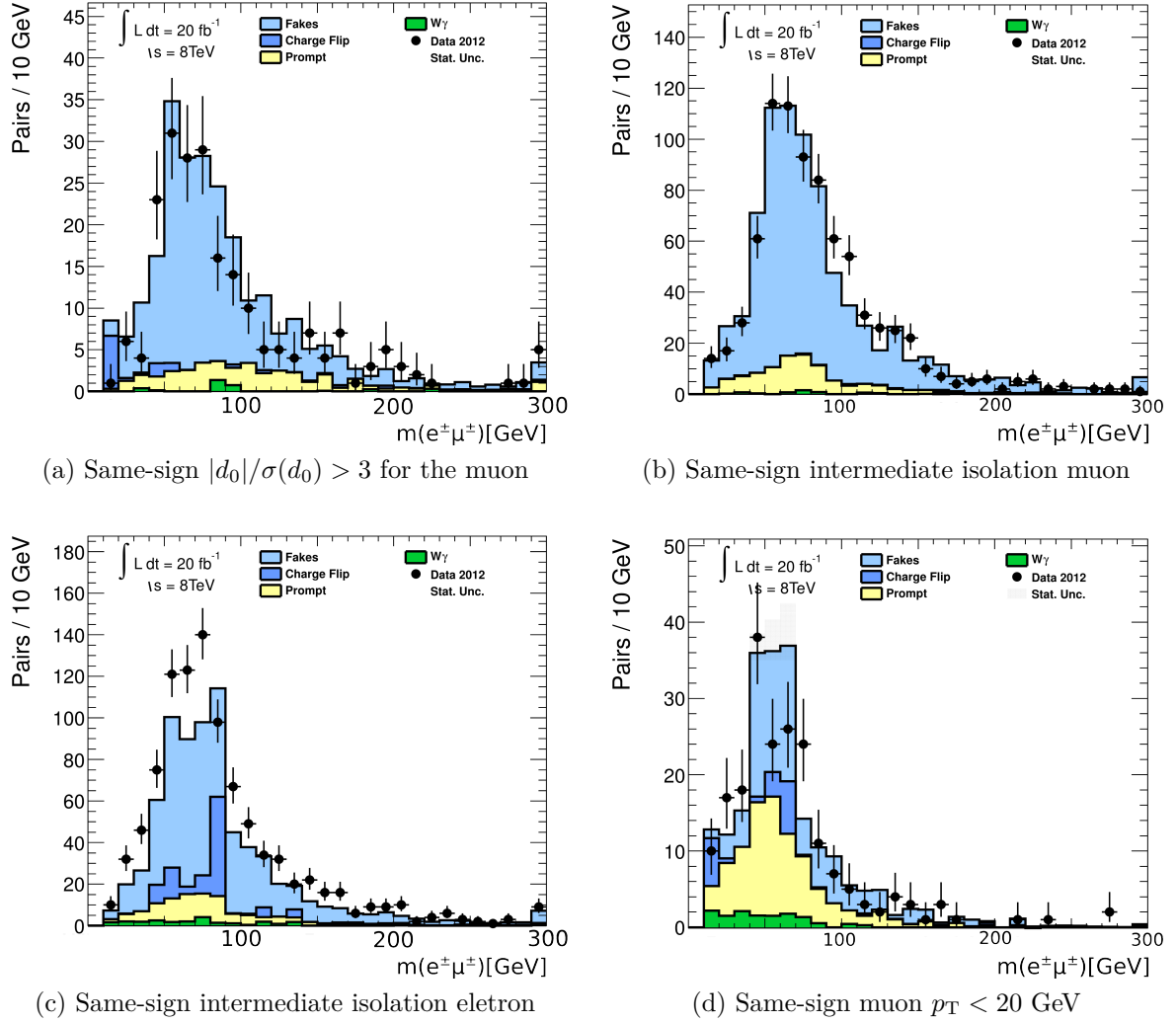


Figure 7.5: Invariant mass distributions for different $e^\pm\mu^\pm$ validation regions enhanced in fake background. The error bars show the statistical error on the data.

and we calculated the charge misidentification scale factors as a function of η hence we do not see perfect agreement. The overall normalisation agreement is shown in Table. 7.7. The mass distribution is shown in Fig. 7.6. The lead electron distributions in η and p_T are shown in Fig. 7.7 and help aid or confidence that the charge-flip scale factors are doing a reasonable job.

Table 7.7: Expected and observed numbers of electron pairs for same-sign z peak closure test.

Region	Total Pred	Data	Agreement(σ)
Charge misidentification closure test	12700 ± 1300	11793	+0.7

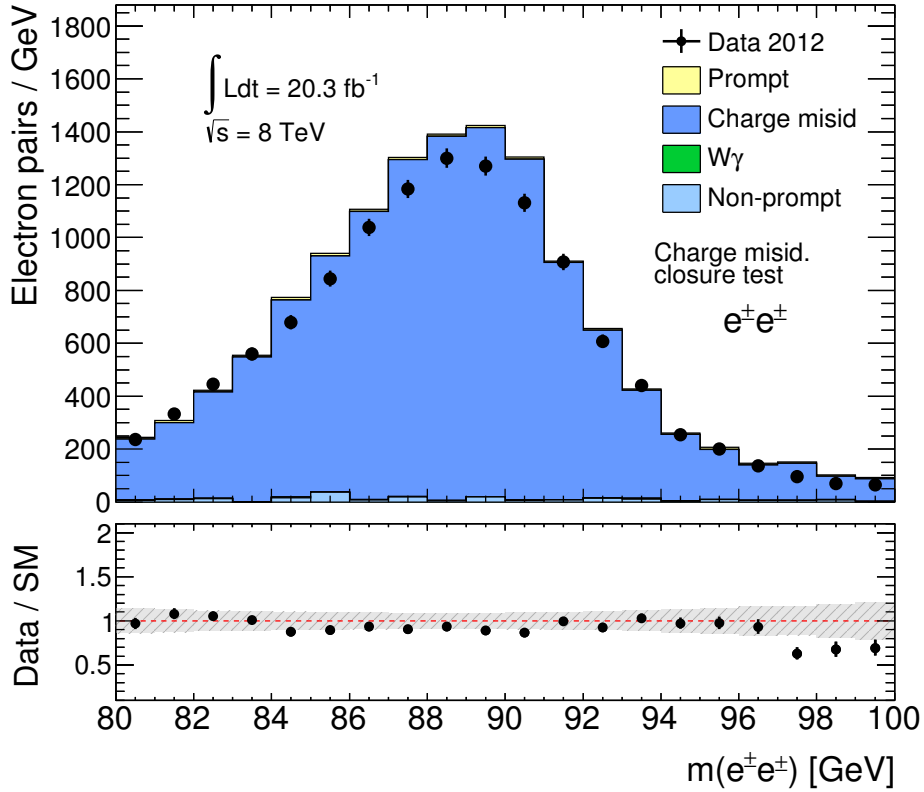


Figure 7.6: Distribution of the invariant mass of the electron pair, in the same-sign Z peak validation region. To test the prediction of charge misidentification two isolated electrons with the same charge whose mass is compatible with a Z boson (defined as $80 < m_{ee} < 100$ GeV) are requested. The lower plots show the ratio of data over the background prediction. The error bars on the data points and the dashed band show the statistical uncertainties.

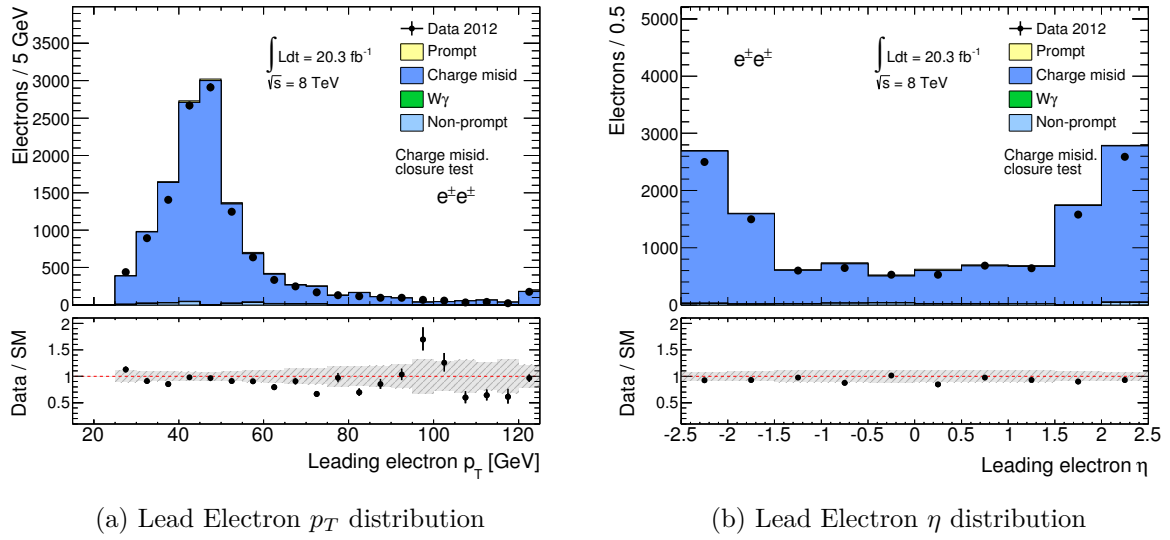


Figure 7.7: Distribution of the lead electron p_t (a) and η (b) distributions, in the same-sign Z peak validation region. To test the prediction of charge misidentification two isolated electrons with the same charge whose mass is compatible with a Z boson (defined as $80 < m_{ee} < 100$ GeV) are requested. The lower plots show the ratio of data over the background prediction. The error bars on the data points and the dashed band show the statistical uncertainties.

*Science, my lad, is made up
of mistakes, but they are mis-
takes which it is useful to
make, because they lead little
by little to the truth*

Jules Verne, *A Journey to the
Centre of the Earth*

8

Same Sign: Uncertainties

An analysis is only as good as its errors. If one does not understand the errors properly or uses a method with which the intrinsic errors entailed are large, then the sensitivity and validity of their results are weakened. Likewise, if one over-estimates the size of their errors, then one is very conservative about the claims one is making and risks losing sensitivity or hiding potential discoveries. We have already discussed in great deal the systematic effects associated with the charge flip and fake background predictions in chapters 6.4.1 and 6.5 respectively. These are the two largest sources of systematic uncertainty for the analysis by far, excepting perhaps the theoretical uncertainty on some of the MC cross-sections. In this chapter I will briefly explain the other sources of systematic errors.

MC Cross-Section Uncertainty

There is of course some uncertainty on the Parton Density Function (PDF)^I functions used to calculate the cross-section, and some error on the cross-section depending on which order the cross-section was calculated to. This lends itself to uncertainties on the overall cross-sections which are summarised in Table. 8.1.

The CT10 [74] PDF is used for WZ , ZZ , WW , $W\gamma$, $W^\pm W^\pm + 2$ jets, $t\bar{t}$, and Wt processes while CTEQ6L1 is used for others. $W^\pm W^\pm + 2$ jets cross sections are calculated at leading order (LO) of QCD. For diboson samples (WZ , ZZ and WW), the cross sections are normalised to next-to-leading order (NLO) using MCFM-6.2 [75]. The next-to-next-to-leading order (NNLO) and the next-to-next-to-leading-log (NNLL) calculations are utilised for top processes. The Drell–Yan simulation is also done at NNLO by DYNNLO-1.1 with MSTW2008 NNLO [80, 82]. These details are also found in Table. 6.1.

^IThe probability density for finding a particle with a certain momentum fraction x at a given resolution scale

Electron Identification Efficiency

There is an uncertainty on the *tight* reconstruction identification of electrons. The efficiency of the identification is estimated by the ATLAS Electron/Photon combined performance group whom utilise a tag-and-probe method on electrons from $Z \rightarrow ee$ [97]. Here the efficiency varies as a function of η and p_T and the overall uncertainty on the electron channels is $\approx 1\%$. For reconstruction, the uncertainties range from 1.3-2.4% depending on η , while for tight++, the uncertainties range from about 2.0-2.8% depending on both E_T and η .

Electron Momentum Measurement

The electron/photon group also provides recommendations for the energy scale and resolution of electrons. By varying the energy scale of electrons one varies the amount of electrons above and below the various cut thresholds in the analysis thereby altering the number of electrons entering the signal selection. The uncertainty associated with these variations is most pronounced at higher mass. This is because the high-mass region suffers from reduced statistics so variations are more apparent.

Muon Identification Efficiency

The uncertainty on the muon reconstruction and identification efficiencies, including track quality requirements in the ID, is estimated by the ATLAS combined muon performance group using a tag-and-probe method with muons from $Z \rightarrow \mu\mu$ decays [98]. Again dependence on the η and p_T for the muons is seen and the uncertainty is in general $< 1\%$.

Muon Momentum Measurement

In general for low p_T muons the momentum resolution is very small $\approx 0.1\%$ as the momentum is well measured. Thus it contributes only a little to the signal region uncertainty. At higher p_T (100 GeV) the resolution degrades but is still relatively small $\approx 1\%$.

Trigger Efficiency

There is also some uncertainty on the efficiency with which the various triggers fire for electrons and muons of differing p_T and η . The uncertainty on the trigger scale factors are estimated to be $< 1\%$ by the ATLAS electron and muon trigger groups.

Integrated Luminosity Uncertainty

In order to normalise the MC datasets to the correct amount of data taken by the LHC one needs to know the integrated luminosity over the data taking period. There is some uncertainty on this number which translates into error on the amount of MC background estimated. For the 2012 data the integrated luminosity had an uncertainty of 2.8% [99].

Full and fast simulation

Some of the signal processes were simulated using the ATLAS fast simulation, AtlFastII [100]. These signals were used to calculate the acceptance for the doubly charged Higgs decay. This acceptance was then used in order to set limits. Studies were done comparing the full and proper simulation [101] and the fast simulation. This was done by simulating a $H^{\pm\pm}H^{\mp\mp} \rightarrow l^{\pm}l^{\pm}l^{\mp}l^{\mp}$ sample with a mass of 300 GeV for both full and fast simulation. Comparing the two simulations in the different channels gives an uncertainty on using the fast simulation compared to the full simulation.

Monte Carlo and control region statistical uncertainties

An additional source of systematic uncertainty is the limited statistics available in the MC samples and the data control samples used for the background predictions. These uncertainties are especially large in the high-mass bins.

All the above efficiencies (as one can see from Table 8.1) are relatively small compared to the charge flip and fake systematics (with the exception of the cross-section uncertainties for various backgrounds) which are really the core of the analysis.

Table 8.1: Sources of systematic uncertainty and their effect on predicted yields in the signal region for the mass range $m_{\ell\ell} > 15$ GeV. The uncertainties quoted for the $e^\pm e^\pm$, $e^\pm \mu^\pm$ and $\mu^+ \mu^-$ final state reflect their relative impact on the different predicted yields coming from the different background components, which are shown in the second column. The numbers shown for the statistical uncertainties due to the limited size of the background MC samples.

Source	Process	Uncertainty		
		$e^\pm e^\pm$	$e^\pm \mu^\pm$	$\mu^+ \mu^-$
Trigger	signal and background from MC simulations	2.1-2.6%	2.1-2.6%	2.1-2.6%
Electron reconstruction and identification	signal, prompt background	1.9-2.7%	1.4%	n/a
Muon reconstruction and identification	signal, prompt background	n/a	0.3%	0.6%
Electron charge misidentification	Opposite-sign backgrounds	9%	1.2%	n/a
Determination of factor f for e/μ	Non-prompt backgrounds	22%	24%	17%
Luminosity	signal, all types of backgrounds	2.8%	2.8%	2.8%
MC statistics	all types of backgrounds	5%	2%	3%
Photon misidentification as electron	$W\gamma$	13%	11%	n/a
Drell-Yan cross section	Drell-Yan (Charge flips)	$\pm 7\%$		
WZ cross section	WZ	7%		
ZZ cross section	ZZ	5%		
$t\bar{t}W$ cross section	$t\bar{t}W, t\bar{t}Z$	22%		
$W^\pm W^\pm$	$W^\pm W^\pm$	50%		
DPI Diboson cross section	DPI WW, WZ, ZZ	100%		
$t\bar{t}$ cross section	$t\bar{t}$	5%		
$W\gamma$ cross section	$W\gamma$	$\pm 14\%$		

*Equipped with his five senses,
man explores the universe
around him and calls the ad-
venture Science*

Edward Hubble

9

Same Sign: Results of the Inclusive Search

At this point we have finalised our event selection, decided on our backgrounds, validated them and evaluated our systematics. So there is nothing more to it than to take the lid off the box and see what we get. The way our analysis (and most particle physics analyses) worked was to do all of the above without looking at or using the data events in our signal region. This is called a blind analysis. Once unblinded, the methods and predictions are locked in and the signal region was looked at. So without further ado, I present the findings for the 8 TeV analysis. Here in Table. 9.1 and Fig. 9.2, the results for the number of same-sign dilepton pairs as a function of invariant mass is displayed. As mentioned in my preface, i was also involved in the 7TeV incarnation of this analysis, hence at the end of this chapter i shall briefly present the 7TeV results in order for comparison.

The observed number of same-sign dilepton pairs is compared to the background expectation in Table 9.1. The data was compared to expectation for seven different ranges of invariant mass, constrained by the lower bound on the mass. This bound ranges from 15 GeV up to 600 GeV. In each channel the different background components build the total background in varying ratios (shown in Fig. 9.1); in the $\mu\mu$ channel the background is dominated by the prompt contribution (74% for $m_{ll} > 15$ and up to 100% for $m_{ll} > 600$), whereas in the ee channel the background is dominated by charge flip events at lower mass (50%). In the $e\mu$ channel there is a more even mix of prompt (40%), non-prompt(35%) and charge flips and conversions(15%). In all channels and across all mass bins there is no significant indication of new BSM physics. All bins agree within the statistical and systematic uncertainties.

The p_T and η distributions for the leading and subleading leptons were also calculated for lepton pairs in the signal region. Although we do not use these distributions to set any limits they also confirm to show the good agreement between data and MC. Fig. 9.3 and

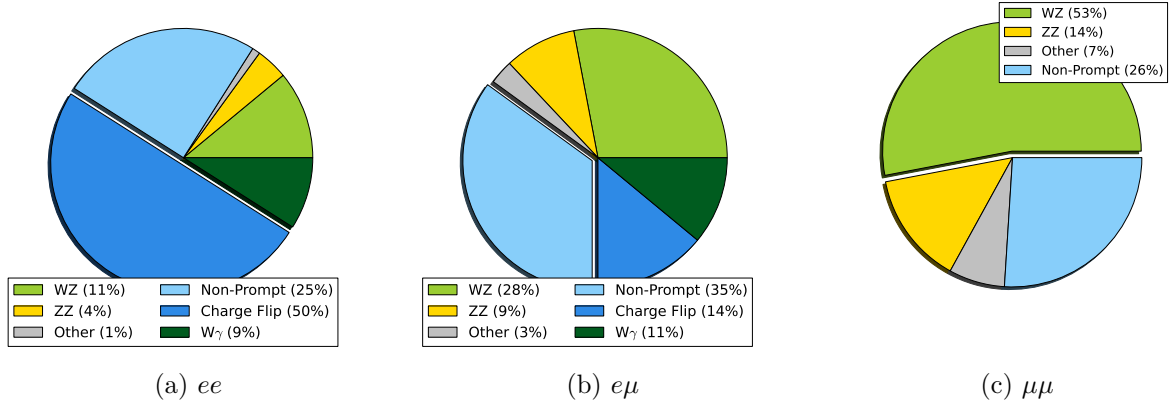


Figure 9.1: A breakdown of the predicted background composition for the three signal regions (a) ee , (b) $e\mu$ and (c) $\mu\mu$ for the mass range $m_{\ell\ell} > 15$. Here *other* means prompt backgrounds other than WZ and ZZ .

Fig. 9.4 show the p_T and η distributions for the three different channels. The subleading lepton distributions are also given in Appendix A.10.

Charge-separated dilepton pairs

As a simple extension one can consider the number of charge-separated pairs separately for $\ell^+\ell^+$ and $\ell^-\ell^-$ pairs. More W^+ than W^- bosons are produced at the LHC due to the fact that there are more valence up quarks in the proton than down hence increasing the production probability. This results in a large number of $\ell^+\ell^+$ in the final state. For all final states, no significant excesses or deficits are observed between the data and the SM background predictions within the total uncertainties. Table 9.2 shows the charge-separated numbers. This is useful, the reason being that some BSM models prefer one charged-pair over another and we wanted to be sensitive to those. Alas, again here no significant discrepancies from the SM are seen in any of the mass bins outside the statistical and systematic errors.

As an aside the number of ATLAS reconstructed jets per dilepton pair was looked at, the results are detailed in Appendix A.11.

9.1 Limit Setting

Unfortunately no significant excess was observed in data above the Standard Model, so no excitement there. However, what this does mean is that our analysis can set limits on the cross-section for new physics. In order to do so one needs to translate between an upper limit on the number of same-sign pairs and a *fiducial* cross-section. This requires an understanding of the efficiency for reconstructing particles occupying a *true fiducial*

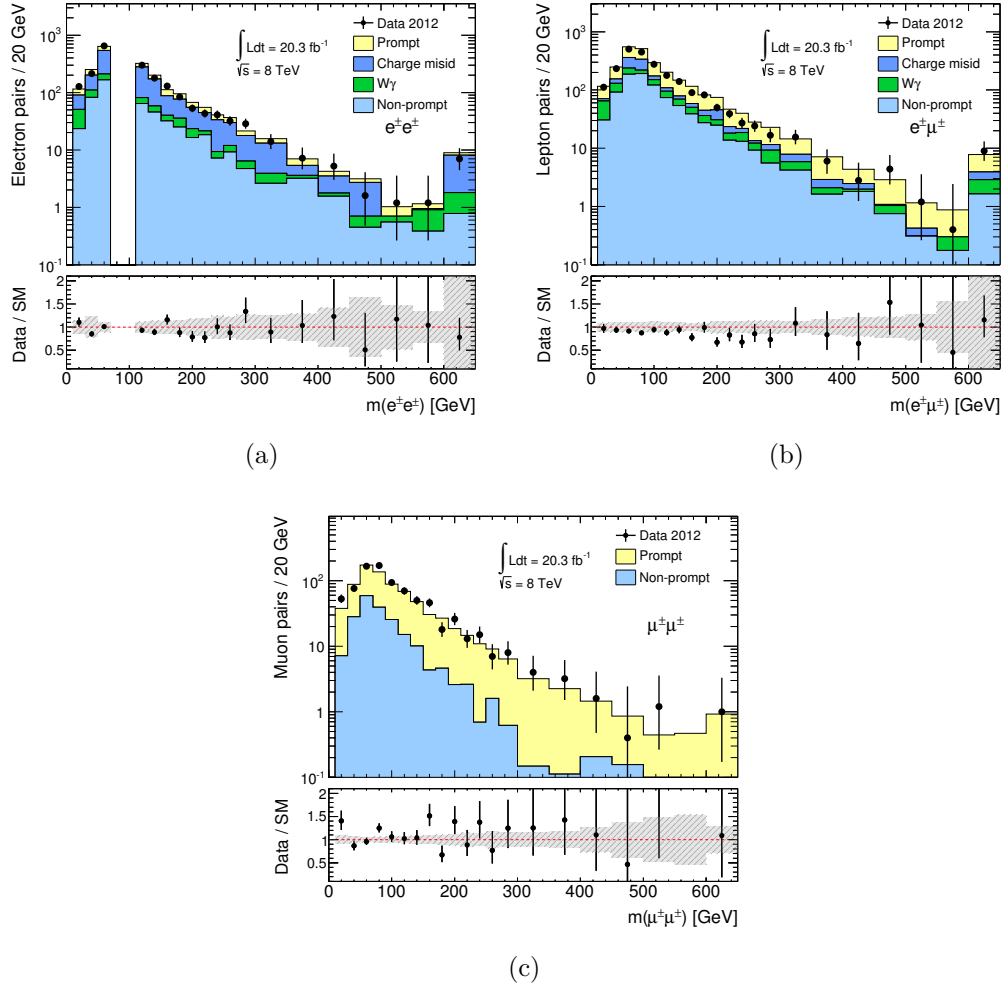


Figure 9.2: Invariant mass distribution of (a) $e^{\pm}e^{\pm}$ (b) $e^{\pm}\mu^{\pm}$ and (c) $\mu^{\pm}\mu^{\pm}$ pairs in the same-sign signal region. The hashed grey area corresponds to the total systematic uncertainties.

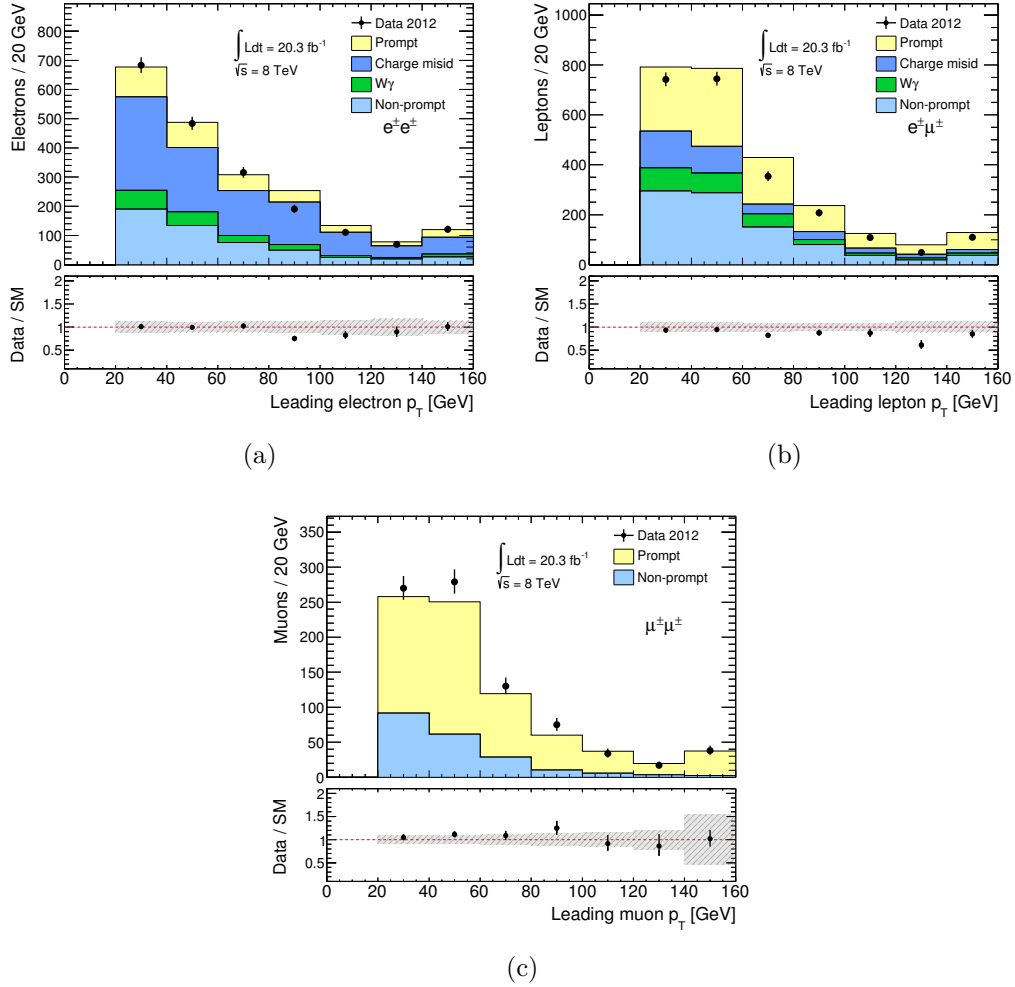


Figure 9.3: The transverse momentum distribution of the lead lepton in (a) $e^\pm e^\pm$ (b) $e^\pm \mu^\pm$ and (c) $\mu^\pm \mu^\pm$ pairs in the same-sign signal region. The hashed grey area corresponds to the total systematic uncertainties.

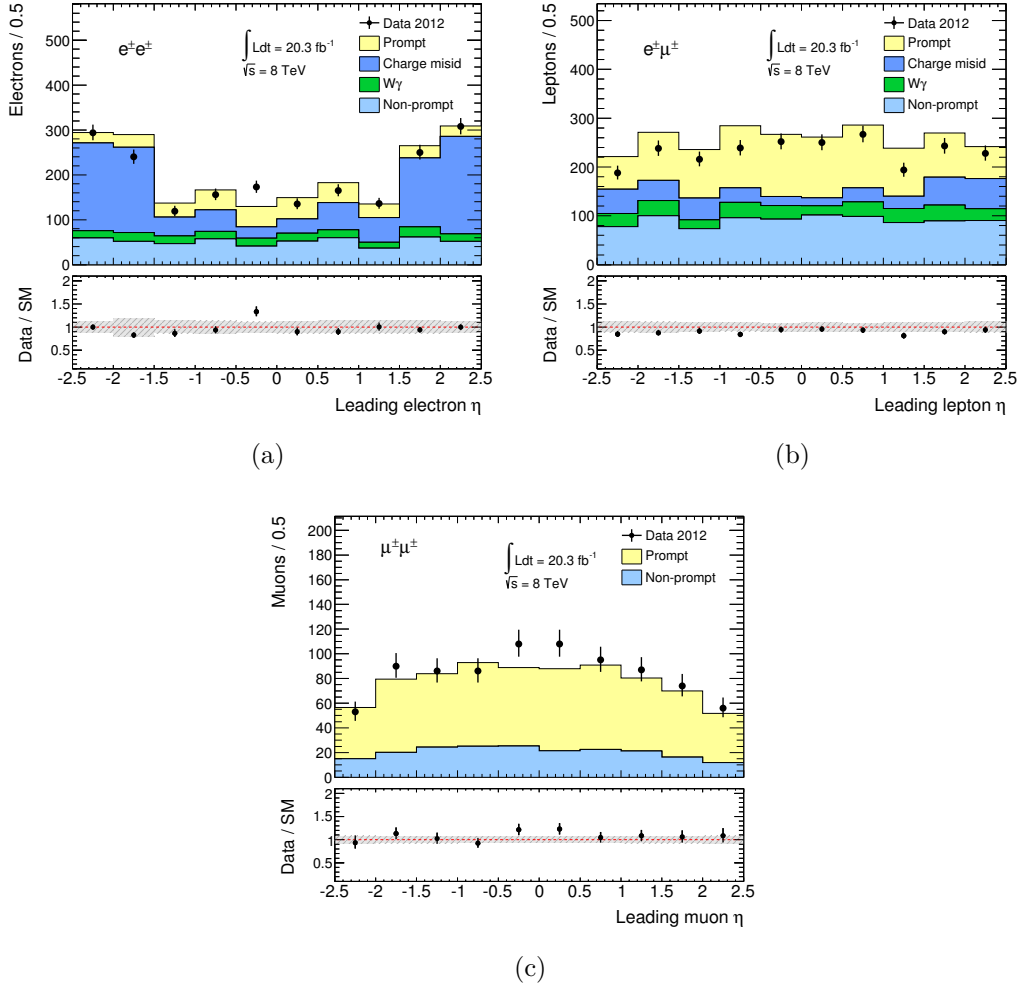


Figure 9.4: The η distribution of the lead lepton in (a) $e^\pm e^\pm$ (b) $e^\pm \mu^\pm$ and (c) $\mu^\pm \mu^\pm$ pairs in the same-sign signal region. The hashed grey area corresponds to the total systematic uncertainties.

$m(e^\pm e^\pm)$ [GeV]	Number of electron pairs					Data
	Prompt	Non-Prompt	e^\pm charge misid.	$W\gamma \rightarrow W_{ee}$	Total bkg	
> 15	347 ± 25	520 ± 120	1020 ± 150	180 ± 40	2060 ± 190	1976
> 100	174 ± 14	250 ± 50	550 ± 80	75 ± 16	1050 ± 100	987
> 200	51.5 ± 4.9	72 ± 13	150 ± 27	22 ± 5	296 ± 31	265
> 300	15.7 ± 1.9	23 ± 5	43 ± 12	8.0 ± 2.3	89 ± 14	83
> 400	5.3 ± 0.9	8.1 ± 2.4	16 ± 8	3.8 ± 1.3	33 ± 8	30
> 500	2.3 ± 0.5	3.1 ± 1.5	6 ± 5	2.7 ± 1.0	14 ± 5	13
> 600	0.91 ± 0.28	$0.8^{+1.0}_{-0.8}$	6 ± 5	1.0 ± 0.6	9.0 ± 5.0	7

$m(e^\pm \mu^\pm)$ [GeV]	Number of electron–muon pairs					Data
	Prompt	Non-Prompt	e^\pm charge misid.	$W\gamma \rightarrow W_{ee}$	Total bkg	
> 15	1030 ± 50	910 ± 220	370 ± 40	270 ± 50	2580 ± 240	2315
> 100	458 ± 26	340 ± 80	87 ± 11	104 ± 20	990 ± 90	859
> 200	130 ± 9	79 ± 17	29 ± 4	28 ± 6	265 ± 22	226
> 300	43 ± 5	24 ± 6	9.5 ± 1.9	8.1 ± 2.4	84 ± 8	85
> 400	16.0 ± 2.1	9.2 ± 3.0	2.5 ± 0.8	2.7 ± 1.1	31 ± 4	31
> 500	6.8 ± 1.1	2.8 ± 1.5	1.5 ± 0.4	1.6 ± 0.8	12.6 ± 2.1	13
> 600	3.5 ± 0.7	1.6 ± 1.0	0.9 ± 0.4	1.2 ± 0.7	7.4 ± 1.5	9

$m(\mu^\pm \mu^\pm)$ [GeV]	Number of muon pairs			
	Prompt	Non-Prompt	Total bkg	Data
> 15	580 ± 40	203 ± 34	780 ± 50	843
> 100	245 ± 21	56 ± 11	301 ± 24	330
> 200	67 ± 7	8.7 ± 2.3	76 ± 8	87
> 300	20.7 ± 2.9	1.9 ± 1.0	22.6 ± 3.1	27
> 400	7.7 ± 1.5	1.2 ± 0.9	9.0 ± 1.7	9
> 500	2.9 ± 0.8	$0.32^{+0.41}_{-0.32}$	3.2 ± 0.9	4
> 600	0.9 ± 0.4	$0.0^{+0.2}_{-0.0}$	0.9 ± 0.4	1

Table 9.1: Expected and observed numbers of isolated same-sign lepton pairs in the $e^\pm e^\pm$, $e^\pm \mu^\pm$ and $\mu^\pm \mu^\pm$ channel for various cuts on the dilepton invariant mass, $m(\ell^\pm \ell^\pm)$. The uncertainties shown are the quadratic sum of the statistical and systematic uncertainties.

region. The fiducial region is a set of criteria one can apply to truth (generated) particles (i.e. particles directly produced and hadronised by for example Pythia) to emulate as closely as possible the analysis selection criteria on the reconstructed objects used in the analysis. The phase space constrained by these criteria is known as the *fiducial region*.

Definition of true fiducial region

First, all leptons (and all the particles used in the true isolation requirements described

$m(\ell\ell)$ [GeV]	e^+e^+ pairs		$e^+\mu^+$ pairs		$\mu^+\mu^+$ pairs	
	Total SM	Data	Total SM	Data	Total SM	Data
> 15	1120 ± 100	1124	1440 ± 130	1327	454 ± 32	502
> 100	610 ± 60	593	570 ± 50	523	184 ± 16	198
> 200	187 ± 22	167	146 ± 13	143	48 ± 6	62
> 300	61 ± 11	48	50 ± 5	56	15.3 ± 2.2	18
> 400	19 ± 6	18	18.4 ± 2.6	21	6.2 ± 1.2	6
> 500	9 ± 5	9	7.8 ± 1.4	8	2.6 ± 0.8	1
> 600	7 ± 5	5	4.8 ± 1.1	6	0.8 ± 0.4	0
$m(\ell\ell)$ [GeV]	e^-e^- pairs		$e^-\mu^-$ pairs		$\mu^-\mu^-$ pairs	
	Total SM	Data	Total SM	Data	Total SM	Data
> 15	940 ± 100	852	1140 ± 110	988	328 ± 23	341
> 100	440 ± 50	394	417 ± 40	336	117 ± 9	132
> 200	109 ± 16	98	119 ± 11	83	27.6 ± 2.8	25
> 300	29 ± 7	34.6	35 ± 4	29	7.3 ± 1.2	9
> 400	14 ± 5	12	12.1 ± 2.3	10	2.7 ± 0.7	3
> 500	5.0 ± 1.3	4	4.9 ± 1.5	5	$0.64^{+0.33}_{-0.26}$	3
> 600	2.7 ± 0.9	2	2.5 ± 1.0	3	$0.09^{+0.23}_{-0.09}$	1

Table 9.2: Expected and observed numbers of positively and negatively charged lepton pairs for various cuts on the dilepton invariant mass, $m(\ell\ell)$. The uncertainties shown are the quadratic sum of the statistical and systematic uncertainties.

later) are required to be prompt and stable. Then we have some simple kinematic cuts on the particles aiming to mimic the actual cuts used in the analysis as close as possible. These are summarised in Table. 9.3.

Selection	Electron requirement	Muon requirement
Leading lepton p_T	$p_T > 25 \text{ GeV}$	$p_T > 25 \text{ GeV}$
Subleading lepton p_T	$p_T > 20 \text{ GeV}$	$p_T > 20 \text{ GeV}$
Lepton η	$ \eta < 1.37$ or $1.52 < \eta < 2.47$	$ \eta < 2.5$
Isolation	$\sum p_T(\Delta R = 0.3)/p_T^e < 0.1$	$\sum p_T(\Delta R = 0.3)/p_T^\mu < 0.07$
Selection	Event selection	
Lepton pair	Same-sign pair with $m_{\ell\ell} > 15 \text{ GeV}$	
Electron pair	Veto pairs with $70 < m_{\ell\ell} < 110 \text{ GeV}$	
Event	No opposite-sign same-flavour pair with $ m_{\ell\ell} - m_Z < 10 \text{ GeV}$	

Table 9.3: Summary of requirements on generated leptons and lepton pairs in the fiducial region at particle level. More information on the calculation of the isolation p_T is given in the text.

Since both electrons and muons are required to be isolated in this analysis, we must also require isolated leptons in the true fiducial region. To do this, a true $ptcone$ and true $Etcone$ variables are defined. The track isolation $ptcone$ is the scalar sum of the p_T of stable charged particles with ($p_T > 1(0.4) \text{ GeV}$ and $|\eta| < 2.5 (2.47)$ for muon (electron)) within a cone of ΔR . The calorimeter isolation, $Etcone$ was defined similarly as the scalar sum of the E_T of stable particles (excluding neutrinos) within a cone of ΔR . Combinations of true $Etcone$ and $ptcone$ isolation were studied. It was found that true and reconstructed $Etcone$ distributions are generally very different because the reconstructed calorimeter isolation is affected by noise. Therefore only $ptcone$ isolation criteria with threshold equal to those used at reconstruction level are imposed on the true electrons and muons. An isolation cut is crucial since it reduces the background contamination from *busy* (that is models with many final state particles, particularly jets) models such as fourth-generation quarks and allows us to select leptons in a more model independent manor. The true $ptcone$ variable is made by summing the p_T of tracks from true particles within a cone of size $\Delta R = 0.3$.

Fiducial Efficiencies

Now that we have defined our true fiducial region we can calculate the *fiducial efficiency*; that is the efficiency, ϵ_f , for a dilepton pair from our true fiducial region (n_f) to pass all the analysis selection cuts (n_s):

$$\epsilon_f = \frac{n_s}{n_f} \quad (9.1)$$

Conversely is the concept of leakage; that is the number of lepton pairs which are in our true fiducial region whom fail the selection cuts. Now ideally we wish for no leakage and full fiducial efficiency. But in reality not all cuts are perfect in efficiency and as we

have tried to be as inclusive as possible we have tried to accommodate all models with wide ranging event topologies. We therefore cannot be completely efficient. So in reality one wants to have a stable and similar fiducial efficiency for a wide range of different models whilst having a very small leakage. For our analysis we used four very different models and calculated their efficiencies and leakages:

- Doubly Charged Higgs. A range of potential masses were explored ranging from 100 -1000 GeV. These models produce pairs of doubly charged Higgs which each decay to two same-sign leptons. These samples represent topologies with little activity outside the isolated leptons.
- Diquarks produced in the Zee-Babu model - leads to a same-sign leptons plus two jets in the final state. These models have slightly more involved final state topologies due to the presence of the two jets. Here we consider diquark masses between 2.5-3.5 TeV and leptoquark masses between 1-1.4 TeV.
- Heavy Majorana Neutrino - This leads to a final state with missing energy, a jet and well isolated leptons. This model was considered for a range of Majorana neutrino masses and W_R propagators, the final state is a fairly typical one but we can test a large range of transverse muon momenta. Here we consider W_R masses between 1 TeV and 2 TeV as well as N_R masses between 250 GeV and 1.5 TeV.
- Fourth-generation down-type chiral quarks - Here we have t and b semi-leptonic decays, hence plenty of heavy flavour jets and isolated leptons. This is the most busy event topology that we consider and the one which is perhaps most prone to fake leptons. Again a variety of different masses are considered for the decaying fourth generation $m_{b\tau}$. The masses range from 400 GeV to 1 TeV.

In the end in order to be most conservative we choose the lowest fiducial efficiency in each channel in order to calculate the final fiducial cross-sections. These were found to be 48%, 50% and 56% in the $e^\pm e^\pm$, $e^\pm \mu^\pm$ and $\mu^\pm \mu^\pm$ channels respectively. The fiducial efficiencies were also calculated for the charge separated pairs but no significant difference from the charge combined pairs was seen. Tables A.10 - A.15 in the appendix show the fiducial efficiency for the entire range of models considered.

Model Dependencies in the Fiducial Efficiency

We found that for different mass-points and for different models the fiducial efficiency varied but was for the most part stable, and the leakage was small. The fiducial efficiencies vary between 46% and 75% with roughly similar values for the different ee , $e\mu$ and $\mu\mu$ final states. Hence it was seen that our selection cuts were doing a reasonable job of being model independent whilst selecting true lepton pairs efficiently. We investigated the cause of the differences in the fiducial efficiencies of different models and we saw that the differences were mainly caused by the differences in the transverse momenta of the leptons produced in decays and the busyness of the final state event topology. In the case of electrons, the electron identification efficiency varies about 15% over the relevant p_T range [65]. In the

case of muons, the higher the invariant mass of the decaying particle the more boosted^I the muons were and hence the more central in our detector. Now, particularly for muons, the detector acceptance at central η is very poor in the sense there is very little to no detector there. Hence the reconstruction efficiency is poor which leads to poor fiducial efficiencies particularly for the models with very boosted and high p_T muons. The affect of detector acceptance can be seen in Figure. 9.5. A further affect on top of this (being a sub effect) is how isolated different models (or how busy) are. For instance the doubly charged Higgs decay are very well isolated and clean, whereas the fourth-gen down type decays are much less isolated and have many messy decays. Since in the truth we could only incorporate a track isolation (no calorimeter isolation) we see some differences due to the isolation of different models. In Figure 9.5 the η distributions for muons for both truth and reco are shown as well as the differences between a few of the models. This displays clearly the differences for muons due to the detector acceptances as a function of the model and more importantly the invariant mass of the decaying particle

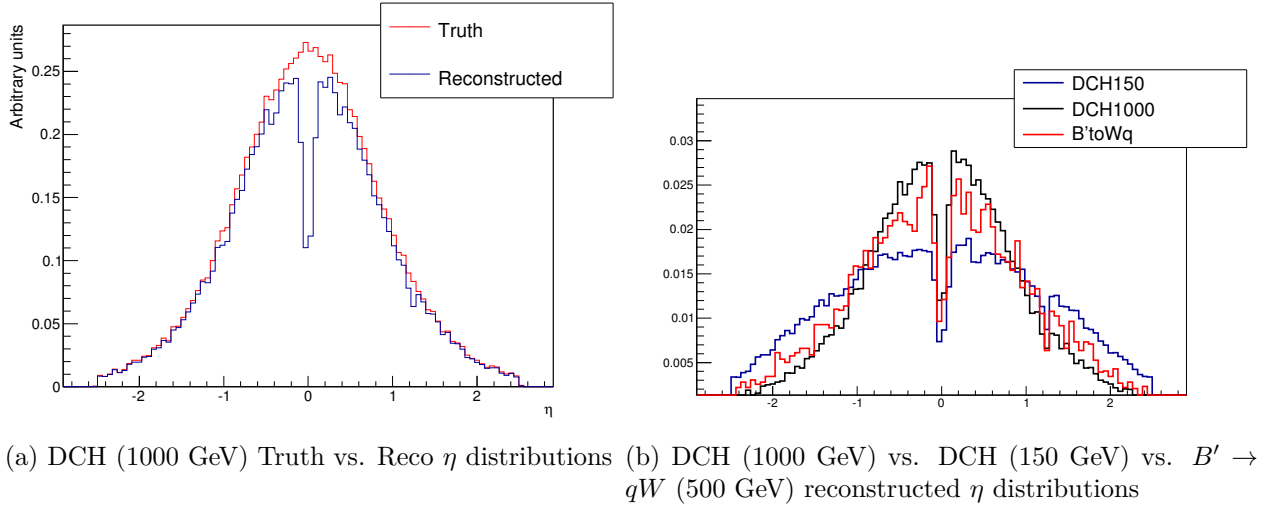


Figure 9.5: Distribution of the η for truth (red) and reconstructed (blue) muons in Doubly Charged Higgs (DCH) $m(H) = 1000$ GeV events; comparison of the reconstructed muon η distribution for DCH $m(H) = 1000$ GeV (black), DCH $m(H) = 150$ GeV (blue) and $B' \rightarrow qW$ $m = 500$ GeV (red)

Fiducial Cross-Section Limits

Finally we can convert the fiducial efficiencies and number of pairs observed into fiducial cross-sections. First we calculate the upper limit on the number of expected pairs which come from non-SM sources. Then based on the 2σ upper limit on the number of lepton

^IA particle is said to be *boosted* if it is of sufficiently high energy

pairs, N_{95} , and the fiducial efficiency, we find:

$$\sigma_{95}^{fid}(ll) = \frac{N_{95}}{\epsilon_f \int \mathcal{L} dt} \quad (9.2)$$

where $\int \mathcal{L} dt$ is the integrated luminosity of the data sample. Finally to move from the fiducial cross-section to the real cross-section one needs to know the average number of pairs per event (R_{pair}) and the fiducial acceptance, A . This is the ratio of the number of pairs which pass the fiducial cuts and the number of pairs generated.

$$\sigma = \frac{\sigma_{95}^{fid}}{R_{pair} A} \quad (9.3)$$

Thus using Eq. (9.3) one can set a limit on any model decaying to same-sign dilepton pairs in the final state. A theorist would need to simply calculate R_{pair} and the fiducial acceptance for their specific model (using our fiducial definition given above) then one could calculate the cross-section, σ , for their model. Implicitly a theorist would need to utilise the fiducial efficiencies used in this analysis (and given above) to calculate the cross-section. As we have argued, since we are an inclusive analysis, this will be a conservative limit due to the fact that we use the lowest fiducial efficiency obtained of all the models evaluated.

The CL_s limit setting

Now we have all we need to calculate the fiducial cross-sections, now using the RooStats framework provided by the ATLAS Statistics Committee [102] [103] one can set limits on *new physics*. For this analysis we adopted the somewhat standard ATLAS procedure for limit setting, that is to say so called CL_s method [102]. This is a very detailed statistical procedure whose details are outside the scope of this thesis. The CL_s method is sometimes known as the modified frequentist confidence limit. It is the ratio of CL_{s+b} , which is the probability for finding the observed data given an expected background plus signal, and CL_b which is the probability for finding the observed data based solely on the expected background.

$$CL_s = \frac{CL_{s+b}}{CL_b} \quad (9.4)$$

The probabilities in the ratio are Poisson distributed and calculated based on the total number of observed and expected lepton pairs in each channel for all of the analysis search regions. The systematic uncertainties on the expected number of lepton pairs (for signal and SM background) are folded into the likelihoods as nuisance parameters with a Gaussian distribution.

For a counting experiment such as this, a simple Poisson distribution is used:

$$P(k|\lambda) = \frac{e^{-\lambda} \lambda^k}{k!} \quad (9.5)$$

Here k is the (observed) number of events and λ is the (expected) mean of the distribution. This poissonian distribution can then be written as a likelihood for a given number of signal

and background events:

$$L(N|\mu) = P(N|\mu \cdot s + b) \quad (9.6)$$

where N is the number of events, and s and b are the number of expected signal and background events respectively. The signal strength, μ , parametrises the strength of a given signal model. In order to take into account systematic uncertainties on s and b , the likelihood needs to be written as:

$$L(N, \Theta|\mu, \theta) = \text{Poi}ss(N|\mu \cdot s \cdot \nu_s(\theta) + b \cdot \nu_b(\theta)) \cdot G(\theta; \Theta, 1) \quad (9.7)$$

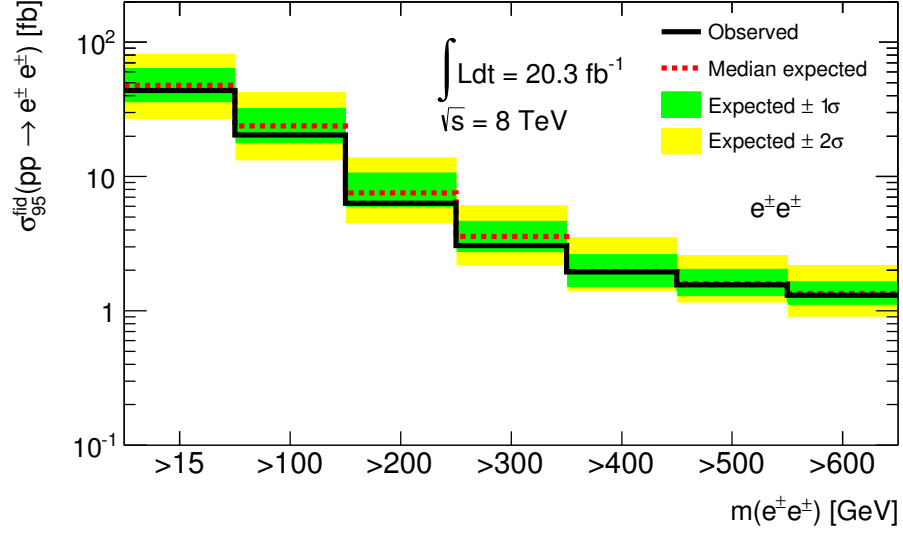
Where here we have introduced the systematic uncertainties as *nuisance parameters* in a vector θ . That is to say we introduce a product of Gaussians G (one for each systematic) with mean(s) Θ and width one, as parameters. Θ is the a vector of *auxiliary measurements* or *global variables* which are measured in order to constrain the systematic uncertainties. For instance, in a separate measurement one can measure the uncertainty on the electron identification scale factors and use this as a *global variable* in order to constrain the value of θ , the nuisance parameter. ν_s and ν_b are sometimes called *response functions*. They basically relate the systematic (based on θ) to the number of expected signal (s) and background (b) events. Now we have a likelihood for the number of expected events based on the expected background and signal as well as their systematics. Here the likelihood for observing N events and measuring the global variables, Θ given some parameters of interest μ and nuisance parameters θ is shown in Eq. (9.7).

The unmodified frequentist confidence intervals should nominally cover the stated value. This means that a 95% confidence level upper limit should cover the *true* value of the cross-section in 95% of the cases, which conversely means that in 5% of the cases the limit will not cover the true value. Therefore, if there is no signal present, 5% of the cases we would be excluding a signal model when we should not be. This does not sit well with the experimentalists whom are very aware that we are not sensitive to arbitrarily small signals. It was for this very reason that the CL_s method was designed, in order to combat this weakness in the standard limit setting procedure. The CL_s by construction over-covers which means that the interval created covers the true value more than the stated level. The coverage for small values of the cross-section approaches 100% whilst the coverage at larger values converge to its nominal level.

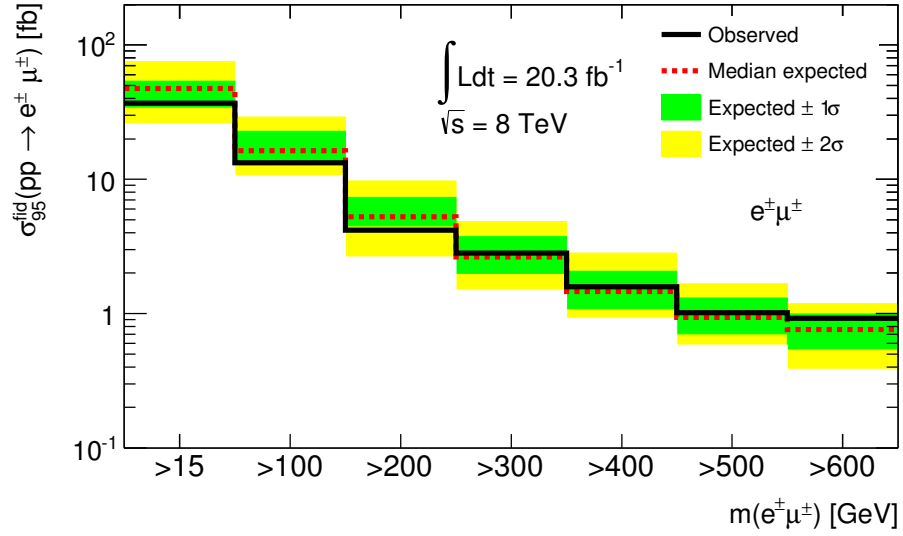
9.1.1 Limit Plots

The final numbers for the fiducial cross-section limits are shown in Table. 9.4 and displayed in Fig 9.6. The cross section limits vary between 0.4 fb and 50 fb depending on the mass cut and the final state for the inclusive analysis. Limits obtained for $\ell^+\ell^+$ and $\ell^-\ell^-$ pairs are also shown in Table. 9.4 and range between 0.3 fb to 27 fb. For all final states the observed limits are generally within 2σ of the expected limits, which are obtained using simulated pseudo-experiments using only SM processes. The limits were also placed on

the charge separated fiducial cross-section for non-SM physics^{II}. These are shown also in Table. 9.4.



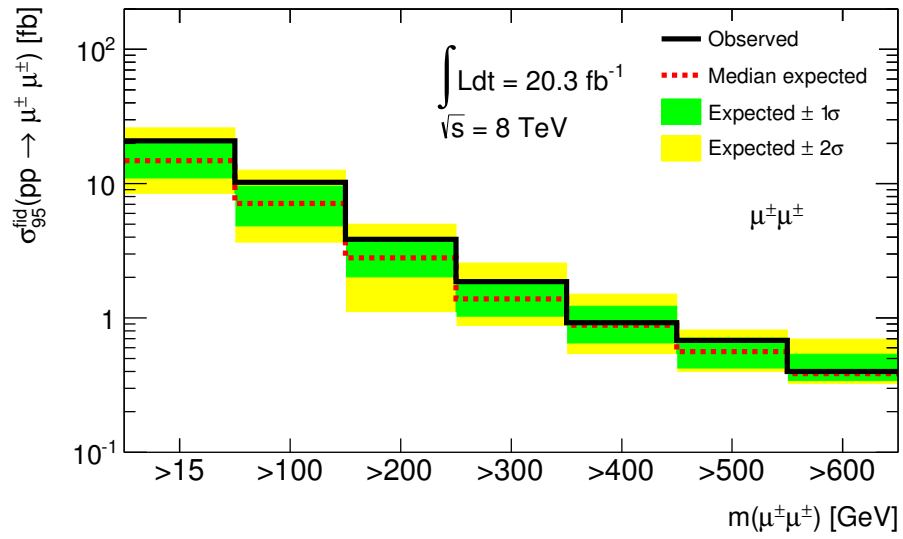
(a)



(b)

Figure 9.6: continues on following page...

^{II}In terms of limit setting procedures the charged separated regions are treated as entirely separate from the charge combined limits



(c)

Figure 9.6: 95% CL upper limits on the fiducial cross section for new physics signal contributing to the fiducial region of (a) $e^\pm e^\pm$, (b) $e^\pm\mu^\pm$, and (c) $\mu^\pm\mu^\pm$ pairs. The green and yellow bands show the 1σ and 2σ bands on the expected limits. The variation from bin to bin in the expected limits is due to fluctuations in the background yields derived from small MC samples.

Mass range	95% CL_s upper limit [fb]					
	$e^\pm e^\pm$		$e^\pm \mu^\pm$		$\mu^\pm \mu^\pm$	
	expected	observed	expected	observed	expected	observed
> 15 GeV	49^{+16}_{-13}	43	47^{+6}_{-13}	36	15^{+5}_{-4}	21
> 100 GeV	24^{+8}_{-6}	20	$15.8^{+6.3}_{-2.3}$	13.3	$7.1^{+2.5}_{-2.3}$	10.2
> 200 GeV	$7.8^{+2.6}_{-2.1}$	6.5	$5.3^{+2.1}_{-0.7}$	4.3	$2.8^{+1.0}_{-0.8}$	3.8
> 300 GeV	$3.7^{+0.8}_{-1.0}$	3.3	$2.5^{+1.2}_{-0.4}$	2.7	$1.4^{+0.5}_{-0.4}$	1.9
> 400 GeV	$1.9^{+0.7}_{-0.5}$	1.9	$1.48^{+0.61}_{-0.23}$	1.60	$0.88^{+0.35}_{-0.23}$	0.92
> 500 GeV	$1.63^{+0.43}_{-0.27}$	1.61	$0.9^{+0.41}_{-0.25}$	0.99	$0.56^{+0.14}_{-0.14}$	0.68
> 600 GeV	$1.32^{+0.43}_{-0.21}$	1.25	$0.78^{+0.23}_{-0.19}$	0.94	$0.348^{+0.101}_{-0.014}$	0.420

Mass range	$e^+ e^+$		$e^+ \mu^+$		$\mu^+ \mu^+$	
	expected	observed	expected	observed	expected	observed
> 15 GeV	23^{+9}_{-7}	19	25^{+10}_{-4}	23	$9.5^{+3.3}_{-3.1}$	14
> 100 GeV	11^{+4}_{-3}	9	$10^{+4}_{-1.5}$	9	$5.0^{+1.6}_{-1.3}$	6.3
> 200 GeV	$3.9^{+1.4}_{-0.9}$	3.6	$3.7^{+1.2}_{-0.8}$	3.6	$2.2^{+0.8}_{-0.5}$	3.6
> 300 GeV	$2.1^{+0.7}_{-0.5}$	2.5	$2.0^{+0.9}_{-0.6}$	2.6	$1.11^{+0.46}_{-0.29}$	1.42
> 400 GeV	$1.55^{+0.44}_{-0.34}$	1.42	$1.12^{+0.44}_{-0.27}$	1.42	$0.74^{+0.27}_{-0.17}$	0.74
> 500 GeV	$0.67^{+0.27}_{-0.16}$	0.61	$0.82^{+0.17}_{-0.20}$	0.90	$0.42^{+0.24}_{-0.10}$	0.38
> 600 GeV	$0.54^{+0.22}_{-0.14}$	0.58	$0.65^{+0.10}_{-0.13}$	0.71	$0.340^{+0.058}_{-0.008}$	0.338

Mass range	$e^- e^-$		$e^- \mu^-$		$\mu^- \mu^-$	
	expected	observed	expected	observed	expected	observed
> 15 GeV	27^{+10}_{-7}	28	$19.0^{+7.3}_{-2.6}$	15.4	$6.8^{+2.7}_{-1.5}$	8.3
> 100 GeV	$14.5^{+3.1}_{-4.0}$	14.0	$7.7^{+2.1}_{-1.7}$	4.9	$3.5^{+1.4}_{-0.9}$	5.1
> 200 GeV	$5.5^{+2.1}_{-0.9}$	4.6	$2.9^{+1.0}_{-0.5}$	1.6	$1.41^{+0.54}_{-0.33}$	1.29
> 300 GeV	$2.5^{+0.9}_{-0.7}$	2.0	$1.5^{+0.6}_{-0.5}$	1.2	$0.79^{+0.30}_{-0.16}$	1.0
> 400 GeV	$1.57^{+0.49}_{-0.30}$	1.66	$0.91^{+0.29}_{-0.21}$	0.79	$0.52^{+0.20}_{-0.01}$	0.59
> 500 GeV	$1.48^{+0.32}_{-0.42}$	1.56	$0.60^{+0.14}_{-0.12}$	0.63	$0.385^{+0.045}_{-0.008}$	0.681
> 600 GeV	$1.31^{+0.25}_{-0.33}$	1.12	$0.51^{+0.14}_{-0.09}$	0.59	$0.410^{+0.059}_{-0.024}$	0.538

Table 9.4: Upper limit at 95% CL_s on the fiducial cross section for $\ell^\pm \ell^\pm$ pairs from non-SM signals. The expected limits and their 1σ uncertainties are given together with the observed limits as found in the data. Limits are given separately for the $e^\pm e^\pm$, $e^\pm \mu^\pm$ and $\mu^\pm \mu^\pm$ channel inclusively and separated by charge.

9.1.2 Comparison to 7 TeV results

For comparison I have included the signal region and limit plots we obtained during the 7 TeV analysis I was also a large part involved with. The signal region mass distributions are shown in Fig. 9.7 and the fiducial cross-sections on new physics are displayed in Fig. 9.8. These plots are the corresponding plots to Fig. 9.2 and Fig. 9.6 respectively. They are perhaps a little hard to compare directly due to their different formats. Nevertheless one can manifestly see the great gain in events observed (statistics) from 7 TeV to 8 GeV. The higher energy analysis also allowed us to probe to much higher masses, allowing us to set limits up to 600 GeV compared to the 400 GeV in the 7 TeV analysis. Additionally to these changes, the largest changes as discussed previously, were that the errors on charge-flip misidentification and non-prompt backgrounds are reduced, predominantly as a result of having higher statistic but also since the systematic errors are improved. Furthermore, the prompt background (particularly in the $\mu\mu$ channel) is reduced by requiring the veto on events with a Z candidate, which allows for more powerful limits.

One cannot directly compare the limit plots in Fig. 9.6 and Fig. 9.8 because the fiducial efficiencies and acceptances used to calculate the fiducial cross-sections are different in both analyses. However, as i have pointed out the 8 TeV can set limits to a higher mass, which can be seen as a great improvement.

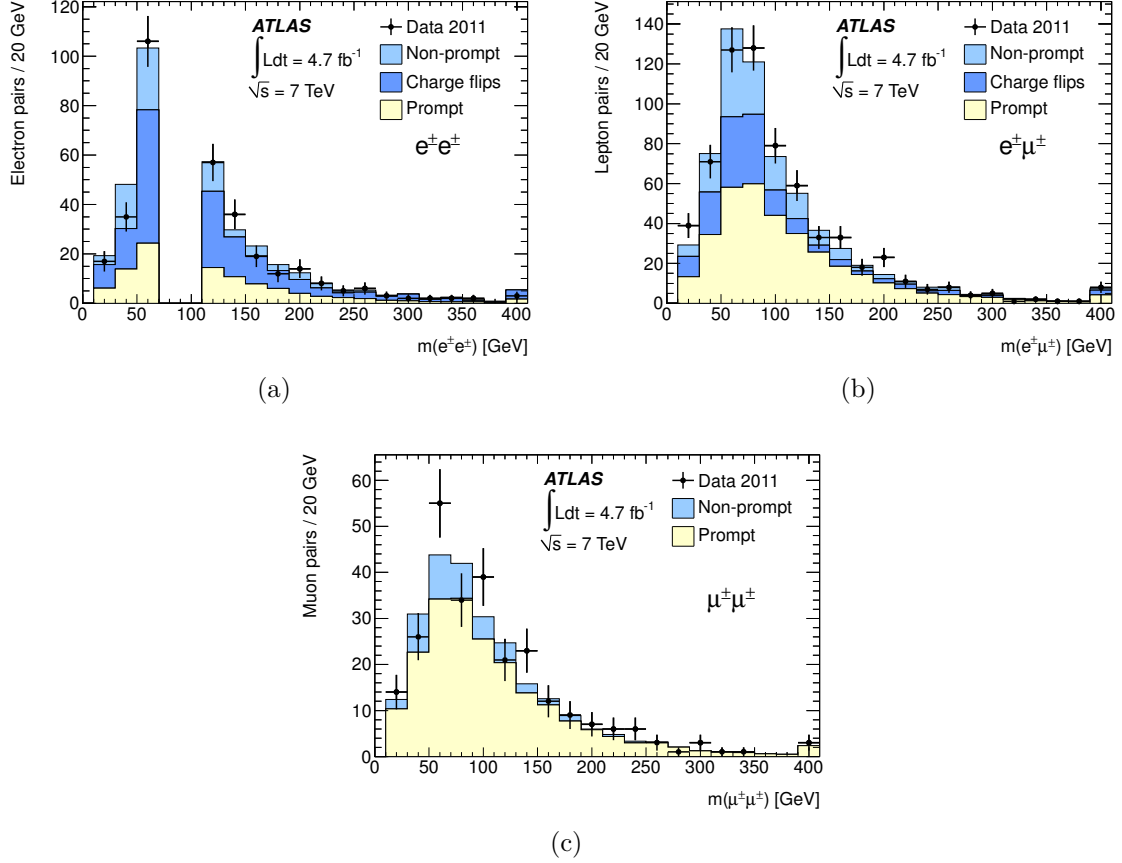


Figure 9.7: Invariant mass distributions for (a) $e^\pm e^\pm$, (b) $e^\pm \mu^\pm$, and (c) $\mu^\pm \mu^\pm$ pairs passing the full event selection. The data are shown as closed circles. The stacked histograms represent the backgrounds composed of pairs of prompt leptons from SM processes, pairs with at least one non-prompt lepton, and for the electron channels, backgrounds arising from charge misidentification and photon conversions. Pairs in the ee channel with invariant masses between 70 GeV and 110 GeV are excluded because of the large background from charge misidentification in $Z \rightarrow e^\pm e^\mp$ decays. The last bin is an overflow bin.

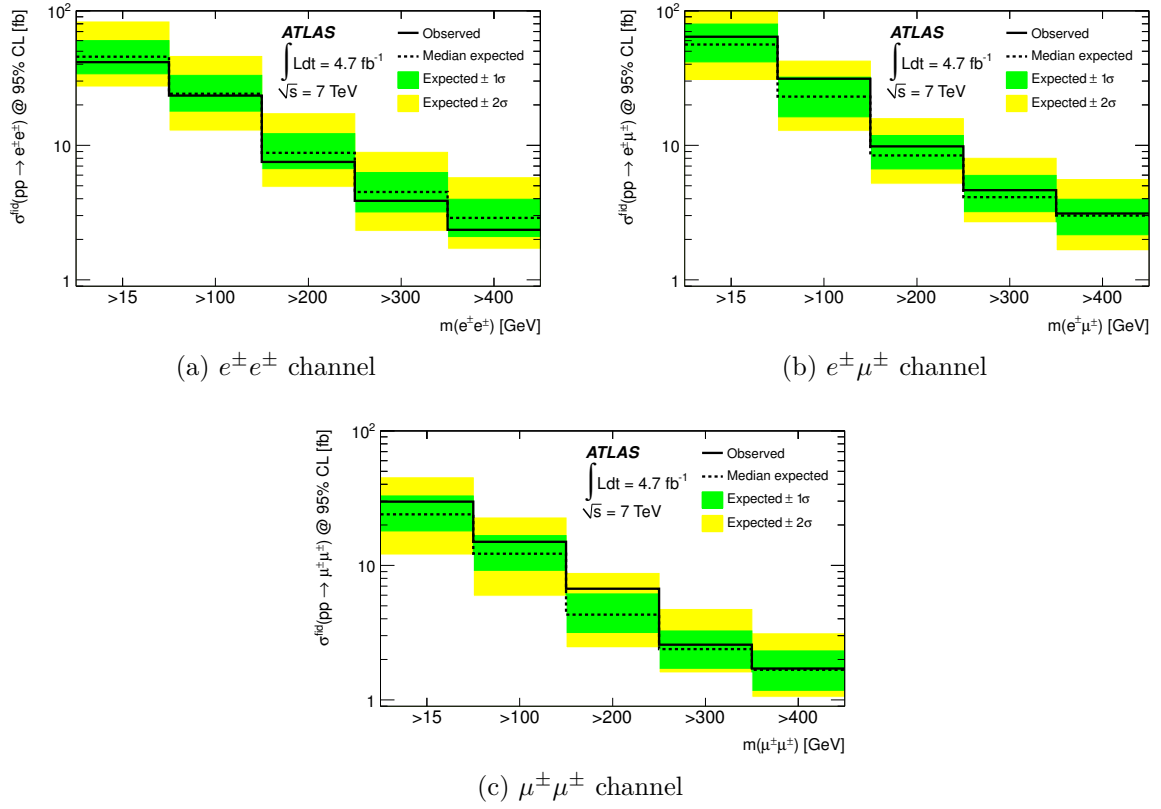


Figure 9.8: 95% C.L. upper limits on the fiducial cross section for new physics contributing to the fiducial region for (a) $e^\pm e^\pm$, (b) $e^\pm \mu^\pm$, and (c) $\mu^\pm \mu^\pm$ pairs.

*Heard melodies are sweet, but
those unheard, are sweeter*

John Keats

10

Same Sign: Doubly Charged Higgs Interpretation

Having wrapped up the inclusive search it was decided to choose a specific BSM model and use it as a benchmark model for our analysis and what could be done with our SS inclusive search. The Doubly Charged Higgs (DCH) model was chosen as our benchmark because of its clean signal and because it required no additional cuts on jets or missing energy, so it required minimal extension from our regular analysis. Furthermore, with the recent discovery of the Higgs there has been large theoretical interest in exotic Higgs models such as these, and no other analysis group within ATLAS was searching for this signal. This extension meant using the exact same dataset with the exact same cuts but this time instead of inclusive bins, because the resonance is narrow, we used a narrow bin search, colloquially known as bump-hunting.¹

For $H^{\pm\pm}$ we generated several mass points with various cross-sections. We considered only the case where the DCH decays leptonically, thereby making some assumptions on the branching ratio. We shall return to these assumptions later. The intrinsic resonance peak for the decaying $H^{\pm\pm}$ is narrow with respect to the mass range of our analysis, hence the reconstructed peak width is dominated by the detector resolution. It is known in ATLAS that the detector resolution for high momentum electrons is better than for muons and hence the reconstructed peak in the dimuon channel is broadest of the three channels. Due to the fact that the DCH could have a whole range of masses it was decided to compare the number of expected and observed pairs in a range of different mass bins. The idea is that each mass bin should contain the majority of any potential DCH resonance if its mass

¹Note:As will be explained we re-optimised the search with better efficiencies specialised for the narrow mass bins. We could have used the same fiducial efficiency as measured for DCH in the inclusive search, but we had much coarser binning (mass bins every 100 GeV) and hence we would have a worse limit.

was at the bins centre. Similarly as the end of the previous chapter i will attach the 7 TeV analysis results on the end of this section and compare that two.

10.0.3 Mass binning

The invariant mass-bins used for the DCH search depend on the $H^{\pm\pm}$ mass and detector resolution for electrons and muons. We wish to maximise the sensitivity of our analysis. This was achieved by calculating for various bin sizes what the significance of a potential signal would be if the signal was at the mass bin centre. The significance was defined as:

$$Sig = \sqrt{2((s+B)\ln(1+s/B) - s)} \quad (10.1)$$

Where s is the expected signal and $B = b + \delta b^2$ is the expected background plus the expected systematic squared. By maximising the significance we can ensure best sensitivity for our analysis. I evaluated this for the muon channel and found that a bin size of $\pm(0.06 \cdot m(H^{\pm\pm}) + 0.00015 \cdot m(H^{\pm\pm})^2)$ on the mass point $m(H^{\pm\pm})$ was optimal. This relation effectively increases the bin size as the mass of the DCH increases and the detector resolution on the muons gets worse. This is clearly seen by the broadening of the resonance peaks in Fig. 10.1.

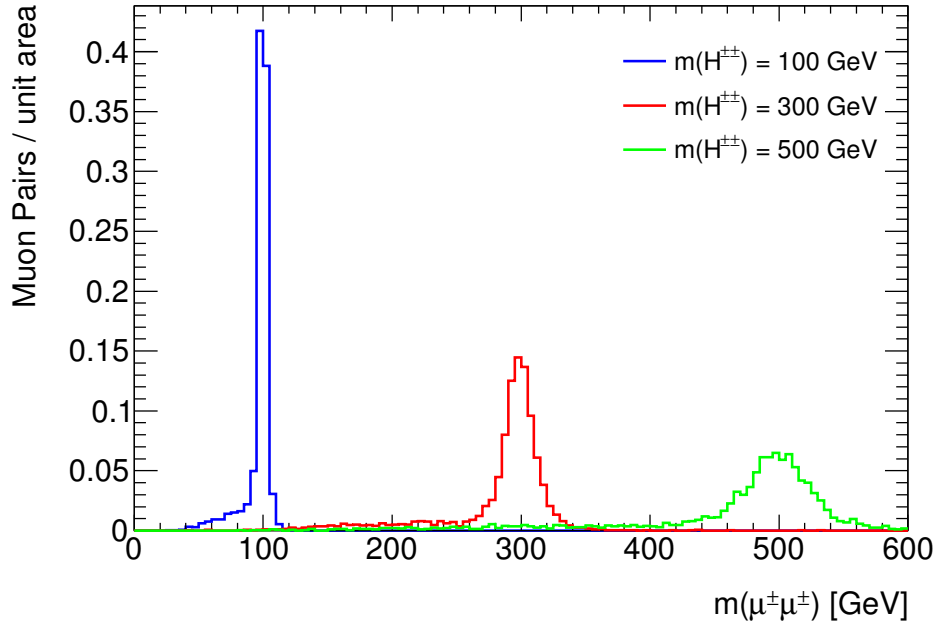


Figure 10.1: The number of reconstructed lepton pairs normalised to unity for three different mass points from Doubly Charged Higgs decays.

The only other thing to consider is to have smooth limit. We do not want to have too many mass bins as this limits statistics in those bins and means the limits made (such as

in Fig. 10.3) would be very *zigg-zaggy* and unsmooth. Furthermore if one uses a piece-wise binning function one can incur strange jumps in the limit plots which are unphysical. For these reasons some of the binning was modified in the ee channel and a continuous binning function was used for $\mu\mu$ as opposed to a piece-wise function for the 7 TeV analysis.

10.0.4 Total Efficiency

Once the mass binning had been optimised the *total efficiency* could then be calculated. In essence what we wish to know is what percentage of doubly-charged Higgs bosons produced will be reconstructed and selected by our cuts and fall inside the mass bins we created as a fraction of all those generated in the MC. This is defined as acceptance times efficiency, or total efficiency ϵ_{total} . The total efficiency, is effectively the number of reconstructed lepton pairs passing the full analysis selection and falling into the appropriate mass bin divided by the number of true simulated $H^{\pm\pm} \rightarrow l^{\pm}l^{\pm}$ decays to the lepton flavour pair of interest.

The total efficiency times acceptance was calculated in each channel for all the mass points available to us. In order to interpolate between the mass points it was then fitted with a piecewise function. The form of the fitted functions are described in Tables 10.1, 10.2 and 10.3 and by equations (10.2), (10.3) and (10.4) for the ee , $e\mu$ and $\mu\mu$ channels respectively. The total efficiency curves as derived from DCH MC can be seen in Fig. 10.2.

$$\epsilon_{tot}(m) = \begin{cases} p_0(1 - e^{-(m-p_1)/p_2}), & \text{if } m < 450 \text{ GeV} \\ p_3 - p_4m, & \text{if } m \geq 450 \text{ GeV} \end{cases} \quad (10.2)$$

Parameter	Value
p_0	$4.89 \cdot 10^{-1}$
p_1	$2.99 \cdot 10^{+1}$
p_2	$1.03 \cdot 10^{+2}$
p_3	$4.64 \cdot 10^{-1}$
p_4	set by requiring continuity

Table 10.1: Fitted parameter values for equation (10.2), which gives $\epsilon_{tot}(m)$ for the ee channel

$$\epsilon_{tot}(m) = \begin{cases} p_0(1 - e^{-(m-p_1)/p_2}), & \text{if } m < 300 \text{ GeV} \\ p_3 + p_4m, & \text{if } m \geq 300 \text{ GeV} \end{cases} \quad (10.3)$$

$$\epsilon_{tot}(m) = \begin{cases} p_0(1 - e^{-(m-p_1)/p_2}), & \text{if } m < 300 \text{ GeV} \\ p_3 - p_4m, & \text{if } m \geq 300 \text{ GeV} \end{cases} \quad (10.4)$$

Parameter	Value
p_0	$5.09 \cdot 10^{-1}$
p_1	$3.09 \cdot 10^{+1}$
p_2	$7.61 \cdot 10^{+1}$
p_3	$4.91 \cdot 10^{-1}$
p_4	set by requiring continuity

Table 10.2: Fitted parameter values for equation (10.3), which gives $\epsilon_{tot}(m)$ for the $e^\pm \mu^\pm$ channel

Parameter	Value
p_0	$4.98 \cdot 10^{-1}$
p_1	$3.00 \cdot 10^{+1}$
p_2	$5.03 \cdot 10^{+1}$
p_3	$5.10 \cdot 10^{-1}$
p_4	set by requiring continuity

Table 10.3: Fitted parameter values for equation (10.4), which gives $\epsilon_{tot}(m)$ for the $\mu^\pm \mu^\pm$ channel

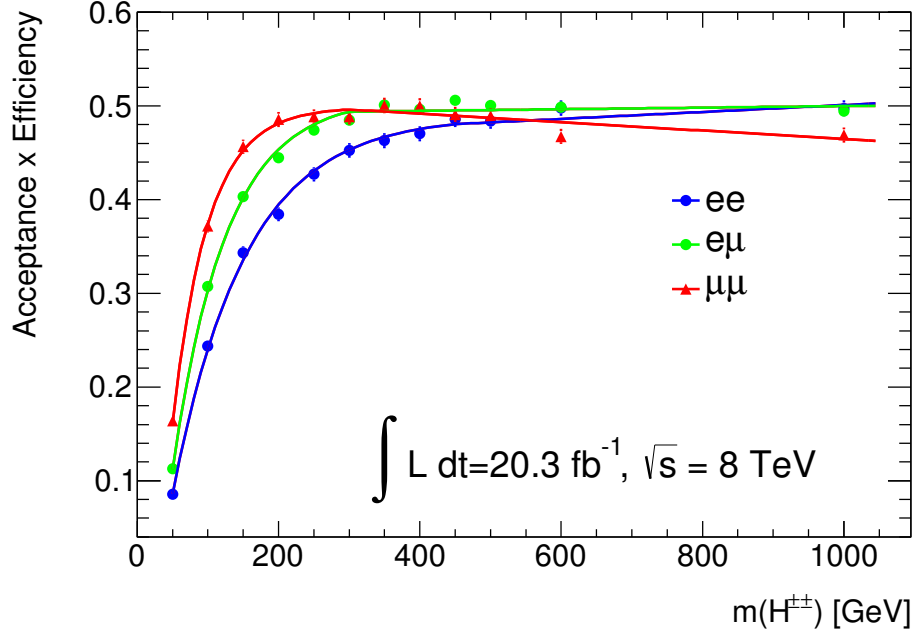


Figure 10.2: Total acceptance times efficiency ($A \cdot \epsilon$) vs simulated $H^{\pm\pm}$ mass for the three channels. These points are fitted with piecewise empirical functions described in the text.

10.0.5 Signal Systematics

Clearly there is some error on the number of signal events predicted in each mass bin. The standard errors on all MC systematics which were summarised in Section. 8 apply here on the signal too. However here an additional uncertainty is needed and this is the uncertainty on the parton distribution function which translates into an uncertainty on the signal acceptance.

The fully simulated $H^{\pm\pm}$ samples are generated with the leading-order PDF set MSTW2008. Using this PDF set we wish to evaluate the uncertainty on the acceptance. We utilise the ratio of the acceptance found with the central PDF with respect to the other 40 sets which vary various parameters in the PDF to evaluate an uncertainty. This uncertainty is evaluated using the prescription from Ref. [104]. The uncertainty on the acceptance was seen to be small, and is evaluated so:

$$\sigma_{PDF}^+ = \sqrt{\sum_{i=1}^{20} [\max(A_i^+ - A_0, A_i^- - A_0, 0)]^2} \quad (10.5)$$

$$\sigma_{PDF}^- = \sqrt{\sum_{i=1}^{20} [\max(A_0 - A_i^+, A_0 - A_i^-, 0)]^2} \quad (10.6)$$

where A_i^\pm is the acceptance evaluated for the positively or negatively varied PDF set and A_0 is the central acceptance. This uncertainty was evaluated for a series of mass points

and seen to vary between 0.4% and 0.5%. A flat 0.5% was chosen to be conservative and used for all channels and mass ranges.

There is of course some inherent uncertainty on the theoretical cross-section for this model. However it is ATLAS policy to include uncertainty on acceptance times efficiency but not the theory uncertainty on the signal. Having said that the k-factor on the cross-section is 1.3 which means the difference between NNLO and NLO is roughly 10% (just to give a qualitative idea).

10.0.6 Setting the Limits on the Doubly Charged Higgs Boson Production Cross-section

Since no significant discrepancy from the SM was observed we aimed to set limits on the production cross section of $H^{\pm\pm}H^{\mp\mp}$. In our analysis we count the number of lepton pairs; the doubly charged Higgses are produced in pairs, hence we expect two pairs per event which can contribute. Therefore we need to convert from number of pairs of leptons to a cross-section.

$$\sigma_{HH} = \frac{N_{HH}}{\int \mathcal{L} dt} \quad (10.7)$$

Where N_{HH} is the true number of events containing a **pair** of DCH bosons. This is then related to the number of DCH bosons decaying to a certain channel (say $\mu\mu$) with a particular branching-ratio (BR): $N_H = 2 \times BR \times N_{HH}$, giving:

$$\sigma_{HH} \times BR = \frac{N_H}{2 \times \int \mathcal{L} dt} \quad (10.8)$$

But we do not know the true number of DCH bosons, N_H , produced by the collision. What we do measure is the number of reconstructed DCH bosons, N_H^{reco} which are detected. The two are related by $N_H^{reco} = N_H \times A \times \epsilon$, leading to:

$$\sigma_{HH} \times BR = \frac{N_H^{reco}}{2 \times A \times \epsilon \times \int \mathcal{L} dt} \quad (10.9)$$

Since we do not know the branching ratios for the DCH decays it makes most sense to express the limits in terms of cross-section times branching ratio as in Eq. (10.9). So now, going from the observed and expected number of lepton pairs per mass-bin we can set limits on the cross-section times branching ratio at a 95% confidence level in accordance to the CL_s method using the RooStats framework provided by the ATLAS statistics Committee [102, 105]. In order to do so one needs to make an assumption on the branching ratios to the various final states, here a BR of 100% is assumed for each channel. This results in the strongest limits on the DCH mass since if the BR were 100% it would give the highest theoretical prediction. The theoretical curves and limits on the production cross-section are given in figure. 10.3.

By looking where the theoretical cross-section curves for left and right handed doubly charge Higgs cross the observed (solid black line) cross-section limits one can predict the

lower limits for the mass of the left and right handed DCH's^{II}. The lower mass limits for the left-handed Higgs bosons varies between 470 and 550 GeV depending on the channel, the best being the ee channel. Similarly the limits range from 370 and 440 GeV for the right handed Higgs, with the $\mu\mu$ channel giving the best limits. The lower limits for left handed and right handed doubly charge Higgs' are included in Table. 10.4. These results are an improvement of about 30-40% compared with the 2011 data [106].

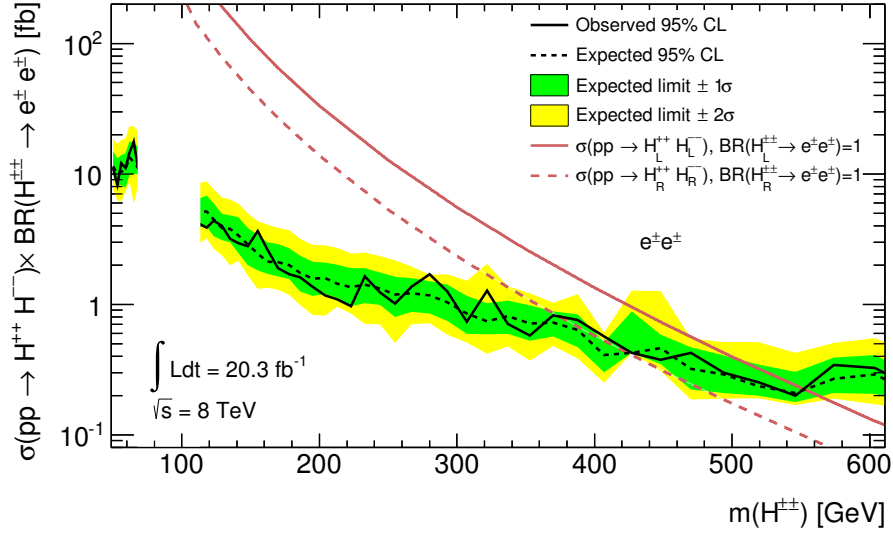
Signal	95% CL upper limit [GeV]					
	$e^\pm e^\pm$		$e^\pm \mu^\pm$		$\mu^\pm \mu^\pm$	
	expected	observed	expected	observed	expected	observed
$H_L^{\pm\pm}$	553 ± 30	551	487 ± 41	468	543 ± 40	516
$H_R^{\pm\pm}$	425 ± 30	374	396 ± 34	402	435 ± 33	438

Table 10.4: Lower limits at 95% CL on the mass of $H_L^{\pm\pm}$ and $H_R^{\pm\pm}$ bosons, assuming a 100% branching fraction to $e^\pm e^\pm$, $e^\pm \mu^\pm$ and $\mu^\pm \mu^\pm$ pairs. The 1σ uncertainties are also shown for the expected limits, they are symmetrised to reduce the effect from bin by bin fluctuations.

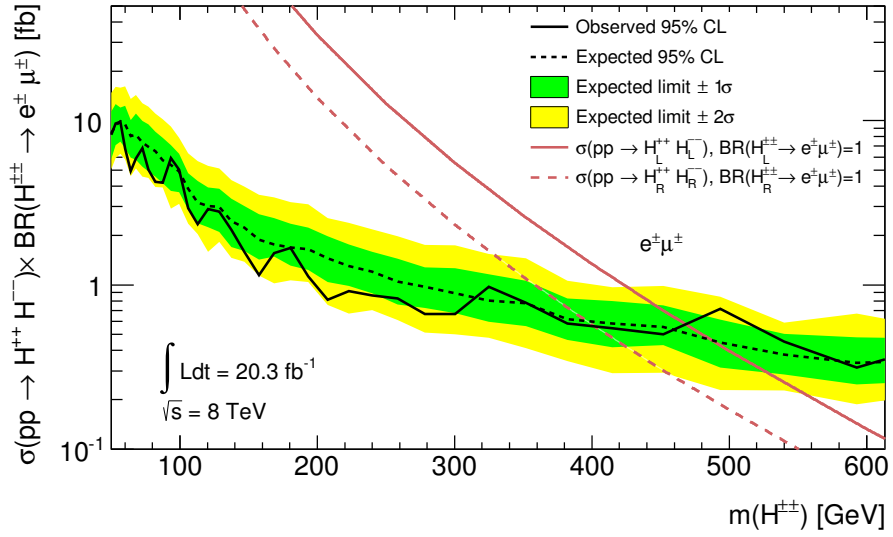
Doubly charged Higgs branching ratio versus invariant mass

The above limits (Fig. 10.3) can then be interpreted as limits on the branching fraction of $H^{\pm\pm} \rightarrow l^\pm l^\pm$ versus its mass. These are shown in Fig. 10.4. From figure. 10.4 it is clear that we can exclude the DCH models to higher masses the larger the branching ratio we assume. That is to say that we exclude the DCH model to the largest mass in the case where we assume a branching ratio to given decay mode of one. Here the fact that the blue front is for the most part in agreement with the black curves means that our observed limits exclude as well as we have expected.

^{II}When the theoretical curve is below the observed limits the cross-section is so small that we are no longer sensitive enough to be able to exclude the model

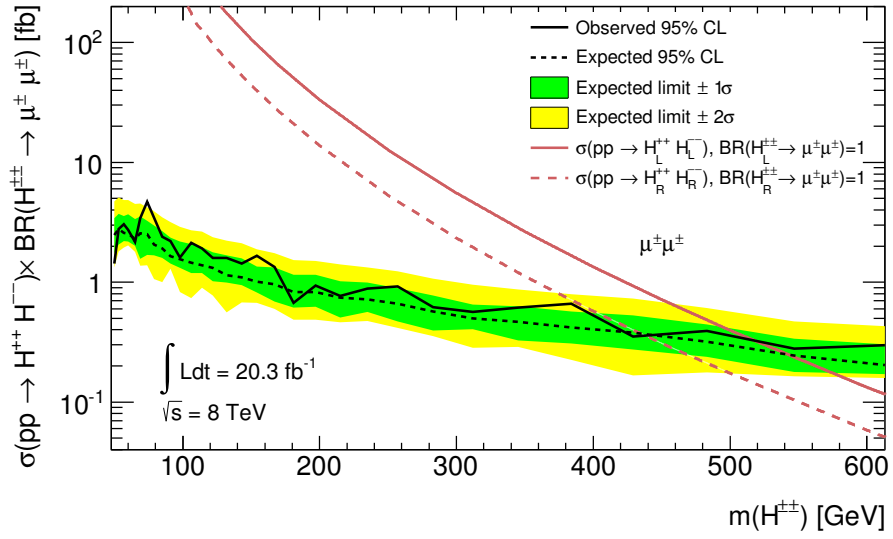


(a)



(b)

Figure 10.3: continues on following page...



(c)

Figure 10.3: 95% CL upper limits on the cross section as a function of the dilepton invariant mass for the production of a Doubly Charged Higgs boson decaying into (a) $e^\pm e^\pm$, (b) $e^\pm \mu^\pm$, and (c) $\mu^\pm \mu^\pm$ pairs with a branching ratio of 100%. The green and yellow bands correspond to the 1σ and 2σ bands on the expected limits respectively. The variation from bin to bin in the expected limits is due to fluctuations in the background yields derived from small MC samples. Also shown are the theory cross sections for left and right-handed $H^{\pm\pm}$.

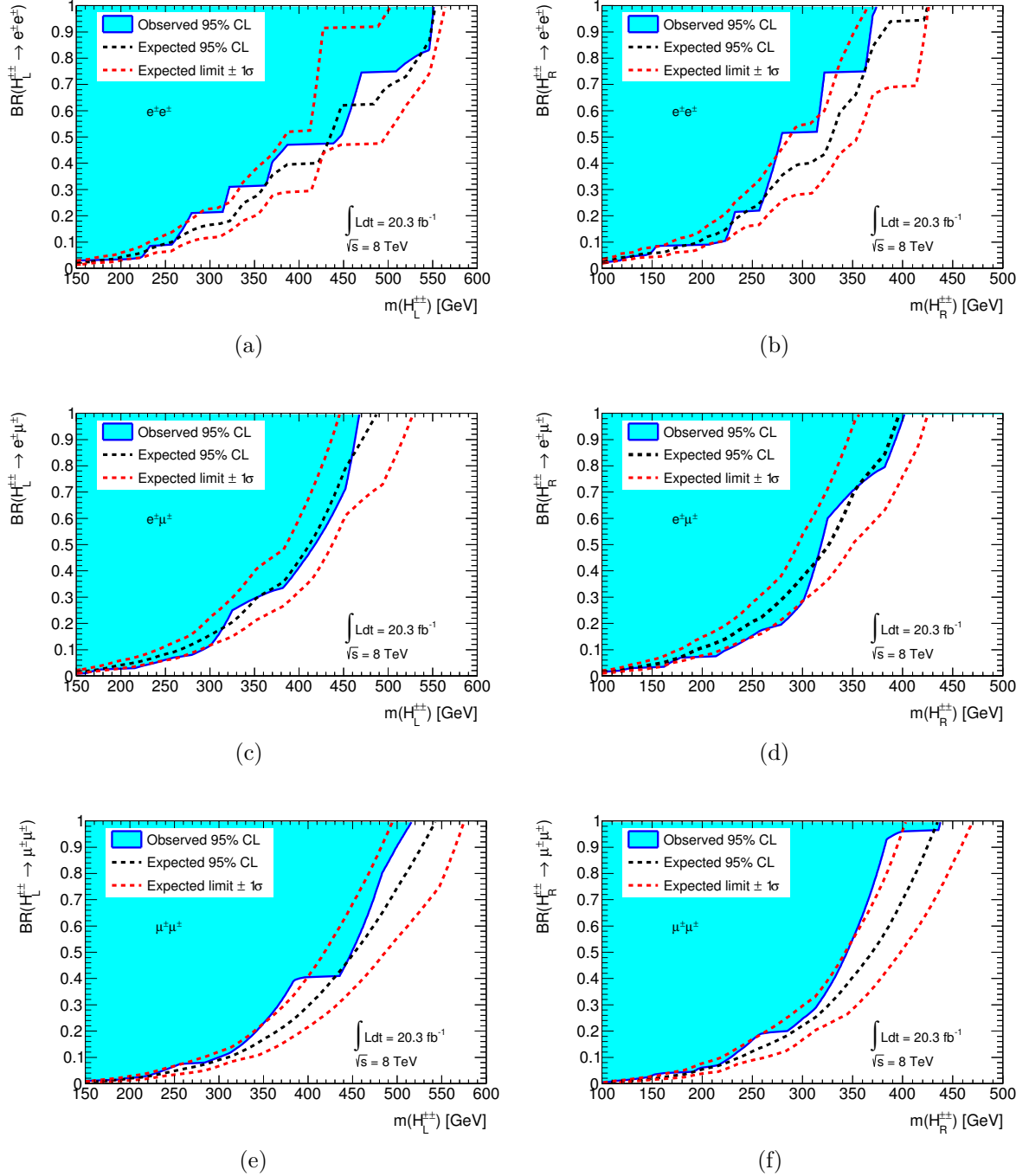


Figure 10.4: Observed and expected 95% CL limits on $H_L^{\pm\pm} \rightarrow \ell^\pm \ell^\pm$ (left column) and $H_R^{\pm\pm} \rightarrow \ell^\pm \ell^\pm$ production (right column) in the branching ratio versus $H^{\pm\pm}$ mass plane for the e^+e^+ (top), $e^+\mu^+$ (middle) and $\mu^+\mu^+$ (bottom) channels.

10.0.7 Comparison to 7 TeV results

The DCH limits are shown for the 7 TeV results in Fig. 10.5 in order for comparison to the 8 TeV results given above in Fig. 10.3. Once can compare these results directly to see the great improvement from 7 TeV to 8 TeV.

Assuming pair production, couplings to left-handed fermions, and a branching ratio of 100% for each final state for 7 TeV (8 TeV), masses below 409 (551) GeV, 398 (516) GeV and 375 (468) GeV are excluded at 95% CL for $e^\pm e^\pm, \mu^\pm \mu^\pm, e^\pm \mu^\pm$, respectively. Similarly pair production, couplings to right-handed fermions, and a branching ratio of 100% for each final state for 7 TeV (8 TeV), masses below 322 (374) GeV, 306 (438) GeV and 310 (402) GeV are excluded at 95% CL for $e^\pm e^\pm, \mu^\pm \mu^\pm, e^\pm \mu^\pm$, respectively. In other words the 8 TeV results present a 30-40% improvements to the 7TeV results. The values for the 95% lower limits on the mass of $H^{\pm\pm}$ for different branching ratios are given in table.10.5

Table 10.5: Lower limits at 95% CL on the mass of $H_L^{\pm\pm}$ and $H_R^{\pm\pm}$ bosons to $e^\pm e^\pm, e^\pm \mu^\pm$ and $\mu^\pm \mu^\pm$ pairs. Mass limits are derived assuming branching ratios to a given decay mode of 100%, 33% and 11%. Both expected and observed limits are given.

$\text{BR}(H_L^{\pm\pm} \rightarrow l^\pm l^\pm)$	95% CL upper limit on $m(H_L^{\pm\pm})$ [GeV]					
	$e^\pm e^\pm$		$\mu^\pm \mu^\pm$		$e^\pm \mu^\pm$	
	expected	observed	expected	observed	expected	observed
100%	407	409	401	398	392	375
33%	318	317	317	290	279	276
11%	228	212	234	216	206	190
$\text{BR}(H_R^{\pm\pm} \rightarrow l^\pm l^\pm)$	95% CL upper limit on $m(H_R^{\pm\pm})$ [GeV]					
	$e^\pm e^\pm$		$\mu^\pm \mu^\pm$		$e^\pm \mu^\pm$	
	expected	observed	expected	observed	expected	observed
100%	329	322	335	306	303	310
33%	241	214	247	222	220	195
11%	160	151	184	176	153	151

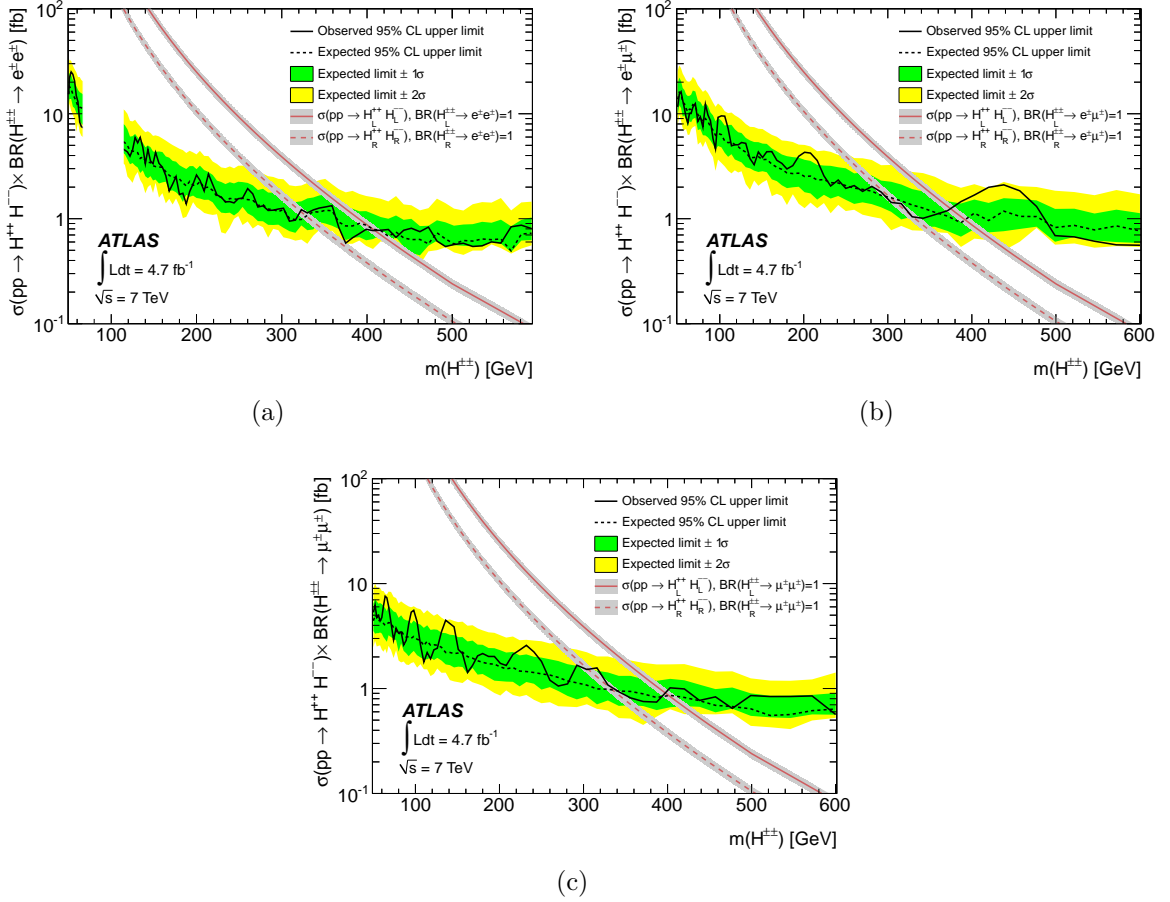


Figure 10.5: Upper limit at 95% CL on the cross section times branching ratio for pair production of $H^{\pm\pm}$ bosons decaying to (a) $e^\pm e^\pm$, (b) $e^\pm \mu^\pm$, and (c) $\mu^\pm \mu^\pm$ pairs. The observed and median expected limits are shown along with the 1σ and 2σ variations in the expected limits. In the range $70 < m(H^{\pm\pm}) < 110$ GeV, no limit is set in the $e^\pm e^\pm$ channel. Also shown are the theoretical predictions at next-to-leading order for the $pp \rightarrow H^{\pm\pm} H^{\mp\mp}$ cross section for $H_L^{\pm\pm}$ and $H_R^{\pm\pm}$ bosons. The variation from bin to bin in the expected limits is due to fluctuations in the background yields derived from small MC samples.

*The fact that we live at the
bottom of a deep gravity well,
on the surface of a gas covered
planet going around a nuclear
fireball 90 million miles away
and think this to be normal
is obviously some indication
of how skewed our perspec-
tive tends to be*

Douglas Adams, *The Salmon
of Doubt*

11

Summary and Conclusions

11.0.8 Conclusions

An inclusive search for the anomalous production of same-sign dilepton pairs ($e^\pm e^\pm$, $e^\pm \mu^\pm$, $\mu^\pm \mu^\pm$) using 20.3 fb^{-1} of $\sqrt{s} = 8 \text{ TeV}$ pp collision data recorded with the ATLAS detector is presented. No significant deviation from the expected Standard Model background was observed. This lead to upper limits on the fiducial cross-section for *new physics* beyond the SM which give rise to same-sign dilepton final states. The fiducial cross-sections were evaluated as a function of invariant mass with cuts ranging from $> 15 \text{ GeV}$ to $> 600 \text{ GeV}$. The limits range from 0.34 fb to 49 fb depending on mass and channel. Although one cannot directly compare the inclusive limits between the 7 TeV and 8 TeV analyses it is clear that the fiducial limits on the cross-section for new physics have improved. These fiducial cross-section limits allow theorists to calculate limits on any given model with same-sign dileptons in the final state.

The dataset and selection was then translated into a narrow bin search for a Doubly Charged Higgs model. Here lower mass limits were set for both right-handed and left-handed Doubly Charged Higgs bosons assuming they decay exclusively into $e^\pm e^\pm$, $e^\pm \mu^\pm$ and $\mu^\pm \mu^\pm$ pairs. The 95% CL lower mass limits for left handed Higgs bosons was found to vary between $470\text{-}550 \text{ GeV}$ depending on the channel, and $370\text{-}440 \text{ GeV}$ for right-handed Higgs bosons. These results showed a significant improvement of roughly 30-40% from the previous $\sqrt{s} = 7\text{TeV}$ analysis in which I was also involved.

11.0.9 Outlook

Potential extensions and improvements

Before wrapping up my final thoughts on the results and particle physics as a whole, I

would like to consider some other possible ways to expand and improve the same-sign dilepton analyses:

- **Charge Flips** - Since starting on 7 TeV analysis where there was little to no methodology and nothing standard to ascertain an estimate of electron charge flips, we have certainly come a long way. Now there is almost a standard method, the so called likelihood method, which is fantastic for lower p_T (< 80 GeV). But, I think that in order to reduce charge-flip we need to include more and more information, for instance: comparison of charge within different inner detector components, using the curvature of tracking to reject some events. Indeed CMS uses three separate methods for checking the electron charge and require that all three agree [107].
- **Fiducial Efficiency** - As we have seen, despite trying to remain as inclusive as possible there is still some model dependency seen for different signals. This mainly boils down to the differences in the lepton p_T spectra of the various different models and their mass points. Henceforth, I think it may be worth pursuing a slightly different approach to defining fiducial efficiency whereby one defines a fiducial efficiency per lepton for a lepton of a given p_T and η , such as that used in [108]. By using a lepton fiducial efficiency one circumvents the differences between models lepton p_T spectra and allows theorists to calculate the exact acceptance of their preferred final state.
- **Including Taus** - Hadronically decaying taus could also be very interesting to include in a dilepton search. The difficulty with taus is that they are much harder to reconstruct than electrons and muons, particularly their charges. But recently there has been vast improvement in the reconstruction algorithms of taus particularly those using neural networks and boosted decision trees [109]. So despite being less clean and less sensitive to the other channels it would be a great complementary result and who knows what surprises are in store there.
- **New Distributions** - It might also be worth including some new signal region distributions. Considering the missing transverse energy, number of jets and H_T (sum of all particle activity: lepton p_T , hadron p_T , MET (missing transverse energy) and photon p_T) whilst not cutting on them in order to maintain inclusivity could be very interesting for theorists. We have seen that many of the BSM models considered in this thesis can be differentiated by all these potential observables.
- **Multi-variate analysis** - For the 2012 dataset ATLAS developed a set of identification criteria for electrons which were based on multi-variate analysis techniques [97] rather than the standard cut-based identification criteria (loose, medium, tight) used in the analyses described in this paper. These multi-variate discriminants as well as benefiting from the multi-variate techniques also include additional information such as d_0 and z_0 and therefore provide a perhaps more stringent identification than the standard cut-based analysis. They can possibly distinguish between background and signal better. For future analyses these likelihood based identification for electrons should be tested.

- **Fake Method** - This is the core of the analysis in my opinion, and here there is still room for improvement. In the future one could develop definitions of fakes to encompass in some way more detector information. Furthermore, one could try and use a more complicated matrix method with more lepton (and other) information than just p_T and η to characterise fakes. For instance the number of jets per event or the missing energy in the detector could be used to improve the definition for what a fake is and which observables to parametrise the fakes with. It is not clear to me that this would improve the situation or to simply complicate things, but as we understand our detector I would hope that we will have a better handle on the how things appear in as fakes in the detector and how to reconstruct particles more precisely.

Final thoughts

High energy particle physics is in many ways at a very exciting juncture, as it has been many times before. With the relatively new discovery of the Higgs boson we have the final piece of the magnanimous Standard Model. This is of course incredibly exciting and fulfilling to see a so yearned after and expected prophecy completed. But on the other hand, excepting some very interesting peculiarities in quarkonia, neutrino physics and cosmology, there is very little experimental evidence of what the physics beyond the Standard Model is or indeed that the SM is incorrect in any way. As I have motivated time again throughout this thesis, there is good grounds to expect new physics and hence it is in some ways disappointing that in the initial running periods at the LHC we have not seen any hints of the elusive new physics. But now as we build up to the next phase of the LHC at 13 TeV we wait with bated breath. There are many theorists and experimentalists alike whom suggest that if their favourite BSM model of choice were to exist and still provide many of its useful features we should see hints of it in the 13 TeV runs.

Inclusive exotics searches such as the ones employed in this analysis are of paramount importance in my, admittedly biased, opinion. The reason being that as scientists we can devise the most incredible theories and search for these with great earnesty, however nature has proven time and time again to be a bizarre and beautiful creature, and therefore to contain it in our current net of understanding and theoretical imagination is to do it, and us, a disservice. Henceforth, the aim at least of such inclusive searches is to try and be sensitive to signals which perhaps the more specific searches miss and to ensure that we both investigate particle physics with both a magnifying glass and a fish-eyes lens. That is to say from a widespread perspective.

Now unfortunately for my sake, nothing new was discovered through our analysis of the 8 TeV data. But that is not to say that ours or indeed the hundreds of other LHC papers returning with no *new physics* are irrelevant. To the contrary, it is with these analyses that we squeeze and constrain theoretical models, guide future searches, improve search techniques, develop expertise, and become the building blocks to future scientific breakthrough.

Appendices

"“Have you thought of an ending?”
"Yes, several, and all are dark and unpleasant."
"Oh, that won't do! Books ought to have good endings. How would this do: and they all settled down and lived together happily ever after?"
"It will do well, if it ever came to that."
"Ah! And where will they live? That's what I often wonder.”"

J.R.R.Tolkien, *The Fellowship of the Ring*



A.1 Standard Model Reference Table

First Generation Names Mass	e Electron 0.511 MeV	ν_e Electron Neutrino < 2 RV	u Up quark ≈ 2 MeV	d Down quark ≈ 2 MeV
Second Generation Names Mass	μ Muon 106 MeV	ν_μ Muon Neutrino < 0.19 MeV	c Charmed quark 1205 MeV	s Strange quark 95 MeV
Third Generation Names Mass	τ Tau 1777 MeV	ν_τ Tau Neutrino <18.2 MeV	t Top quark 172×10^3 MeV	b Bottom quark 4500 MeV
Electric Charge Interacts via	-1 EM, Weak	0 EM, Weak	$+\frac{2}{3}$ EM, Weak, Strong	$-\frac{1}{3}$ EM, Weak, Strong

Table A.1: Summary of fundamental fermion particles in the Standard Model.

Boson	Name	Mass	Charge	Spin	Mediator for
W^\pm	W boson	80.4 GeV	\pm	1	Electroweak
Z^0	Z boson	91.2 GeV	0	1	Electroweak
γ	Photon	0	0	1	Electromagnetic
g	Gluon	0	0	1	Strong
H	Higgs Boson	126 GeV	0	0	Higgs Field

Table A.2: Summary of fundamental boson particles in the Standard Model.

A.2 7 TeV Results Appendix

In this section the number of expected and observed pairs for the 7TeV analysis are shown in Table. A.3 and their corresponding upperlimits are shown in Table. A.4 for completeness sake. Furthermore the kinematic distributions of leading lepton η and p_T for the 7TeV signal region is shown in Fig. A.1. Similarly for completeness here I include the doubly charge higgs mass versus branching ratio plots for the 7TeV analyses in Fig. A.2.

Table A.3: Expected and observed numbers of pairs of isolated like-sign leptons for various cuts on the dilepton invariant mass, $m(\ell^\pm\ell^\pm)$. The uncertainties shown are the quadratic sum of the statistical and systematic uncertainties. The prompt background contribution includes the WZ , ZZ , $W^\pm W^\pm$, $t\bar{t}W$, and $t\bar{t}Z$ processes. When zero events are predicted, the uncertainty corresponds to the 68% confidence level upper limit on the prediction.

Sample	Number of electron pairs with $m(e^\pm e^\pm)$				
	> 15 GeV	> 100 GeV	> 200 GeV	> 300 GeV	> 400 GeV
Prompt	101 ± 13	56.3 ± 7.2	14.8 ± 2.0	4.3 ± 0.7	1.4 ± 0.3
Non-prompt	75 ± 21	28.8 ± 8.6	5.8 ± 2.5	$0.5^{+0.8}_{-0.5}$	$0.0^{+0.2}_{-0.0}$
Charge flips and conversions	170 ± 33	91 ± 16	22.1 ± 4.4	8.0 ± 1.7	3.4 ± 0.8
Sum of backgrounds	346 ± 44	176 ± 21	42.8 ± 5.7	12.8 ± 2.1	4.8 ± 0.9
Data	329	171	38	10	3
	Number of muon pairs with $m(\mu^\pm \mu^\pm)$				
	> 15 GeV	> 100 GeV	> 200 GeV	> 300 GeV	> 400 GeV
Prompt	205 ± 26	90 ± 11	21.8 ± 2.8	5.8 ± 0.9	2.2 ± 0.4
Non-prompt	42 ± 14	12.1 ± 4.6	1.0 ± 0.6	$0.0^{+0.3}_{-0.0}$	$0.0^{+0.3}_{-0.0}$
Charge flips	$0.0^{+4.9}_{-0.0}$	$0.0^{+2.5}_{-0.0}$	$0.0^{+1.8}_{-0.0}$	$0.0^{+1.7}_{-0.0}$	$0.0^{+1.7}_{-0.0}$
Sum of backgrounds	247^{+30}_{-29}	102 ± 12	$22.8^{+3.4}_{-2.9}$	$5.8^{+1.9}_{-0.9}$	$2.2^{+1.7}_{-0.4}$
Data	264	110	29	6	2
	Number of lepton pairs with $m(e^\pm \mu^\pm)$				
	> 15 GeV	> 100 GeV	> 200 GeV	> 300 GeV	> 400 GeV
Prompt	346 ± 43	157 ± 20	36.6 ± 4.7	10.8 ± 1.5	3.9 ± 0.6
Non-prompt	151 ± 47	45 ± 13	9.2 ± 4.1	2.6 ± 1.1	1.0 ± 0.6
Charge flips and conversions	142 ± 28	33 ± 7	10.5 ± 2.8	2.9 ± 1.2	2.2 ± 1.1
Sum of backgrounds	639 ± 71	235 ± 25	56.4 ± 7.0	16.3 ± 2.3	7.0 ± 1.4
Data	658	259	61	17	7

Table A.4: Upper limits at 95% C.L. on the fiducial cross section for $\ell^+\ell^-$ pairs from non-SM physics. The expected limits and their 1σ uncertainties are given, as well as the observed limits in data, for the ee , $e\mu$, and $\mu\mu$ final state inclusively and separated by charge.

Mass range	95% C.L. upper limit [fb]					
	expected observed $e^\pm e^\pm$		expected observed $e^\pm \mu^\pm$		expected observed $\mu^\pm \mu^\pm$	
$m > 15$ GeV	46^{+15}_{-12}	42	56^{+23}_{-15}	64	$24.0^{+8.9}_{-6.0}$	29.8
$m > 100$ GeV	$24.1^{+8.9}_{-6.2}$	23.4	$23.0^{+9.1}_{-6.7}$	31.2	$12.2^{+4.5}_{-3.0}$	15.0
$m > 200$ GeV	$8.8^{+3.4}_{-2.1}$	7.5	$8.4^{+3.4}_{-1.7}$	9.8	$4.3^{+1.8}_{-1.1}$	6.7
$m > 300$ GeV	$4.5^{+1.8}_{-1.3}$	3.9	$4.1^{+1.8}_{-0.9}$	4.6	$2.4^{+0.9}_{-0.7}$	2.6
$m > 400$ GeV	$2.9^{+1.1}_{-0.8}$	2.4	$3.0^{+1.0}_{-0.8}$	3.1	$1.7^{+0.6}_{-0.5}$	1.7
	$e^+ e^+$		$e^+ \mu^+$		$\mu^+ \mu^+$	
$m > 15$ GeV	$29.1^{+10.2}_{-8.6}$	22.8	$34.9^{+12.2}_{-8.6}$	34.1	$15.0^{+6.1}_{-3.3}$	15.2
$m > 100$ GeV	$16.1^{+5.9}_{-4.3}$	12.0	$15.4^{+5.9}_{-4.1}$	18.0	$8.4^{+3.2}_{-2.4}$	7.9
$m > 200$ GeV	$7.0^{+2.9}_{-2.2}$	6.1	$6.6^{+3.5}_{-1.8}$	8.8	$3.5^{+1.6}_{-0.7}$	4.3
$m > 300$ GeV	$3.7^{+1.4}_{-1.0}$	2.9	$3.2^{+1.2}_{-0.9}$	3.2	$2.0^{+0.8}_{-0.5}$	2.1
$m > 400$ GeV	$2.3^{+1.1}_{-0.6}$	1.7	$2.4^{+0.9}_{-0.6}$	2.5	$1.5^{+0.6}_{-0.3}$	1.8
	$e^- e^-$		$e^- \mu^-$		$\mu^- \mu^-$	
$m > 15$ GeV	$23.2^{+8.6}_{-5.8}$	25.7	$26.2^{+10.6}_{-7.6}$	34.4	$12.1^{+4.5}_{-3.5}$	18.5
$m > 100$ GeV	$12.0^{+5.3}_{-2.8}$	18.7	$11.5^{+4.2}_{-3.5}$	16.9	$6.0^{+2.3}_{-1.9}$	10.1
$m > 200$ GeV	$4.9^{+1.9}_{-1.2}$	4.0	$4.6^{+2.1}_{-1.2}$	4.5	$2.7^{+1.1}_{-0.7}$	4.4
$m > 300$ GeV	$2.9^{+1.0}_{-0.6}$	2.7	$2.7^{+1.1}_{-0.6}$	3.5	$1.5^{+0.8}_{-0.3}$	1.7
$m > 400$ GeV	$1.8^{+0.8}_{-0.4}$	2.3	$2.3^{+0.8}_{-0.5}$	2.5	$1.2^{+0.4}_{-0.0}$	1.2

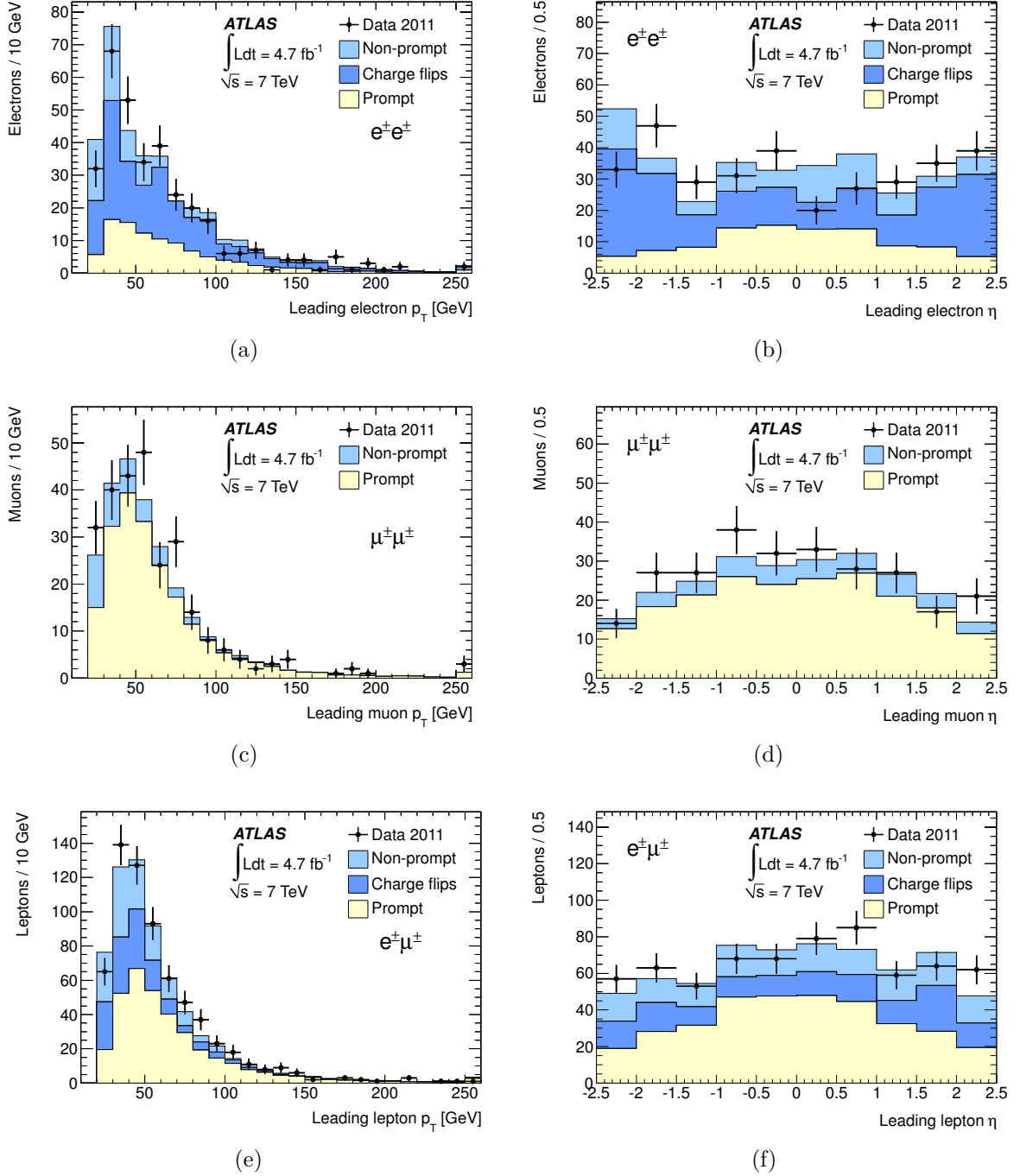


Figure A.1: Leading lepton p_T, η distributions for (a,b) $e^\pm e^\pm$ (c,d) $\mu^\pm \mu^\pm$ and (e,f) $e^\pm \mu^\pm$ pairs passing the full event selection. The data are shown as closed circles, and the stacked histograms represent the background predictions.

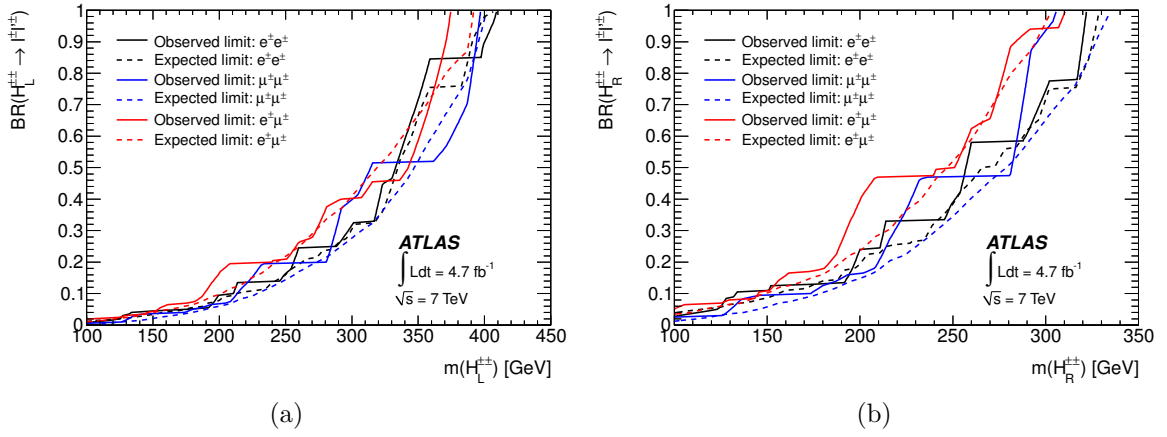


Figure A.2: The mass limits as a function of the branching ratio for the $H^{\pm\pm}$ decaying to $e^\pm e^\pm$, $e^\pm \mu^\pm$ and $\mu^\pm \mu^\pm$ for (a) $H_L^{\pm\pm}$ and (b) $H_R^{\pm\pm}$ bosons. Shown are both the observed limits (solid lines) and the expected limits (dashed lines). The stepping behaviour, where the same mass limit is valid for a range of branching ratios, results from fluctuations in the observed cross-section limits

A.3 Electron Charge Flip Systematics for 8TeV analysis

The 8TeV analysis had much more statistics than the 7TeV analysis. Furthermore the charge-flip measurement was no longer new and we had had a chance to understand it better. Henceforth we were able to get a better hold on the systematic effects. The sources of systematic uncertainty considered were:

- Changing the invariant mass cut window around the Z peak from $75 < m_{ll} < 105$ GeV to $85 < m_{ll} < 95$ GeV. In other words using a narrower region of the Z peak to see how much the new values differ with respect to the nominal values.
- The track and calorimeter cuts are loosened each by 4 GeV. Testing the resilience of the charge-flip rates against non-prompt electrons.¹

The systematic uncertainties from the above sources were added in quadrature along with the inherent error in the likelihood function fit which ascertained the charge-flip rates. Additional for high momentum electrons ($p_T > 100$ GeV) there is a 20% affect coming from using a distorted geometry with respect to the nominal as talked about in the charge-flip section.

A.4 Electron Fake Factor systematics

A.4.1 Away side jet kinematics and prompt subtraction

As mentioned in section on backgrounds, two of the systematics considered for the electron fake factors was the prompt subtraction variation shown in Fig. A.3 and the away side jet variation shown in Fig. A.4.

A.4.2 Systematic Uncertainty Associated with the light/heavy Flavour Components

To assess the impact of the light flavour (LF) versus heavy flavour (HF) composition of the fake background sample for electrons, an alternative method was developed. This method also uses fake factors as described in Section. 6.5.2. The numerator and denominator definitions are the same as in the nominal method, and the same data samples are used to derive the fake factors. The difference is that the alternative method described here incorporates b-tagging information to attempt to separate the LF and HF components of the fake background. This alternative method was used to cross check the fake prediction in the signal region and as such, full systematics for this method were not evaluated.

¹N.B. we also tested the effect of using medium++ electrons instead of tight++ and saw that the variation here is negligible compared to the isolation

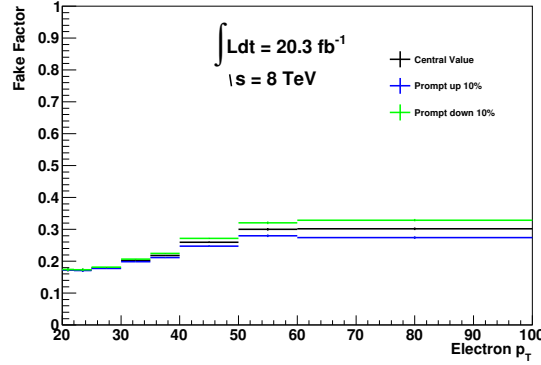


Figure A.3: Electron fake factor versus p_T with prompt subtraction variations. The error bars are purely statistical error.

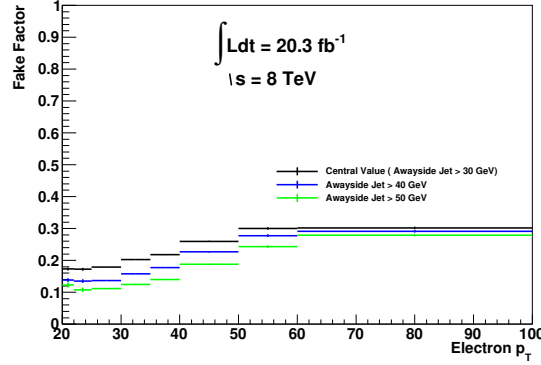


Figure A.4: Electron fake factor versus p_T and with away side jet p_T requirement variations. The error bars are purely statistical error.

MV1 b-tagger

The MV1 b-tagger is the recommended tagger from the Flavor Tagging group for release 17 analyses [110]. This algorithm is based on a neural network using the output weights of the various algorithms on jet like objects as input. For this method, the idea is to use the b-tag weight of the jet overlapping with an electron candidate to try to classify it as a light or heavy flavor fake.

A complication arises in that the b-tagging efficiency is correlated with the identification cuts on the electron candidate. Not surprisingly, the cuts which are most effective at rejecting heavy flavor background (track isolation and $\sigma(d_0)$) are the most correlated with the b-tagging weight, as they cut on the same information used by the b-tagging algorithms (tracks for secondary vertices, impact parameters).

By assuming (i) that the requirement of MV1 weight > 0.9 selects a pure sample of HF fakes and (ii) the efficiency for a true HF fake to pass the requirement of MV1 weight

> 0.9 is known, one can estimate the total number of true HF fakes in a fake-dominated data control region. This information will be used to derive “true” HF and LF fake factors.

Derivation of HF and LF Fake factors

First we define the following quantities, which will be used in deriving the fake factors:

- N_{tag}, D_{tag} : the number of numerators/denominators with the overlapping jet passing MV1 weight > 0.9
- N_{notag}, D_{notag} : the number of numerators/denominators with the overlapping jet failing MV1 weight > 0.9
- ε_{tag} : the MC efficiency for a true HF fake passing the numerator selection to also have the overlapping jet passing MV1 weight > 0.9 . This number is $\sim 30\%$ for the numerator selection, taken from the flavour tagging group.

Then we can define the following:

$$N_{HF} \equiv \frac{N_{tag}}{\varepsilon_{tag}}, \quad N_{LF} = N_{tot} - N_{HF} \quad (\text{A.1})$$

where N_{HF} and N_{LF} are the estimated numbers of true HF and LF fakes in the numerator selection. Effectively, the number of true HF fakes is estimated by scaling up the pure HF sample N_{tag} by ε_{tag} . Then the remaining numerators which are not HF are considered to be LF.

These can be used to derive what will be called the “true” HF and LF fake factors:

$$f_{HF} \equiv \frac{N_{HF}}{D_{tag}}, \quad f_{LF} \equiv \frac{N_{LF}}{D_{notag}} \quad (\text{A.2})$$

These fake factors use the D_{tag} selection, which is fairly pure in HF fakes, to predict the number of true HF fakes, and the D_{notag} selection, which is dominated by LF, to predict the true number of LF fakes. This idea is similar to binning the fake factor in two bins of b-tagging weight, as is done in some analyses. The main difference here is the efficiency correction applied to the numerator, to account for the fact that the MV1 b-tagging efficiency is low after the analysis electron selection.

Application of HF and LF Fake factors and Systematic Error

The fake factors using f_{HF} and f_{LF} are applied in essentially the same way as is described in Section. 6.5.2. The only difference is that the MV1 b-tagging weight of the overlapping jet is checked for denominator objects. If the MV1 weight is greater than 0.9, f_{HF} is applied; otherwise f_{LF} is applied.

The HF/LF method is then used to compare predictions with the nominal method in the signal region. The resulting predictions are in very good agreement. As this HF/LF method relies on the assumption of ε_{tag} from MC, this number was varied by 10 % to see the impact on the signal region prediction. Using these alternative fake factors a maximum discrepancy from the nominal fake factors was seen to be at 4.8% in the signal region. Thus a conservative value of 5% was chosen as the LF/HF uncertainty on the fake factors.

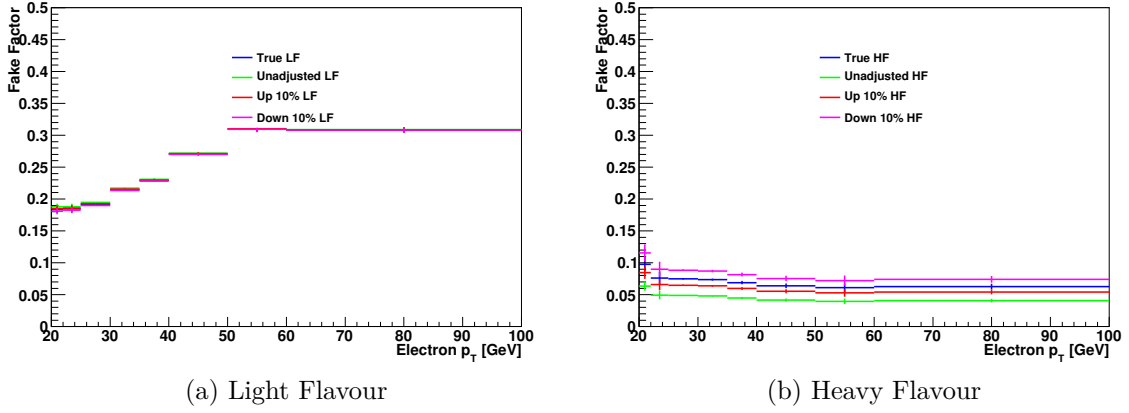


Figure A.5: The LF Electron fake factors (a) and HF fake factors (b) versus p_T computed using the definitions in the text. The error bars are purely statistical error.

A.5 Electron Intermediate Isolation Fakes

A.5.1 Intermediate isolation Numerator and Denominator

Several control regions used to validate the fake prediction use a different isolation requirement, referred to as *intermediate* isolation. The intermediate isolation selection is:

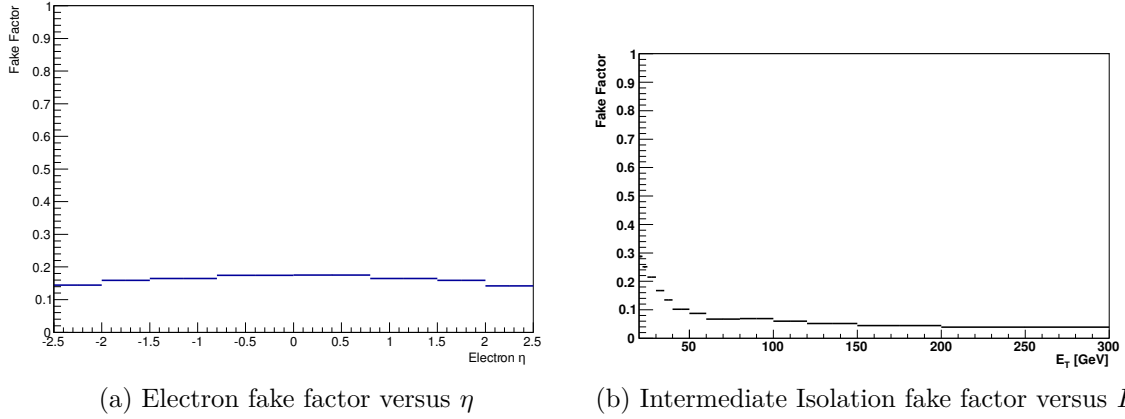
Numerator object selection The numerator objects are given by the standard electron analysis selection, except

- Fail signal track isolation or calo isolation:
 - $\text{ptcone30} > 0.1p_T$ OR $\text{etcone20} > 3 + (p_T - 20) \times 0.037$
- But pass intermediate calorimeter and track isolation
 - $\text{ptcone30} < 4 + 0.1p_T$ AND $\text{etcone20} < 7 + (p_T - 20) \times 0.037$

Intermediate isolation is 4 GeV looser than signal isolation.

Denominator object selection The denominator objects use the same nominal selection except that they must:

- Fail intermediate isolation:
 - $\text{Etcone20_pt_nPV_corrected} > 7 + (E_T - 20) \times 0.037$
OR $\text{ptcone30} > 4 + 0.1E_T$

Figure A.6: Electron fake factor versus E_T and η for intermediately isolated electrons

A.5.2 Medium++ Numerator and Denominator

Some control regions to validate the fake prediction use a different electron ID requirement, referred to as Medium++

Numerator object selection The numerator objects are given by the standard electron analysis selection, except

- Fail "isEM tight++", but pass "isEM medium++"

Denominator object selection The denominator objects are given by

- Pass isEM loose++ but fail isEM medium++

A.6 Muon Fake Systematics

A.6.1 Systematic uncertainty associated with the light-flavor component

To get a handle on the fraction of light-flavor muons in the signal region compared to the region where the muon fake factor is estimated, we use the fractional difference in muon momentum between the Inner Detector and the Muon Spectrometer (correcting for the expected muon energy loss in the calorimeters of around 3 GeV). This fractional momentum loss is defined as

$$\Delta p = (p^{ID} - p^{MX})/p^{ID} \quad (\text{A.3})$$

where p^{ID} is the muon momentum as measured in the inner detector and p^{MX} is the momentum measured in the muon spectrometer extrapolated back to the interaction point,

correcting for the energy loss in the calorimeter. For prompt muons or muons from heavy-flavor decays, the fractional momentum loss is expected to be more or less symmetric around $\Delta p = 0$. However, for muons originating from light-flavor sources such as pion or kaon decay-in-flights, a large positive momentum loss is expected, shown in Fig. A.7 for muons in fully simulated $t\bar{t}$ events.

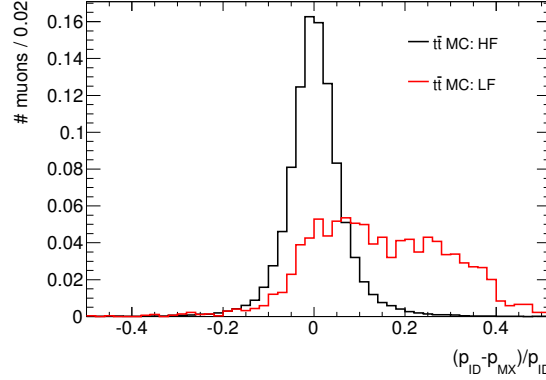


Figure A.7: Relative momentum loss for muons from heavy-flavor and light-flavor, respectively, in Monte Carlo simulated $t\bar{t}$ events.

This different behaviour of heavy-flavor vs light-flavor muons can be used to derive a systematic uncertainty on the fraction of light-flavor muons in the region where the fake muon background is determined for the signal region. To do so we first define the fractional momentum-loss asymmetry as

$$\Delta p^{asym} = \frac{N(\Delta p > 0.10) - N(\Delta p < -0.10)}{N(\Delta p)} \quad (\text{A.4})$$

where $N(\Delta p > 0.10)$ and $N(\Delta p < -0.10)$ are the number of muons with fractional momentum-loss asymmetry larger than 0.10 and less than -0.10 , and $N(\Delta p)$ the total number of muons. Using the asymmetry of the fractional momentum loss means that the component from prompt muons and muons from heavy-flavor cancels to first order, and the asymmetry is then directly probing the light-flavor component. We determine the momentum-loss asymmetry for denominator muons in the signal region and for denominator muons with $p_T > 20$ GeV in the control sample where the muon fake factor is derived. Using MC templates of the momentum-loss asymmetry for heavy-flavor and light-flavor muons, a given momentum-loss asymmetry can be translated into a corresponding light-flavor fraction. The measured asymmetries and the corresponding estimated light-flavor fractions are shown in Table A.5.

Derivation of LF Fake factors

The fake factor for light-flavor muons is derived from data. For this purpose we select single-muon event with at least one jet with $p_T > 25$ GeV and transverse mass $m_T < 10$ GeV.

Table A.5: Momentum-loss asymmetry and corresponding light-flavor fraction for denominator muons in the signal region and in the control sample where the fake factor is determined.

Region	Δp^{asym}	Light-flavor fraction
Signal region	$5.97 \pm 0.10 \%$	$1.50 \pm 0.03 \%$
Fake factor	$2.60 \pm 0.05 \%$	$0.61 \pm 0.01 \%$

Among muons in these events we derive the light-flavor fake factor as

$$f_{LF} = \frac{N_N(\Delta p > 0.10) - N_N(\Delta p < -0.10)}{N_D(\Delta p > 0.10) - N_D(\Delta p < -0.10)} \quad (\text{A.5})$$

where N_N (N_D) is the number of numerator (denominator) muons. The motivation for this definition is again that prompt muons and muons from heavy-flavor are assumed to be symmetric around $\Delta p = 0$ and should cancel with this definition, isolating a sample largely dominated by light-flavor muons. Fig. A.8 shows the fake factor central value, and light-flavor fake factors. In order to probe the light-flavor fake factor also in dimuon events, we define an additional control sample, completely different to the signal region, where one muon *fails* the impact parameter significance cut. For the second muon in these events, we then derive a light-flavor fake factor using the same method illustrated in Eq. A.5. Due to poor statistics in this dimuon control samples, we integrate over muon $p_T > 20$ GeV. The results are shown in Table A.6. The largest observed light-flavor fake factor is a factor of 1.7 higher than the central value.

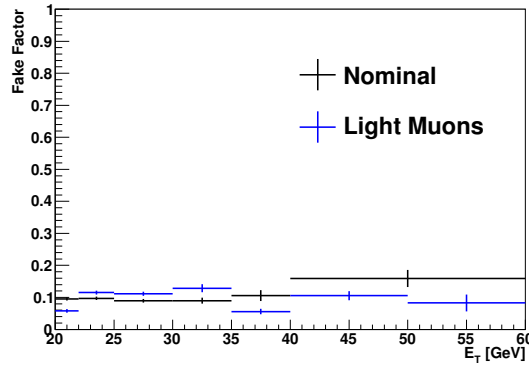


Figure A.8: Fake factor for light-flavor control samples compared to the fake factor central value.

Table A.6: Light-flavor fake factors

Control sample	Average fake factor ($p_T > 20$ GeV)
Central value	0.096 ± 0.001
Single μ	0.103 ± 0.001
Dimuon ($p_T < 40$ GeV)	0.094 ± 0.001
Dimuon (all)	0.17 ± 0.01

Calculating a systematic

Since the derivation of the fake factor central value assumes that the non-prompt muons primarily originate from heavy-flavor decays, we derive an upper systematic uncertainty on the fake factor associated with the different light-flavor fractions for the denominator muons in the signal region and the denominator muons where the fake factor is derived. The systematic uncertainty is derived as a correction to the central value. This is defined as

$$f_{LFsystematic} = f_{central} \cdot (1 - x_{LF}) + f_{LF} \cdot x_{LF} \quad (A.6)$$

where $f_{central}$ is central value of the fake factor as determined from data, x_{LF} is the 1σ upper systematic on the light-flavor fraction measured using momentum-loss asymmetry from data, and f_{LF} is the fake factor for light-flavor muons.

Combining the light-flavor fraction and the light-flavor fake factor, Eq. A.6 translates to an upper light-flavor systematic of:

$$f_{LFsystematic} = f_{central} \cdot 0.991 + 1.7 \cdot f_{central} \cdot 0.009 = 1.006 \cdot f_{central} \quad (A.7)$$

I.e. the systematic uncertainty associated with the light-flavor component is $\pm 0.6\%$.

A.7 Muon Intermediately Isolated Fakes

Several control regions used to validate the fake prediction use a different isolation requirement, referred to as *intermediate* isolation. The intermediate isolation selection is:

Numerator object selection Numerator objects for the intermediate isolation fake factor pass all muon selection cuts, except

- Fail signal track or Calo isolation:
 - $ptcone30/p_T > 0.07$ OR $etcone30 > 3.5 + (p_T - 20) \times 0.06$
- Pass looser track and Calo isolation cut:
 - $ptcone30 < 4 + 0.07p_T$
 - $Etcone30 < 7.5 + (p_T - 20) \times 0.06$

- special requirements on $|d_0|$ and $|d_0|/\sigma(d_0)$ as described in Section. 6.5.3.

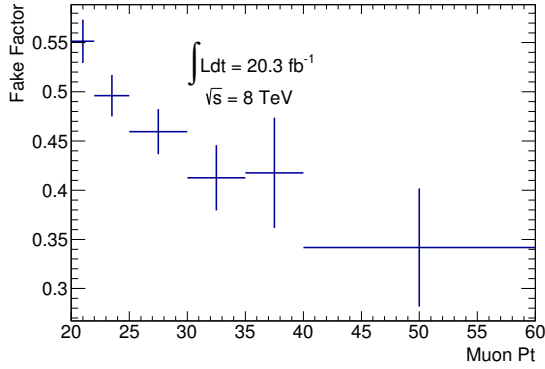
Intermediate isolation is 4 GeV looser than signal isolation.

Denominator object selection Denominator objects pass all muon selection cuts, but must fail the signal and intermediate isolation selections, yet pass the very loose requirement of ptcone40:

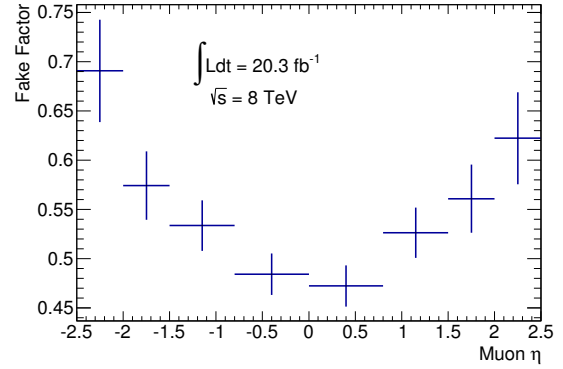
- **Fail intermediate track or calo isolation but satisfy looser isolation:**

$$- \text{ptcone30} > 4 + 0.07p_T \text{ OR } \text{etcone30} > 7.5 + (p_T - 20) \times 0.06$$

- special requirements on $|d_0|$ and $|d_0|/\sigma(d_0)$ as described below in Section. 6.5.3.



(a) Intermediate isolation region



(b) Intermediate isolation region

Figure A.9: Fake factor as function of muon p_T and η after applying correction factor for high vs low impact parameter significance. For the intermediate isolation fake factors. The error bars are purely statistical error.

A.8 Additional Validation Region Plots

In this section additional kinematic plots are given for the prompt (A.8.1) and fake (A.8.2) validation regions in the $\mu\mu$ channel.

A.8.1 Prompt Validation Region

Additional prompt validation region distributions shown in Fig. A.10 and Fig. A.11.

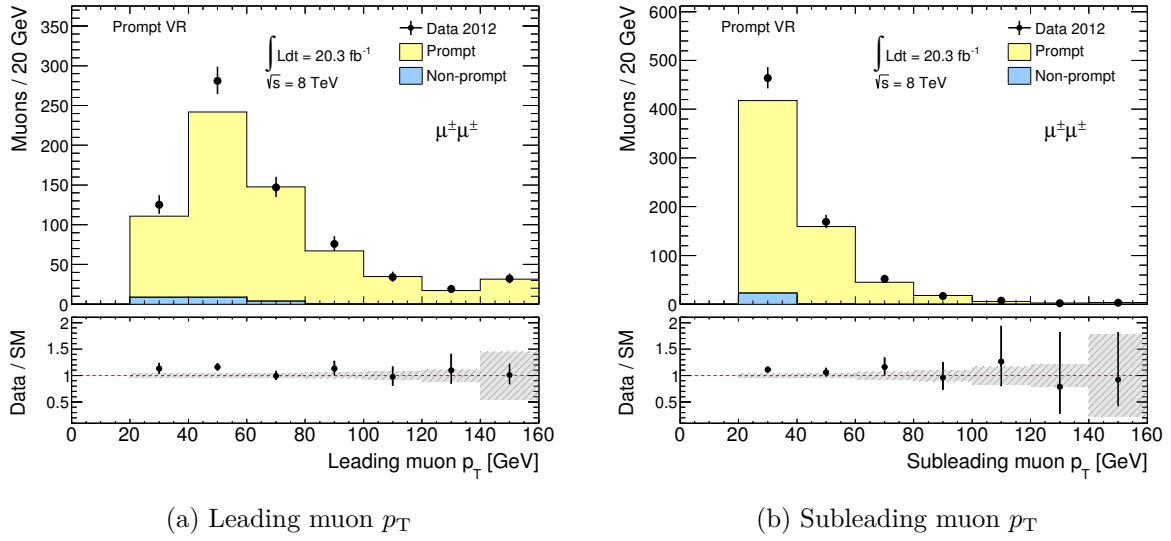


Figure A.10: Leading and subleading muon p_T distributions in events with a same-sign $\mu\mu$ pair and a Z decay candidate lepton pair.

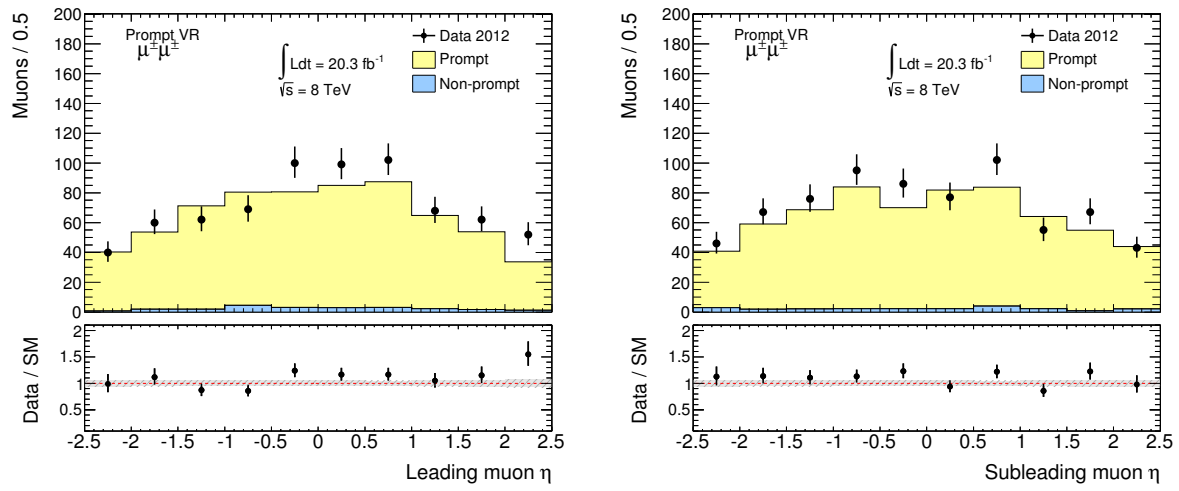
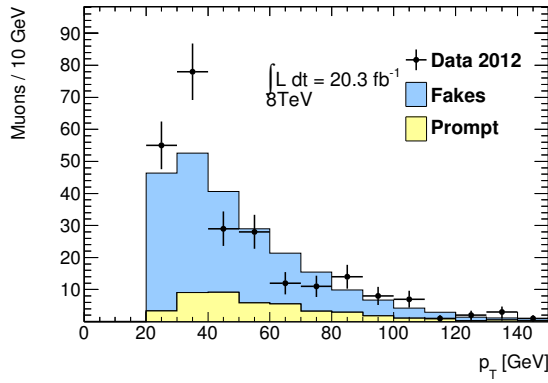
(a) Leading muon η (b) Subleading muon η

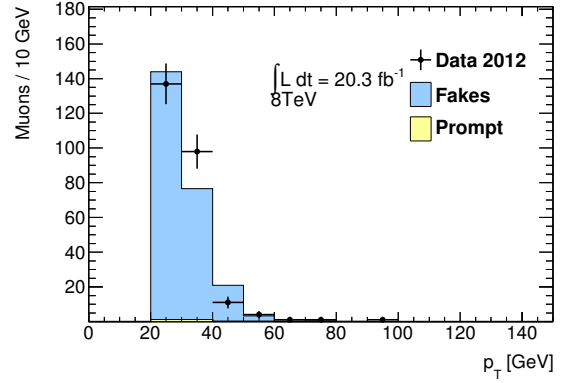
Figure A.11: Leading and subleading muon η distributions, in events with a same-sign $\mu\mu$ pair and a Z decay candidate lepton pair.

A.8.2 Fake Validation Region

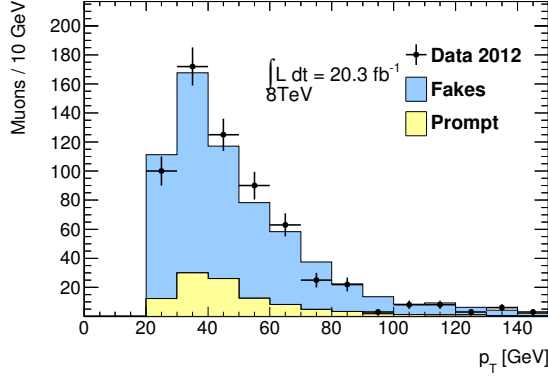
This subsection shows the leading and subleading muon p_T spectra, Figures A.12-A.13, for the four control regions enhanced in the non-prompt muon background. The uncertainties shown are the combined statistical and systematic uncertainties on the background prediction. For the systematic uncertainty associated with the fake factor, a value of 34% is used (which is the effect of the systematic uncertainty on the fake-factor as propagated through to the fake prediction in the signal region).



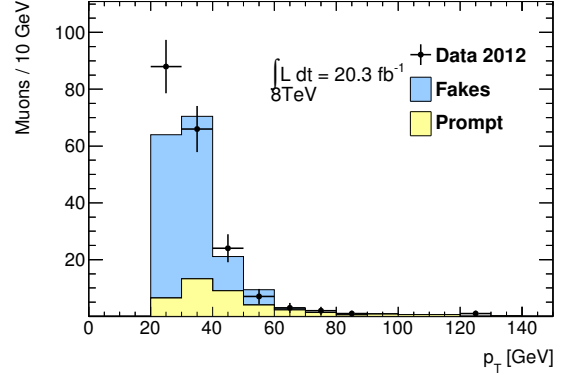
(a) Like-sign $\sigma(d_0)/d_0 > 3$ for ≥ 1 muon



(b) Like-sign intermediate isolation

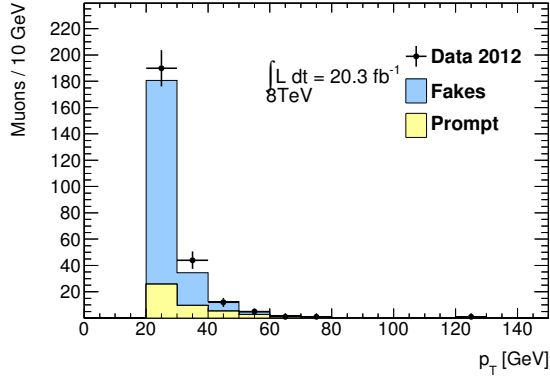
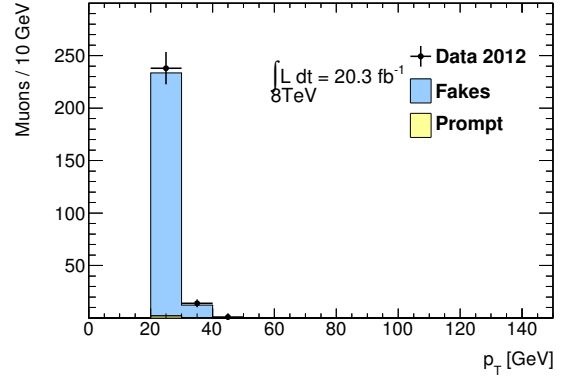


(c) Like-sign muon pairs with leading muon isolated and subleading muon intermediately isolated

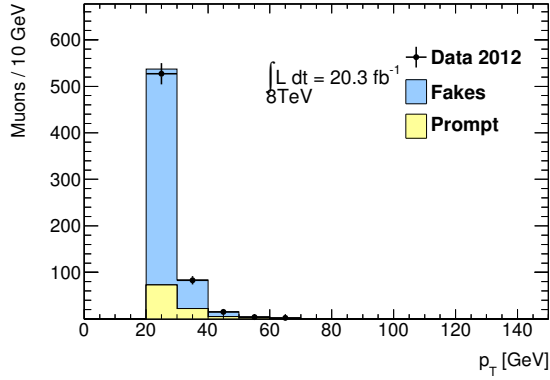


(d) Like-sign muon pairs with leading muon intermediately isolated and subleading muon isolated

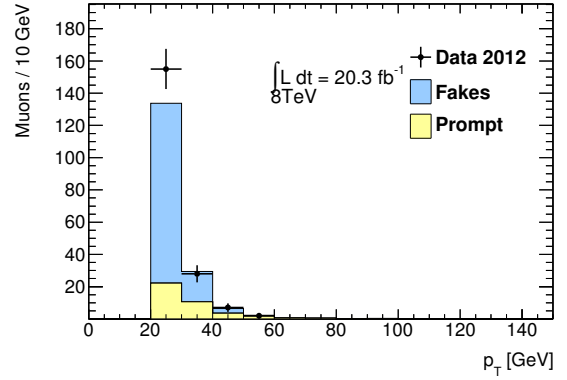
Figure A.12: Leading muon p_T spectrum for the four control regions that are sensitive to the non-prompt muon background.

(a) Like-sign $\sigma(d_0)/d_0 > 3$ for ≥ 1 muon

(b) Like-sign intermediate isolation

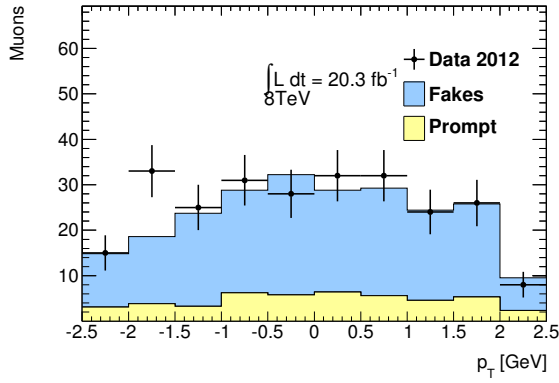
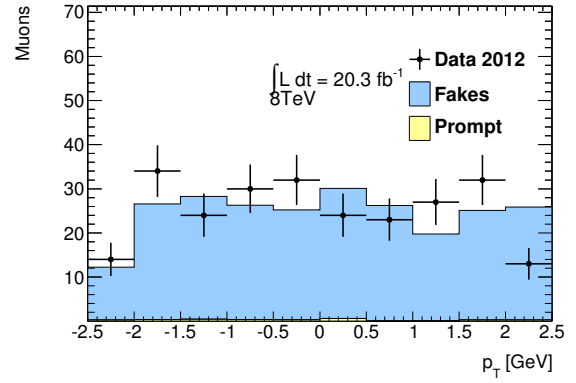


(c) Like-sign muon pairs with leading muon isolated and subleading muon intermediately isolated

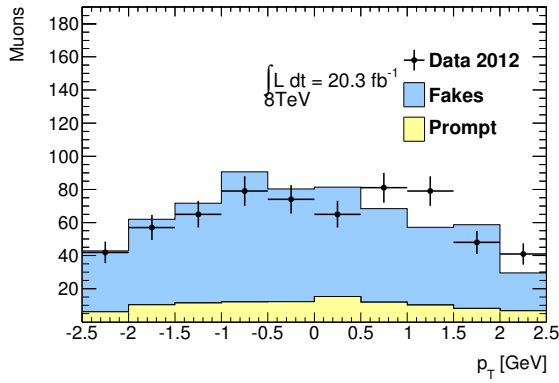


(d) Like-sign muon pairs with leading muon intermediately isolated and subleading muon isolated

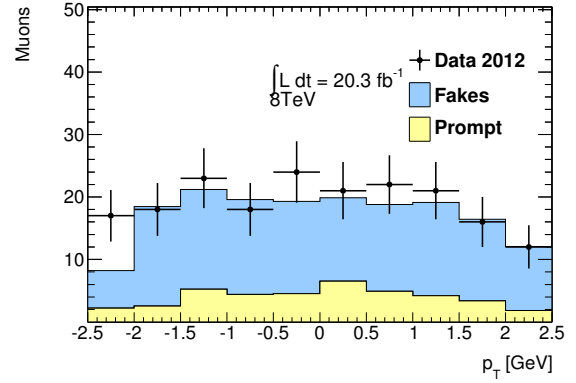
Figure A.13: Subleading muon p_T spectrum for the four control regions that are sensitive to the non-prompt muon background.

(a) Like-sign $\sigma(d_0)/d_0 > 3$ for ≥ 1 muon

(b) Like-sign intermediate isolation

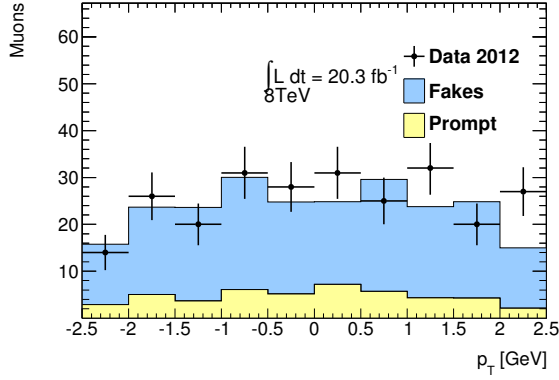
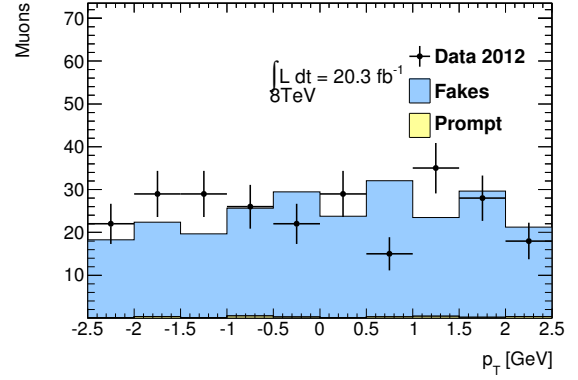


(c) Like-sign muon pairs with leading muon isolated and subleading muon intermediately isolated

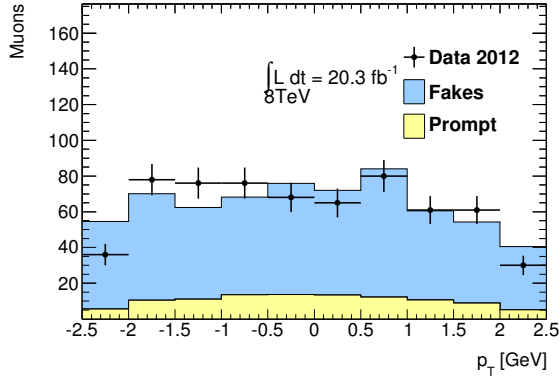


(d) Like-sign muon pairs with leading muon intermediately isolated and subleading muon isolated

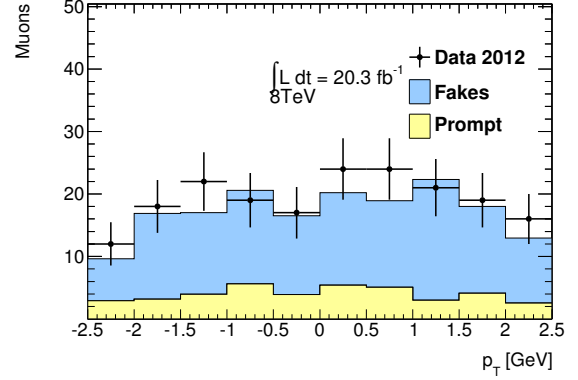
Figure A.14: Leading muon η spectrum for the four control regions that are sensitive to the non-prompt muon background.

(a) Like-sign $\sigma(d_0)/d_0 > 3$ for ≥ 1 muon

(b) Like-sign intermediate isolation



(c) Like-sign muon pairs with leading muon isolated and subleading muon intermediately isolated



(d) Like-sign muon pairs with leading muon intermediately isolated and subleading muon isolated

Figure A.15: Subleading muon η spectrum for the four control regions that are sensitive to the non-prompt muon background.

A.9 Fake Rate Dependence on Pile-Up

The Electron and Muon Fake Factors derived in the previous sections are designed such that they are a pile-up independent. This is particularly important as the derived fake factors both use isolation as the variable to discriminate between numerator and denominator objects which if uncorrected is pile-up dependent. However with the appropriate corrections one can show that the derived fake factors are indeed pile-up independent as displayed in Fig. A.16. Here npv stands for number of primary vertices. The number of primary vertices is proportional to the ammount of pile-up. Hence by comparing

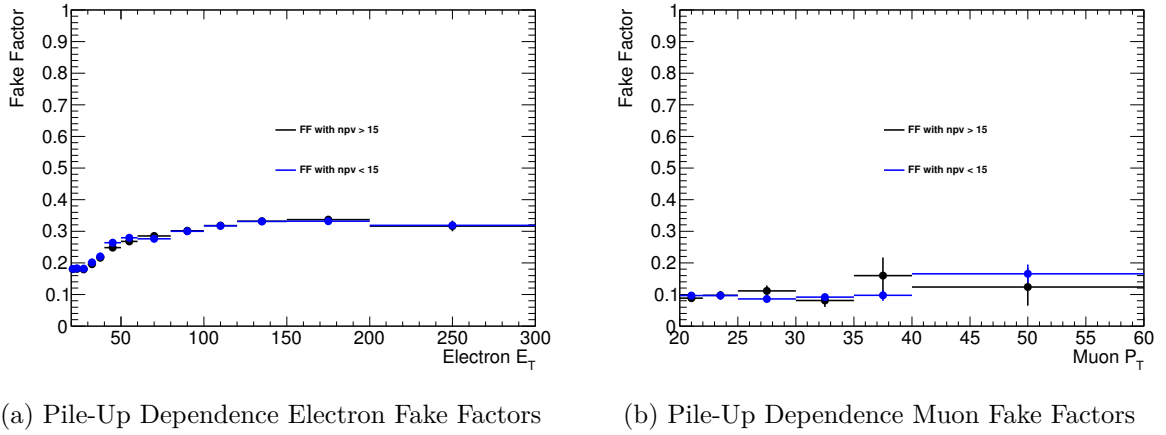


Figure A.16: Raw Unscaled Fake Factors for Electrons (left) and Muons (right) displaying their pile-up dependency

A.10 Additional plots for 8 TeV signal Regions

In the main part of my thesis the invariant mass distributions for the different channels in the signal channel are given. Furthermore the distributions for the leading leptons η and p_T distributions are given. Appended here are the distributions for the subleading leptons in η and p_T in Fig. A.18 and Fig. A.17 respectively.

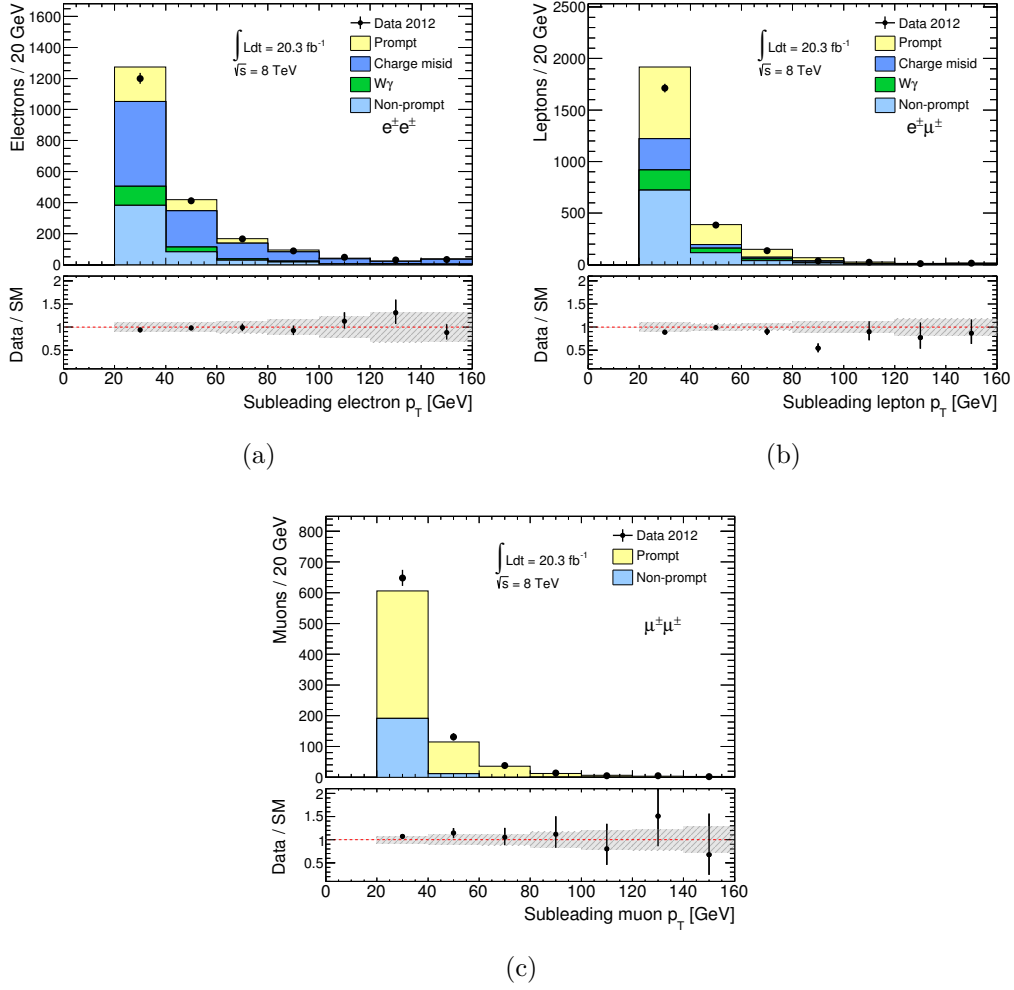


Figure A.17: The p_T distributions for the subleading lepton in (a) $e^\pm e^\pm$ (b) $e^\pm \mu^\pm$ and (c) $\mu^\pm \mu^\pm$ pairs in the same-sign signal region. The hashed grey area corresponds to the total systematic uncertainties.

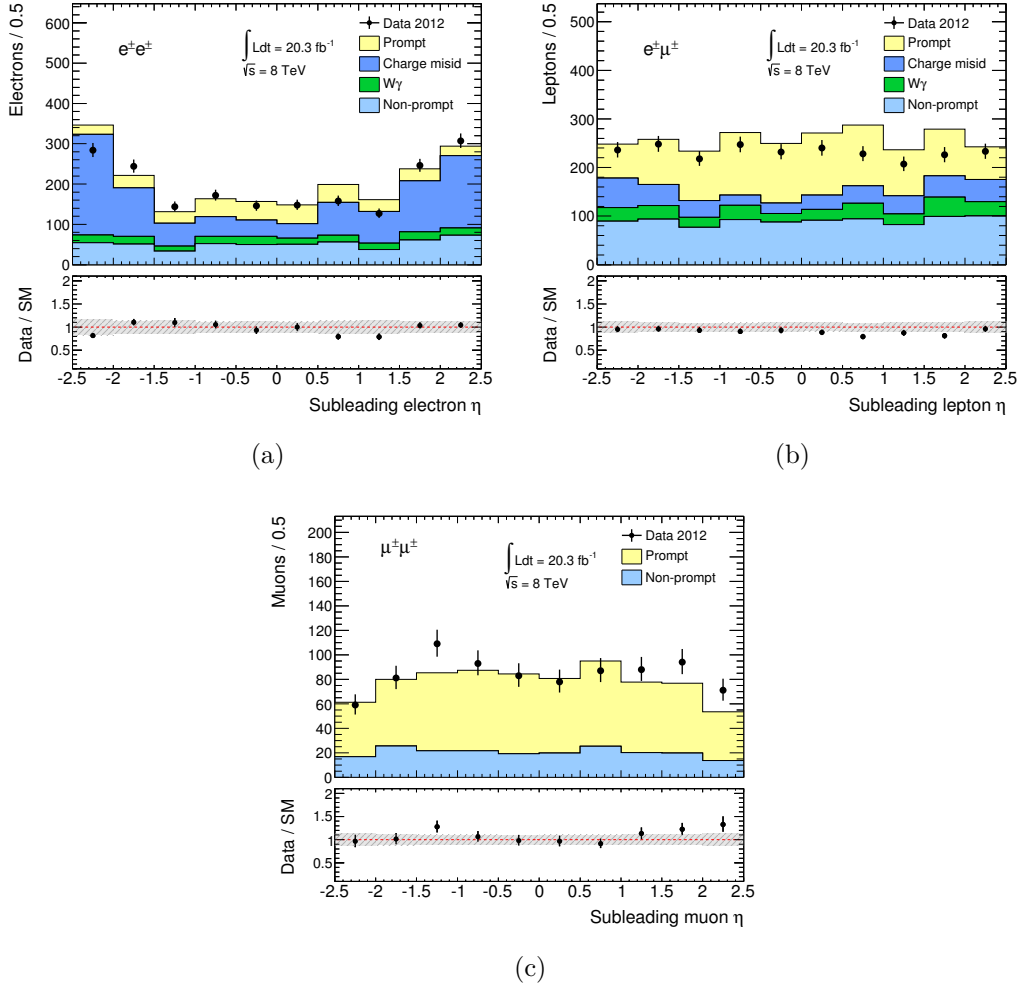


Figure A.18: The η distribution of the subleading lepton in (a) $e^{\pm}e^{\pm}$ (b) $e^{\pm}\mu^{\pm}$ and (c) $\mu^{\pm}\mu^{\pm}$ pairs in the same-sign signal region. The hashed grey area corresponds to the total systematic uncertainties.

A.11 Jet Multiplicity Distributions

Unlike the 7 TeV, this year we wished to investigate the number of reconstructed jets distribution as well as the mass distribution. The reason being, that many BSM theories predict a specific number of associated jets with the events, hence for theorists checking their models having a handle on the number of jets is important.

The number of reconstructed jets per SS dimuon pair are shown in Fig. A.19. The number of events in 3 regions, number of jets is zero, equal or greater than 1, and equal or greater than 2, are given in Tables A.7.

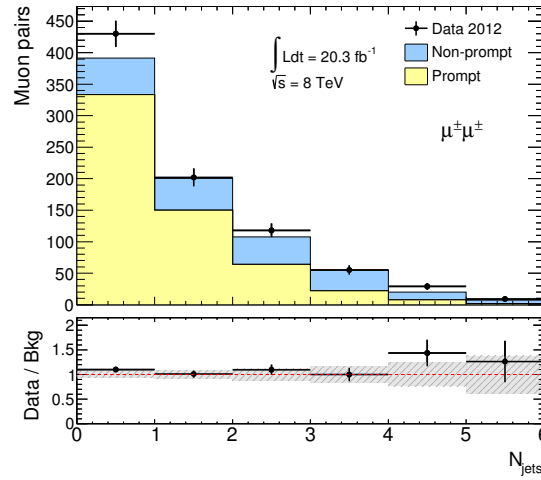


Figure A.19: Number of jets with $p_T > 30$ GeV and $|\eta| < 2.8$ per $\mu^\pm\mu^\pm$ pairs in the signal region. The lower panels show the ratio of pairs found in data compared to the SM predictions. The error bars on the data points show the statistical uncertainty and the dashed band shows the total uncertainties of the predictions. The total uncertainties are the statistical and systematic uncertainties added in quadrature.

nJets	$\mu^\pm\mu^\pm$		
	= 0	≥ 1	≥ 2
Non-prompt	56.6 ± 7.7	145 ± 27	95 ± 19
Prompt	345 ± 22	249 ± 23	95 ± 15
Sum of Backgrounds	401 ± 23	394 ± 36	190 ± 24
Data	430 ± 21	413 ± 20	211 ± 15

Table A.7: Expected and observed number of pairs as a function of jet multiplicity for Signal Region.

Cross section limits of same-sign lepton pairs in association with jets

Similarly, the final numbers for the cross-section limits on the number of lepton pairs with associated reconstructed jets is given in table A.8 and shown in figure A.20. The limits vary between 8 fb and 31 fb depending on the jet requirement and the final state.

number of jets	95% CL upper limit [fb]	
	$\mu^\pm\mu^\pm$ expected	observed
= 0	$6.7^{+2.6}_{-1.9}$	10
≥ 1	$8.8^{+2.3}_{-2.3}$	10
≥ 2	$5.8^{+2.0}_{-1.8}$	8

Table A.8: Upper limits at 95% CL on the fiducial cross section for same-sign dilepton pairs with $m_{\ell\ell} > 15$ GeV from non-SM signals with no jet or at least one or two jets reconstructed in the event with $p_T > 30$ GeV and $|\eta| < 2.8$. The expected limits and their 1σ uncertainties are given together with the observed limits as obtained from the data.

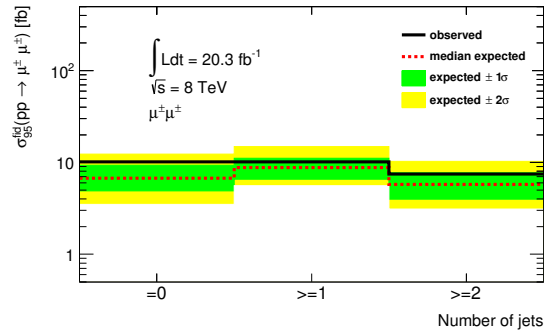


Figure A.20: 95% CL upper limits on the fiducial cross section for events with $\mu^\pm\mu^\pm$ pairs as a function of the accompanying jets with $p_T > 30$ GeV and $|\eta| < 2.8$. The 1 and 2 sigma uncertainty bands are shown in green and yellow respectively.

A.12 Number of Same Sign pairs per Event

In the 8 TeV analysis the number of same-sign pairs were used to set limits on the production of non-SM same-sign dilepton pairs. However, one event can theoretically contain more than one same-sign pair candidate hence the same event can be used in multiple channels and even more than once in the same channel. For instance if you had $e^+\mu^-\mu^-\mu^+$ then you would have one same-sign pair in the $e\mu$ channel and one in the $\mu\mu$ channel. Multiple pairs in the same events is however expected to happen at a low rate (0.1% in each channel). The number of expected events with more than one pair for each channel and corresponding process is given in Table A.9.

Sample	Multipair events (%)		
	ee	$e\mu$	$\mu\mu$
Non-prompt	0.0	0.0	0.0
WZ	0.2	0.1	0.0
$ZZ \rightarrow lll$	0.6	1.5	0.8
$W^\pm W^\pm jj$	0.0	0.0	0.0
DPI	0.0-1.7	0.0-1.3	0.0-0.7
$t\bar{t}W$	0.0-0.2	0.0	0.0
$t\bar{t}Z$	0.0-0.5	0.0-0.2	0.0-0.3
W/γ	0.0	0.0	0.0
Drell-Yan	0.0-0.8	0.0	0.0
$t\bar{t}$	0.0	0.0	0.0
WW	0.0	0.0	0.0
Wt	0.0	0.0	0.0
Total Background	0.1	0.1	0.1
$H^{\pm\pm}$	0.5-6.4	2.9-9.6	1.0-4.4

Table A.9: Percentage of events with multiple same-sign pairs in the $e^\pm e^\pm$, $e^\pm \mu^\pm$, $\mu^\pm \mu^\pm$ channels.

A.13 Fiducial Efficiencies

The fiducial efficiency for various BSM models were measured as a function of different model parameters and in the three SS dilepton channels. The lowest fiducial efficiency across all the models for each channel was taken to be the fiducial efficiency. Tables A.10 - A.15 show the fiducial efficiency for the entire range of models considered.

Table A.10: Fiducial Efficiency (%) in the ee final state for several new physics models. The uncertainties are statistical.

Model	fiducial efficiency (%)			
	$M > 15$ GeV	$M > 100$ GeV	$M > 200$ GeV	$M > 300$ GeV
$H^{\pm\pm}$ ($m = 100$ GeV)	n/a	n/a	n/a	n/a
$H^{\pm\pm}$ ($m = 150$ GeV)	63.4 ± 1.2	64.5 ± 1.2	n/a	n/a
$H^{\pm\pm}$ ($m = 200$ GeV)	62.4 ± 1.1	62.9 ± 1.1	n/a	n/a
$H^{\pm\pm}$ ($m = 250$ GeV)	62.3 ± 1.0	62.6 ± 1.0	69.3 ± 1.2	n/a
$H^{\pm\pm}$ ($m = 300$ GeV)	63.7 ± 1.0	63.8 ± 1.0	69.0 ± 1.1	n/a
$H^{\pm\pm}$ ($m = 350$ GeV)	63.3 ± 1.0	63.3 ± 1.0	67.0 ± 1.1	73.5 ± 1.3
$H^{\pm\pm}$ ($m = 400$ GeV)	63.0 ± 0.9	63.0 ± 1.0	66.1 ± 1.0	71.2 ± 1.2
$H^{\pm\pm}$ ($m = 450$ GeV)	62.9 ± 0.9	63.0 ± 0.9	65.1 ± 1.0	69.2 ± 1.1
$H^{\pm\pm}$ ($m = 500$ GeV)	63.1 ± 0.9	63.2 ± 0.9	65.0 ± 1.0	68.4 ± 1.1
$H^{\pm\pm}$ ($m = 600$ GeV)	63.2 ± 0.9	63.2 ± 0.9	64.6 ± 1.0	66.9 ± 1.0
$H^{\pm\pm}$ ($m = 1000$ GeV)	60.4 ± 0.9	60.4 ± 0.9	60.8 ± 0.9	61.8 ± 0.9
W_R ($m(W_R) = 1000$ GeV, $m(N_R) = 250$ GeV)	66.8 ± 3.3	66.8 ± 3.3	68.3 ± 3.5	70.8 ± 3.9
W_R ($m(W_R) = 1000$ GeV, $m(N_R) = 500$ GeV)	68.6 ± 3.1	69.1 ± 3.2	70.6 ± 3.4	72.8 ± 3.9
W_R ($m(W_R) = 1000$ GeV, $m(N_R) = 750$ GeV)	66.5 ± 3.2	67.4 ± 3.2	69.7 ± 3.6	71.4 ± 4.4
W_R ($m(W_R) = 1400$ GeV, $m(N_R) = 350$ GeV)	65.4 ± 3.2	65.7 ± 3.2	66.4 ± 3.3	67.3 ± 3.4
W_R ($m(W_R) = 1400$ GeV, $m(N_R) = 700$ GeV)	70.2 ± 3.1	70.6 ± 3.1	71.5 ± 3.3	72.4 ± 3.5
W_R ($m(W_R) = 1400$ GeV, $m(N_R) = 1050$ GeV)	70.8 ± 3.1	71.0 ± 3.2	72.6 ± 3.4	73.3 ± 3.7
W_R ($m(W_R) = 2000$ GeV, $m(N_R) = 500$ GeV)	63.9 ± 3.0	64.0 ± 3.0	64.8 ± 3.0	65.1 ± 3.1
W_R ($m(W_R) = 2000$ GeV, $m(N_R) = 1000$ GeV)	65.4 ± 2.9	65.4 ± 2.9	66.1 ± 3.0	66.9 ± 3.1
W_R ($m(W_R) = 2000$ GeV, $m(N_R) = 1500$ GeV)	71.0 ± 3.1	71.1 ± 3.1	72.9 ± 3.3	73.6 ± 3.5

Table A.11: Fiducial Efficiency (%) in the ee final state for several new physics models. The uncertainties are statistical.

Model	fiducial efficiency (%)			
	$M > 15$ GeV	$M > 100$ GeV	$M > 200$ GeV	$M > 300$ GeV
$b' \rightarrow qW$ (400 GeV)	48.3 ± 3.8	50.3 ± 4.4	61.4 ± 7.7	67.2 ± 12.9
$b' \rightarrow qW$ (500 GeV)	52.5 ± 3.5	54.4 ± 3.9	58.4 ± 6.0	57.9 ± 9.2
$b' \rightarrow qW$ (600 GeV)	53.0 ± 3.4	54.4 ± 3.7	60.6 ± 5.5	60.8 ± 8.3
$b' \rightarrow qW$ (650 GeV)	52.7 ± 3.3	56.8 ± 3.8	62.7 ± 5.3	67.6 ± 8.1
$b' \rightarrow qW$ (700 GeV)	55.9 ± 3.4	58.6 ± 3.7	63.0 ± 5.0	70.8 ± 7.5
$b' \rightarrow qW$ (800 GeV)	53.9 ± 3.1	56.0 ± 3.3	59.5 ± 4.4	64.4 ± 6.1
$b' \rightarrow qW$ (900 GeV)	49.5 ± 2.9	51.4 ± 3.1	55.4 ± 4.0	56.8 ± 5.3
$b' \rightarrow qW$ (950 GeV)	52.3 ± 3.1	52.8 ± 3.2	57.5 ± 4.1	62.3 ± 5.6
$b' \rightarrow qW$ (1000 GeV)	50.3 ± 2.9	52.6 ± 3.2	56.2 ± 4.0	61.1 ± 5.2
$b' \rightarrow tW$ (450 GeV)	53.1 ± 2.2	57.8 ± 2.6	68.1 ± 4.4	71.6 ± 7.3
$b' \rightarrow tW$ (500 GeV)	52.6 ± 2.1	55.1 ± 2.3	61.0 ± 3.7	72.2 ± 6.7
$b' \rightarrow tW$ (550 GeV)	50.5 ± 2.0	53.6 ± 2.2	61.2 ± 3.5	64.9 ± 5.3
$b' \rightarrow tW$ (600 GeV)	51.6 ± 2.0	53.4 ± 2.2	57.3 ± 3.1	60.0 ± 4.9
$b' \rightarrow tW$ (650 GeV)	51.1 ± 1.9	54.3 ± 2.2	62.2 ± 3.2	66.1 ± 4.9
$b' \rightarrow tW$ (700 GeV)	48.9 ± 1.9	50.9 ± 2.0	55.6 ± 2.8	58.0 ± 4.0
$b' \rightarrow tW$ (800 GeV)	49.2 ± 1.8	51.3 ± 2.0	56.4 ± 2.7	58.6 ± 3.8
$b' \rightarrow tW$ (900 GeV)	50.4 ± 1.8	52.2 ± 1.9	56.6 ± 2.5	60.2 ± 3.4
$b' \rightarrow tW$ (1000 GeV)	49.0 ± 1.8	50.6 ± 1.9	52.7 ± 2.4	57.2 ± 3.2
$cZBM$ ($m(DQ)$ = 2500 GeV, $m(LQ)$ = 1000 GeV)	61.3 ± 2.1	61.3 ± 2.1	62.1 ± 2.2	62.3 ± 2.2
$cZBM$ ($m(DQ)$ = 2500 GeV, $m(LQ)$ = 1200 GeV)	62.1 ± 2.1	62.1 ± 2.1	62.5 ± 2.2	63.8 ± 2.3
$cZBM$ ($m(DQ)$ = 3000 GeV, $m(LQ)$ = 1000 GeV)	55.7 ± 2.0	55.7 ± 2.0	56.0 ± 2.0	56.0 ± 2.1
$cZBM$ ($m(DQ)$ = 3000 GeV, $m(LQ)$ = 1200 GeV)	56.0 ± 2.0	56.0 ± 2.0	56.3 ± 2.0	57.0 ± 2.1
$cZBM$ ($m(DQ)$ = 3500 GeV, $m(LQ)$ = 1000 GeV)	51.2 ± 1.9	51.2 ± 1.9	51.3 ± 1.9	51.0 ± 1.9
$cZBM$ ($m(DQ)$ = 3500 GeV, $m(LQ)$ = 1200 GeV)	51.3 ± 1.9	51.3 ± 1.9	51.5 ± 1.9	51.6 ± 1.9
$cZBM$ ($m(DQ)$ = 3500 GeV, $m(LQ)$ = 1400 GeV)	49.7 ± 1.8	49.7 ± 1.8	50.1 ± 1.9	50.4 ± 1.9

Table A.12: Fiducial Efficiency (%) in the $e\mu$ final state for several new physics models. The uncertainties are statistical.

Model	fiducial efficiency (%)			
	$M > 15$ GeV	$M > 100$ GeV	$M > 200$ GeV	$M > 300$ GeV
$H^{\pm\pm}$ ($m = 100$ GeV)	63.1 ± 0.9	n/a	n/a	n/a
$H^{\pm\pm}$ ($m = 150$ GeV)	65.6 ± 0.8	68.9 ± 0.8	n/a	n/a
$H^{\pm\pm}$ ($m = 200$ GeV)	64.4 ± 0.7	66.4 ± 0.7	n/a	n/a
$H^{\pm\pm}$ ($m = 250$ GeV)	64.9 ± 0.7	66.0 ± 0.7	72.3 ± 0.8	n/a
$H^{\pm\pm}$ ($m = 300$ GeV)	64.2 ± 0.7	64.8 ± 0.7	69.4 ± 0.8	n/a
$H^{\pm\pm}$ ($m = 350$ GeV)	63.9 ± 0.7	64.3 ± 0.7	68.1 ± 0.7	73.5 ± 0.9
$H^{\pm\pm}$ ($m = 400$ GeV)	63.2 ± 0.7	63.5 ± 0.7	66.6 ± 0.7	71.1 ± 0.8
$H^{\pm\pm}$ ($m = 450$ GeV)	63.2 ± 0.6	63.4 ± 0.7	65.8 ± 0.7	69.9 ± 0.8
$H^{\pm\pm}$ ($m = 500$ GeV)	62.5 ± 0.6	62.6 ± 0.6	64.4 ± 0.7	67.5 ± 0.7
$H^{\pm\pm}$ ($m = 600$ GeV)	62.0 ± 0.6	62.1 ± 0.6	63.5 ± 0.7	65.9 ± 0.7
$H^{\pm\pm}$ ($m = 1000$ GeV)	59.1 ± 0.6	59.2 ± 0.6	59.5 ± 0.6	60.5 ± 0.6
W_R ($m(W_R) = 1000$ GeV, $m(N_R) = 250$ GeV)	67.1 ± 2.3	67.6 ± 2.3	67.5 ± 2.3	68.9 ± 2.5
W_R ($m(W_R) = 1000$ GeV, $m(N_R) = 500$ GeV)	72.4 ± 2.3	72.8 ± 2.3	73.3 ± 2.4	74.9 ± 2.7
W_R ($m(W_R) = 1000$ GeV, $m(N_R) = 750$ GeV)	71.7 ± 2.3	72.6 ± 2.4	73.9 ± 2.6	74.5 ± 3.1
W_R ($m(W_R) = 1400$ GeV, $m(N_R) = 350$ GeV)	68.7 ± 2.2	69.0 ± 2.3	69.6 ± 2.3	71.0 ± 2.4
W_R ($m(W_R) = 1400$ GeV, $m(N_R) = 700$ GeV)	70.8 ± 2.2	71.3 ± 2.2	72.2 ± 2.3	73.0 ± 2.4
W_R ($m(W_R) = 1400$ GeV, $m(N_R) = 1050$ GeV)	70.6 ± 2.2	71.2 ± 2.2	72.7 ± 2.4	73.2 ± 2.5
W_R ($m(W_R) = 2000$ GeV, $m(N_R) = 500$ GeV)	65.7 ± 2.2	65.7 ± 2.2	66.1 ± 2.2	66.5 ± 2.2
W_R ($m(W_R) = 2000$ GeV, $m(N_R) = 1000$ GeV)	70.7 ± 2.2	70.7 ± 2.2	71.7 ± 2.2	72.2 ± 2.3
W_R ($m(W_R) = 2000$ GeV, $m(N_R) = 1500$ GeV)	69.5 ± 2.1	69.8 ± 2.1	70.5 ± 2.2	71.7 ± 2.3

Table A.13: Fiducial Efficiency (%) in the $e\mu$ final state for several new physics models. The uncertainties are statistical.

Model	fiducial efficiency (%)			
	$M > 15$ GeV	$M > 100$ GeV	$M > 200$ GeV	$M > 300$ GeV
$b' \rightarrow qW$ (400 GeV)	51.7 ± 2.5	58.7 ± 3.3	70.5 ± 6.0	69.6 ± 9.7
$b' \rightarrow qW$ (500 GeV)	51.6 ± 2.2	56.4 ± 2.8	61.4 ± 4.3	62.5 ± 6.2
$b' \rightarrow qW$ (600 GeV)	52.1 ± 2.1	55.3 ± 2.5	58.9 ± 3.5	61.2 ± 5.2
$b' \rightarrow qW$ (650 GeV)	52.4 ± 2.1	55.6 ± 2.4	61.1 ± 3.4	68.0 ± 5.3
$b' \rightarrow qW$ (700 GeV)	51.4 ± 2.1	54.4 ± 2.4	59.7 ± 3.3	62.7 ± 4.7
$b' \rightarrow qW$ (800 GeV)	51.2 ± 2.0	53.3 ± 2.3	54.9 ± 2.9	59.9 ± 4.2
$b' \rightarrow qW$ (900 GeV)	51.3 ± 2.0	53.6 ± 2.2	56.3 ± 2.8	58.2 ± 3.8
$b' \rightarrow qW$ (950 GeV)	51.4 ± 1.9	54.4 ± 2.2	59.5 ± 2.9	61.9 ± 3.7
$b' \rightarrow qW$ (1000 GeV)	50.2 ± 1.9	52.9 ± 2.2	55.1 ± 2.7	56.1 ± 3.5
$b' \rightarrow tW$ (450 GeV)	52.6 ± 1.3	57.2 ± 1.6	62.5 ± 2.7	65.8 ± 4.6
$b' \rightarrow tW$ (500 GeV)	51.0 ± 1.3	55.1 ± 1.5	62.4 ± 2.5	64.2 ± 4.0
$b' \rightarrow tW$ (550 GeV)	51.5 ± 1.2	55.2 ± 1.5	61.4 ± 2.4	66.5 ± 3.7
$b' \rightarrow tW$ (600 GeV)	51.5 ± 1.3	55.0 ± 1.5	59.9 ± 2.2	62.3 ± 3.3
$b' \rightarrow tW$ (650 GeV)	50.0 ± 1.2	52.7 ± 1.4	56.9 ± 2.1	61.5 ± 3.1
$b' \rightarrow tW$ (700 GeV)	52.0 ± 1.2	55.4 ± 1.4	61.4 ± 2.0	64.2 ± 2.9
$b' \rightarrow tW$ (800 GeV)	50.0 ± 1.2	52.1 ± 1.4	56.1 ± 1.8	60.9 ± 2.6
$b' \rightarrow tW$ (900 GeV)	50.1 ± 1.2	52.7 ± 1.4	56.3 ± 1.8	60.3 ± 2.5
$b' \rightarrow tW$ (1000 GeV)	49.7 ± 1.2	52.4 ± 1.3	56.1 ± 1.7	59.1 ± 2.3
$cZBM$ ($m(DQ)$ = 2500 GeV, $m(LQ)$ = 1000 GeV)	64.9 ± 1.2	65.0 ± 1.2	65.4 ± 1.2	66.0 ± 1.3
$cZBM$ ($m(DQ)$ = 2500 GeV, $m(LQ)$ = 1200 GeV)	64.0 ± 1.2	64.2 ± 1.2	64.7 ± 1.2	65.5 ± 1.2
$cZBM$ ($m(DQ)$ = 3000 GeV, $m(LQ)$ = 1000 GeV)	62.8 ± 1.2	62.9 ± 1.2	63.2 ± 1.2	63.8 ± 1.2
$cZBM$ ($m(DQ)$ = 3000 GeV, $m(LQ)$ = 1200 GeV)	63.7 ± 1.2	63.8 ± 1.2	63.9 ± 1.2	64.5 ± 1.2
$cZBM$ ($m(DQ)$ = 3500 GeV, $m(LQ)$ = 1000 GeV)	60.5 ± 1.1	60.6 ± 1.1	60.8 ± 1.1	61.0 ± 1.2
$cZBM$ ($m(DQ)$ = 3500 GeV, $m(LQ)$ = 1200 GeV)	61.5 ± 1.1	61.5 ± 1.1	61.8 ± 1.1	62.2 ± 1.2
$cZBM$ ($m(DQ)$ = 3500 GeV, $m(LQ)$ = 1400 GeV)	61.1 ± 1.1	61.2 ± 1.1	61.4 ± 1.2	61.7 ± 1.2

Table A.14: Fiducial Efficiency (%) in the $\mu\mu$ final state for several new physics models. The uncertainties are statistical.

Model	fiducial efficiency (%)			
	$M > 15$ GeV	$M > 100$ GeV	$M > 200$ GeV	$M > 300$ GeV
$H^{\pm\pm}$ ($m = 100$ GeV)	72.2 ± 1.3	n/a	n/a	n/a
$H^{\pm\pm}$ ($m = 150$ GeV)	69.4 ± 1.1	72.5 ± 1.2	n/a	n/a
$H^{\pm\pm}$ ($m = 200$ GeV)	67.4 ± 1.0	69.0 ± 1.1	n/a	n/a
$H^{\pm\pm}$ ($m = 250$ GeV)	64.3 ± 1.0	65.3 ± 1.0	70.6 ± 1.1	n/a
$H^{\pm\pm}$ ($m = 300$ GeV)	62.6 ± 0.9	63.3 ± 0.9	67.2 ± 1.0	n/a
$H^{\pm\pm}$ ($m = 350$ GeV)	61.7 ± 0.9	62.0 ± 0.9	65.3 ± 1.0	69.1 ± 1.1
$H^{\pm\pm}$ ($m = 400$ GeV)	60.7 ± 0.9	61.0 ± 0.9	63.5 ± 0.9	67.5 ± 1.1
$H^{\pm\pm}$ ($m = 450$ GeV)	59.3 ± 0.9	59.4 ± 0.9	61.4 ± 0.9	64.5 ± 1.0
$H^{\pm\pm}$ ($m = 500$ GeV)	58.9 ± 0.9	59.1 ± 0.9	60.6 ± 0.9	63.6 ± 1.0
$H^{\pm\pm}$ ($m = 600$ GeV)	56.6 ± 0.8	56.6 ± 0.8	57.6 ± 0.8	59.5 ± 0.9
$H^{\pm\pm}$ ($m = 1000$ GeV)	51.1 ± 0.8	51.1 ± 0.8	51.4 ± 0.8	52.2 ± 0.8
W_R ($m(W_R) = 1000$ GeV, $m(N_R) = 250$ GeV)	65.2 ± 3.0	65.2 ± 3.0	64.8 ± 3.1	64.1 ± 3.3
W_R ($m(W_R) = 1000$ GeV, $m(N_R) = 500$ GeV)	67.1 ± 3.0	67.8 ± 3.0	68.7 ± 3.2	69.8 ± 3.6
W_R ($m(W_R) = 1000$ GeV, $m(N_R) = 750$ GeV)	65.3 ± 2.9	66.1 ± 3.0	67.2 ± 3.3	68.1 ± 3.9
W_R ($m(W_R) = 1400$ GeV, $m(N_R) = 350$ GeV)	63.6 ± 2.9	63.6 ± 2.9	64.1 ± 3.0	64.0 ± 3.1
W_R ($m(W_R) = 1400$ GeV, $m(N_R) = 700$ GeV)	63.6 ± 2.8	63.6 ± 2.8	64.2 ± 2.9	63.9 ± 3.0
W_R ($m(W_R) = 1400$ GeV, $m(N_R) = 1050$ GeV)	64.6 ± 2.8	65.4 ± 2.9	66.2 ± 3.0	67.0 ± 3.3
W_R ($m(W_R) = 2000$ GeV, $m(N_R) = 500$ GeV)	58.3 ± 2.8	58.3 ± 2.8	58.6 ± 2.8	58.7 ± 2.9
W_R ($m(W_R) = 2000$ GeV, $m(N_R) = 1000$ GeV)	59.0 ± 2.7	59.4 ± 2.7	59.5 ± 2.8	59.2 ± 2.8
W_R ($m(W_R) = 2000$ GeV, $m(N_R) = 1500$ GeV)	60.2 ± 2.7	60.3 ± 2.7	60.7 ± 2.8	60.5 ± 2.9

Table A.15: Fiducial Efficiency (%) in the $\mu\mu$ final state for several new physics models. The uncertainties are statistical.

Model	fiducial efficiency (%)			
	$M > 15$ GeV	$M > 100$ GeV	$M > 200$ GeV	$M > 300$ GeV
$b' \rightarrow qW$ (400 GeV)	54.0 ± 3.5	56.4 ± 4.2	57.8 ± 6.8	66.7 ± 11.9
$b' \rightarrow qW$ (500 GeV)	56.5 ± 3.4	57.2 ± 3.9	58.5 ± 5.8	62.5 ± 9.2
$b' \rightarrow qW$ (600 GeV)	54.6 ± 3.1	57.3 ± 3.7	62.3 ± 5.3	69.6 ± 8.6
$b' \rightarrow qW$ (650 GeV)	54.1 ± 2.9	55.2 ± 3.3	58.7 ± 4.6	62.1 ± 6.7
$b' \rightarrow qW$ (700 GeV)	54.7 ± 3.0	56.8 ± 3.3	60.0 ± 4.8	61.9 ± 6.8
$b' \rightarrow qW$ (800 GeV)	53.6 ± 2.9	55.0 ± 3.2	57.2 ± 4.0	57.2 ± 5.2
$b' \rightarrow qW$ (900 GeV)	48.8 ± 2.7	48.9 ± 2.9	50.6 ± 3.6	49.4 ± 4.7
$b' \rightarrow qW$ (950 GeV)	46.0 ± 2.6	47.5 ± 2.9	48.1 ± 3.5	48.8 ± 4.6
$b' \rightarrow qW$ (1000 GeV)	48.2 ± 2.7	50.3 ± 3.0	52.0 ± 3.7	53.4 ± 4.8
$b' \rightarrow tW$ (450 GeV)	55.4 ± 1.9	57.0 ± 2.3	60.0 ± 3.8	62.5 ± 6.2
$b' \rightarrow tW$ (450 GeV)	55.4 ± 1.9	57.0 ± 2.3	60.0 ± 3.8	62.5 ± 6.2
$b' \rightarrow tW$ (500 GeV)	53.7 ± 1.8	55.6 ± 2.2	61.6 ± 3.6	65.3 ± 5.8
$b' \rightarrow tW$ (550 GeV)	54.1 ± 1.8	55.5 ± 2.1	60.8 ± 3.3	61.6 ± 5.0
$b' \rightarrow tW$ (600 GeV)	52.7 ± 1.8	55.5 ± 2.1	57.4 ± 3.0	58.6 ± 4.4
$b' \rightarrow tW$ (650 GeV)	54.1 ± 1.8	55.1 ± 2.0	56.4 ± 2.8	56.1 ± 4.0
$b' \rightarrow tW$ (700 GeV)	52.7 ± 1.8	54.0 ± 2.0	56.5 ± 2.7	56.8 ± 3.8
$b' \rightarrow tW$ (800 GeV)	52.9 ± 1.8	54.3 ± 2.0	55.8 ± 2.6	57.2 ± 3.5
$b' \rightarrow tW$ (900 GeV)	49.7 ± 1.7	51.3 ± 1.9	51.7 ± 2.3	54.2 ± 3.0
$b' \rightarrow tW$ (1000 GeV)	48.8 ± 1.7	49.8 ± 1.8	51.5 ± 2.3	52.3 ± 3.0
$cZBM$ ($m(DQ)$ = 2500 GeV, $m(LQ)$ = 1000 GeV)	56.6 ± 1.2	56.7 ± 1.2	56.9 ± 1.2	57.0 ± 1.2
$cZBM$ ($m(DQ)$ = 2500 GeV, $m(LQ)$ = 1200 GeV)	55.8 ± 1.1	55.9 ± 1.1	56.3 ± 1.2	56.7 ± 1.2
$cZBM$ ($m(DQ)$ = 3000 GeV, $m(LQ)$ = 1000 GeV)	53.8 ± 1.1	53.8 ± 1.1	53.9 ± 1.1	54.0 ± 1.2
$cZBM$ ($m(DQ)$ = 3000 GeV, $m(LQ)$ = 1200 GeV)	54.3 ± 1.1	54.4 ± 1.1	54.4 ± 1.1	54.6 ± 1.2
$cZBM$ ($m(DQ)$ = 3500 GeV, $m(LQ)$ = 1000 GeV)	51.9 ± 1.1	51.9 ± 1.1	51.9 ± 1.1	52.2 ± 1.1
$cZBM$ ($m(DQ)$ = 3500 GeV, $m(LQ)$ = 1200 GeV)	52.2 ± 1.1	52.2 ± 1.1	52.5 ± 1.1	52.6 ± 1.1
$cZBM$ ($m(DQ)$ = 3500 GeV, $m(LQ)$ = 1400 GeV)	52.4 ± 1.1	52.4 ± 1.1	52.5 ± 1.1	52.6 ± 1.1

*Don't gobblefunk around
with words*

Roald Dahl, *BFG*

Glossary

Caveat: These concise definitions aim to serve as helpful prompts for phrases used throughout this thesis and as such are not necessarily complete in and of themselves. Furthermore some definitions are specific to this thesis and may be used alternatively elsewhere.

SM - Standard Model.

LHC - Large Hadron Collider

ATLAS - A multi-purpose detector at LHC, CERN

TRT - Transition Radiation Tracker, part of the inner detector in ATLAS.

Dilepton - A pair of leptons (In this case not including taus, ee , $e\mu$, $\mu\mu$)

QCD - Quantum Chromo Dynamics, the description of the strong force.

QED - Quantum Electro Dynamics, the description of the electroweak force.

ToT - Time over Threshold, is a observable in the TRT whereby one measures the time in which the electric signal (created by ionisation in the straws) is above a well defined threshold.

Express Stream - A dataset which contains roughly 10% of the data from a given run, most of which being high p_T events with triggered leptons and jets.

Impact Parameters, d_0, z_0 - Parameters which describe how close a particles trajectory is to the initial collision point. These include d_0 the distance from origin in the transverse direction (with error $\sigma(d_0)$) and z_0 the longitudinal distance of the perigee to the origin (often used as the projection $z_0 \sin\theta$).

Clusters - A grouping of hits or energy deposits in a detector, often used in tracking

algorithms and energy reconstruction.

ToF - Time of flight (of a particle in the detector).

Drift Radius - The reconstructed distance from the closest ionisation cluster in a TRT straw to the wire anode at the centre.

SUSY - Supersymmetry

Jets - An algorithmically reconstructed object made from energy depositions in a detector with aim to reconstruct a hadronic shower.

Prompt - Particles which originate from (or very close to) the primary interaction.

Isolated - A particle is isolated if it has little showering and few associated jets accompanying the trajectory of the particle within some pre-defined spatial cone

Loose, Medium, Tight - These are ATLAS electron identification criteria categories. These selections apply cuts on the transverse shower shapes in the first and second layer of the electromagnetic calorimeter, leakage into the hadronic calorimeter, ID track quality, cluster-track matching and vetoing of conversions. The selection is done by applying cuts on each of these criteria and are optimised as a function of η and p_T . With increasing tightness of the selection more criteria are used and more stringent requirements are applied.

LAr - Liquid Argon

PtcconeXX - This is an ATLAS constructed isolation variable. It is the sum of the transverse momenta of all particles in a cone of size $\Delta R = XX$ (constructed in the $\eta - \phi$ phase space) excepting that of the lepton itself.

EtconeXX - a cone of specific size $\Delta R = XX$ is constructed in the $\eta - \phi$ phase space centred on the calorimeter cell with which the electron track passes. Then the energy deposited in the adjacent cells within the cone are summed (ignoring the 5x7 cells in the centre cone).

Primary Vertex - The primary vertex here is defined as the vertex which has the highest squared p_T sum of associated tracks (with $p_T > 0.4$ GeV) found in the event.

JVF -Jet Vertex Fraction, the sum of the transverse momenta of tracks associated to the jet and originating from the primary vertex divided by the sum p_T of all tracks associated

to the jet.

Q_{ID} - The muon charge measured in the Inner Detector of ATLAS.

Q_{MX} - The muon charge measured in the muon spectrometer of ATLAS.

$m_{\ell\ell}$ - The invariant mass of a lepton pair.

EF_mu18_tight_mu8_EFFS - A dimuon trigger where the lead muon must have $p_T > 18$ and subleading $p_T > 8$, the *tight* and *EFFS* parts refer to the level of reconstruction and electronic requirements on the muon signal.

EF_e12vh_medium_mu8 - A dilepton trigger where the electron must have $p_T > 12$ and the muon $p_T > 8$ in order to be triggered. The *vh* and *medium* refer to the reconstruction requirements on the electron which fires the trigger.

EF_2e12Tvh_loose1 - A dielectron trigger where both electrons must have $p_T > 12$ in order to be triggered. The *Tvh* and *loose1* refer to the reconstruction requirements on the electrons which fires the trigger.

Prompt Backgrounds - SM processes which lead to prompt same-sign dileptons (for *prompt* definition see above).

Charge Flips Background - SM processes which produce prompt opposite sign leptons where one or more of the leptons has its charge misidentified.

Conversion Backgrounds - SM processes where a prompt photon converts into an electron-positron pair.

Fakes (Non-prompts) - A fake lepton is either a) A jet, hadron or photon which is reconstructed as an electron or muon (in that sense a *true* fake). b) Another particle from the primary interaction (e.g. a b-jet) which decays in flight to give an electron or muon (in this sense a *real* lepton which is non-prompt).

Tag and Probe - A standard method in ATLAS which compares two objects (a tag object and a probe object) which are assumed to have very similar properties, whereby one sets stringent criteria on the *tag* and uses less stringent criteria on the *probe* object in order to investigate a desired property.

Charge flip probability - The probability for an electron of a given η to have its charge misidentified.

Staco combined muon - A muon which is reconstructed using the ATLAS Staco algorithm and uses the combined hits from the muon track in the inner detector and the muon

spectrometer.

Z peak - The invariant mass resonance peak observed when studying decay products from the Z boson.

Signal Region - This is the region of interest to the analysis, the region is defined by a series of selection criteria on the event and objects reconstructed in the events.

Validation Region - A region which is strictly separate from the signal region, which is used to test and validate a background, method or scale factors to be used in the Signal Region.

Fake factor - Is the probability for an lepton of a given p_T and η (with some distinguishing criteria which is mutually exclusive from the signal criteria) to pass the signal criteria.

Numerator Object - A lepton whom fulfils all the signal region selection criteria.

Denominator Object - An object whom is a *fake* candidate and as such fails one or more of the signal selection criteria.

Underlying Jet - Is a jet which *fakes* as another object such as an electron or photon.

Awayside jet - A jet which is separated in $\eta - \phi$ space from another object (such as an electron) by some ΔR is considered an *awayside jet*.

Prompt Contamination - In regions defined to be fake enriched (ideally solely fakes) there is a probability whereby some prompt SM processes still permeate the region, and thus contaminate the fake region.

Weak Isolation - An isolation requirement on the electron or muon which is weaker than the signal region isolation.

Fail- D_0 - Lepton fails the D_0 requirement on the signal selection.

Leading - The lepton in the pair of leptons which has greatest transverse momentum.

Subleading - The lepton in the pair of leptons which has the second greatest transverse

momentum.

NLO - Next-to-leading order, mostly to describe to what level the cross-section of a particular process was evaluated at.

LO - Leading Order.

NNLO - Next-to-next-to-leading Order.

PDF - Parton Distribution Function, the probability density for finding a particle with a certain momentum fraction x at a given resolution scale.

Egamma - A working group in ATLAS studying photons and electrons.

Fiducial Region - A set of criteria one can apply to particles at generator (truth) level (i.e. particles directly produced and hadronised by for example Pythia) to emulate as closely as possible the analysis selection criteria on the reconstructed objects used in the analysis. The phase space constrained after these criteria is known as the *fiducial region*.

Fiducial Cross-section - The cross-section for a process with respect to the efficiency of reconstructing particles occupying the fiducial region.

PDG ID - Particle Data Group Identification Number, for a specific particle.

Event Topology - The shape, number and distribution of final state particles in an event.

Boosted - A particle is said to be *boosted* if it is of sufficiently high energy that even with respect to the frame of centre-of-momentum (or sometimes Lab frame) it gets a Lorentz boost.

CL_s - Modified frequentist confidence limit.

Likelihood - In statistics a likelihood function is a function of the *parameters* of a statistical model. Thus the likelihood function provides the likelihood for a set of parameters θ given a particular outcome x . This likelihood is equivalent to the probability for a observing outcome x given a set of parameters, θ . Although often used synonymously *probability* and *likelihood* are distinguished on the roles of the outcomes and parameters of a model, $L(\theta|x) = P(x|\theta)$.

DCH - Doubly Charged Higgs.

New Physics - Physics beyond the Standard Model.

MET or E_T^{miss} - Missing transverse energy is a variable which describes the transverse

component of the energy unaccounted for by the detector. It is obtained from the negative vector sum of the momenta of all particles detected in the event.

M_T - A transverse mass variable which helps to discriminate in the case where one of the decay products is invisible (undetectable). The transverse mass $m_T = \sqrt{2 \cdot E_T^l \cdot E_T^{miss} \cdot (1 - \cos \Delta\phi)}$. Here, $\Delta\phi$ is the azimuthal angle between the directions of the electron and the missing transverse momentum (with magnitude E_T^{miss}).

Bibliography

- [1] “CERN Courier Nov 1, 2002.” <http://cerncourier.com/cws/article/cern/28742>.
- [2] Henry Enfield, *John Dalton and the Rise of Modern Chemistry*. Century science, 2011.
- [3] J.J.Thomson, *Cathode rays*, Philosophical Magazine **44** (1897) 293.
- [4] E.Rutherford, *The scattering of α and β particles by Matter and the Structure of the Atom*, Philosophical Magazine **21** (1911) 669–688.
- [5] C.D.Anderson, *The positive electron*, Physical Review **43** no. 6, (1933) 491–494.
- [6] M. Gell-Mann, *A Schematic Model of Baryons and Mesons*, Phys.Lett. **8** (1964) 214–215.
- [7] G. Zweig, *An $SU(3)$ model for strong interaction symmetry and its breaking. Version 1,*.
- [8] D.Griffiths, *Introduction to Elementary Particles*. Wiley, 2010.
- [9] G.Kane, *Modern Elementary Particle Physics: Updated Edition*. Perseus, 1993.
- [10] E. Noether, *Invariante Variationsprobleme*, Nachr. Akad. Wiss. Göttingen, II no. 2, (1918) 235–257.
- [11] “Waldegrave illustration of higgs.”
<https://www.hep.ucl.ac.uk/~djm/higgsa.html>.
- [12] H.Arodz, J.Dziarmaga, W.H.Zurek, *Patterns of Symmetry Breaking*. Nato Science Series, 2002.
- [13] Super-Kamiokande Collaboration Collaboration, Y. Fukuda et al., *Measurements of the solar neutrino flux from Super-Kamiokande’s first 300 days*, Phys.Rev.Lett. **81** (1998) 1158–1162, `hep-ex/9805021`.
- [14] “Cern Website.” www.cern.ch.
- [15] “Cern CDS Website.” www.cds.cern.ch.

- [16] CMS Collaboration Collaboration, *CMS Physics: Technical Design Report Volume 1: Detector Performance and Software*. Technical Design Report CMS. CERN, Geneva, 2006.
- [17] ATLAS Collaboration Collaboration, *ATLAS detector and physics performance: Technical Design Report, 1*. Technical Design Report ATLAS. CERN, Geneva, 1999.
- [18] ALICE Collaboration Collaboration, *ALICE: Technical proposal for a Large Ion collider Experiment at the CERN LHC*. LHC Tech. Proposal. CERN, Geneva, 1995.
- [19] *LHCb : Technical Proposal*. Tech. Proposal. CERN, Geneva, 1998.
- [20] W. Herr, B.J.Holzer, B.Muratori, *Concept of Luminosity*, Landolt-Börnstein - Group I Elementary Particles, Nuclei and Atoms (2013), [hep-ph/9306204](#).
- [21] S. van der Meer, *Calibration of the effective beam height in the ISR*, Tech. Rep. CERN-ISR-PO-68-31. ISR-PO-68-31, CERN, Geneva, 1968.
- [22] “ATLAS website.” www.atlas.ch.
- [23] ATLAS Collaboration Collaboration, *ATLAS magnet system: Technical Design Report, 1*. Technical Design Report ATLAS. CERN, Geneva, 1997.
- [24] ATLAS Collaboration Collaboration, *ATLAS inner detector: Technical Design Report, 1*. Technical Design Report ATLAS. CERN, Geneva, 1997.
- [25] G.Aad et al., *ATLAS pixel detector electronics and sensors*, Journal of Instrumentation **3** no. 07, (2008) P07007.
<http://stacks.iop.org/1748-0221/3/i=07/a=P07007>.
- [26] A. Abdesselam, T. Akimoto, P. Allport, J. Alonso, B. Anderson, et al., *The barrel modules of the ATLAS semiconductor tracker*, Nucl.Instrum.Meth. **A568** (2006) 642–671.
- [27] ATLAS Collaboration Collaboration, *ATLAS liquid-argon calorimeter: Technical Design Report*. Technical Design Report ATLAS. CERN, Geneva, 1996.
- [28] ATLAS Collaboration Collaboration, G. Aad et al., *Expected performance of the ATLAS experiment: detector, trigger and physics*,.
- [29] ATLAS Collaboration Collaboration, *ATLAS tile calorimeter: Technical Design Report*. Technical Design Report ATLAS. CERN, Geneva, 1996.
- [30] ATLAS Collaboration Collaboration, *ATLAS muon spectrometer: Technical Design Report*. Technical Design Report ATLAS. CERN, Geneva, 1997. distribution.
- [31] *Roman pots for the LHC*,.

- [32] N. Corso-Radu, H. Hadavand, M. Hauschild, R. Kehoe and S. Kolos., *Data Quality Monitoring Framework for the ATLAS experiment at the LHC*, IEEE Transactions on Nuclear Science **55** (2008).
- [33] ATLAS Collaboration Collaboration, *Particle Identification Performance of the ATLAS Transition Radiation Tracker*, Tech. Rep. ATLAS-CONF-2011-128, CERN, Geneva, Sep, 2011.
- [34] T. Cornelissen, M. Elsing, S. Fleischmann, W. Liebig, E. Moyse, and A. Salzburger, *Concepts, Design and Implementation of the ATLAS New Tracking (NEWT)*, Tech. Rep. ATL-SOFT-PUB-2007-007. ATL-COM-SOFT-2007-002, CERN, Geneva, Mar, 2007.
- [35] T. G. Cornelissen, N. Van Eldik, M. Elsing, W. Liebig, E. Moyse, N. Piacquadio, K. Prokofiev, A. Salzburger, and A. Wildauer, *Updates of the ATLAS Tracking Event Data Model (Release 13)*, Tech. Rep. ATL-SOFT-PUB-2007-003. ATL-COM-SOFT-2007-008, CERN, Geneva, Jun, 2007.
- [36] T. G. Cornelissen, P. F. van der Heijden, F. L. Linde, S. C. M. Bentvelsen, and P. M. Kluit, *Track Fitting in the ATLAS Experiment*. PhD thesis, U. Amsterdam, Amsterdam, 2006. Presented on 12 Dec 2006.
- [37] R. Fruhwirth, *Application of Kalman filtering to track and vertex fitting*, Nucl.Instrum.Meth. **A262** (1987) 444–450.
- [38] A. Alonso, *Transition Radiation Tracker calibration, searches beyond the Standard Model and multiparticle correlations in ATLAS*. PhD thesis, Lund U., Apr, 2012. Presented 20 May 2012.
- [39] ATLAS Collaboration Collaboration, *Calibration of the ATLAS Transition Radiation Tracker*, Tech. Rep. ATLAS-CONF-2011-006, CERN, Geneva, Feb, 2011.
- [40] S. P. Martin, *A Supersymmetry Primer*, Tech. Rep. hep-ph/9709356, Sep, 1997.
- [41] J. Wess and B. Zumino, *Supergauge transformations in four dimensions*, Nucl. Phys. B **70** no. CERN-TH-1753. 1, (1974) 39–50.
- [42] J.-L. Gervais and B. Sakita, *Field Theory Interpretation of Supergauges in Dual Models*, Nucl.Phys. **B34** (1971) 632–639.
- [43] S. Weinberg, *Implications of Dynamical Symmetry Breaking*, Phys.Rev. **D13** (1976) 974–996.
- [44] R. M. Barnett, J. F. Gunion, and H. E. Haber, *Discovering supersymmetry with like sign dileptons*, Phys. Lett. **B 315** (1993) 349, hep-ph/9306204.
- [45] B. Kayser, *Neutrino Mass, Mixing, and Flavor Change*, Tech. Rep. hep-ph/0211134, Nov, 2002.

- [46] R. Franceschini, T. Hambye, and A. Strumia, *Type-III see-saw at LHC*, Phys. Rev. **D 78** (2008) 033002, [arXiv:0805.1613 \[hep-ph\]](#).
- [47] P. M. Gell-Mann and R. Slansky, *Supergravity*. North Holland, 1979.
- [48] W. Chao, Z. Si, Z. Xing, and S. Zhou, *Correlative signatures of heavy Majorana neutrinos and doubly-charged Higgs bosons at the Large Hadron Collider*, Phys. Lett. **B 666** (2008) 451–454, [arXiv:0804.1265 \[hep-ph\]](#).
- [49] A. Pilaftsis, *Radiatively Induced Neutrino Masses and Large Higgs-Neutrino Couplings in the Standard Model with Majorana Fields*, Z. Phys. C **55** no. hep-ph/9901206, (1992) 275–282.
- [50] A. G. Akeroyd and M. Aoki, *Single and pair production of doubly charged Higgs bosons at hadron colliders*, Phys. Rev. **D 72** (2005) 035011, [hep-ph/0506176](#).
- [51] A. Hektor, M. Kadastik, M. Muntel, M. Raidal, and L. Rebane, *Testing neutrino masses in little Higgs models via discovery of doubly charged Higgs at LHC*, Nucl. Phys. **B 787** (2007) 198–210, [arXiv:0705.1495 \[hep-ph\]](#).
- [52] M. Muhlleitner and M. Spira, *A Note on doubly charged Higgs pair production at hadron colliders*, Phys. Rev. **D 68** (2003) 117701, [hep-ph/0305288](#).
- [53] K. Huitu and J. Maalampi, *The Higgs sector of a supersymmetric left-right model*, Phys. Lett. B **344** (1995) 217–224.
- [54] G. Senjanovic and R. N. Mohapatra, *Exact left-right symmetry and spontaneous violation of parity*, Phys. Rev. **D 12** (1975) 1502.
- [55] M. Schmaltz and D. Tucker-Smith, *Little Higgs Review*, Ann. Rev. Nucl. Part. Sci **55** (2005) 229–270.
- [56] N. Arkani-Hamed et al., *The Minimal Moose for a Little Higgs*, JHEP **08** (2002) 021, [hep-ph/0206020](#).
- [57] M. Nebot, J. F. Oliver, D. Palao, and A. Santamaria, *Prospects for the Zee-Babu model at the CERN LHC and low energy experiments*, Phys. Rev. **D 77** (2008) 093013, [arXiv:0711.0483 \[hep-ph\]](#).
- [58] K. S. Babu, *Model of ‘Calculable’ Majorana Neutrino Masses*, Phys. Lett. **B 203** (1988) 132.
- [59] N. Arkani-Hamed, S. K. Dimopoulos, and G. Dvali, *The Hierarchy Problem and New Dimensions at a Millimeter*, Phys. Lett. B **429** no. hep-ph/9803315. SLAC-PUB-7769. SU-ITP-98-13. 33-4, (1998) 263–72. 16 p.
- [60] S. Dimopoulos and G. Landsberg, *Black Holes at the Large Hadron Collider*, Phys. Rev. Lett. **87** (2001) 161602. <http://link.aps.org/doi/10.1103/PhysRevLett.87.161602>.

- [61] S.Hawkins, *Particle creation by black holes*, Comm. Math. Phys. **43** no. 3, (1975) 199–200.
- [62] ATLAS Collaboration Collaboration, G. Aad et al., *Search for Microscopic Black Holes in a Like-sign Dimuon Final State using large Track Multiplicity with the ATLAS detector*, Phys. Rev. D **88** no. arXiv:1308.4075. CERN-PH-EP-2013-120, (2013) 072001. 10 p. Comments: 10 pages plus author list (22 pages total), 7 figures, 4 tables, submitted to PRD, All figures including auxiliary figures are available at <http://atlas.web.cern.ch/Atlas/GROUPS/PHYSICS/PAPERS/EXOT-2013-04/>.
- [63] ATLAS Collaboration, *Search for same-sign top-quark production and fourth-generation down-type quarks in pp collisions at $\sqrt{s} = 7$ TeV with the ATLAS detector*, JHEP **04** (2012) 069, arXiv:1311.6736 [hep-ex].
- [64] J. Aguilar-Saavedra and M. Perez-Victoria, *No like-sign tops at Tevatron: Constraints on extended models and implications for the t \bar{t} asymmetry*, Phys.Lett. **B701** (2011) 93–100.
- [65] ATLAS Collaboration, *Electron reconstruction and identification efficiency measurements with the ATLAS detector using the 2011 LHC proton–proton collision data*, Eur. Phys. J. C **74** (2014) 2941, arXiv:1404.2240 [hep-ex].
- [66] Inga Run Helgadottir, *Search for same-sign dilepton signatures with the ATLAS detector*. PhD thesis, U. Lund, Lund, 2014. Masters thesis presented Jan, 2014.
- [67] H. M.Hance, D.Olivito, *Performance Studies for e/γ Calorimeter Isolation*,.
- [68] R. Nicolaidou, L. Chevalier, S. Hassani, J. F. Laporte, E. L. Menedeu, and A. Ouraou, *Muon identification procedure for the ATLAS detector at the LHC using Muonboy reconstruction package and tests of its performance using cosmic rays and single beam data*, Journal of Physics: Conference Series **219** no. 3, (2010) 032052.
- [69] M. Cacciari, G. P. Salam, and G. Soyez, *The anti- k_t jet clustering algorithm*, JHEP **04** (2008) 063, arXiv:0802.1189 [hep-ph].
- [70] T. Gleisberg et al., *Event generation with SHERPA 1.1*, J. High Energy Phys. **02** (2009) 007, arXiv:0811.4622 [hep-ph].
- [71] J. Alwall, M. Herquet, F. Maltoni, O. Mattelaer, and T. Stelzer, *MadGraph/MadEvent v4: The New Web Generation*, J. High Energy Phys. **09** (2007) 028, arXiv:0706.2334 [hep-ph].
- [72] T. Sjöstrand, S. Mrenna, and P. Skands, *A Brief Introduction to PYTHIA 8.1*, Comput. Phys. Commun. **178** (2008) 852, arXiv:0710.3820 [hep-ph].
- [73] T. Sjöstrand, S. Mrenna, P. Skands, *PYTHIA 6.4 physics and manual*, JHEP **05** (2006) 026, arXiv:hep-ph/0603175.

- [74] H. L. Lai et al., *New parton distributions for collider physics*, Phys. Rev. **D 82** (2010) 074024, [arXiv:0802.0007](#) [hep-XX].
- [75] J. M. Campbell and R. K. Ellis, *MCFM for the Tevatron and the LHC*, Nucl.Phys.Proc.Suppl. (2010) 205–206, [arXiv:1007.3492](#) [hep-ph].
- [76] J. Pumplin, D. R. Stump, J. Huston, H. L. Lai, P. Nadolsky, and W. K. Tung, *New Generation of Parton Distributions with Uncertainties from Global QCD Analysis*, JHEP **07** (2002) 012, [hep-ph/0201195](#).
- [77] A. Kardos et al., *Top quark pair production in association with a Z-boson at NLO accuracy*, Phys. Rev. **D 85** (2012) 054015, [arXiv:1111.0610](#) [hep-ph].
- [78] J. M. Campbell and R. K. Ellis, *$t\bar{t}W^\pm$ production and decay at NLO*, JHEP **07** (2012) 052, [arXiv:1204.5678](#) [hep-ph].
- [79] M. Mangano et al., *ALPGEN, a generator for hard multiparton processes in hadronic collisions*, JHEP **07** (2003) 001, [arXiv:hep-ph/0206293](#).
- [80] S. Catani et al., *Vector boson production at hadron colliders: A Fully exclusive QCD calculation at NNLO*, Phys. Rev. Lett. **103** (2009) 082001, [arXiv:0903.2120](#) [hep-ph].
- [81] G. Corcella et al., *HERWIG 6: An Event generator for hadron emission reactions with interfering gluons (including supersymmetric processes)*, JHEP **01** (2001) 010, [hep-ph/0011363](#).
- [82] A. D. Martin, W. J. Stirling, R. S. Thorne, G. Watt, *Parton distributions for the LHC*, Eur. Phys. J. **C 63** (2009) 189–285, [arXiv:0901.0002](#) [hep-ph].
- [83] S. Frixione, B. R. Webber, *Matching NLO QCD computations and parton shower simulations*, JHEP **06** (2002) 029, [arXiv:0709.2092](#) [hep-ph].
- [84] S. Frixione, F. Stoeckli, P. Torrielli, B. R. Webber, C. D. White, *The MC@NLO 4.0 Event Generator*, [arXiv:1010.0819](#) [hep-ph].
- [85] M. Cacciari et al., *Top-pair production at hadron colliders with next-to-next-to-leading logarithmic soft-gluon resummation*, Phys. Lett. **B 710** (2012) 612–622, [arXiv:1111.5869](#) [hep-ph].
- [86] P. Bernreuther, M. Czakon, and A. Mitov, *Percent Level Precision Physics at the Tevatron: First Genuine NNLO QCD Corrections to $q\bar{q} \rightarrow t\bar{t} + X$* , Phys. Rev. Lett. **109** (2007) 132001, [arXiv:1204.5201](#) [hep-ph].
- [87] M. Czakon and A. Mitov, *NNLO corrections to top-pair production at hadron colliders: the all-fermionic scattering channels*, JHEP **12** (2012) 054, [arXiv:1207.0236](#) [hep-ph].

- [88] M. Czakon and A. Mitov, *NNLO corrections to top pair production at hadron colliders: the quark-gluon reaction*, JHEP **01** (2013) 080, [arXiv:1210.6832 \[hep-ph\]](#).
- [89] M. Czakon, P. Fiedler, and A. Mitov, *The total top quark pair production cross-section at hadron colliders through $O(\alpha_s^4)$* , Phys. Rev. Lett. **110** (2013) 252004, [arXiv:1303.6254 \[hep-ph\]](#).
- [90] M. Czakon and A. Mitov, *Top++: A Program for the Calculation of the Top-Pair Cross-Section at Hadron Colliders*, [arXiv:1112.5675 \[hep-ph\]](#).
- [91] N. Kidonakis, *NNLL resummation for s-channel single top quark production*, Phys. Rev. D **81** (2010) 054028, [arXiv:1001.5034 \[hep-ph\]](#).
- [92] N. Kidonakis, *Two-loop soft anomalous dimensions for single top quark associated production with a W- or H-*, Phys. Rev. D **82** (2010) 054018, [arXiv:1005.4451 \[hep-ph\]](#).
- [93] J. M. Butterworth, J. R. Forshaw, M. H. Seymour, *Multiparton interactions in photoproduction at HERA*, Z. Phys. C **72** (1996) 637, [arXiv:hep-ph/9601371 \[hep-ph\]](#).
- [94] ATLAS Collaboration Collaboration, *ATLAS inner detector: Technical Design Report, 1*. Technical Design Report ATLAS. CERN, Geneva, 1997.
- [95] ATLAS Collaboration Collaboration, K.Hamano, A.Hawkins, E.Lytken, F.Nuti, I.Run-Helgadottir, O.Viazlo, M.Wielers, *Internal Note in ATLAS for publication: Search for anomalous production of prompt like-sign lepton pairs and doubly charged Higgs bosons with $\sqrt{s} = 8$ TeV pp collisions using the ATLAS detector*, Internal Note (2014) .
- [96] ATLAS Collaboration Collaboration, G. Aad et al., *Search for supersymmetry at $\sqrt{s}=8$ TeV in final states with jets and two same-sign leptons or three leptons with the ATLAS detector*, JHEP **1406** (2014) 035, [arXiv:1404.2500 \[hep-ex\]](#).
- [97] T. A. collaboration, *Electron efficiency measurements with the ATLAS detector using the 2012 LHC proton-proton collision data*.
- [98] *Preliminary results on the muon reconstruction efficiency, momentum resolution, and momentum scale in ATLAS 2012 pp collision data*, Tech. Rep. ATLAS-CONF-2013-088, CERN, Geneva, Aug, 2013.
- [99] ATLAS Collaboration Collaboration, *Luminosity Determination in pp Collisions at $\sqrt{s} = 7$ TeV using the ATLAS Detector in 2011*, Tech. Rep. ATLAS-CONF-2011-116, CERN, Geneva, Aug, 2011.
- [100] ATLAS Collaboration, *The simulation principle and performance of the ATLAS fast calorimeter simulation FastCaloSim*, ATL-PHYS-PUB-2010-013, <http://cds.cern.ch/record/1300517>.

- [101] ATLAS Collaboration, *The ATLAS Simulation Infrastructure*, Eur. Phys. J. **C 70** (2010) 823, [arXiv:1005.4568 \[physics.ins-det\]](#).
- [102] A. L. Read, *Presentation of search results: the CL s technique*, Journal of Physics G: Nuclear and Particle Physics **28** no. 10, (2002) 2693.
- [103] L. Moneta, K. Belasco, K. Cranmer, A. Lazzaro, D. Piparo, G. Schott, W. Verkerke, M. Wolf, K. Belasco, K. Cranmer, A. Lazzaro, D. Piparo, G. Schott, W. Verkerke, and M. Wolf, *The RooStats Project*, PoS **ACAT2010** no. arXiv:1009.1003, (2010) 057. Comments: 11 pages, 3 figures, ACAT2010 Conference Proceedings.
- [104] J. M. Campbell, J. Huston, and W. Stirling, *Hard Interactions of Quarks and Gluons: A Primer for LHC Physics*, Rept.Prog.Phys. **70** (2007) 89.
- [105] “Frequentist limit recommendation implementation (Internal).”
<https://twiki.cern.ch/twiki/bin/viewauth/AtlasProtected/FrequentistLimitRecommendationImplementation>.
- [106] ATLAS Collaboration, *Search for doubly-charged Higgs bosons in like-sign dilepton final states at $\sqrt{s} = 7$ TeV with the ATLAS detector*, Eur. Phys. J. **C 72** (2012) 2244, [arXiv:1210.5070 \[hep-ex\]](#).
- [107] CMS Collaboration Collaboration, S. Chatrchyan et al., *Search for new physics in events with same-sign dileptons and b jets in pp collisions at $\sqrt{s} = 8$ TeV*, JHEP **1303** (2013) 037.
- [108] *Search for New Physics in Events with Three Charged Leptons with the ATLAS detector*, Tech. Rep. ATLAS-CONF-2013-070, CERN, Geneva, Jul, 2013.
- [109] *Identification of the Hadronic Decays of Tau Leptons in 2012 Data with the ATLAS Detector*, Tech. Rep. ATLAS-CONF-2013-064, CERN, Geneva, Jul, 2013.
- [110] ATLAS Collaboration Collaboration, *Commissioning of the ATLAS high-performance b-tagging algorithms in the 7 TeV collision data*, Tech. Rep. ATLAS-CONF-2011-102, CERN, Geneva, Jul, 2011.